



MODELLING, MATERIALS AND METHODS FOR NEEDLE INSERTION
INVESTIGATION IN BIOMECHANICS

Sarah Elizabeth Falconer, M.Eng

Thesis submitted for the degree of
Doctor of Philosophy

February 2020

The University of Sheffield
Department of Mechanical Engineering

ABSTRACT

This project aimed to investigate the forces that both needle and tissue experienced during a needle insertion, and how they altered the needles trajectory. An investigation into the current literature showed that existing skin tissue surrogates did not perform similarly to real skin tissue *in vivo* during needle insertions. A new surrogate is required to aid with validation for computational models of needle insertions, while avoiding the ethical issues raised from testing real tissue. This study developed an improved skin tissue surrogate for use in photoelastic testing which focused on replicating the fracture mechanism observed during a needle insertion through human skin tissue.

It is demonstrated that konjac glucomannan gel fractures in the same way as human skin tissue. Experimental assessments determined that at a concentration of 1.5% gel powder to water konjac jelly had a stiffness which closely matched the stiffness of human skin tissue *in vivo*.

In order to use the surrogate in photoelastic analysis it must be clear and exhibit temporary birefringence, and it is shown that with careful preparation konjac satisfies these criteria. The strain optic coefficient for the gel is determined, which links the optical response to the strain and stress experienced by the surrogate.

A variety of needle insertion experiments were conducted which assess how varying the insertion speed, needle length, and needle gauge affect the overall response. The results prove that konjac jelly accurately replicates needle insertion response through soft tissue better than existing surrogates.

With use of the GFP2500 poleidoscope, a novel digital polariscope, full field and directional information from a needle insertion is obtained. The results identify never-before-seen locations of principal strain magnitude near the puncture surface. For the first time the forces directional response was reported, and show how a bending moment acts on the needle; resulting in deflection.

ACKNOWLEDGEMENTS

I would like to thank both my Ph.D. supervisors Dr. Rachel Tomlinson and Dr. Zeike Taylor, whose guidance and advice over the years has been astounding. I have been incredibly fortunate to have two supervisors who have been engaged and encouraging throughout the course of this research project.

I am deeply grateful for the help provided by my partner, Shaun Smith, who has supported me throughout my time at Sheffield. His love and advice has helped me reach the end of this marvellous journey.

I am indebted to the technical staff within the Department of Mechanical Engineering. In particular I would like to thank Richard Kay and Jamie Booth, who were always willing to assist with the experimental work.

I am thankful to my family for supporting me throughout this journey. I am forever grateful to my parents; Robert and Christine Falconer, for their unconditional love, encouragement, and support for everything I have attempted. I am also fortunate to have two supporting brothers; Richard and Graham Falconer, who also helped me throughout this research journey. I am also thankful to my partner's family; Sue, Daryl, and Stacey Smith, who have been there for me when my own family could not.

I am grateful to have an optimistic support network of friends who have helped me see the positive outcomes of events when I was disheartened; Samantha Abrego, Emily Dwyer, and Emma Roberts. Thank you for your kindness.

CONTENTS

ABSTRACT	II
ACKNOWLEDGEMENTS	III
CONTENTS	IV
NOMENCLATURE	IX
GLOSSARY	X
INTRODUCTION	1
1 LITERATURE REVIEW	4
1.1 Needle insertion	4
1.1.1 Phases and forces involved in a needle insertion	4
1.1.2 Different needle tip types	6
1.1.3 Different needle diameters	7
1.1.4 Speed of needle insertion	8
1.2 Biomechanical behaviour of human skin tissue	11
1.2.1 Skin tissue structure	11
1.2.2 Material resistance to crack growth	13
1.2.3 Mechanical properties	15
1.3 Photoelasticity	21
1.3.1 Birefringence	21
1.3.2 Photo-viscoelasticity	22
1.3.3 Plane polariscope	23
1.3.4 Circular polariscope	26
1.3.5 Phase stepping	31
1.3.6 Grey field polariscope	33
1.3.7 GFP2500 Poleidoscope	34
1.4 Potential tissue surrogates	40
1.4.1 Available skin tissue surrogates	40
1.4.2 Summary	42
1.4.3 Ballistic gelatine	43
1.4.4 Konjac	43
1.4.5 Carrageenan	45
1.4.6 Potential additives	45
1.5 Conclusion and direction of research	46

1.5.1	Material requirements	46
1.5.2	Optical properties	47
1.5.3	Needle investigation	47
1.5.4	Homogenous or heterogenous surrogate material	48
2	MECHANICAL CHARACTERISATION	50
2.1	Experimental considerations	51
2.2	Development of gelling process	52
2.3	Compression testing	54
2.3.1	Moulding of compression specimens	54
2.3.2	Compression test setup	54
2.3.3	Range of compression tests	56
2.3.4	Concentration analysis	57
2.3.5	Compression test results: Gelatine	62
2.3.6	Compression test results: Carrageenan	65
2.3.7	Compression test results: Konjac	68
2.3.8	Compression Results: Comparison	71
2.4	Tensile testing	73
2.4.1	Moulding of tensile specimens	73
2.4.2	Tensile test setup	74
2.4.3	Range of tensile tests	76
2.4.4	Tensile test results: Sugar addition	77
2.4.5	Tensile test results: Gelatine	79
2.4.6	Tensile test results: Carrageenan	80
2.4.7	Tensile test results: Konjac	81
2.4.8	Tensile test results: Comparison	82
2.5	Compressive and tensile summary	85
2.6	Continued assessment with konjac glucomannan	86
2.6.1	Effect of loading rate on mechanical properties	86
2.6.2	Assessing konjac jelly's birefringence and clarity	88
2.6.3	Conclusion	89
3	OPTICAL CHARACTERISATION	90
3.1	Strain optic coefficient theory	91
3.2	Experimental setup	93
3.2.1	Tensile optical experiments	94
3.3	Processing limitations	101
3.3.1	Motion	101
3.3.2	Heat errors	102

3.3.3	Uneven retardation maps	103
3.4	Strain optic coefficient validation	105
3.5	Conclusion	108
4	NEEDLE INSERTION EXPERIMENTS	109
4.1	Experimental Setup	110
4.1.1	Tanks	110
4.1.2	Needle Setup	111
4.1.3	Measurement of deflection	112
4.1.4	Optical analysis method	115
4.2	Homogenous surrogate: Biopsy needle insertion at various speeds	116
4.2.1	Overall force response during needle insertion and removal	116
4.2.2	Puncture force with biopsy needle	122
4.2.3	Average insertion force	123
4.2.4	Work done at varying insertion rates	124
4.2.5	Deflection angle at various insertion speeds	126
4.2.6	Deflection angle at various insertion depths	129
4.2.7	Optical analysis at the varying insertion speeds	129
4.2.8	Conclusion	132
4.3	Homogenous surrogate: Various needles at the same insertion speed	134
4.3.1	Optical analysis of needle insertions	135
4.3.2	Puncture force results for range of needle gauges	145
4.3.3	Deflection results for range of needle gauges	147
4.3.4	Conclusion	149
4.4	Inhomogeneous laminate surrogate: Biopsy insertion at same speed	150
4.4.1	Surrogate structure	150
4.4.2	Overall force response during needle insertion and removal	152
4.4.3	Deflection angle through different surrogate types	154
4.4.4	Optical analysis of the layered samples	155
4.4.5	Conclusion	157
4.5	Inhomogeneous particulate surrogate: Biopsy insertion at same speed	159
4.5.1	Overall force response during needle insertion and removal	160
4.5.2	Deflection angle through different surrogate types	161
4.5.3	Optical analysis of the particulate surrogate	162
4.5.4	Conclusion	166
4.6	Conclusion	167
5	DISCUSSION	169
5.1	Summary	169

5.2	Overall impact	170
5.2.1	Robotic surgery	170
5.2.2	Training physicians	170
5.2.3	Further needle development experimentations	170
5.3	Behaviour of developed surrogate	171
5.3.1	Experimental comparison	171
5.4	Theoretical Modelling	173
5.5	Discussion of main results	174
5.5.1	Development of a new skin tissue surrogate	174
5.5.2	Needle insertion experimentation	175
5.5.3	Speed assessment	176
6	FUTURE DEVELOPMENT	180
6.1.1	Modifying konjac surrogate	180
6.1.2	Microscopic analysis of needle insertion	181
6.1.3	Range of needles	182
6.1.4	Modified experimental setup	182
6.1.5	Measurement of deflection	183
6.1.6	Three-dimensional analysis	184
6.1.7	Modifying angle of insertion	185
6.1.8	Mechanical characterisation	185
7	CONCLUSION	186
7.1	Surrogate development	186
7.2	Optical analysis	187
7.3	Needle insertion experiments	187
7.3.1	Varying insertion speed	187
7.3.2	Various needle geometries	188
7.3.3	Inhomogeneous analysis	188
7.4	Optical analysis of needle insertions	188
	REFERENCES	190
8	APPENDIX	200
8.1	Full results for material development chapter	200
8.1.1	Concentration analysis	200
8.1.2	Compression results: Gelatine	204
8.1.3	Compression results: Carrageenan	207
8.1.4	Compression results: Konjac	210
8.1.5	Tensile results: sugar addition	213

8.1.6	Tensile results: Gelatine	214
8.1.7	Tensile results: Carrageenan	215
8.1.8	Tensile results: Konjac	216
8.1.9	Tensile results: with and without puncture	219
8.2	Numerical results used for determining strain optic coefficient in optical characterisation chapter	220
8.3	Full results from needle insertion experiments chapter	224
8.3.1	Needle response through inhomogeneous laminate surrogates	224
8.3.2	Needle response through inhomogeneous particulate surrogates	229

NOMENCLATURE

Symbol	Variable	Unit
a	Amplitude	mm
c	Speed of light in a vacuum	m/s
C_1, C_2	Resolved light vectors	cd
C'_1, C'_1	Phase shifted light vectors exiting specimen	cd
C''_1, C''_2	Separate electric light vector exiting analyser	cd
C_{ax}	Electric light vector exiting analyser	cd
C_f, C_s	Electric light vector change from quarter wave plate	cd
C'_f, C'_s	Electric light vectors exiting quarter wave plate	cd
C_{py}	Electric vector of linearly polarised light	cd
E	Elastic modulus	Pa
F	Force	N
f_ε	Strain optic coefficient specific to a wavelength	mm/fringe
h	Thickness	mm
I	Intensity of light	cd
$I_\#$	Output intensities at various orientations	cd
i_m	Intensity of stray light	cd
I_0	Background light intensity	cd
i_v	Intensity of light with parallel polariscope axis	cd
k	Constant	-
K_ε	Strain optic coefficient	fringe
$K_{\varepsilon S}$	Strain optic coefficient specific to software	-
L	Strength of light source	cd

m	Fringe order to be 'moved'	-
n_1, n_2	Principal indices of refraction	-
n	Index of refraction	-
N	Fringe order	-
S	Signal Response from camera	nm
t	Time	s
ν	Poisson ratio	-
w	Speed of light through material	m/s
α	Polariser angle	°
β	Rotation of output polariser	rad
γ	Degree of rotation	rad
δ	Retardation	nm
Δ	Relative retardation	nm
Δ_1, Δ_2	Phase shift	nm
$\varepsilon_1, \varepsilon_2$	Principal strains	-
θ	Isoclinic angle	rad
λ	Wavelength of light	nm
σ_1, σ_2	Principal stresses	Pa
φ	Rotation of output quarter wave plate	rad
ω	Angular frequency	m/s

GLOSSARY

Term	Meaning
<i>In vivo</i>	Performed or measured within a living organism
<i>Ex vivo</i>	Performed or measured in an external environment
Adipose Tissue	Loose connective tissue which stores fat

INTRODUCTION

The aim of this project is to investigate the forces that both needles and tissue experience during a needle insertion, and how said forces alter the needles trajectory. When a needle is inserted deep into tissue it can miss its intended target due to the needle deflecting from its intended path. Needle deflection can be due to a variety of factors:

1. Asymmetrical needle shape

During a needle insertion the needle may experience uneven load distributions caused by the shape of the needle. These forces can cause large deflections and make it difficult to accurately predict the path which the needle will take.

2. Thin needles can bend during an insertion.

Many medical procedures require thin needles which have a low flexural rigidity; as a result they are susceptible to bending. Needle bending can emphasise the uneven load distribution along the length of the needle and cause it to deflect further.

3. Tissue moving during insertion.

The tissue also moves under the needles load which causes further difficulties when trying to access a target deep within the tissue, especially as the target may also move within the subject [1].

These deflections can cause problems in procedures requiring high accuracy; which can potentially lead to misdiagnosis, or having to repeat a procedure and thus causing otherwise unnecessary trauma to a patient.

Investigating the interaction between needles and tissues has been the topic of many researchers in recent years [2]. A 'surrogate material' is required for needle insertion experimentation; therefore tissue surrogates must be created which closely replicate the complex properties of soft tissue. Many materials have been developed to simulate tissue, such as ballistic gel and silicone. These are commonly used for large scale testing and therefore can neglect the small scale properties of tissue [3], such as its resistance to tearing. Existing surrogates 'tear' when punctured with a needle; where the crack propagates on the tissue surface either side of the needle. Skin tissue does not fracture in this way; when a needle is

inserted into skin tissue it clings to the needle. Previous work has had difficulty finding a suitable material which fractures in the same way as skin tissue [4, 5]. However, Tomlinson and Taylor discovered that konjac glucomannan clings to the needle when punctured [4].

Material assessment

Two gels were investigated for their potential as a skin tissue surrogate: carrageenan and konjac glucomannan. Carrageenan is the thickening agent found within konjac, which may also resist crack growth. Ballistic gelatine will also be subjected to the same mechanical tests in order to provide a comparison, as gelatine is often used as a skin tissue surrogate. Different concentrations of carrageenan and konjac will be created and subjected to mechanical testing in order to compare their properties to the published properties of human skin tissue. This will be done using compression and tensile testing on a Tinius Olsen machine. The gels' optical properties will also be assessed to determine their suitability for photoelastic testing.

Optical analysis

Photoelastic analysis will be used to assess the principal strain distribution in the surrogate material caused by a needle insertion. Within photoelastic analysis a complete and continuous strain field is acquired, rather than discrete points. A new GFP2500 poleidoscope will be used for the analysis; it is a digital polariscope which allowed for the capture of instantaneous, dynamic, full field magnitude and directional data using one piece of apparatus [6]. Previous research on the deflection and motion of needles through soft tissue has only recorded the magnitude of the force response along the length of the needle. With use of the GFP2500 poleidoscope the direction of the force response can also be recorded. It is hoped that this directional data will shed light on the circumstances which cause needle deflection through soft tissue.

Photoelastic analysis will be used for the following study as it not only allows for the live recording of the principal strains in the material, but also viewing of the needle as it travels through the material. Therefore any deflections can be easily recorded, analysed, and related to the stresses and strains experienced by the surrogate material due to needle insertion.

Needle experiments

A variety of needle insertion experiments will be conducted to determine how changing aspects of a needle insertion change the force response, principal strain field in the surrogate, and overall deflection of the needle. The results will be compared to needle insertion experiments through human skin tissue to assess whether the new surrogate produces the same response.

The biopsy needle will be the main focus of this particular research project. Biopsy needles have a long shaft with complex asymmetrical tip geometry, and an example of a biopsy needle with a shaft thickness of 2 mm is shown in Figure 0-1.



Figure 0-1: Tru-cut biopsy needle

Biopsy needles will be inserted into the new surrogate material at varying speeds to assess whether insertion speed affects the resulting puncture force and deflection amount. Within the literature there is conflict between the effect of changing needle insertion speed between tissue surrogates and real tissue. It was found that increased insertion speed through tissue surrogates corresponded to an increase in force response, and increased insertion speed through real tissue corresponded to a decrease in force response. The biopsy needles will also be inserted at varying depths to determine whether insertion depth has an effect on the deflection. It is hypothesized that an increased insertion amount will correspond with an increased deflection angle.

Different needle shapes will also be investigated as previous research has shown that even altering the tip geometry alone can cause significant effects on the strain experienced by the tissue [7].

Biopsy needles will also be inserted into inhomogeneous tissue surrogates. It is hypothesized that the deflection amounts through inhomogeneous surrogate will be greater as there may be more uneven loading on the needle, which could lead to greater deflection.

All of the needle insertion experiments will be recorded using the GFP2500 poleidoscope. Full field principal strain maps will be presented, along with directional information. It is hoped that this new data reveals how the needle affects the surrogate as a whole during a needle insertion.

1 LITERATURE REVIEW

Before any work could begin, a study on the previous research was conducted. This chapter will outline some of the main research findings that relate to the aims of this project.

1.1 Needle insertion

The main focus of this study is to develop an understanding of the forces experienced by both needle and tissue during a needle insertion.

1.1.1 Phases and forces involved in a needle insertion

There are three distinct phases during needle insertion into soft tissue. These phases may be repeated if the needle encounters additional tissue boundaries within the material, such as pockets of varying material properties.

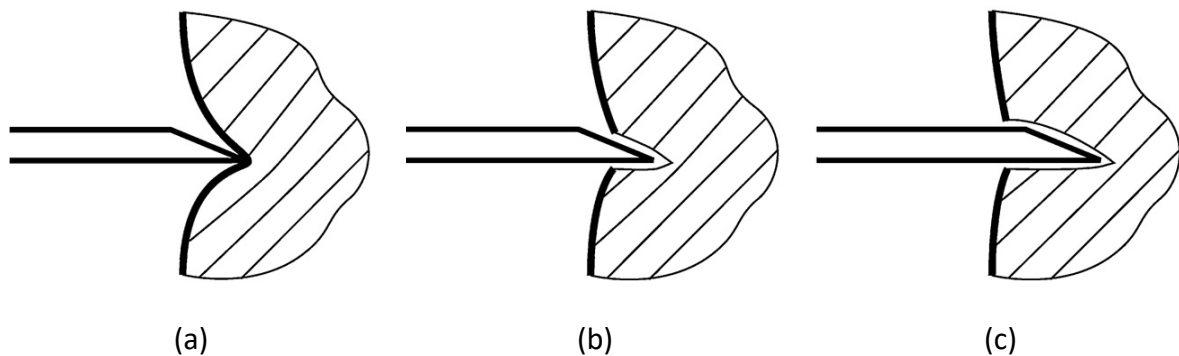


Figure 1-1: Depiction of basic phases in needle insertion: a) boundary displacement; b) tip insertion; c) tip and shaft insertion. [2]

The first phase, depicted in Figure 1-1 (a), begins when a needle contacts the tissue boundary and ends when the boundary is breached. During this phase the tissue boundary deforms under the load provided by the needle.

It was shown that there is a non-linear increase in force response as the needle presses against the tissue boundary [8, 9]. Eventually, a puncture will occur and this can be pinpointed when the force response drops significantly, which signals the end of this phase.

The second phase, depicted in Figure 1-1 (b), starts when the needle breaches the tissue boundary, and ends when the tissue slides from the needle tip to the shaft. During this stage the contact area between the needle tip and tissue will increase, and the crack in the tissue will widen. The widening can increase gradually or rupture. For a given insertion rate, the speed of the crack growth mainly depends on the toughness of the material and the strain-energy stored due to the material's deformation. A needle can undergo a repeated puncture phase in internal tissue if it reaches an internal tissue boundary [2]. This can cause uneven or inconsistent force readings when puncturing inhomogeneous tissue.

The third phase, depicted in Figure 1-1 (c), starts shortly after the tissue travels from the tip of the needle to the needle shaft, and ends either when the needle is stopped, or when a new internal tissue boundary is met. During this phase the contact area between the tip and tissue is constant, and the boundary crack does not increase in size. Therefore, any increase in force to advance the needle would mostly be due to friction as more of the needle shaft is inserted. The force changes associated with the three phases are depicted in Figure 1-2.

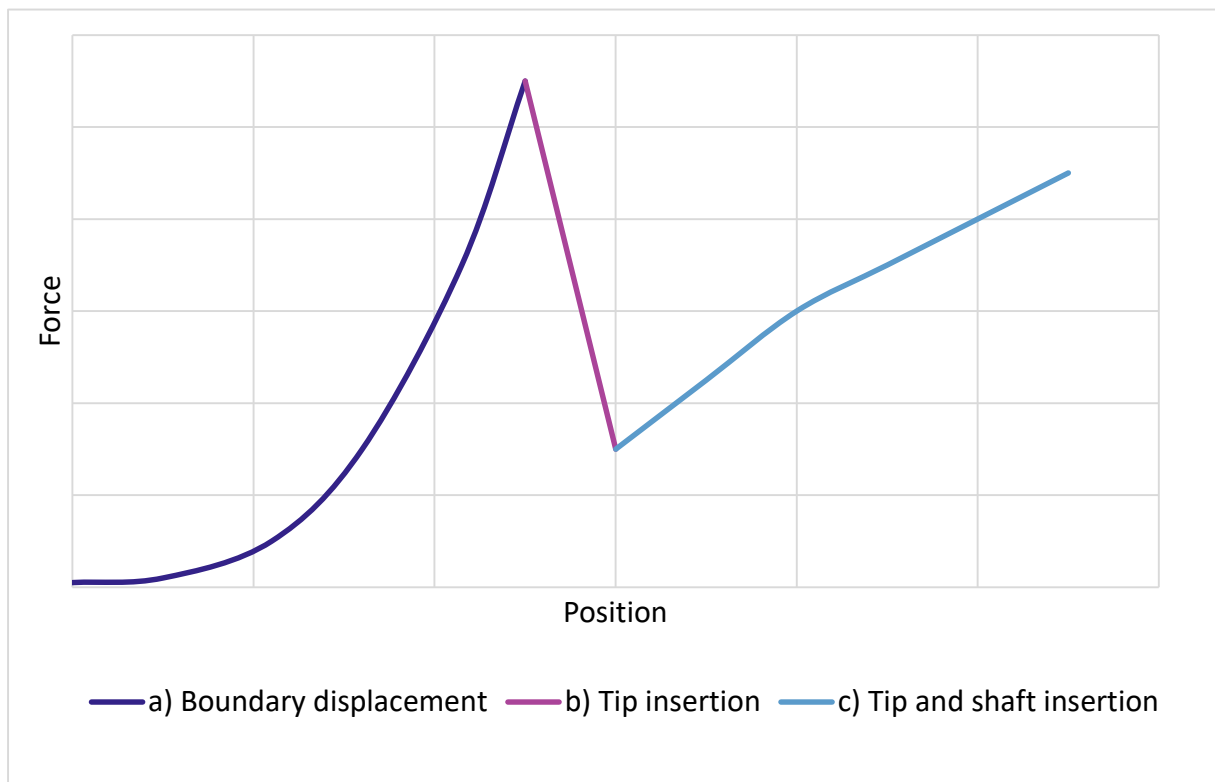


Figure 1-2: Figure depicting the general force response during the puncture stage of a needle insertion [10]

Okamura *et al.* used experiments to validate theoretical models of force involving material stiffness, friction, and cutting [11]. Their study considered the total force acting on the needle to be the sum of three components:

$$F_{needle}(x) = F_{cutting}(x) + F_{stiffness}(x) + F_{friction}(x) \quad \text{Equation 1.1}$$

where $F_{cutting}$ is the force required to continue tissue fracture, $F_{stiffness}$ is the resultant force from tissue deformation, and $F_{friction}$ exists between the needle and tissue due to the tissue's clamping effect.

1.1.2 Different needle tip types

Different needle tips are required for the different medical procedures. Biopsy procedures require a solid back bevel needle stylet tip, where the compartment for the biopsy sample is located further along the needle shaft. Whereas needles for drug delivery or fluid removal require a hollow needle. A selection of the various needle types are shown in Figure 1-3.

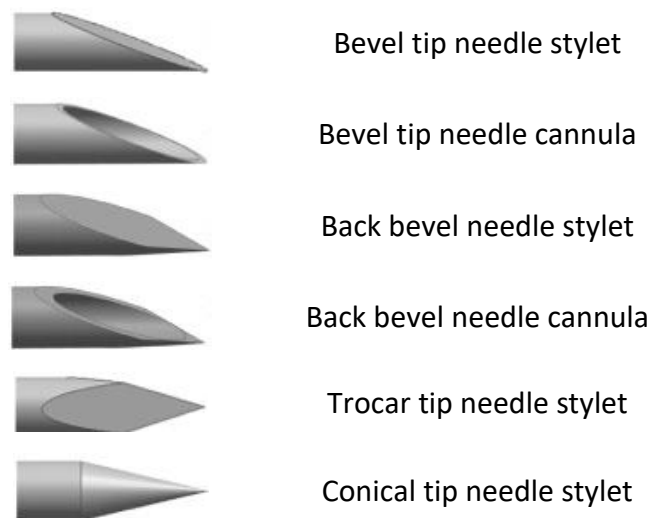


Figure 1-3: Examples of common needle tip types [12]

Okamura *et al.* and O'Leary *et al.* showed that needle tip geometry has a great effect on the recorded forces when inserted into silicone rubber [11, 13]. It was found that bevel needles experience more bending than conical or triangular (trocar) tipped needles as they receive higher force reactions on one side due to their asymmetrical shape.

Webster *et al.* conducted experiments to assess how the angle of the bevel tip affects the needle deflection [14], where bevel angle is the angle between the centre of the needle shaft and the slope of the needle tip. Needles with bevel angles between 5° and 80° were inserted

into a rubber muscle surrogate and results showed that decreasing the bevel angle increased the amount of needle deflection from the vertical path. This was reiterated in a study by Misra *et al.* [15], who also used finite element analysis to determine the forces experienced along the needle. It was also shown that the forces change further with varying bevel angles. It was assumed that the symmetrical triangular and conical needles only experienced bending due to encountering random density variations in the surrogate tissue. It was therefore assumed that these density variations affect the asymmetric needles more than their symmetrical counterpart as they are already prone to uneven force distribution from their asymmetrical shape.

Kataoka *et al.* and Alterovitz *et al.* discussed that the needle deflection is generally due to the bevel tip geometry and diameter of the needle, and not influenced greatly by material inhomogeneity [16, 17]. This will be investigated in chapter 4, where needles will be inserted into the newly developed homogenous and inhomogeneous surrogates and the deflection amounts will be compared.

1.1.3 Different needle diameters

Along with the different needle tip types, different needle gauges (diameters) are also used for a variety of medical procedures. Anecdotal evidence indicates that higher gauge (thinner) needles deflect more than those of lower gauge [18]. This was confirmed in a study by Okamura *et al.* where smaller diameter needles experienced more bending [11]. It was also shown that with greater needle diameters more material was displaced in the vicinity of the needle. As the needle diameter increased so does the overall surface area, this then increased the magnitude of reaction forces experienced by the needle from greater frictional forces.

Thompson *et al.* and Morton *et al.* used scaled-up needle models in order to aid visual analysis during their experiments [7, 19]. The needle models were made from 5 mm diameter solid steel rods. Unfortunately, this approach meant that the flexural stiffness of the needles was great, and did not accurately represent the flexural stiffness's of real needles with relation to skin tissue. The higher gauge needles (which have a reduced diameter) will have a lower flexural stiffness, and the flexural stiffness of cannula needles will be even lower due to their hollow geometry. Therefore, higher gauge needles will not resist bending as much as their lower gauge counterparts. Consequently, the difference between the stiffness of skin tissue

and the flexural stiffness of needles is greater for higher gauge needles. This relative difference in stiffness is likely what causes the greater needle deflection in higher gauge needles, as they have a reduced resistance to bending. Whereas the lower gauge needles will cause the material to deform greater amounts.

This study will use real needles commonly used in medicine and assess how flexural stiffness affects the overall deflection and force response. The results from the needle gauge assessment will be investigated in section 4.3.

1.1.4 Speed of needle insertion

A survey of results presented by van Gerwen *et al.* discussed that limited information was documented on the typical velocities of the needle during clinical procedures [2]. Anecdotal evidence indicates that the average speed for a biopsy procedure would lie around 10 mm/s. In cases where records of the velocities are taken, the velocities are found to be inconsistent [18]. It was noted that the speed of needle insertion is not a set variable; the speed that the physician inserts the needle will depend on a variety of factors, such as, but not limited to:

- Type of procedure
- Physician performing procedure
- Condition of patient

In van Gerwen’s survey four studies were presented which gathered some data on the average needle insertion velocity; a summary of the results is presented in Table 1-1 [2]. The table clearly shows the variance in needle insertion speeds between procedures.

Author	Procedure	Speed, mm/s
Hiemenz <i>et al.</i> 1997 [20]	Epidural	0.4 – 10
Healey <i>et al.</i> 2005 [21]	Interventional radiology	8.3
Abolhassani <i>et al.</i> 2006 [22]	Prostate brachytherapy	1 – 20
Podder <i>et al.</i> 2005 [23]	Prostate brachytherapy	1 – 1000

Table 1-1: Summary of values for approximate needle insertion speed.

Podder *et al.* showed that the needle speed within a single procedure is not consistent [23-25]. In the case of the prostate brachytherapy procedures the needle had an average speed of 100 mm/s during the initial insertion and 1 mm/s during the final approach. However, the overall range of the speed was between 1 mm/s and 1000 mm/s.

Conversely, nearly all experimental work in this area has employed constant insertion speeds [2]. Many investigations do not approach speeds faster than 10 mm/s. However, Podder *et al.* investigated the difference between a hand-held needle insertion with an average speed of 100 mm/s, and a robotic needle insertion at a constant speed of 100 mm/s [23]. It was found that the force response between the robotic and human experiments were similar. This study did neglect to mention whether the needle deflected different amounts with the different insertion methods.

A number of studies have assessed whether changing the speed of a needle insertion changes the force response in soft tissue surrogates. Crouch *et al.* investigated the effect of speed on needle insertion in silicone gel. It was found that an increased speed increased the insertion force, and overall slope of the force position curve [26]. Studies by DiMaio and Salcudean, and Podder *et al.* used PVC gel for their investigations [27, 28]. Both studies concluded that axial forces on the needle increased as the insertion speed was increased. Naemura *et al.* used silicon rubber in their analysis, however no clear relationship between needle insertion speed and force response was noted [29]. Meltsner *et al.* inserted needles into porcine gelatine [30], and found that at faster speeds the force vs. position curve was steeper, indicating a greater force response when the needle is inserted at greater velocities. It is apparent that there is a general trend in soft tissue surrogates where the speed of the needle insertion will affect the force response.

Further studies have conducted similar experiments assessing the effect of needle speed on force response in real tissues *ex vivo*. Kobayashi *et al.* performed needle insertions into porcine liver. In one study it was found that the puncture force was independent of needle velocity [31]. A further study by Kobayashi *et al.* attempted to assess the effects of needle insertion velocity on the frictional force. It was shown that friction increases with increasing velocity up to 2 mm/s. At higher speeds the frictional force remained constant [8]. Mahvash and Dupont investigated the effect of insertion velocity on puncture force into porcine heart

muscle [32]. They found a decrease in puncture force with increasing needle insertion velocities. Hing *et al.* used porcine liver as their assessment tissue for human operated needle insertions, and they found that an increase in needle insertion velocity led to a decrease in puncture force [33, 34]. They also found that an increased needle insertion speed led to an increased needle deflection [34]. Frick *et al.* investigated the effect of velocity on needle insertion into sheep skin [35]. Over a total of 135 needle insertions they found that velocity variations had no significant effect on axial force.

As described in the foregoing, soft tissue surrogates have generally produced higher reaction forces at higher insertion speeds, yet the opposite was found for the soft tissues tested *ex vivo*. This difference in response could also be due to an observed difference in the crack development between human skin tissue and conventional surrogates, which will be discussed in section 1.2.2. It has been observed that tissue surrogates ‘tear’ when punctured with a needle, which does not happen in skin tissue. This difference could also be due to the differences in the tribological behaviour of the needle-tissue interface. A needle inserting human skin tissue will be lubricated from the moisture within the skin tissue, whereas soft tissue surrogates like silicone rubber are relatively dry and tend to grip the needle. The combination of the dissimilar crack development, and differences in the tribological behaviour between real skin tissue and surrogates, could lead to the surrogates reporting inaccurate data.

In section 4.2 needles will be inserted into the newly developed surrogate at varying speeds to assess whether there is a link between speed of insertion and amount of needle deflection and force response.

1.2 Biomechanical behaviour of human skin tissue

This study will focus on developing a surrogate for human skin tissue, as current surrogates do not accurately replicate the fracture mechanism when a needle is inserted. In order for a suitable surrogate material to be developed a greater understanding on the interface between needle and skin tissue is required. This section will cover the properties of human skin tissue and discuss the viable material substitutes already available. The fracture differences will be discussed in section 1.2.2.

1.2.1 Skin tissue structure

Human skin tissue is a complex material; it can be separated into three main layers which have different functions and therefore different mechanical properties. These layers are depicted in Figure 1-4.

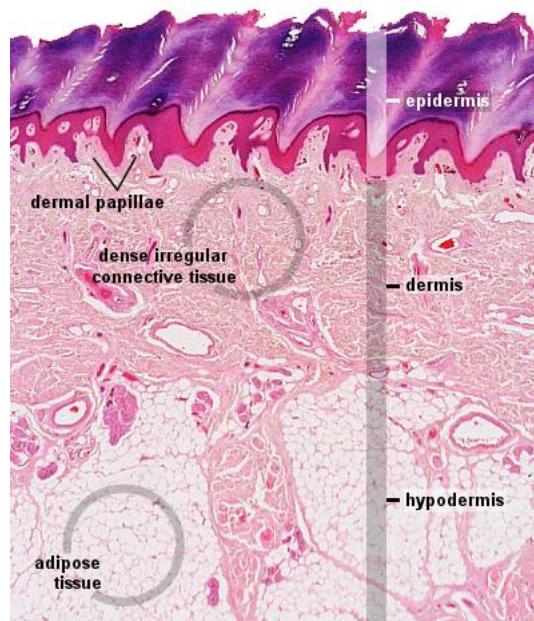


Figure 1-4: Micrograph displaying different layers of skin [36]

Epidermis

The epidermis is the outermost layer and consists of several layers of tissue. Depending on the location the thickness can vary between 0.032 mm to 1.5 mm [37-39]. The outermost layer has a 25 µm waterproof covering which prevents fluid ingestion and loss, it is constructed of corneocytes which lay flat and are held together by lipids which form a “brick-and-mortar” structure [40]. The outermost layer is greatly influenced by humidity and temperature compared with lower skin layers since it is in direct contact with the external environment [41]. The epidermis contributes minimally to the overall mechanical properties of tissue, although it was assumed that it does have an effect on puncture toughness [42].

Dermis

The dermis is a fibrous network of tissue that provides structure and resilience to the skin. It can be split further into the outermost papillary and the underlying reticular dermis. Their combined thickness is between 1 mm to 4 mm [37, 43]. The dermis layer contains elastin and collagen fibres in a matrix structure. The papillary dermis is thinner and contains smaller and more loosely connected collagen fibres in a vertical arrangement; this connects the epidermis to the reticular dermis. The reticular dermis' fibre matrix is orientated in plane with the skin [44], and it is also made up of collagen fibres and collagen fibrils. Due to its fibrous nature the dermis can allow for high levels of deformation as it can stretch and re-orientate [45]. Silver *et al.* noted differences between the collagen fibre structures in different age groups [42]. In young adults the collagen in the papillary dermis is a framework of randomly orientated fine fibres. The fibres appear as large, loose collagen bundles in the reticular dermis. With increasing age the collagen fibre density increases, and the bundles appear to unravel. This change in fibres also affects the mechanical properties of skin tissue.

Hypodermis

The hypodermis consists of fat and loose connective tissue. It is used for energy storage and has larger blood vessels and nerves than those found in the outer layers of skin. The thickness of this layer is between 1.9 mm and 7.1 mm, but varies considerably depending on the location [37, 46]; it is thickest on the palms of the hands, soles of the feet, and the rear.

1.2.2 Material resistance to crack growth

When skin is punctured with a needle the surrounding tissue doesn't tear; the material clings to the needle, which produces the friction force described in section 1.1.1. An example of a BD blood fill needle puncturing skin tissue can be seen in Figure 1-5.



Figure 1-5: Photograph of a BD blood fill needle puncturing skin.

Previous work has had difficulty finding a suitable material that doesn't tear when punctured with a needle [4, 5]. However, Tomlinson and Taylor discovered a potential tissue surrogate which, when punctured, clings to the needle [4]. Figure 1-6 shows an example of the same model of BD blood fill needle shown in Figure 1-5 puncturing konjac jelly. It can be seen that the crack profile between Figure 1-5 and Figure 1-6 is similar.

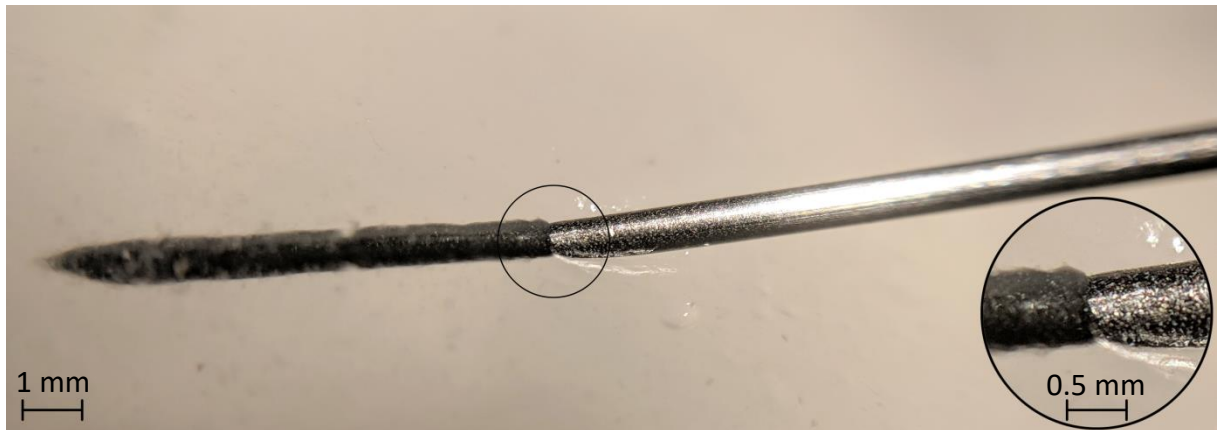


Figure 1-6: Photograph of a BD blood fill needle puncturing konjac jelly.

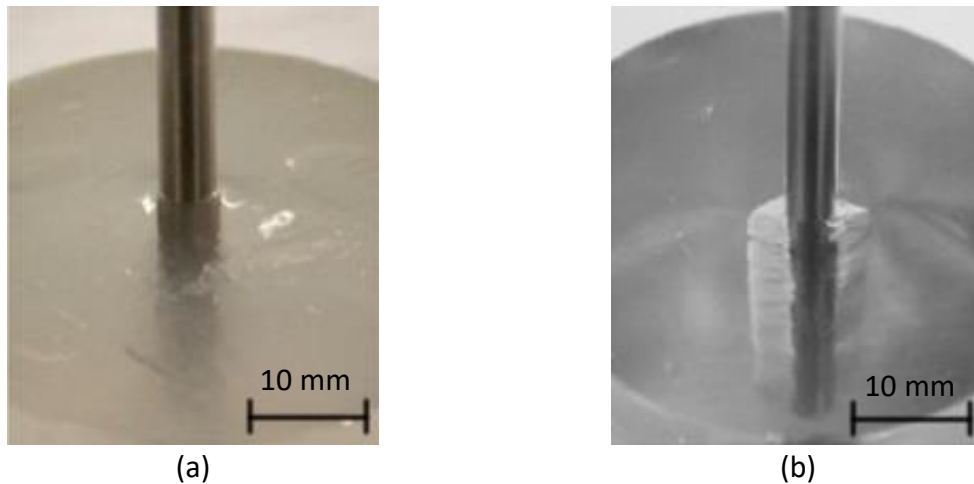


Figure 1-7: Photograph of needle inserted into a) konjac jelly and b) gelatine [4].

Figure 1-7 shows a comparison between the new konjac surrogate clinging to the needle, and an existing gelatine surrogate which tears. It can be seen that when the needle is inserted into gelatine the material tears, and parts of the needle are not in contact with the material. As a result of tearing the material does not clamp down on the needle as Okamura described [11], and as shown in Figure 1-5; the friction force experienced would be less than the friction found when inserting the needle into real skin. This tearing effect has been highlighted in the illustrations in Figure 1-8.

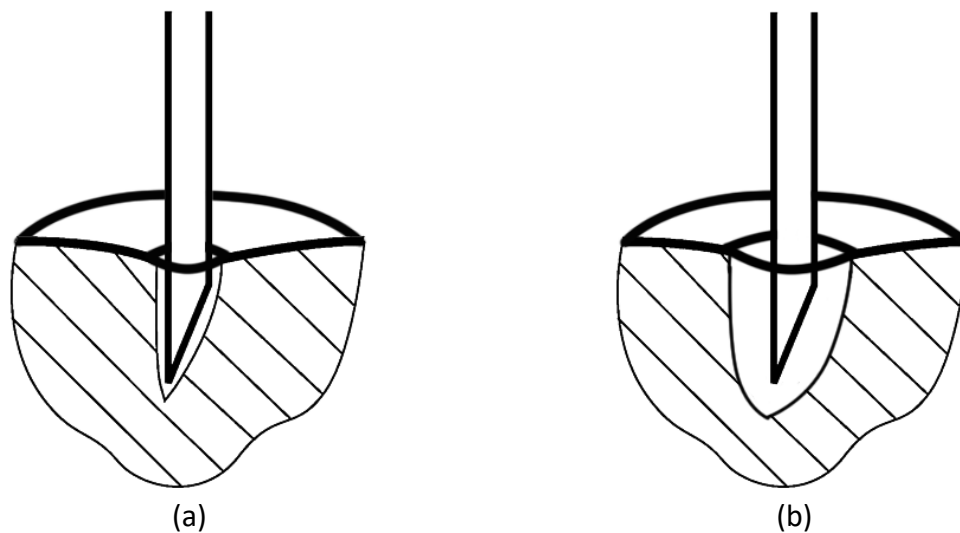


Figure 1-8: Illustration of needle inserted into a) non-tearing surrogate and b) tearing surrogate.

It is essential that the developed skin tissue surrogate does not tear when punctured with a needle, as the failure pattern would affect the trajectory of the needle by altering the strain/stress field ahead of the needle tip. It's not clear how the results can be translated to the case of real tissues if the potential surrogate fractures in a fundamentally different way.

Skin is not a homogenous material; it is made up of a fibrous network of tissue [44, 45, 47]. It is possible that the fibrous nature of tissue may also help with its resistance to tearing. Konjac jelly, the surrogate which resisted tearing, is made of plant extract. It may contain plant fibres which could cause its resistance to tearing [4].

The effect of including various lengths of plant fibres into ballistic gelatine was investigated by Aziz *et al.* [5]. Results from tensile experiments and from initial needle insertion experiments showed that fibre addition did not increase the material's resistance to crack growth. The fibres also trapped bubbles in the gel; the combination of bubbles and fibres resulted in an opaque gel which was no longer suitable for the planned optical analysis.

In chapter 2, a surrogate will be created which exhibits 'resistance to tearing'. This will ensure that the stress/strain field around the needle tip accurately emulates that developed in real tissue.

1.2.3 Mechanical properties

Skin exhibits viscoelastic behaviour; therefore, its stiffness should be defined using the dynamic modulus [48, 49]. The dynamic modulus describes the viscoelastic behaviour of the material through the storage modulus, which describes the stored energy in the elastic region, and the loss modulus, which describes the energy dissipated through heat in the viscous portion. Skin also exhibits some time-dependant behaviour, as such it may be ineffectual to characterise it only with a single elastic modulus – or, equivalently, to model it as purely elastic. Many studies have investigated the mechanical properties of tissue, both *in vivo* and *ex vivo*. Within the tissue engineering community, it is common to use a single elastic modulus to quantify stiffness of skin. Therefore, for the purpose of this investigation, it is more meaningful to measure the elastic modulus of the proposed skin tissue surrogate in order to present a comprehensible comparison. Furthermore, the analysis software required for the planned experiments requests an input of elastic modulus to process the results; this software will be discussed in chapter 3.

A summary of the results for elastic modulus of human skin tissue from various papers can be found in Table 1-2. The results of these studies differ greatly as the properties of tissue vary with location, age, and hydration.

Author	Test	Failure strain	Elastic modulus, kPa	Location	Age
Jansen & Rottier, 1958 [50]	<i>Ex vivo</i> , Tension	0.17 - 2.07	2900 - 54100	Abdomen	0 - 99
Dunn & Silver, 1983 [51]	<i>Ex vivo</i> , Tension		18800	Abdomen & Thorax	47 - 86
Vogel, 1987 [52]	<i>Ex vivo</i> , Tension	0.30 - 1.15	15000 - 150000	Various	0 - 90
Jacque-moud <i>et al.</i> 2007 [53]	<i>Ex vivo</i> , Tension	0.27 - 0.59	19500 - 87100	Forehead & Arm	62 - 98
Ni Annaidh <i>et al.</i> 2012 [54]	<i>Ex vivo</i> , Tensile	0.37 - 0.71	48400 - 118200	Back	81 - 97
Sanders <i>et al.</i> 1973 [55]	<i>In vivo</i> , Torsion		20 - 110	Forearm	6 - 61
Agache <i>et al.</i> 1980 [56]	<i>In vivo</i> , Torsion		420 - 850	Forearm	3 - 89
Diridollou <i>et al.</i> 1998 [57]	<i>In vivo</i> , Suction		120 - 250	Abdomen & Forehead	20 - 30
Khatyr <i>et al.</i> 2004 [58]	<i>In vivo</i> , Tension		130 - 660	Forearm	22 - 68
Jachowicz <i>et al.</i> 2007 [59]	<i>In vivo</i> , Indentation		7 - 33	Face & Forearm	28 - 65
Pailler-Mattei <i>et al.</i> 2008 [60]	<i>In vivo</i> , Indentation		4.5 - 8	Arm	30
Boyer <i>et al.</i> 2009 [61]	<i>In vivo</i> , Indentation		5 - 13.2	Forearm	18 - 70
Zahouani <i>et al.</i> 2009 [62]	<i>In vivo</i> , Indentation & static friction		5.2 - 10.4	Arm	55 - 70
Liang & Boppart, 2010 [63]	<i>In vivo</i> , elastography		24.9 - 101.1	Forearm & Palm	-

Table 1-2: Summary of values for elastic modulus of human skin tissue

The results for elastic modulus found for human skin tissue displayed in Table 1-2 are all vastly different. This could be due to a variety of factors:

i) In vivo vs. ex vivo

The percentage difference between *in vivo* and *ex vivo* results for elastic modulus is just under 200%. *Ex vivo* experiments afford a greater range of test conditions, which are impossible to replicate *in vivo*, e.g. loading until fracture. Edwards *et al.* [64] mention that experiments on tissue conducted *ex vivo* can only be performed once, due to damage, so ensuring repeatability is difficult.

A study by Barbe *et al.* [65] states that *in vivo* experiments are flawed as variations are caused by blood flow and breathing of the test subject. However, as such variations are representative of reality, it's desirable to replicate the mechanical properties from the *in vivo* experiments such that they fall within the range of fluctuation.

A target range for the elastic modulus of the soft tissue surrogate was calculated using the results for elastic modulus of skin tissue *in vivo* presented in Table 1-2. The upper and lower limits for the elastic modulus were averaged to achieve a target range of 81.8 kPa – 226.2 kPa.

ii) Inhomogeneity and layers

Skin is an inhomogeneous material as each layer has different mechanical properties, and the layers vary in thickness depending on location. The overall thickness of skin tissue is 8.4 mm \pm SD 3.0 mm [37], but there is further variability within that range for the three skin tissue layers.

In Figure 1-4 it can be seen that although these layers do have some uniformity, their thickness does vary. It is clear that tissue isn't homogenous in any direction due to the cell matrix orientation changing between layers.

Table 1-3 contains a summary of results for the recorded thickness of the individual skin layers and their elastic moduli. The different components of skin are rarely tested separately; it is more common to test skin tissue as a whole. Yet the study by Delalleau *et al.* highlights how different thickness in skin layers can affect the overall mechanical properties, as the properties of the layers vary greatly [38].

	Elastic modulus, MPa	Thickness, mm	References
Epidermis	265.2 (1.5 – 1,000)	0.256 (0.032 – 1.5)	[37-39, 66-68]
Dermis	0.02 (0.008 – 0.035)	1.68 (0.95 – 4)	[37, 43, 60, 62, 66, 67]
Hypodermis	0.0034 (0.00002 – 0.0082)	3.95 (0.8 – 7.1)	[37, 38, 46, 60]

Table 1-3: Brief summary of average values for thickness and separate elastic moduli of human skin tissue, range of collected values shown in parenthesis

Comley *et al.* produced a model for the elastic modulus of adipose tissue, and their findings suggested that the mechanical properties are more reliant on the cell boundaries in skin than its other components [69]. It was stated that the adipose tissue behaved like “a closed cell foam such that the effective modulus is controlled by the stiffness of the reinforced basement membrane” [69].

Silver *et al.* showed that the different constituents of skin have vastly different mechanical properties [42]. They found the spring constants of elastin and collagen to be 4 MPa and 4.4 GPa respectively.

iii) Location

In Table 1-3 it can be seen that each layer of skin has different mechanical properties. The thickness of the skin layers can vary greatly depending on where the samples were taken from, which can affect the results for mechanical properties. This can be seen in Table 1-2 as results obtained from testing skin located on the arm are fairly similar, but when compared to results obtained from testing back skin a significant difference is observed. The toughness of skin can also vary depending on the concentration of blood vessels in the specimen [69].

Some of the papers presented also explored the effect of taking skin at different specimen orientations [54, 63]. It was generally found, for example, that skin specimens adjacent to the spine were stiffer in the direction of the spine axis than perpendicular to it. Wong *et al.*[70] also show that significant changes in elastic modulus were noted with different tissue orientations [70].

iv) Different methods of testing

The effects of using different testing methods are clear in the *in vivo* results in Table 1-2. The torsion and suction based tests produce similar results but the indentation tests return much lower values for elastic modulus. van Kuilenburg *et al.* noted that the measured elastic modulus for skin tissue depends on the penetration depth of the test method, where indentation tests which penetrated deeper gave a lower value for elastic modulus [71]. This explains the differences in the results in Table 1-2, where the torsion and suction results would only be influenced by the top layers of skin, yet indentation tests penetrate deeper and the results would be influenced by the less stiff, fatty layers of skin.

v) Gender and age

Taylor *et al.* showed that the mechanical properties also vary with gender and age [72]. Agache *et al.* noted an increase in elastic modulus after the age of 45 within their test subjects [56]. This most likely relates to the different thickness of skin layers, as we age our skin becomes noticeably thinner and more brittle. Changes may also be due to the variations that occur in the collagen layout of skin as we age [42].

vi) Time dependant effects

The effect of testing tissue under different loading rates is also widely discussed [54]. Since skin exhibits viscoelastic behaviour loading rates have a large impact on the obtained results [42]. It was found that higher loading rates produce higher stiffness results [70].

Flynn *et al.* [73] show that a non-linear stress strain relationship was caused due to uncramping of undulated collagen fibres within the tissue upon stretching. It was discussed earlier that as we age the layout of collagen fibres changes in the skin; as these collagen fibres re-orientate the non-linearity behaviour may also change slightly.

vii) Environmental Factors

Factors outside of the test control also contribute to the different recorded results; such as the subjects' hydration levels, blood pressure, temperature, and breathing which have all been shown to have effects on the recorded mechanical properties [41, 63, 65, 74].

Papir *et al.* and van Kuilenburg *et al.* demonstrated that the temperature and relative humidity strongly affected both the thickness of the skin layers, and its mechanical properties [41, 71].

The study by Liang *et al.* tested the changes in properties of dehydrated and hydrated skin [63]. It was found that in hydrated skin the outermost layer had a lower elastic modulus, whereas the epidermis and dermis layers showed increasing values when dehydrated.

Hendriks *et al.* investigated how hydration affects the properties of skin tissue. It was found that “Hydration caused stiffer material behaviour in eight of thirteen cases, whereas it caused a less stiff material behaviour in four of thirteen cases [74]. In one case, no clear effect was found.” However, in this study liquid was applied to the outermost layer of skin. Thus the results may depend on how quickly each individual’s skin absorbed the water. As in the study by Liang *et al.* [63], the results changed depending on which layer of skin had been hydrated.

A study by Dabrowska *et al.* discusses the inconsistency in mechanical properties of skin and remarks that it may just be a result of skins inherent variability from person to person [75]. Thus it is difficult to quantify the effect of environmental factors independently.

1.3 Photoelasticity

Photoelasticity is a full field experimental method which can be used to determine the strain distribution through transparent materials. It will be used as the analysis method for the planned experiments. Part of the motivation for using photoelasticity is that it can be used visually and quantitatively to understand the stress and strain field around a needle insertion. It is presumed that the stress and strain field in this region determine the failure pattern and trajectory of the needle. Since the materials used in photoelastic analysis must be transparent the motion of the needle insertion can be recorded easily, rather than attaching force sensors or trackers to the needle tip.

Photoelasticity relies on the phenomenon of temporary birefringence, where polarised light enters a loaded material and splits into two light waves in orthogonal directions caused by different indices of refraction. Stress and strain data are obtained by measuring the interference patterns from the recombined light waves.

1.3.1 Birefringence

Birefringence is an optical property of some crystalline materials, such as quartz or calcite, which have multiple indices of refraction [76]. An index of refraction, n , is the ratio between the speed of light in a vacuum, c , and the speed of light through the material, w .

$$n = \frac{c}{w} \quad \text{Equation 1.2}$$

Birefringence can also be observed in non-crystalline and initially optically isotropic materials when subject to a load. When these materials experience stress they behave like crystals. However this crystalline nature vanishes when the load is released, along with its birefringence, hence the term “*temporary birefringence*” [77].

When linearly polarised light passes through a birefringent material its electromagnetic wave components are resolved along the two principal stress directions. Each resolved component experiences a different refractive index resulting from the birefringence of the subject material. In linear elastic materials, changes in the indices of refraction are linearly proportional to the loads and thus to stresses or strains [77]. This relationship allows the determination of stresses and strains through the strain optic law:

$$n_2 - n_1 = \frac{\lambda}{K_\varepsilon} (\varepsilon_1 - \varepsilon_2) \quad \text{Equation 1.3}$$

where n_1 and n_2 are the principal indices of refraction, λ is the wavelength of light, K_ε is the strain optic coefficient, and ε_1 and ε_2 are the principal strains. Light will travel through the analysed material at different speeds proportional to the principal strains. As a result of this, the two beams will exit the material at different times. One beam is essentially travelling behind the other, which results in a phase difference or retardation between the beams. If the light passes through a second polariser, this retardation can be observed in the form of interference or fringe patterns. The fringe patterns can be used to calculate the magnitude and orientation of the principal strains and stresses. As soon as the material is unloaded, its birefringence will cease, and no fringe patterns will be observed. In photoelasticity the fringes are counted from a reference point, usually a free edge where the stress and fringe number are zero. Fringes are counted sequentially, and the fringe number is known as fringe order, N .

1.3.2 Photo-viscoelasticity

Photoelasticity is usually described as a stress analysis technique. In linear elastic experiments the differences between the principal stresses and strains are directly proportional [77, 78]:

$$(\varepsilon_1 - \varepsilon_2) = \frac{(1 + \nu)}{E} (\sigma_1 - \sigma_2) \quad \text{Equation 1.4}$$

where ν is the Poisson's ratio of the material, E is the elastic modulus, and σ_1 and σ_2 are the principal stresses. However, this relationship does not apply to non-linear materials. Viscoelastic materials also exhibit "stress relaxation", in which stress decreases over time when the material is subject to a constant strain. Such phenomena are important features of the mechanical response of most biological tissues, and should be represented in tissue surrogates. Photoelastic analyses of these materials must correspondingly be capable of accounting for these non-linear effects [42]. Zhao and Hung noted that strain, instead of stress, should be measured when testing viscoelastic materials [79]. Therefore, it is more meaningful and accurate to express the optical characteristics through the strain optic law:

$$(\varepsilon_1 - \varepsilon_2) = \frac{N\lambda}{hK_\varepsilon} \quad \text{Equation 1.5}$$

where N is the fringe order, and h is the thickness of the specimen.

1.3.3 Plane polariscope

The optical instrument used to measure the strain distribution is a polariscope. Two types of polariscope are frequently used: plane and circular. A plane polariscope utilises plane or linear polarisers, whereas a circular polariscope utilises linear polarisers and quarter wave plates.

Polariscopes can also be set to be dark-field or light-field. Dark-field is where the input and output polarisers are perpendicular to each other, light-field is where the input and output polarisers are parallel.

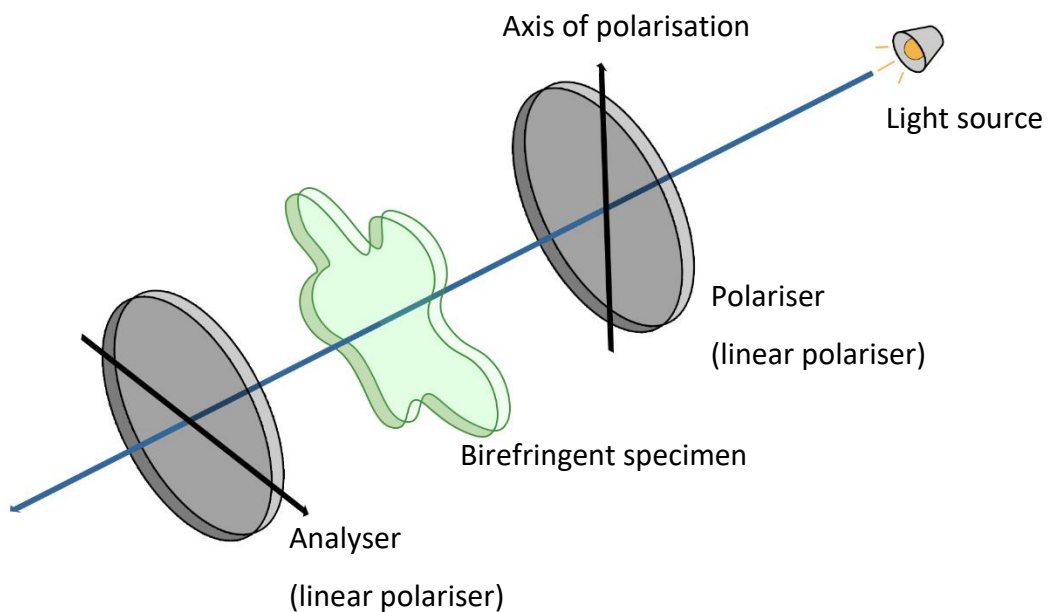


Figure 1-9 Plane Polariscope in dark field orientation

Figure 1-9 illustrates the setup of a dark-field plane polariscope. The linear polarisers absorb any light waves which aren't parallel to the axis of polarisation; therefore, only light parallel to the axis of polarisation is transmitted. The mathematical explanation of the formation of interference patterns follows.

Plane polarised light emerging from the polariser is represented by:

$$C_{py} = k \cos(\omega t) \quad \text{Equation 1.6}$$

$$\text{where } k = a \cos(\alpha) \quad \text{Equation 1.7}$$

where C_{py} is the light vector, k is the constant in Equation 1.7, ω is the angular frequency, t is time, a is the amplitude of the light wave, and α is the angle between the axis

of polarisation and the incident light vector. After exiting the polariser, the light passes through the birefringent specimen. The light is resolved into two components:

$$C_1 = k \cos(\alpha) \cos(\omega t) \quad \text{Equation 1.8}$$

$$C_2 = k \sin(\alpha) \cos(\omega t) \quad \text{Equation 1.9}$$

where C_i , ($i = 1, 2$) are the two resolved light vectors. These vectors travel parallel to the principal stress and strains. As the refractive indices of the birefringent specimen are different the two light vectors will travel at different speeds, and thus will experience a relative phase shift. The equations for the light beams exiting the birefringent specimen are given by:

$$C'_1 = k \cos(\alpha) \cos(\omega t - \Delta_1) \quad \text{Equation 1.10}$$

$$C'_2 = k \sin(\alpha) \cos(\omega t - \Delta_2) \quad \text{Equation 1.11}$$

where C'_i , ($i = 1, 2$) are the two phase shifted light vectors, and Δ_i , ($i = 1, 2$) is the amount of phase shift, which is represented by:

$$\Delta_1 = \frac{2\pi h}{\lambda} (n_1 - 1) \quad \text{Equation 1.12}$$

$$\Delta_2 = \frac{2\pi h}{\lambda} (n_2 - 1) \quad \text{Equation 1.13}$$

where h is the thickness, and n_i , ($i = 1, 2$) are the two principal indices of refraction of the birefringent specimen. The light vectors exit the material and pass through air with no change to their electric vector. When the light vectors C'_1 and C'_2 pass through the analyser their vertical components are absorbed, and their horizontal components are as follows:

$$C_{ax} = C''_2 - C''_1 = C'_2 \cos(\alpha) - C'_1 \sin(\alpha) \quad \text{Equation 1.14}$$

where C_{ax} is the emerging light vector, C''_i , ($i = 1, 2$) are the two light vectors after emerging from the analyser. Substituting Equation 1.10 and Equation 1.11 into Equation 1.14 gives:

$$C_{ax} = k \sin(2\alpha) \sin\left(\frac{\Delta_2 - \Delta_1}{2}\right) \sin\left(\omega t - \frac{\Delta_2 + \Delta_1}{2}\right) \quad \text{Equation 1.15}$$

In Equation 1.15 the angular phase shift does not affect the intensity of light emerging from the analyser, so it does not affect the fringe patterns observed in the material. The intensity

depends on the relative retardation and the amplitude of the wave emerging from the analyser. The intensity of light is proportional to the square of the amplitude of the light wave [77], and can be determined from Equation 1.15 as:

$$I = L \sin^2(2\alpha) \sin^2\left(\frac{\Delta}{2}\right) \quad \text{Equation 1.16}$$

where I is the intensity, L is the strength of the light source, and Δ is the relative retardation given in Equation 1.17:

$$\Delta = \Delta_2 - \Delta_1 = \frac{2\pi h}{\lambda} (n_2 - n_1) = \frac{2\pi h K_\varepsilon}{\lambda} (\varepsilon_1 - \varepsilon_2) \quad \text{Equation 1.17}$$

Equation 1.16 contains both magnitude and direction information regarding the load applied to the birefringent material. These components produce different types of fringes: isoclinic for the direction of the principal strains, and isochromatic for the magnitude of the principal strains.

Directional component

“ $\sin^2(2\alpha)$ ” is the principal strain direction component in Equation 1.16. When $2\alpha = 0, \pi, 2\pi, 3\pi, \dots$ dark isoclinic fringes are produced. These fringes are loci of points where the principal strain directions, either ε_1 or ε_2 , coincide with the axis of the polariser.

Magnitude component

“ $\sin^2(\Delta/2)$ ” is the component for principal strain difference in Equation 1.16. When $\Delta/2 = 0, \pi, 2\pi, 3\pi, \dots$ dark isochromatic fringes are produced. Isochromatic fringes are lines of constant principal strain difference; $(\varepsilon_1 - \varepsilon_2)$. The location of the fringes also depends on the wavelength of light. This is shown in the strain optic law presented in Equation 1.5, which includes the wavelength of light, λ . If the source light is monochromatic then these fringes will appear as dark and light, if the source light is white then a series of coloured fringes are produced.

Resulting fringe pattern for plane polariscope

Figure 1-10 shows an example of both isoclinic and isochromatic fringes through a disk in vertical compression. The isoclinic fringes are the thick dark vertical and horizontal band, and the isochromatic fringes are the numerous thin curved fringes.

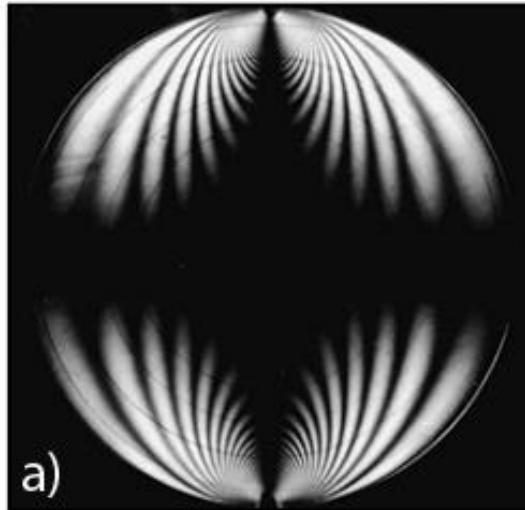


Figure 1-10: isoclinic fringes [80]

With use of a circular polariscope the isoclinic fringes are excluded using quarter wave plates and only the isochromatic fringes are observed. The description for a circular polariscope follows.

1.3.4 Circular polariscope

Figure 1-11 illustrates the setup of a circular polariscope. Comparison between Figure 1-9 and Figure 1-11 reveals the only difference is the two quarter wave plates either side of the birefringent specimen.

Quarter wave plates, as depicted in Figure 1-11, are constructed out of a birefringent material. If plane polarised light is directed at a quarter wave plate the light is further resolved into two components. The quarter wave plates induce a $\pi/2$ radian phase difference between the two light waves which changes the linearly polarised light exiting the linear polariser into elliptically polarised light. The birefringent specimen acts similarly to the wave plates except the phase difference which it induces is unknown.

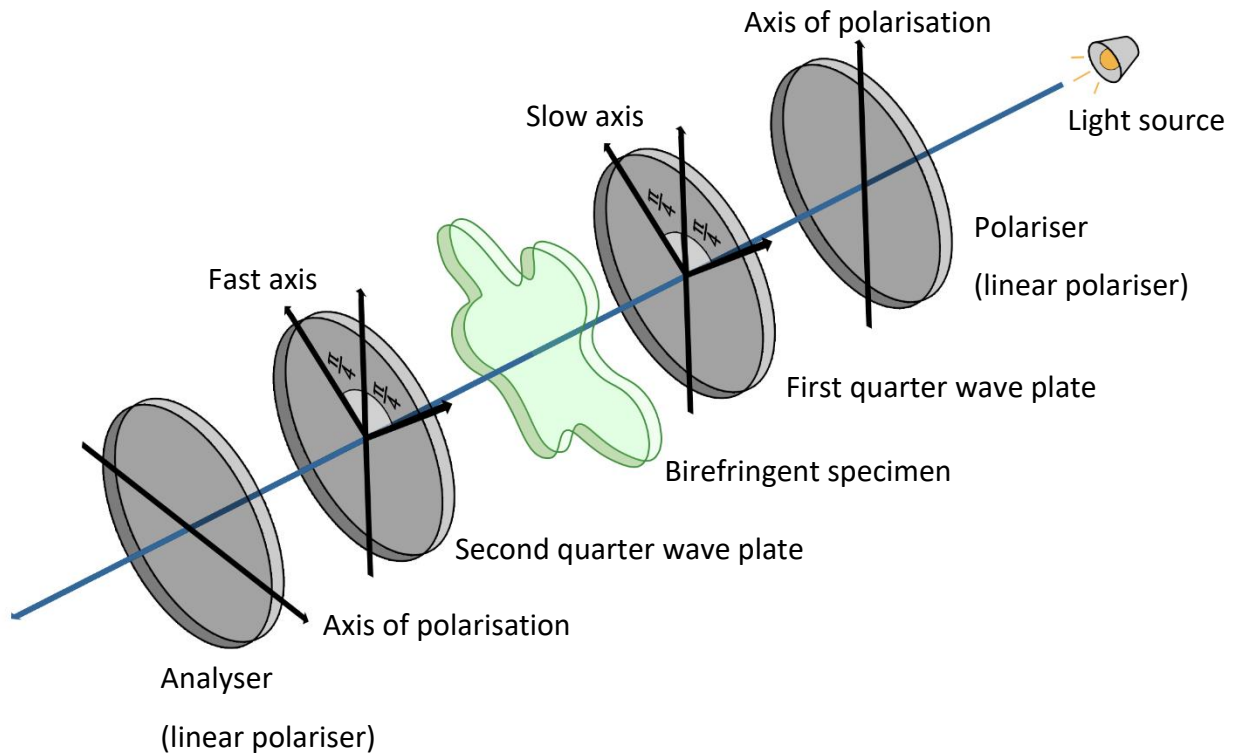


Figure 1-11: Circular Polariscope in dark field orientation

As the light passes through the second quarter wave plate and analyser the two waves are recombined. Since the two waves travelled at different speeds through the birefringent specimen there will be a phase difference between them as they exit the specimen. This interference is observed in the form of light and dark fringes. The mathematical explanation of the formation of interference patterns follows:

Plane polarised light emerging from the polariser is represented by the same expression as shown for the plane polariscope:

$$C_{py} = k \cos(\omega t) \quad \text{Equation 1.18}$$

$$\text{where } k = a \cos(\alpha) \quad \text{Equation 1.19}$$

After exiting the polariser, the light passes through the first quarter wave plate. The axes of the quarter wave plate are orientated at $\pi/4$ to the axis of the polariser. The light is resolved into two components: C_f and C_s , which correspond to the fast axis, where the light travels quicker, and the slow axis:

$$C_f = \frac{\sqrt{2}}{2} k \cos(\omega t) \quad \text{Equation 1.20}$$

$$C_s = \frac{\sqrt{2}}{2} k \cos(\omega t) \quad \text{Equation 1.21}$$

After exiting the quarter wave plate the light waves will have developed a phase shift of $\Delta = \pi/2$. The out of phase components of the light exiting the wave plate are:

$$C'_f = \frac{\sqrt{2}}{2} k \cos(\omega t) \quad \text{Equation 1.22}$$

$$C'_s = \frac{\sqrt{2}}{2} k \cos\left(\omega t - \frac{\pi}{2}\right) = \frac{\sqrt{2}}{2} k \sin(\omega t) \quad \text{Equation 1.23}$$

The birefringent specimen acts as a wave plate with unknown retardation and axes angles. The light waves will resolve into components C_1 and C_2 which correspond to the magnitude and directions coincident with the principal strains in the specimen:

$$C_1 = C'_f \cos\left(\frac{\pi}{4} - \alpha\right) + C'_s \sin\left(\frac{\pi}{4} - \alpha\right) \quad \text{Equation 1.24}$$

$$C_2 = C'_s \cos\left(\frac{\pi}{4} - \alpha\right) - C'_f \sin\left(\frac{\pi}{4} - \alpha\right) \quad \text{Equation 1.25}$$

With substitution of Equation 1.22 and Equation 1.23 into Equation 1.24 and Equation 1.25 the following equations for the effect of the birefringent specimen are obtained:

$$C_1 = \frac{\sqrt{2}}{2} k \cos\left(\omega t + \alpha - \frac{\pi}{4}\right) \quad \text{Equation 1.26}$$

$$C_2 = \frac{\sqrt{2}}{2} k \sin\left(\omega t + \alpha - \frac{\pi}{4}\right) \quad \text{Equation 1.27}$$

The components of light pass through the birefringent specimen at different velocities and accumulate a relative retardation, Δ ; proportional to the specimen thickness, optic coefficient, wavelength, and change in principal strains, shown in Equation 1.17. The emerging wave can be expressed as:

$$C'_1 = \frac{\sqrt{2}}{2} k \cos\left(\omega t + \alpha - \frac{\pi}{4}\right) \quad \text{Equation 1.28}$$

$$C'_2 = \frac{\sqrt{2}}{2} k \sin\left(\omega t + \alpha - \frac{\pi}{4} - \Delta\right) \quad \text{Equation 1.29}$$

The light waves will then enter the second quarter wave plate, the components for the fast and slow axes of the second quarter wave plate are:

$$C_f = C'_1 \sin\left(\frac{\pi}{4} - \alpha\right) + C'_2 \cos\left(\frac{\pi}{4} - \alpha\right) \quad \text{Equation 1.30}$$

$$C_s = C'_1 \cos\left(\frac{\pi}{4} - \alpha\right) - C'_2 \sin\left(\frac{\pi}{4} - \alpha\right) \quad \text{Equation 1.31}$$

Substituting Equation 1.28 and Equation 1.29 into Equation 1.30 and Equation 1.31 returns the light wave value as the light enters the wave plate:

$$C_f = \frac{\sqrt{2}}{2} k \left[\cos\left(\omega t + \alpha - \frac{\pi}{4}\right) \sin\left(\frac{\pi}{4} - \alpha\right) + \sin\left(\omega t + \alpha - \frac{\pi}{4} - \Delta\right) \cos\left(\frac{\pi}{4} - \alpha\right) \right] \quad \text{Equation 1.32}$$

$$C_s = \frac{\sqrt{2}}{2} k \left[\cos\left(\omega t + \alpha - \frac{\pi}{4}\right) \cos\left(\frac{\pi}{4} - \alpha\right) - \sin\left(\omega t + \alpha - \frac{\pi}{4} - \Delta\right) \sin\left(\frac{\pi}{4} - \alpha\right) \right] \quad \text{Equation 1.33}$$

When the light wave exists the second quarter wave plate a further phase shift of $\Delta = \pi/2$ is applied between the fast and slow axes of the wave plates:

$$C'_f = \frac{\sqrt{2}}{2} k \left[\cos\left(\omega t + \alpha - \frac{\pi}{4}\right) \sin\left(\frac{\pi}{4} - \alpha\right) + \sin\left(\omega t + \alpha - \frac{\pi}{4} - \Delta\right) \cos\left(\frac{\pi}{4} - \alpha\right) \right] \quad \text{Equation 1.34}$$

$$C'_s = \frac{\sqrt{2}}{2} k \left[\sin\left(\omega t + \alpha - \frac{\pi}{4}\right) \cos\left(\frac{\pi}{4} - \alpha\right) + \cos\left(\omega t + \alpha - \frac{\pi}{4} - \Delta\right) \sin\left(\frac{\pi}{4} - \alpha\right) \right] \quad \text{Equation 1.35}$$

Finally, the light enters analyser and the vertical components of C'_f and C'_s are absorbed, while the horizontal components return the following:

$$C_{ax} = \frac{\sqrt{2}}{2} (C'_s - C'_f) \quad \text{Equation 1.36}$$

Substituting Equation 1.34 and Equation 1.35 into Equation 1.36 gives the value for the light emerging from the analyser:

$$C_{ax} = k \sin\left(\frac{\Delta}{2}\right) \sin\left(\omega t + 2\alpha - \frac{\Delta}{2}\right) \quad \text{Equation 1.37}$$

As described for the plane polariscope; the intensity of light is proportional to the square of the light wave. Hence, the intensity of light emerging from the circular polariscope in dark field is given as:

$$I = L \sin^2 \left(\frac{\Delta}{2} \right) \quad \text{Equation 1.38}$$

Comparing Equation 1.16 and Equation 1.38 shows that Equation 1.38 does not have the directional component of $\sin^2(2\alpha)$. Therefore, no isoclinic fringes will be observed, and dark isochromatic fringes will occur when $\sin^2(\Delta/2) = 0$; corresponding to the change in principal strain; $(\varepsilon_1 - \varepsilon_2)$.

Resulting fringe pattern for circular polariscope

Figure 1-12 shows an example of isochromatic fringes through a disk in compression. Comparison with Figure 1-10 shows how the removal of the isoclinic fringes has revealed more detailed isochromatic fringes.

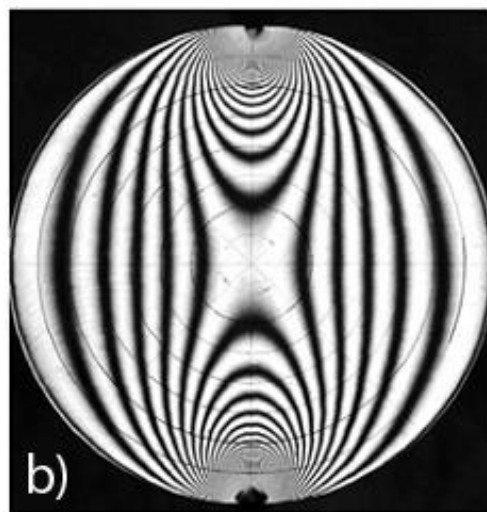


Figure 1-12: isochromatic fringes [80]

Conventionally, circular polariscopes are more prevalent for experimental photoelasticity. They reveal strain concentrations and the directional information is usually ignored from the plane polariscope. However, directional information may be revealing when investigating the deflection of a needle through soft tissue. Therefore, with use of photoelastic analysis the experimental work will be able to display both magnitude and direction of the forces created by a needle insertion. This information may shed light on why a needle deflects when travelling through soft tissue, and reveal insights into information ahead of the needle tip.

1.3.5 Phase stepping

In Figure 1-12 it can be seen that the fringes are unevenly spaced. Areas where the fringes are closer together are the locations of stress concentrations. This uneven spacing produces a problem as simple interpolation cannot be used to obtain an accurate fringe number for a point at an arbitrary distance between two fringes.

To resolve this issue Tardy compensation can be used, wherein the analyser is moved until a fringe fully covers the point of interest, and the fractional fringe order is determined from the amount of movement [77]:

$$N = m \pm \gamma/\pi \quad \text{Equation 1.39}$$

where N is the fringe order at the point of interest, m is the original fringe order that has been 'moved' over the point of interest, and γ is the amount of rotation in radians. However, this would be impractical if full field data are desired as only point data is obtained.

Phase stepping is a method to obtain full field data which was first introduced by Hecker and Morche in 1986 [81]. It requires four to six images of the birefringent specimen at varying output wave-plate and analyser angles if circularly polarised light is used as the input light. As a result of changing the output optic angles, additional intensity distributions can be obtained. The fractional fringe order at any point of interest can be determined as a function of the intensity data recorded at that point. The arrays of images are recombined using computational software to calculate the stress and strain data across the whole specimen.

The general equation for the intensity of light at a specific point on the specimen after passing through the output optical elements is given in Equation 1.40 [82]:

$$I = i_m + i_v[\cos \delta \sin 2(\beta - \varphi) - \sin \delta \sin 2(\theta - \varphi) \cos 2(\beta - \varphi)] \quad \text{Equation 1.40}$$

where i_m represents the intensity of the stray light, and i_v represents the intensity emerging when all the axes of the polariscope and specimen are parallel. δ is the phase retardation, and φ and β represent the rotation of the output quarter wave plate and polariser respectively.

Complete explanations for i_v and i_m are shown in Equation 1.41 and Equation 1.42, with a representing the waves' amplitude, and I_0 representing the background light intensity;

$$i_m = I_0 + \frac{a^2}{2} \quad \text{Equation 1.41}$$

$$i_v = \frac{a^2}{2} \quad \text{Equation 1.42}$$

The orientations of the output optic elements used for six step phase stepping, developed by Patterson and Wang [82], are shown in the Table 1-4. The equations are derived from Equation 1.40 by substituting the indicated wave plate and polariser angles.

Iteration	Orientation of quarter-wave plate $\varphi, ^\circ$	Orientation of polariser $\beta, ^\circ$	Intensity equation
1	0	$\pi/4$	$I_1 = i_m + i_v \cos \delta$
2	0	$3\pi/4$	$I_2 = i_m - i_v \cos \delta$
3	0	0	$I_3 = i_m - i_v \sin \delta \sin 2\theta$
4	$\pi/4$	$\pi/4$	$I_4 = i_m + i_v \sin \delta \cos 2\theta$
5	$\pi/2$	$\pi/2$	$I_5 = i_m + i_v \sin \delta \sin 2\theta$
6	$3\pi/4$	$3\pi/4$	$I_6 = i_m - i_v \sin \delta \cos 2\theta$

Table 1-4: Equations and orientations required for phase stepping described by Patterson and Wang [82, 83]; where $I_{\#}$ represent the different output intensities at the various orientations

Using the results from the equations in Table 1-4 the principal stress direction from the isoclinic angle, θ , and fractional retardation, δ , can then be found using Equation 1.43 and Equation 1.44:

$$\theta = \frac{1}{2} \tan^{-1} \frac{I_5 - I_3}{I_4 - I_6} \quad \text{Equation 1.43}$$

$$\delta = \tan^{-1} \left[\frac{2(I_5 - I_4)}{(I_1 - I_2)(\sin 2\theta \cos 2\theta)} \right] \quad \text{Equation 1.44}$$

This method can be prone to significant errors as each image has to be captured separately and the analyser positions are usually moved manually. A small misplacement of the analyser could cause large errors in the calculated results [77]. It is significant to note that six separate rotation arrangements are presented when only four unknowns are found in the relevant equations. Six images at the varying orientations are commonly captured to mitigate any

errors in rotation of the optical elements. Since time is required to move the analyser manually phase stepping cannot be used to gather dynamic photoelastic data. Therefore, further data acquisition methods which can obtain dynamic data are discussed.

Alternative phase stepping methods are available, which utilise different optical element angles [84, 85]. However, these are not the angles used in the GFP2500 Poleidoscope, which is discussed in section 1.3.7.

1.3.6 Grey field polariscope

Grey field photoelasticity was introduced in 1997 [86]. It is similar to standard photoelasticity except for three changes to the polariscope: the second quarter wave plate is removed, the analyser is motorised to do manual phase stepping, and a video camera is used instead of a standard camera.

The GFP's (Grey field polariscope) advantage lies in its automatic and precise phase stepping, thus mitigating any errors from rotating the optical elements by incorrect intervals. However, the rotation of the analyser is not instantaneous; requiring approximately 3 minutes to capture the six required images [87]. In a photoelasticity study of needle insertion, Tomlinson *et al.* [4] found that when the needle was paused to take measurements the force response relaxed slightly. Therefore, a method which captures dynamic data is required.

1.3.7 GFP2500 Poleidoscope

The poleidoscope was introduced following research on the simultaneous capture of multiple images at different output wave-plate and analyser position, outlined in the following research papers [82, 83, 87-89]. The GFP2500 poleidoscope is a digital polariscope which allows for simultaneous capture of multiple images at different output wave-plate and analyser positions [6]. A commercially available version was released by Stress Photonics; a schematic of the poleidoscope is shown in Figure 1-13:

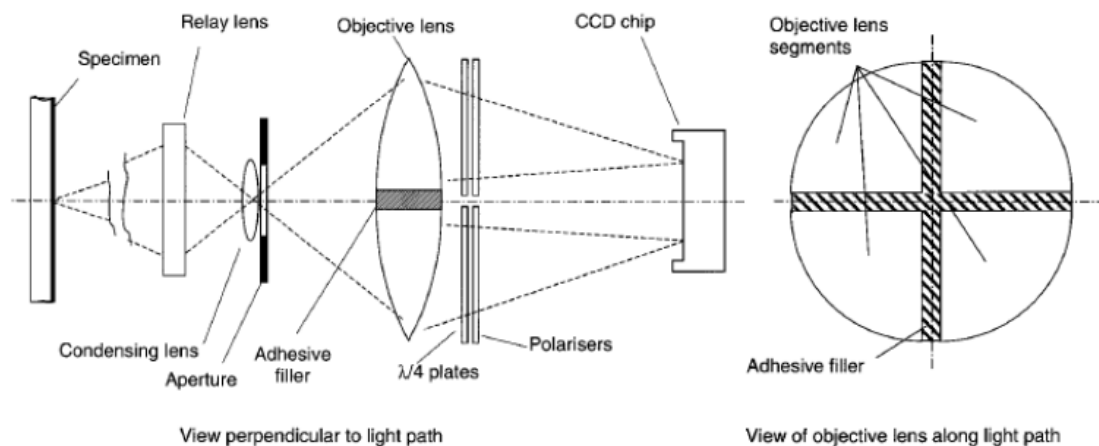


Figure 1-13: Schematic of poleidoscope [6]

As polarised light exits the loaded birefringent specimen the two beams will be experiencing a relative phase difference proportional to the magnitude of the load on the specimen. The light then enters the relay lens and passes through a kaleidoscopic objective lens. The kaleidoscopic lens is made by sectioning a conventional lens into four quadrants and separating them by a small amount, thereby returning four identical images of the same section of the specimen [84]. These four beams pass through pre-orientated analyser elements, which polarise the light beam back on to the same plane so the interference patterns can be observed. This setup is essentially grouping four polariscopes together with parallel optical axes.

Four interference images are produced as that is the minimum number of intensity images required for phase stepping analysis when background stray light is accounted for [6, 88]. The camera captures the data in video format, and a complete data set can be captured in as little as 1/25th of a second [87]. Each individual data set, or frame of the video, can be analysed individually to investigate the development of the fringes through a dynamic loading

environment. Therefore, instantaneous, dynamic, full-field data can be captured using one piece of photoelastic apparatus. Table 1-5 shows the required wave plate and polariser rotations for four step phase stepping within the poleidoscope.

Iteration	Orientation of quarter-wave plate $\varphi, ^\circ$	Orientation of polariser $\beta, ^\circ$	Intensity equation
1	$\pi/4$	$\pi/4$	$i_1 = i_m(i_v - \sin \delta \cos 2\theta)$
2	0	0	$i_2 = i_m(i_v + \sin \delta \sin 2\theta)$
3	0	$3\pi/4$	$i_3 = i_m(i_v - \cos \delta)$
4	$\pi/2$	$\pi/2$	$i_4 = i_m(i_v - \sin \delta \sin 2\theta)$

Table 1-5: Equations and orientations required for four step phase stepping in the poleidoscope [6, 88, 89]; where $i_{\#}$ represent the different output intensities at the various orientations.

Similar to the six step phase stepping method, the isoclinic angle, θ , and relative retardation, δ , can be found by substituting the results from the equations in Table 1-5 into Equation 1.45 and Equation 1.46 respectively [6, 88].

$$\theta = \frac{1}{2} \tan^{-1} \frac{2(i_2 - i_3)}{i_2 + i_3 - 2i_1} \quad \text{Equation 1.45}$$

$$\delta = \tan^{-1} \left[\frac{(i_2 - i_3)}{\sin 2\theta (i_2 + i_3 - 2i_4)} \right] \quad \text{Equation 1.46}$$

With use of the poleidoscope full field, dynamic intensity data can be obtained. Using the intensity images from the phase steps outlined in Equation 1.45 and Equation 1.46 the retardation map and isoclinic angle according to the load can be presented. In order to display the results in terms of stress and strain instead of retardation the data requires processing.

Data processing

The poleidoscope camera utilises the “GFP2500 c” software developed by Stress Photonics [90]. The four intensity data images are saved in Audio Video Interleave (.avi) format which can be viewed within the software. An example of four intensity images at the same point in time during needle insertion is shown in Figure 1-14.

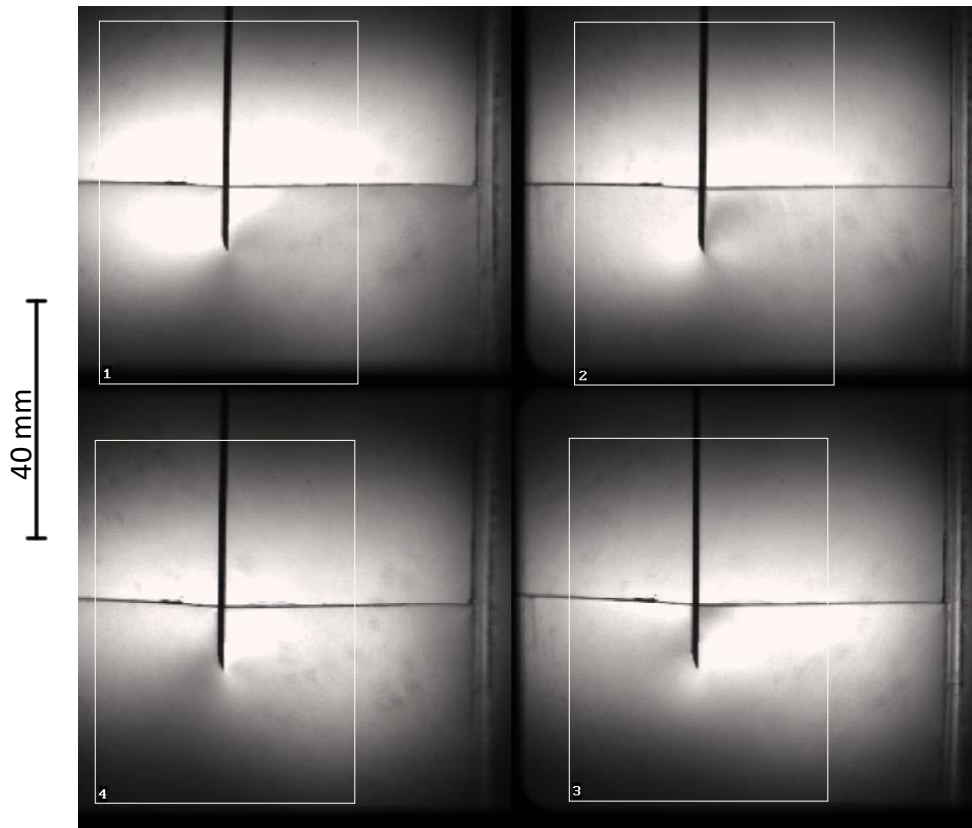


Figure 1-14: Example of the four intensity images captured from a needle insertion experiment

The software combines the intensity data from the four images in to Equation 1.45 and Equation 1.46 to return the retardation and directional data. A simple visualisation of the retardation is previewed in the interface, shown in Figure 1-15. Three images are displayed, one showing the light through the sample, one of the shear strains acting in the horizontal plane at 0° , and one of the shear strains acting in the planes at 45° to the horizontal.

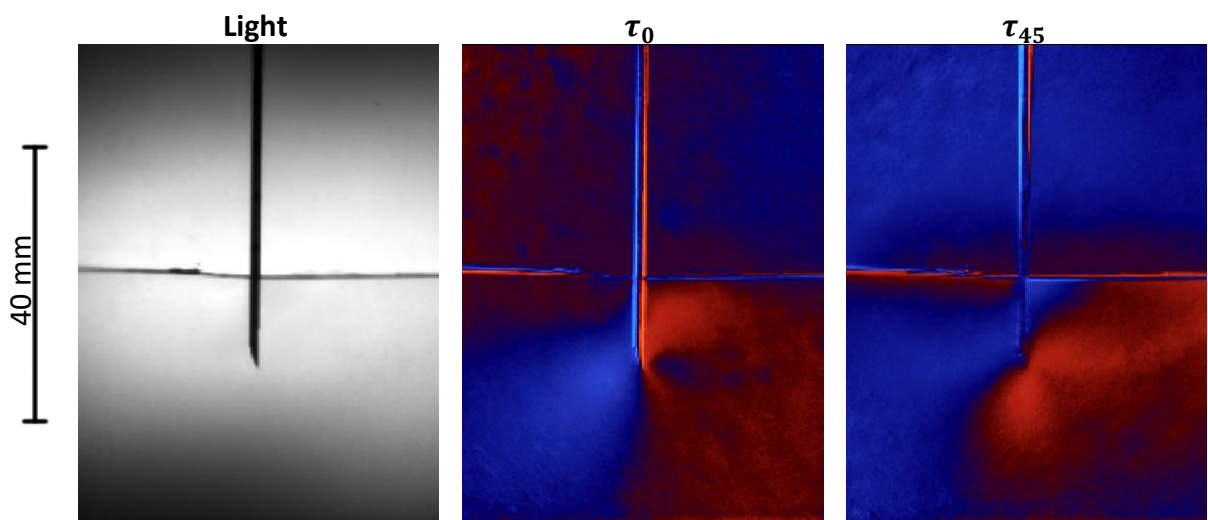


Figure 1-15: Example of a video frame from a needle insertion experiment

The software can be used to save chosen frames of the captured video to get detailed information about the retardation at that point in time. These frames can be from either the processed or unprocessed data, and are viewed in a separate program “Deltavision v2” [91].

The GFP2500 c software utilises Equation 1.45 and Equation 1.46 to obtain the retardation, which both contain the tangential function. This function causes the retardation map to cycle whenever the fringe order is increased by 0.25. An example of this is shown in Figure 1-16, where a line of interest shows the development of the increasing fringes from a point of fringe order 0, to the point of maximum fringe order.

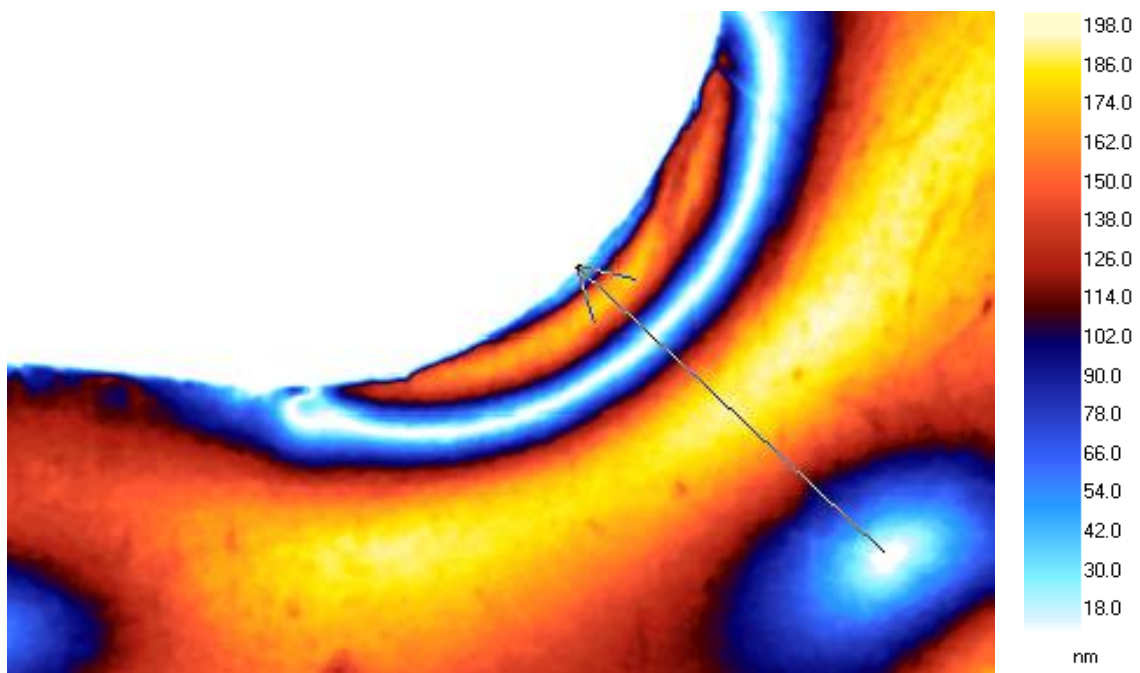


Figure 1-16: Example of fringe pattern for an unprocessed birefringent specimen [92]

Figure 1-16 shows the development of retardation through an unprocessed image. A change in colour from the ice blue to the bright yellow indicates a fringe order increase of 0.25. By dragging a line across the image in the analysis software the retardation development along that section can be analysed, a graph of this is shown in Figure 1-17 .

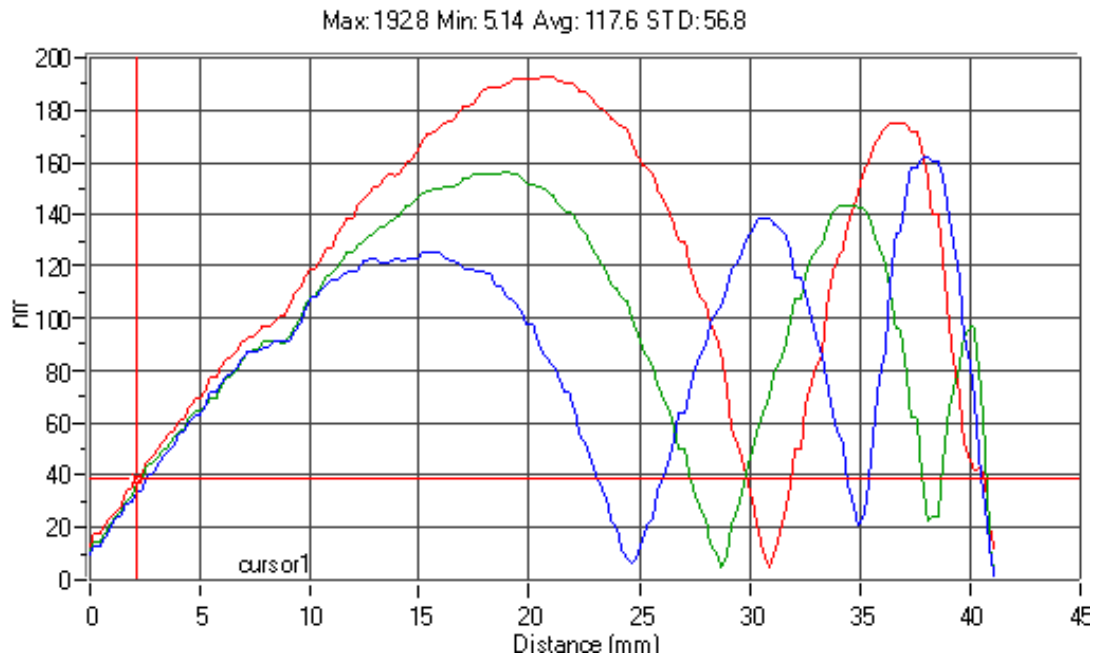


Figure 1-17: Example of unprocessed retardation progression along the line of interest in Figure 1-16 [92]

Figure 1-17 shows the cyclic retardation values for three wavelengths of light. The gradient of the red curve changes sign three times which indicates that the fringe order will be slightly lower than 1 fringe, as each sign change indicates a fringe order increase of 0.25.

In order to get the precise magnitude of retardation across the line of interest, or to get the precise fringe order, the data requires processing. Within the software developed by Stress Photonics there is a processing tool which converts the oscillating retardation value to a continuous slope [90]. Examples of the processed data and graph are shown in Figure 1-18 and Figure 1-19 respectively.

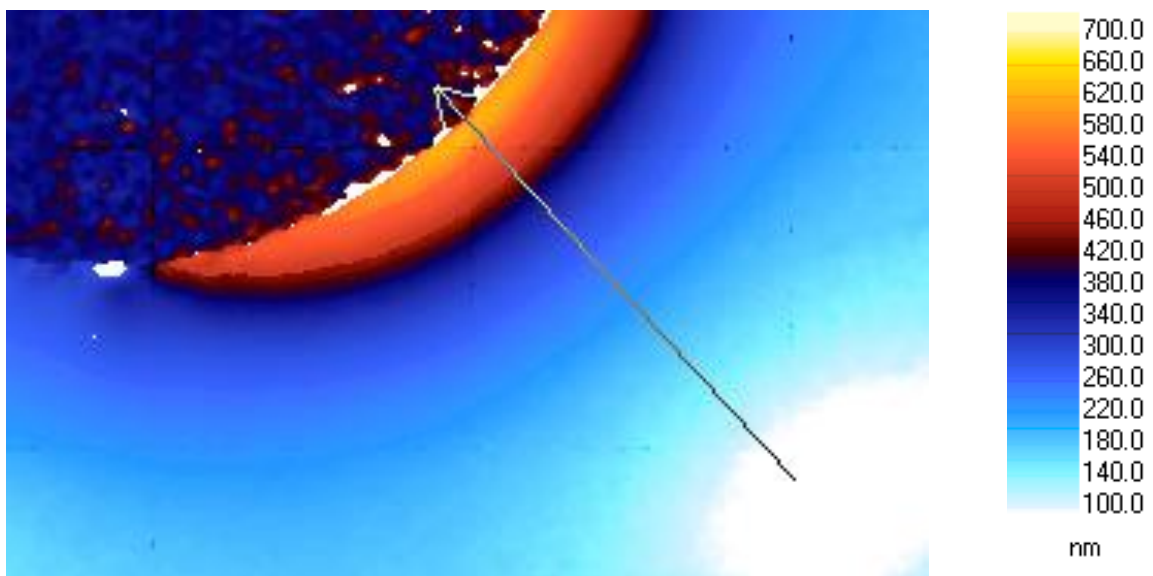


Figure 1-18: Example of fringe pattern for an processed birefringent specimen [92]

Comparing Figure 1-16 with Figure 1-18 shows that the retardation amount is now a continuous data presentation.



Figure 1-19: Example of processed retardation progression along the line of interest shown in Figure 1-18

[92]

In Figure 1-19 the maximum retardation amount is highlighted to be 611 nm, which corresponds to a fringe order of 0.94. After results have been processed the retardation data can be converted into stress and strain data with the application of an optic coefficient. An optic coefficient relates the regularity of the fringes, or amount of retardation, to stress and strain experienced by the material. Optic coefficients are specific to each type of birefringent material, and an optic coefficient for the developed material will be established in chapter 3.

With use of this photoelastic apparatus and software, experiments can be conducted which analyse the changes in stress and strain within a material due to a needle insertion. Full field directional results can also be gathered from the isoclinic angle. Previous research investigating the needle insertion through soft tissue has focused on the magnitude of the forces and little information has been published on the directions of these loads [2]. It is anticipated that full field directional data will provide an insight into what causes a needle to deviate from its intended path, and a means of assessing how the material moves ahead of the needle.

1.4 Potential tissue surrogates

This study will involve developing a human skin tissue surrogate for use in photoelastic analysis. There is no practical way to measure strain or stress directly in real skin tissue *in vivo*, so an analysis method like photoelasticity is needed. Photoelasticity requires a transparent material, and since skin tissue is not transparent a surrogate is required for the planned experiments. Therefore, a surrogate is required which mimics the properties of human tissue but also has good optical properties; birefringence and clarity.

Using a transparent surrogate instead of an opaque one is also advantageous as it allows direct viewing of the needle as it travels through the material, rather than gathering the displacement data from force readings or tracking methods. However, many experimental approaches to investigating needle-tissue deformation behaviour have not required transparent tissue surrogates, merely translucent, or even opaque [46, 93, 94].

1.4.1 Available skin tissue surrogates

A significant discussion point is whether tissue surrogates actually mimic the results from needle insertions through human skin. A range of tissue surrogates have been used throughout the studies referenced so far, with porcine and bovine gelatine used most frequently. Many studies also use PVC gel, silicone gel, or silicone rubber as the tissue surrogate.

Gelatine

Meltsner *et al.* used porcine gelatine in their study and compared results to bovine muscle tissue. It was demonstrated that gelatine has a linear response to needle insertion, whereas the response from bovine muscle tissue was highly non-linear [30]. Further studies have discussed the use of gelatine as a tissue surrogate [4, 7, 19, 80]. It has been suggested that gelatine is suitable as a bulk surrogate but during small scale testing its linear behaviour, and lack of resistance to crack growth, renders it unviable for use in needle insertion investigation.

Silicone Rubber

Okamura *et al.* used silicone rubber as the soft tissue surrogate to show that needle tip geometry has a great effect on needle bending [11, 95]. Naemura *et al.* used silicone rubber to assess whether increasing the needle speed affected the force response with no correlation found [29], which mimicked the results from human tissue *ex vivo* [8, 31-35]. However, Shergold and Fleck's assessment on puncture response for silicone rubber revealed it had little resistance to crack growth [96]. Silicone rubber is also an opaque material so it would be unviable for use in the planned photoelastic assessments.

Silicone gel and PVC gel

A number of studies assessed the effect of increasing needle speed on force response, where Crouch *et al.* used silicone gel as the surrogate [26], and DiMaio and Salcudean, and Podder *et al.* used PVC gel [27, 28]. All studies found that an increased speed gives an increased force response, which contradicted results from soft tissue tested *ex vivo* [8, 31-35]. None of the studies discuss the crack development so it is unclear whether the materials resist crack growth. The surrogates are transparent, but it is also unclear whether they exhibit temporary birefringence.

Konjac

Tomlinson and Taylor introduced konjac as a possible soft tissue surrogate [4]. It was shown to exhibit resistance to crack growth, and in Thompson and Tomlinson's study it displayed some non-linear behaviour [19]. However, the optical performance of the gel was poor as it was cloudy.

Carrageenan

Thompson and Tomlinson found that carrageenan was the gelling agent in the konjac gel [19]. Initial assessment showed that the carrageenan gel exhibited resistance to crack growth and it had excellent optical properties. However, no further material analysis was conducted.

1.4.2 Summary

The importance of crack resistance in surrogate materials has been noted in section 1.2.2. It is hypothesised that if skin tissue fractures in a fundamentally different way to a potential surrogate, it's not clear how the results can be translated to the case of real tissues. It is imperative that the developed surrogate also exhibits crack resistance.

It is also required that the surrogate tissue is transparent and has temporary birefringence so that it can be used for photoelastic analysis. Table 1-6 contains a brief review of the above surrogates with respect to the discussed criteria.

Material	Transparent	Resistance to crack growth
Ballistic gelatine	✓	×
Porcine gelatine	✓	×
Silicone rubber	×	×
Silicone gel	✓	?
PVC gel	✓	?
Carrageenan	✓	?
Konjac	✓	✓

Table 1-6: Brief review of potential tissue surrogates

With reference to the criteria in Table 1-6 and the previous discussion, it has been decided that konjac and carrageenan gel will be investigated for their suitability as a skin tissue surrogate. Both gels are transparent and konjac definitely exhibits a resistance to crack growth. Carrageenan is a component of konjac jelly with better optical properties; initial assessment has shown that it may also be resistant to crack growth so this will be investigated further. Ballistic gelatine samples will also be produced to use as a comparison between the new developed gel and the existing standard surrogate.

1.4.3 Ballistic gelatine

Ballistic gelatine is commonly used as a soft tissue surrogate [75, 97, 98], and will therefore be used as a base line comparison. It also has excellent optical properties so it is often used in photoelasticity [4, 77]. However, gelatine does not accurately replicate the properties of soft tissue. Gelatine has a near linear elastic behaviour, with lower rate dependency compared to soft tissue, which is generally non-linear [99]. It also tears when punctured with a needle, as discussed in section 1.2.2 and shown in Figure 1-20; which is a repeat of Figure 1-7 for ease of reference.

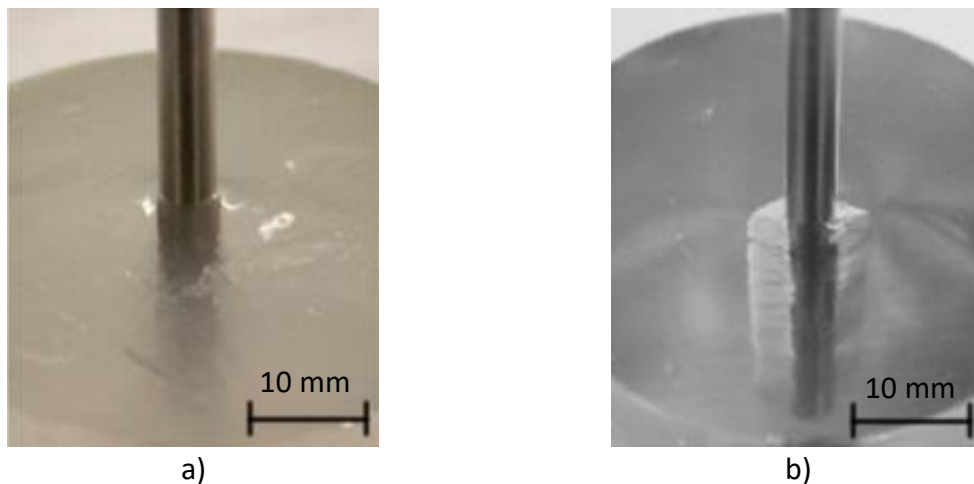


Figure 1-20 a) konjac gel clinging to punctured needle b) gelatine which exhibits tearing [4].

This is a problem as human tissue doesn't tear when punctured with a needle, instead it 'clings' to the needle as it is inserted. If the surrogate tissue tears then it won't produce an accurate friction force, and will not correctly emulate the strain field around the needle tip.

1.4.4 Konjac

Previous research on this topic has used "Jim Willie" konjac powder as the surrogate material [4, 7, 19, 80]. Konjac glucomannan is an amorphous polymer. It's derived from the konjac plant and used as a food thickening agent to make transparent jellies. A recent report by Tomlinson and Taylor showed that when a needle punctures konjac gel it produces a different puncture crack than conventional gels [4]; it does not tear and resists crack formation as seen in Figure 1-20. It also demonstrates viscoelastic behaviour which the gelatine surrogates were lacking [80].

A recent study by Daud *et al.* concluded that konjac glucomanan could be a potential medical surrogate as its mechanical properties were comparable to that of soft tissue [100]. The konjac used in the study by Daud is the same type of konjac used by Tomlinson and Taylor.

Unfortunately, konjac jelly has poor optical properties; the powder sets quickly during mixing which led to pockets of higher density material appearing within the mixture. It also has poor birefringent properties; the fringes appear faint and blurry in comparison to the fringes shown in Gelatine in Figure 1-21.

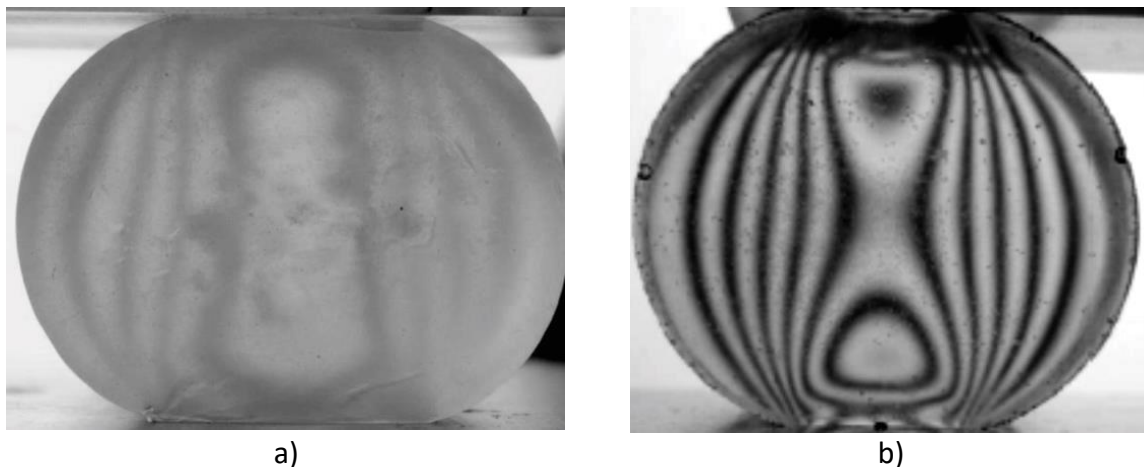


Figure 1-21: a) fringes in konjac Jelly b) fringes in gelatine [4]

Previous work showed that it was difficult to create consistent and homogeneous samples of konjac jelly [7, 19]. However, the processing instructions for the gel were brief and were based off instructions for making the gel for culinary purposes. The lack of clarity could be fixed by modifying the manufacturing technique, as the main cause of the cloudy appearance was from bubble inclusions or clumps of unmixed powder. Therefore, the process to create konjac samples should be assessed and modified to create consistent, homogenous samples.

The difficulties in manufacturing the konjac gel prompted Thompson and Tomlinson to investigate the components of the konjac jelly to see whether the gelling agent would also produce a gel which resisted crack growth [19]. They determined that the gelling component in konjac jelly is carrageenan gel.

1.4.5 Carrageenan

Carrageenan is the food thickening agent found in konjac jelly [19]. There are three different types of carrageenan; Kappa, Iota and Lambda [101]. Kappa and Iota both form gels with varying properties. The following study focussed on the properties of Kappa carrageenan as it is the type used in konjac jelly. Initial research showed it displayed resistance to tearing, viscoelastic behaviour, and excellent optical properties [19].

Only preliminary tests were conducted on carrageenan where its concentration was low and therefore produced a very soft material [19]. Further tests are required to assess its optical and mechanical properties with increasing concentrations.

1.4.6 Potential additives

A number of additives could be used in the gel preparation to alter their mechanical or optical properties, where required.

Sugar

The recipe for the konjac jelly required large additions of sugar [7, 19], therefore it was hypothesized that sugar could be contributing to the material's resistance to crack growth by making the gel 'stick' to the needle. This will be investigated by creating samples with and without sugar as assessing whether the resistance to crack growth changes.

Beads

Some studies added tracking elements to the surrogate material to assess how it deformed during needle insertion. Hong *et al.* added ink tracking dots to the outer surface [102], and Leibinger *et al.* added beads within the mixture to track its motion using volumetric DIC [99].

Within the photoelastic analysis a complete and continuous strain field of the deformation is acquired, rather than discrete points. Hence the addition of tracking elements is not necessary to monitor the material movement. However, beads could still be added to the surrogate to mimic a biopsy target, and the strain field ahead of the needle could be analysed as it approaches a 'biopsy target'. This could provide insight on how material inconsistencies affect the needle trajectory.

1.5 Conclusion and direction of research

The presented literature review has shown the concept and development of photoelastic techniques and the related research on needle insertion investigation with the potential tissue surrogates. It is clear that the development of a new birefringent tissue surrogate is required in order to progress. The materials that currently exist either do not replicate tissue's material properties correctly or have poor optical properties.

1.5.1 Material requirements

This research is concerned with needle guidance through live tissue, consequently the elastic modulus of the surrogate tissue will be fabricated such that it has a similar elastic modulus to that of human skin tissue *in vivo*. Mimicking the properties of the *in vivo* experiments will create a more lifelike surrogate material. Using the results presented in Table 1-2 the desired range for elastic modulus was found to be 81.8 kPa – 226.2 kPa. A study by Lehmann *et al.* showed that a needle insertion through two gelatine surrogates with different stiffnesses produced different amounts of needle deflection [103]. Therefore, a close match of stiffness between tissue surrogate and skin tissue *in vivo* is required in order to replicate a real environment. The development of a soft tissue surrogate will be presented in chapter 2.

In section 1.1.4 the effect of increasing needle insertion speed on force response was discussed. Both tissue surrogates and *ex vivo* real tissues were subject to needle insertion tests at increasing speeds. It was found that the surrogates responded with a greater force reaction with increased insertion speeds, but real tissues responded with the same force reaction at the range of insertion speeds. Therefore, the developed surrogate material should be tested to assess whether it responds differently at varying loading rate, as skin tissue does [49, 56, 70, 104]. If it does exhibit loading-rate dependencies, then it will be used to assess whether it gives different force responses at the varying insertion speeds.

Resistance to crack growth

In section 1.2.2 the importance of the surrogate material's resistance to crack growth was discussed. It was argued that the different failure pattern could alter the trajectory of the needle by altering the strain/stress field ahead of the needle tip. If tissues fracture in a fundamentally different way from a potential surrogate, it's not clear how the results can be

translated to the case of real tissues. It is therefore vital that the developed gel exhibits a resistance to crack growth in order to advance analysis methods within this area.

Values for failure strain were presented in Table 1-2, with a range between 0.27 – 1.13. These results were gathered from skin tissue *ex vivo*, however it will still be beneficial to compare this value to the failure strain of the developed surrogate to assess whether it is suitable.

It was discussed in section 1.4.6 that sugar could be used to enhance the tissue surrogate. It is possible that sugar may increase the material's resistance to crack growth. This will be tested as it could be used to enhance existing tissue surrogates which currently tear when punctured with a needle. This will be assessed in section 2.4.4.

1.5.2 Optical properties

In order to use the developed surrogate in photoelastic testing it must be clear, colourless, and exhibit temporary birefringence. The optical properties should be checked to be independent of strain in order to ensure the viscoelastic phenomenon of 'stress relaxation' does not interfere with the optical results. The optical properties of the developed gel will be assessed in section 2.6.2, and the strain optic coefficient will be determined in chapter 3.

1.5.3 Needle investigation

Once a suitable skin tissue surrogate which is viable for use in photoelastic testing has been developed, there are some key points which involving needle insertion which will be investigated. These points will be presented in sections 4.2 and 4.3.

Effect of needle type

It would be beneficial to investigate the effect of changing needle tip shape and gauge on overall deflection and stress/strain profile ahead of the needle tip. Existing research showed that different needle tip types had a large effect on the recorded forces [2, 11, 95]. Further research showed that the axial force response increases with increasing needle diameter [11, 18]. Similar results are presented for needle tip angles, where blunter needles respond with a greater axial force [14, 15]. However, few studies elaborate on the deflections of the needles

as a function of needle type. It would also be revealing to assess whether there is a link between axial force response and resultant deflection.

Directional information

Within the Stress Photonics software for the poleidoscope it is possible to get directional data, as well as data on the magnitude of the stresses and strains. Generally, research is concerned with the magnitude of forces but no indication is given about the direction. Since the main topic of this research is regarding deflection of needles, it is likely that the direction of the forces will yield some significant information on how and why the needle deflects as it travels through soft tissue.

Effect of needle speed on force response

Within the literature there is conflict between the effect of increasing the speed of needle insertion. When inserting a needle into soft tissue surrogates the research showed that an increasing speed often led to an increase in axial force response [26-30]. However, when inserting needles at increasing speeds into real tissue no such trend was reported [8, 31-35]. It is essential that the effect of increasing needle insertion speed is investigated on this new skin tissue surrogate. It is hypothesized that the force responses were different as a result of the surrogate tissue tearing issue, or due to different tribological profiles between the surrogate and real tissue.

1.5.4 Homogenous or heterogenous surrogate material

Most of the studies which use a tissue surrogate create a homogenous surrogate [11, 26-30, 105, 106]. It was stated that homogenous tissue surrogates were used in the study by Okamura *et al.* in order to aid a consistent testing environment [11]. However, as discussed previously, biological tissue is not homogenous. Therefore, it may be assumed that different load distributions will be obtained if an inhomogeneous material was used.

Studies have shown that even when the complex structure of skin tissue is accounted for, the force required to insert a needle into skin was found to depend heavily on sharpness and the size of the needle [16, 17, 107]. It may be possible that the needle dimensions dictate the resultant deflection more than any material inconsistencies. It is likely that both contribute to

the overall needle deflection, but comparison will be drawn between the effect of changing tip type and material inconsistencies on resultant deflection to assess which contributes more.

It was also noted that asymmetrical needles are more susceptible to changes in the material as they experience greater bending loads than their symmetrical counterparts. This was found during studies where the surrogate material was mostly homogenous. It was assumed that this effect would only increase when tested on inhomogeneous materials [11, 15, 95].

It was also discussed that beads could be added to the surrogate to mimic the biopsy target, and the strain field ahead of the needle could be analysed as it approaches the 'biopsy target'. This could provide insight on how material inconsistencies affect the needle trajectory.

The response from needle insertion into homogenous tissue surrogates and inhomogeneous surrogates will be investigated in chapter 4.

2 MECHANICAL CHARACTERISATION

Before any needle insertion experiments could be conducted, a material that simulated the properties of skin had to be developed. As discussed in section 1.2, the properties of tissue are complex, therefore initial work will focus on construction of a simple model material which satisfies the following desired criteria:

Stiffness: In section 1.2.3 the varying mechanical properties of skin were discussed. A sample range of 81.8 kPa – 226.2 kPa was found for elastic modulus *in vivo*. The material will be tested for elastic modulus and mixtures will be altered to fit within this range by modifying the concentration of powder within the mixture.

Tear Resistance: In section 1.2 the importance of a material which resists crack growth was argued, as it changes the strain profile and potentially alters the needle trajectory. Hence the final material should be resistant to crack growth.

Optical Properties: Clarity and birefringence need to be assessed to determine whether the material will be suitable for photoelastic testing. The optical properties of the developed gel will be assessed in section 2.6.2. The material's strain optic coefficient also needs to be determined, which will be presented in chapter 3.

The present chapter covers the material development process and results from mechanical testing. Compression tests were performed to assess the gels' non-linear effects and elastic modulus in compression. Tensile tests were also performed to assess the gels' resistance to crack growth and elastic modulus in tension. Previous work with these gels was used as a starting point for this development on material properties [7, 19, 108].

Three different gels were investigated for use as a possible skin tissue surrogate, as introduced in section 1.4. Gelatine samples were tested and used as a base line comparison as gelatine is commonly used as a soft tissue surrogate [75, 97, 98]. Carrageenan and konjac samples were also investigated to assess their viability as a potential skin tissue surrogate.

2.1 Experimental considerations

In section 1.2 of the literature review it was discussed that skin exhibits some time-dependant and non-linear behaviour. Nonetheless, as discussed in section 1.2.3, elastic modulus is commonly used within the tissue engineering community to quantify skin tissue stiffness, for example by focusing on linear regions of the stress-strain curves and by considering only constant strain rates. For consistent comparison a similar approach is adopted in the present work. Furthermore, the software to be used in chapter 3 requires an input of elastic modulus and will not consider any variabilities from time dependant affects or non-linear behaviour. With consideration of the requirements of the photoelastic software, using elastic modulus for measuring stiffness with certain assumptions is suitable.

The apparent stiffness of viscoelastic materials also depends on the loading rate [109]. If the loading rate is increased the material will respond with a greater apparent stiffness, therefore leading to higher reaction forces. In order to use elastic modulus to describe the gels they must be subject to rigorous testing. It has been shown that carrageenan, konjac, and human skin tissue behave differently at varying loading rates [19, 49, 80]. The skin tissue surrogates will be subject to loading rate assessments to ensure consistent results at constant speeds, and to evaluate the significance of changing speeds.

Previous research has shown that the gels respond differently at different temperatures [19, 80]. As a result, all the samples will be stored in a fridge prior to testing to ensure an even and consistent temperature is reached. The samples will be removed from the fridge and the test will be started as quickly as possible to avoid heat transfer.

The data presented within this chapter shows the average result of numerous tests within each test type. The full results are available in the appendix in section 8.1.

2.2 Development of gelling process

The process for preparing the gels was developed and refined as the original preparation method was flawed. Previous work with these gels expressed the difficulty to make consistent batches and homogenous specimens [7, 19, 80]. Therefore, critical analysis of the processing technique was required in order to produce reliable specimens. The final preparation technique of the gels is as follows:

- The water and gel powder were weighed on a digital scale. The water was added to the gastronorm basin first and the powder was added in small increments and mixed in until homogenised. A gastronorm is a rectangular container used in a bain-marie, shown in Figure 2-1.



Figure 2-1: Photograph of plastic gastronorm

- The mixture was covered with cellophane and left for a twenty-four-hour period at room temperature to allow for the gel powder to absorb the water. If this step was skipped the gel would not absorb all of the water, even after heating. This step also allowed for any lumps to absorb water and disband.
- The gastronorm was placed in a wet-heat bain-marie and the water temperature was set at 70°C for konjac, 60°C for carrageenan, and 50°C for gelatine. The temperature for gelatine was chosen following work by Ravikumar *et al.* [110]. However, the konjac and carrageenan did not fully melt at this temperature so it had to be increased.
- The gel was left to heat for one hour, and part-way through it was shaken to promote even heat distribution. This step is necessary for the konjac gel as it tended to heat unevenly which promoted the development of lumps.



Figure 2-2: Photograph wet-heat bain-marie

- The molten konjac jelly was poured through a metal sieve into a warmed jug prior to moulding. The konjac jelly solidified very quickly, therefore the jug was heated to delay it from setting before moulding. The carrageenan and gelatine gels did not require this step as they were homogenous after melting, if they were poured through a sieve it added many bubbles which did not dissipate.
- The gel was then carefully decanted into moulds and left to cool at room temperature. The gelatine and carrageenan samples took 24 hours to set completely, whereas the konjac samples took under 1 hour to set and cool completely.
- The solidified gel was carefully removed from the moulds and placed in a refrigerator at $4\pm 1^{\circ}\text{C}$ to set overnight. The gels were covered with cellophane to prevent dehydration while in the fridge.
- After setting overnight, the gel was ready to test. It was kept refrigerated until required for testing. It could be stored up to three days, after which it began to decompose. To promote consistency all the tests were carried out after 24 hours of setting time.

2.3 Compression testing

Compression testing was conducted to obtain mechanical properties of the gels, such as its elastic modulus in compression and non-linear response.

2.3.1 Moulding of compression specimens

The gels were formed into cylinders of 50 mm diameter and 25 mm height for compression testing, shown in Figure 2-3 (a). The gelatine samples were cut from a thick gelatine sheet using a cylindrical cutter. The molten konjac and carrageenan were poured straight into cylindrical moulds, shown in Figure 2-3 (b). The cylindrical moulds were cut from a single tube of aluminium, ensuring the cross section was consistent across all the moulds.

This difference in formation of the cylindrical samples was due to gelatine's sticky outer surface. If the gelatine was set in the moulds it would be damaged when it was removed. Whereas if the carrageenan or konjac were cut from a set sheet their slippery surface would result in uneven sides, but this slippery surface meant that they could be easily removed from the moulds.

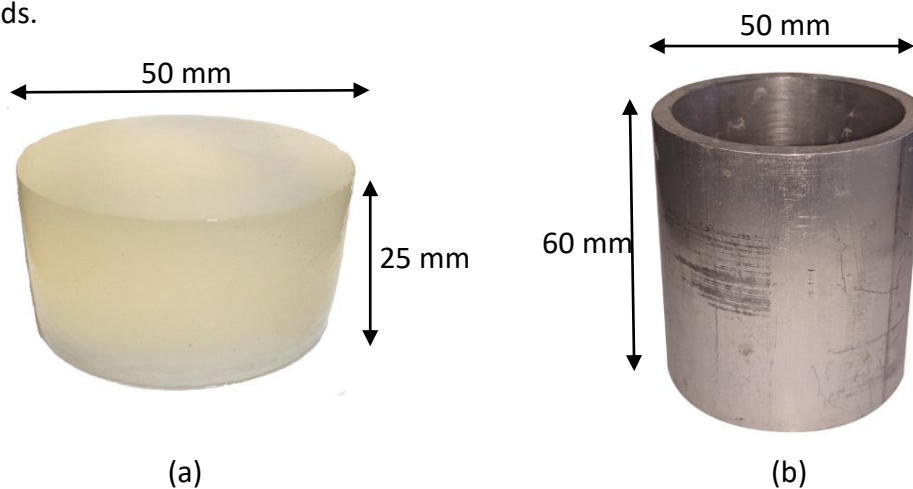


Figure 2-3 (a) Photograph of compression sample (b) Photograph of compression mould

2.3.2 Compression test setup

All samples were tested on a Tinius Olsen 5 kN benchtop tester, using a 250 N load cell. New samples were used for each test, and the number of samples used for each experiment will be stated with the presented data.

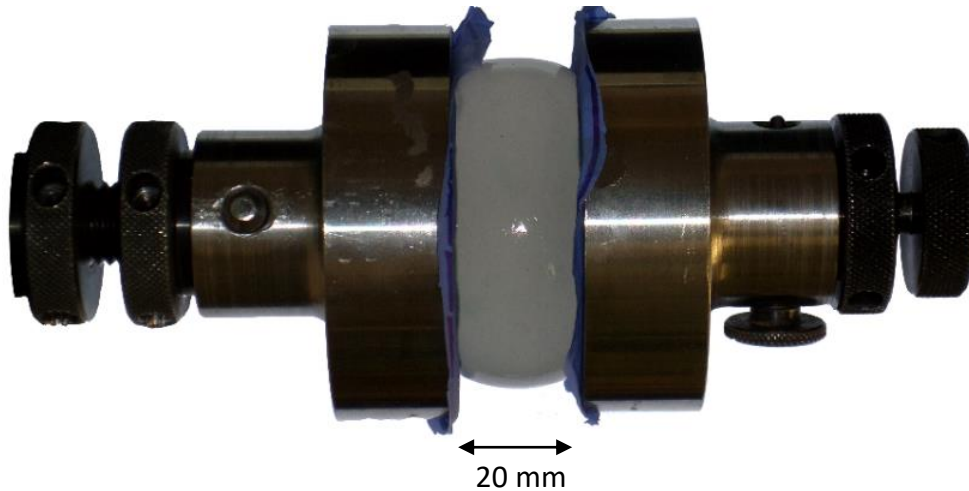


Figure 2-4: Image of sample between compression grips at 0.25 strain – Image rotated 90° for best fit

The samples were secured in the grips using Loctite super glue in order to prevent them from slipping during the test. A disposable rubber sheet was placed between the grips and the sample, as can be seen in Figure 2-4. This was added to avoid gluing the sample directly to the grips as this caused a residue to be left on the grips. It is evident from Figure 2-4 that barrelling does occur; at a strain of 0.25 the maximum diameter has increased by 5 mm. While this is a significant increase and will affect the recorded properties of the material, the *in vivo* experiments used to characterise skin tissue also overlooked the effects of barrelling [59-62]. In order to produce a relevant material comparison between the different gels and skin tissue it is logical to ignore the effects of barrelling for now.

All the tests were conducted using displacement control rather than load control. This avoided any potential errors caused by the stress relaxation observed. During the tests the force response, position, and time were recorded.

The skin tissue substitutes tested previously by Thompson *et al.* have been heavily temperature dependant [19]. Zhao and Huang had similar findings with the material they created for their experiments [111]. Therefore, care should be taken to maintain a constant temperature when testing any materials. The tests were performed at an ambient temperature of $24\pm 1^{\circ}\text{C}$. The samples were refrigerated at $4\pm 1^{\circ}\text{C}$ until they were required for testing. Once removed, they were quickly loaded into the grips and testing began to prevent heat absorption.

2.3.3 Range of compression tests

The compression samples were loaded until a strain of 0.25 was reached, as when deformations exceeded 0.30 strain the samples began to deteriorate. The compression amount was also restricted to prevent excessive barrelling, which would result in erroneous results. The same constraints were used on a recent study by Remache *et al.* for testing the properties of porcine tissue [49].

For the complete range of experiments the samples were compressed to 0.25 strain, and the elastic modulus was calculated using the data within the range of 0.2 to 0.25 strain. This period was chosen for use in the calculations as during a needle insertion the material around the crack will be experiencing large strains. The elastic modulus of the gels was then compared to the range of elastic modulus for human skin tissue.

Concentration analysis

Compression tests were used to assess the elastic modulus of the gels at varying concentrations. Previous work with these gels has not attempted to match the stiffness of the gels to the stiffness of human skin tissue [7, 19, 80]. Therefore, an initial assessment of the optimum gel concentration is required.

Loading rate analysis

Tests were conducted at loading rates of 1 mm/min and 20 mm/min. The different speeds were selected to see whether an increase in loading rate affected the recorded results; a common observation in skin tissue [104, 106, 112-119]. These speeds were chosen as they were within the recording capabilities of the software; higher testing rates produced noisy results.

Stress relaxation analysis

After the loading rate analysis, the test was paused and the test head was held in the same position until the load relaxed. This was done to visualise the stress relaxation of the materials.

Preconditioning assessment

A secondary set of tests loaded the samples cyclically between 0 and 0.25 strain for three cycles. This was completed to assess whether the materials behave differently after subsequent loading cycles; a characteristic of skin tissue [49].

2.3.4 Concentration analysis

Before any comparisons could be drawn between the different gels, the ideal concentration of gel powder to water needed to be determined for each gel. In section 1.2.3 the elastic modulus of skin tissue *in vivo* was found to lie within the range of 81.8 kPa – 226.2 kPa. The new skin tissue surrogate should also have an elastic modulus within this range to mimic the actual response during needle insertion. The stiffness of gels is controlled by modifying the gel powder to water ratio. In this section the elastic modulus of carrageenan and konjac gel was assessed at increasing concentrations. Previous work involving these gels was used at a starting point for choosing concentrations [7, 19, 80].

2.3.4.1 Carrageenan

The carrageenan powder used in the following experiments was purchased from SpecialIngredients on 25 September 2016 [120].



Figure 2-5: Photograph of carrageenan powder pot

Previous work by Thompson and Tomlinson reported that carrageenan is the gelling agent in konjac jelly [19]. Hence, similar concentrations were used for both carrageenan and konjac gel preparations in their study to make the gel surrogates with comparable properties. However, no quantitative material comparisons were drawn between the elastic modulus of the final gel preparation and human skin tissue *in vivo*. Thompson's and Tomlinson's mixture also contained large quantities of sugar, as the original recipe for the konjac gel required the

addition of sugar to spread out the gel powder. It has been hypothesized that sugar may promote the material's resistance to crack growth. Therefore, preparations with and without sugar will be prepared in the tensile analysis to test this hypothesis in section 2.4.4.

In the study by Thompson and Tomlinson a mixture of 10 g carrageenan powder, 250 g sugar, and 650 ml water was prepared [19], which roughly equals a 1% concentration of gelling agent. The final gel was shown to deform heavily under its own weight; and higher concentrations were suggested in future work. Therefore, preparations were created which contained 1%, 2%, and 3% concentrations of carrageenan powder to water by weight. All the gel mixtures were prepared in accordance to the procedure described in section 2.2.

The gels were subject to compression testing at a loading rate of 1 mm/min, and were compressed until a strain of 0.25 was reached. The position and force response were recorded and used to calculate the engineering stress and engineering strain for each concentration. The results are plotted in Figure 2-6, with the error bars displaying the standard error.

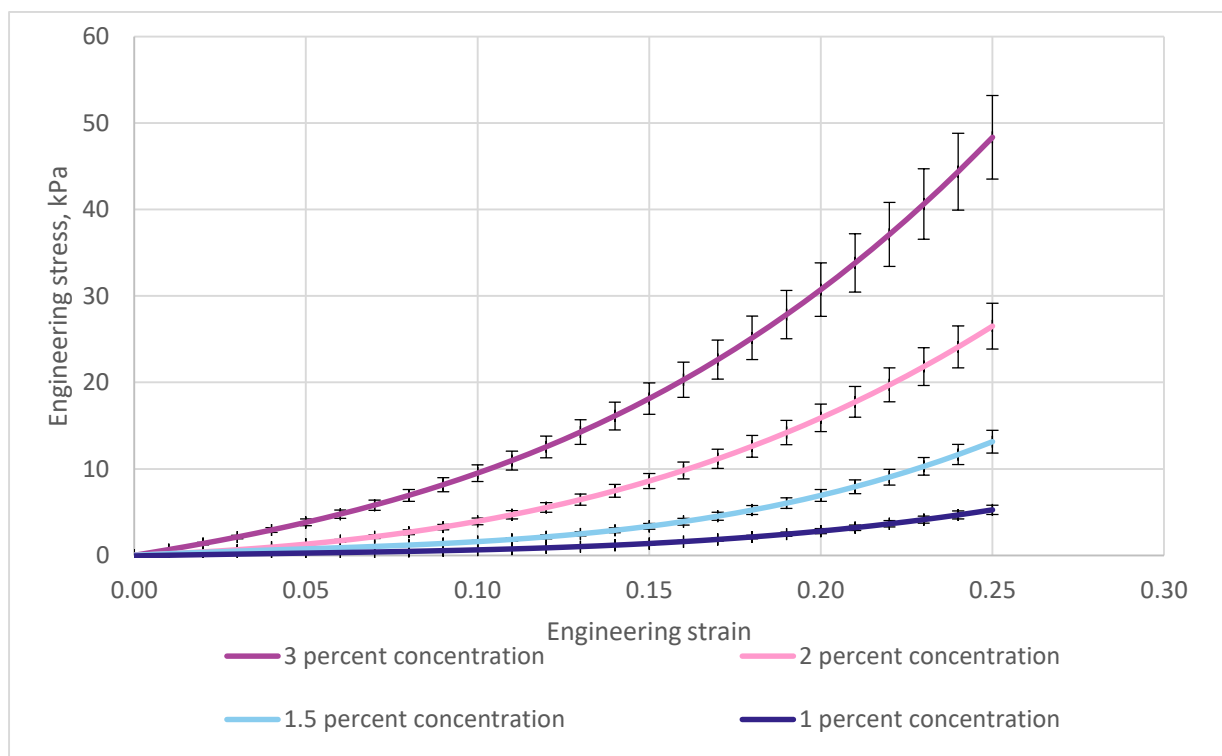


Figure 2-6: Carrageenan compressive concentration analysis

The elastic modulus for each concentration was calculated using the slope of the curves between the strain of 0.20 and 0.25; results are presented in Table 2-1.

Concentration, %	Elastic modulus, kPa
3.0	352.3 ± 17.6
2.0	212.2 ± 10.6
1.5	124.3 ± 6.2
1.0	49.0 ± 2.5

Table 2-1: Results for elastic modulus in compression for various concentrations of carrageenan at 1 mm/min

The gel requires an elastic modulus between 81.8 kPa – 226.2 kPa to act as a surrogate for human skin tissue. With reference to the results in Table 2-1 it can be seen that the concentration of 2% is on the upper limit of this range, and the 1% samples were too flexible. Therefore, another batch of samples with a 1.5% concentration was created, results for this batch are also presented in Figure 2-6 and Table 2-1. With an elastic modulus of 124.26 kPa it fits perfectly within the desired range of 81.8 kPa – 226.2 kPa. Therefore, subsequent testing with carrageenan used a concentration of 1.5% carrageenan powder to water by weight.

2.3.4.2 Konjac

The konjac powder used in this study was the “Jim Willie Konnyaku Jelly Powder” ordered from Malaysia. An image of the packet is shown in Figure 2-7.



Figure 2-7: Photograph of konjac powder packet

Previous studies investigating konjac for use as a tissue surrogate had opposing conclusive remarks [7, 80]. Both studies report varying optical properties of the gel, such as its clarity, when the same concentrations were used. However, both studies also mention the difficulty in manufacturing a consistent, homogenous gel. It is postulated that the different manufacturing methods could have resulted in gels with different properties.

Morton *et al.* chose a high concentration of approximately 2.4% gel to water weight for the final concentration of his gel surrogate, as it was comparable porcine fat *ex vivo* [7]. However, as shown in section 1.2.3, tissue has a greater stiffness *ex vivo* than *in vivo*. It is possible that this percentage is too high when comparing to human skin tissue *in vivo*. A large amount of sugar was also added to Morton’s mixture, and it is unclear how this sugar would affect the mechanical properties of the gel. The recipe for the konjac requires a large amount of sugar to disperse the konjac powder, which prevented large lumps from forming when the water was added. It was hypothesised that the sugar addition could lead to the reported resistance to crack growth; this is investigated in section 2.4.4. Aui Yong *et al.* created a gel with a concentration of 1.2% to water weight, and remarked that at that concentration the gel “did not deform under its own weight” [80].

However, similar to work with the carrageenan gel, there were no quantitative comparisons between the mechanical properties of konjac and human skin tissue *in vivo* [7, 80]. Reflecting on results from the carrageenan gel, and what previous studies have reported, concentrations of 1% and 1.5% konjac powder to water by weight were prepared.

As with the carrageenan gel; the konjac samples were compressed at 1 mm/min until a strain of 0.25 was reached. The position and force response were recorded and used to calculate the engineering stress and engineering strain for each concentration.

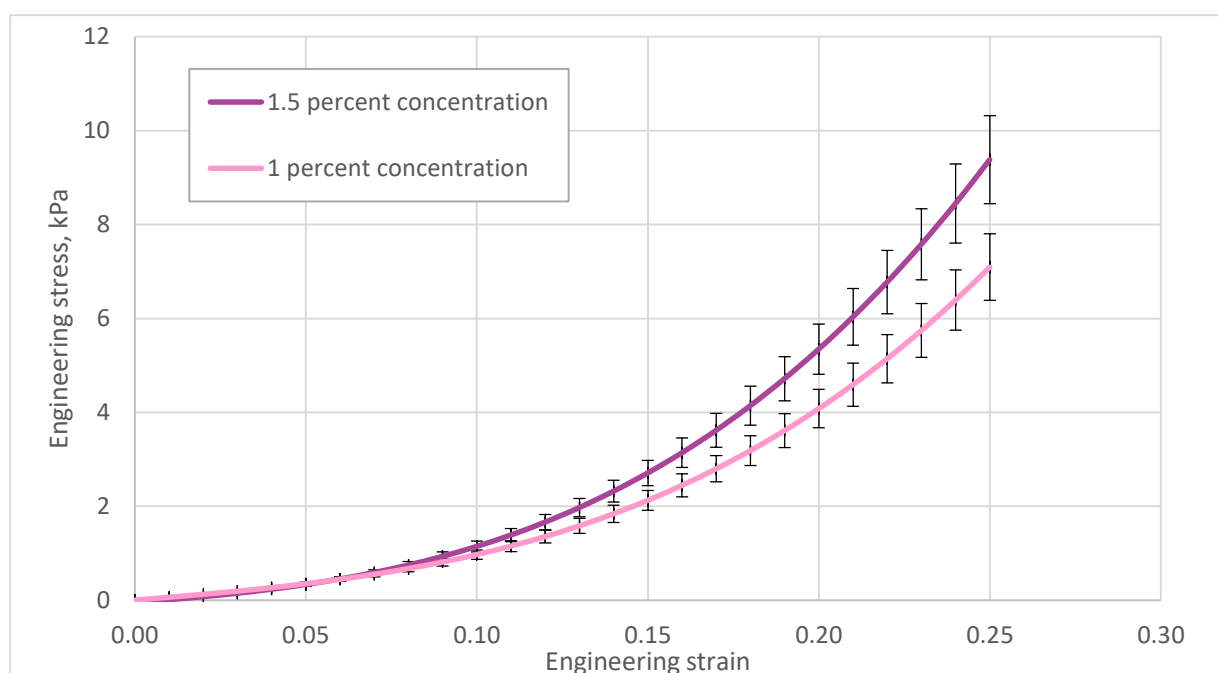


Figure 2-8: Konjac compressive concentration analysis

The elastic modulus for each concentration was calculated using the slope of the curves between the strain of 0.2 and 0.25, and results are presented in Table 2-2.

Concentration, %	Elastic modulus, kPa
1.5	80.7 ± 4.0
1.0	60.3 ± 3.0

Table 2-2: Results for elastic modulus in compression of the various concentrations of carrageenan at 1 mm/min

It is interesting to note that even if carrageenan is the gelling agent in konjac jelly they still have significantly different responses at the same concentrations. It is likely that the konjac jelly has other non-gelling components which cause its recorded resistance to crack growth.

The gel requires an elastic modulus between 81.8 kPa – 226.2 kPa to act as a surrogate for human skin tissue. A concentration of 1.5% is still marginally too low to fit within the stated range of stiffness. However, preliminary batches at concentrations over 1.5% were not homogenous, and contained stiff inclusions where the gel powder had not been completely absorbed; it appeared that the gel was at its saturation point at this time. It was therefore decided to proceed with a 1.5% concentration gel for konjac; to ensure consistent and homogenous samples were created.

2.3.4.3 Concentration conclusion

It was found that both carrageenan and konjac jelly produce a gel with a stiffness comparable to the stiffness of human skin tissue *in vivo* at a concentration of 1.5% powder to water by weight. Initial results show that both gels exhibit non-linear behaviour. Further compression tests with these gels will continue in sections 2.3.6 and 2.3.7.

The following experiments involve all three gels; gelatine, carrageenan, and konjac. The average results of each material will be presented in turn and then a comparison of all the gels will be presented section 2.3.8. This section will contain discussions on the gels response with respect to the response of skin tissue. Graphs containing all the individual results from each experiment are located in the appendix in section 8.1.

2.3.5 Compression test results: Gelatine

Compressive response

In this assessment the gel samples were loaded to a strain of 0.25 at loading rates of 20 mm/min and 1 mm/min. The deflection and force was recorded and used to calculate the engineering stress and engineering strain for each sample. The same method was used for subsequent gel assessments presented.

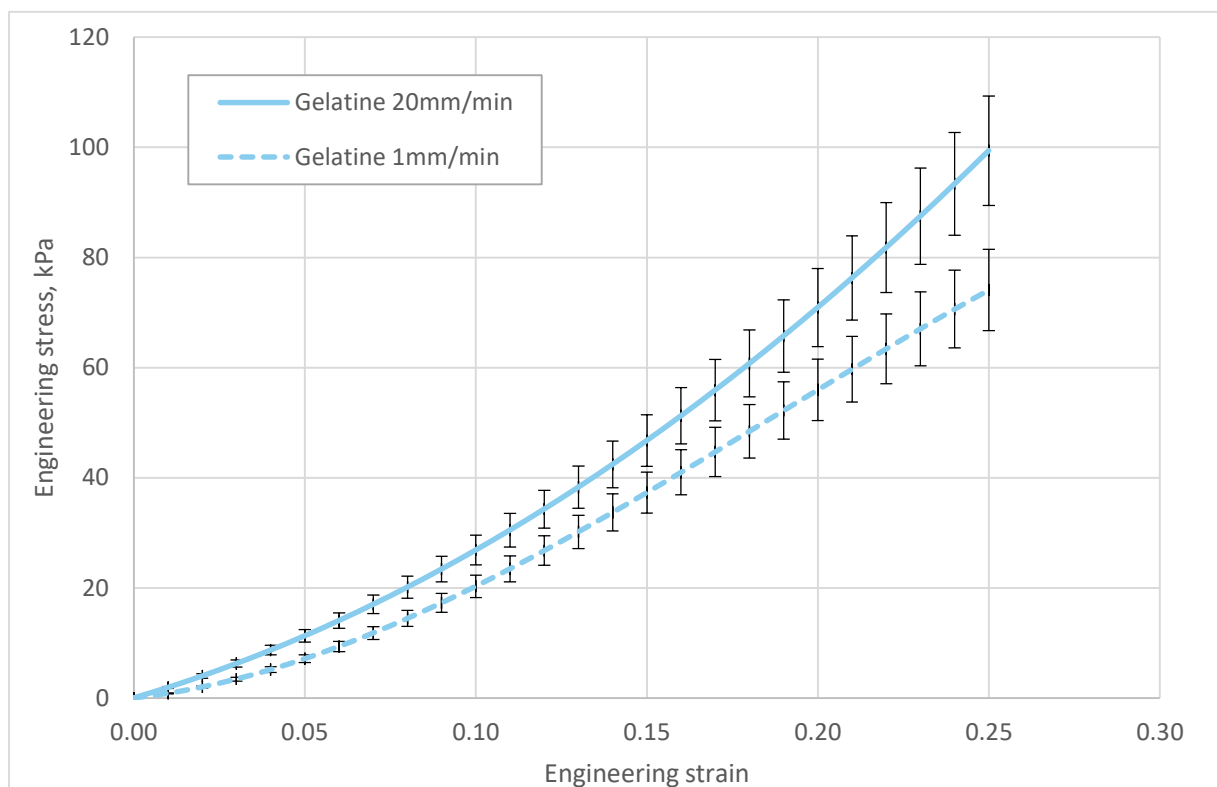


Figure 2-9 Compression of gelatine to 0.25 strain at 1 mm/min and 20 mm/min loading rate

Figure 2-9 contains the average response of gelatine specimens loaded at 20 mm/min and 1 mm/min, five samples were tested at each speed and the average is displayed. It can be seen that above 0.15 strain the response is near linear up to the end of the test, and the different loading rates did cause a different response.

Stress-relaxation observation

In the previous analysis the samples were loaded to a strain of 0.25 and then the compression heads were stopped. The same samples were then held at this strain in order to view the stress relaxation response. The force response was recorded and used to calculate the engineering stress, which was plotted against the time which the sample was held at this strain. This allowed for an analysis of the stress-relaxation behaviour. The same method was used for subsequent gel assessments presented.

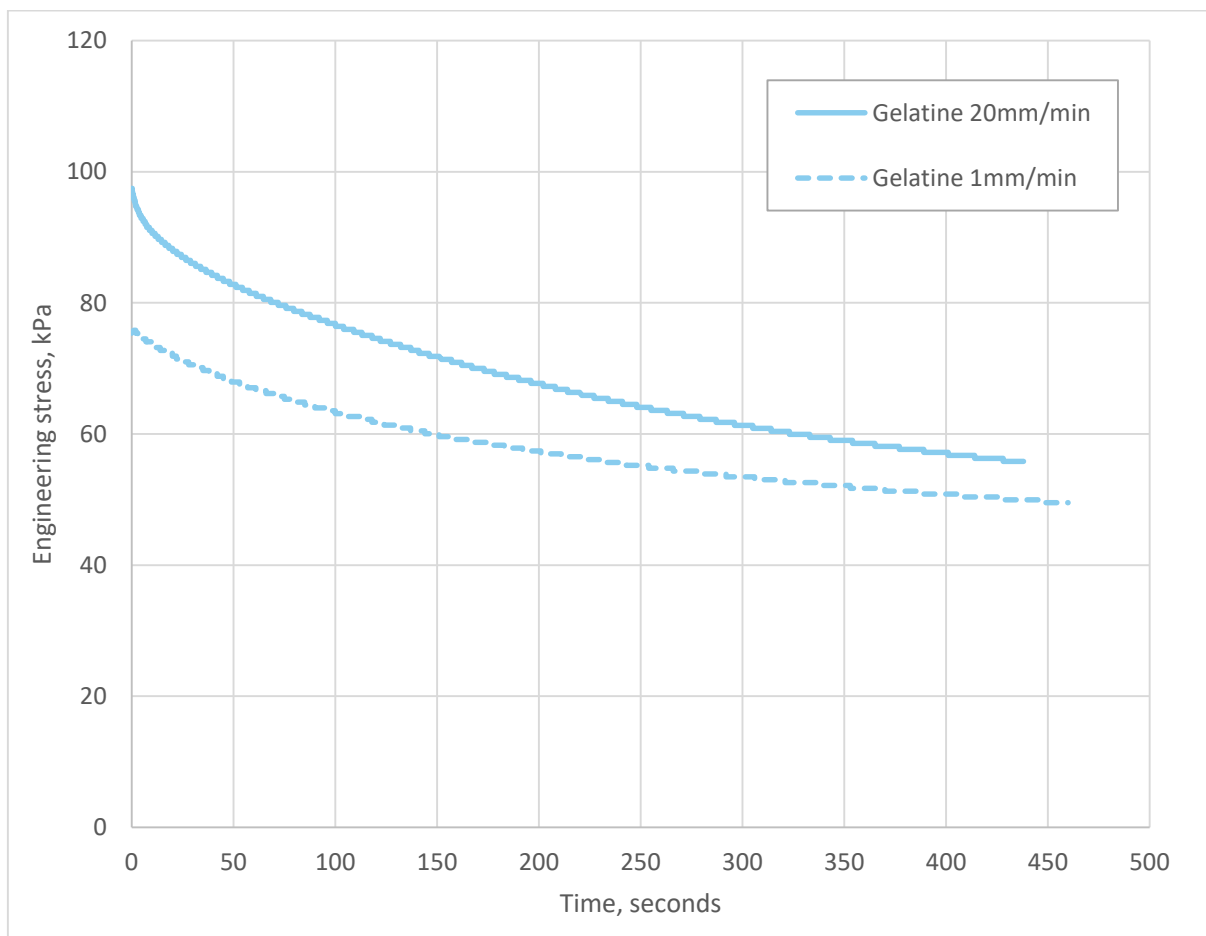


Figure 2-10 Stress relaxation response of gelatine at 0.25 strain after loading rates of 1 mm/min and 20 mm/min

Five samples were tested at each speed, and the average result is displayed. In Figure 2-10 we can see that as soon as the compression heads were stopped the reaction force produced by the samples began to decrease.

Hysteresis loop

In this analysis the samples were compressed to a strain of 0.25 and then unloaded back to 0 displacement. This was repeated for three cycles to see whether the response of the material changes through subsequent cycles, much like human skin tissue which undergoes an initial preconditioning cycle [49]. The same method was used for both subsequent gel assessments presented.

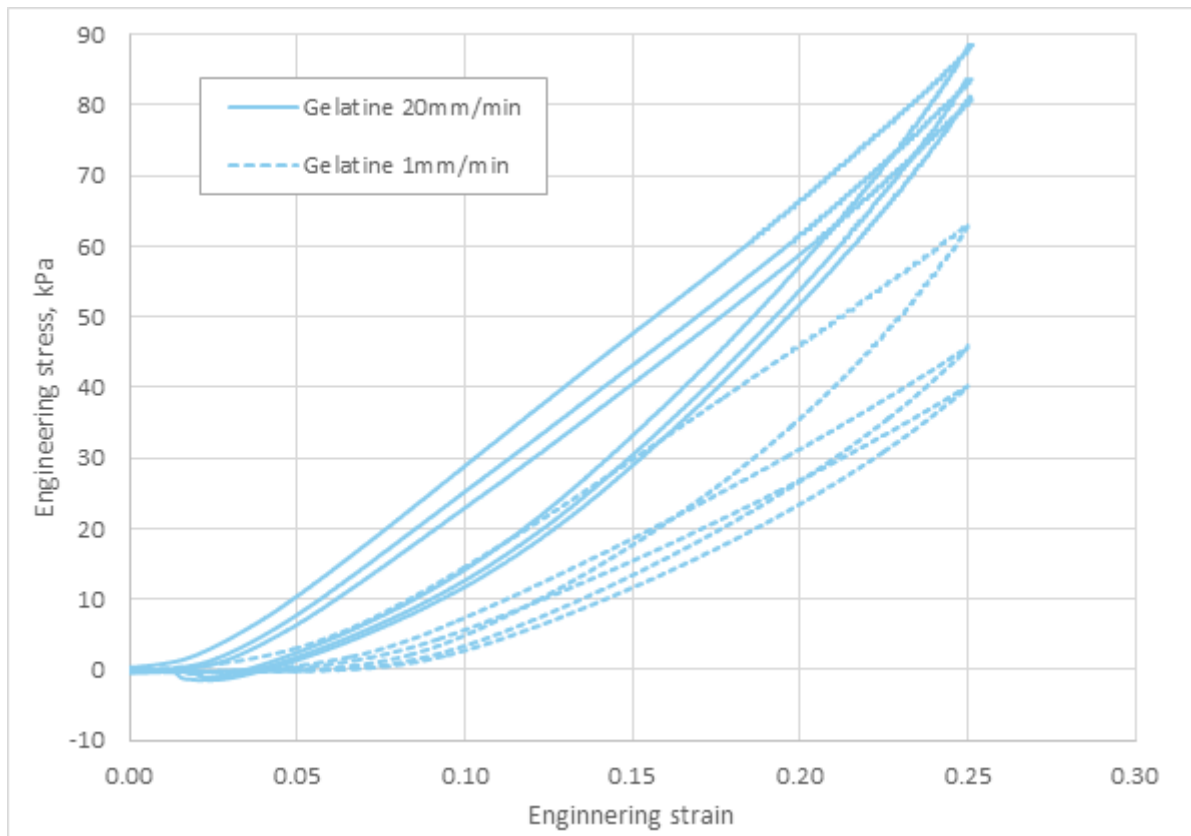


Figure 2-11 Cyclic compression response of gelatine at 1 mm/min and 20 mm/min

A total of eight new samples were subject to cyclic loading, four at each loading rate. Figure 2-11 contains the average result at each loading rate. Figure 2-11 shares the same initial response as seen in Figure 2-9 where the samples loaded at 20 mm/min exhibited a higher end stress than those loaded at 1 mm/min.

It is interesting to note that the samples loaded, and unloaded, at 1 mm/min appeared to have a more defined pre-conditioning cycle than the higher loading rate. This may be due to the test taking longer and the sample increasing in temperature and therefore becoming less stiff.

The tests at 1 mm/min took approximately 25 minutes to complete, whereas the tests at 20 mm/min were completed in under 5 minutes.

2.3.6 Compression test results: Carrageenan

Compressive response

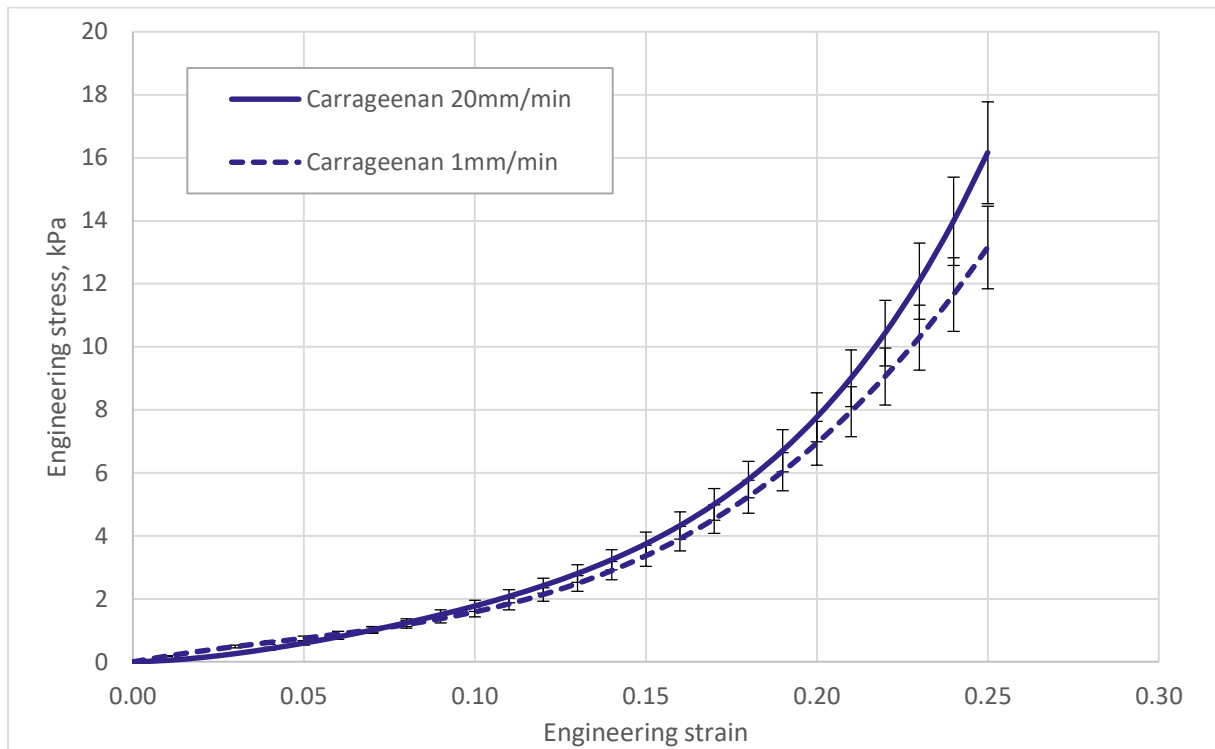


Figure 2-12 Compression of carrageenan to 0.25 strain at 1 mm/min and 20 mm/min loading rate

Four samples were tested at a loading rate of 20 mm/min and 3 samples at 1 mm/min, the average response of the samples tested has been plotted in Figure 2-12. The response from the previously tested gelatine was near linear for both loading rates, whereas carrageenan has shown the classic J-shape which is consistent with the behaviours of many soft tissues [121].

Stress-relaxation observation

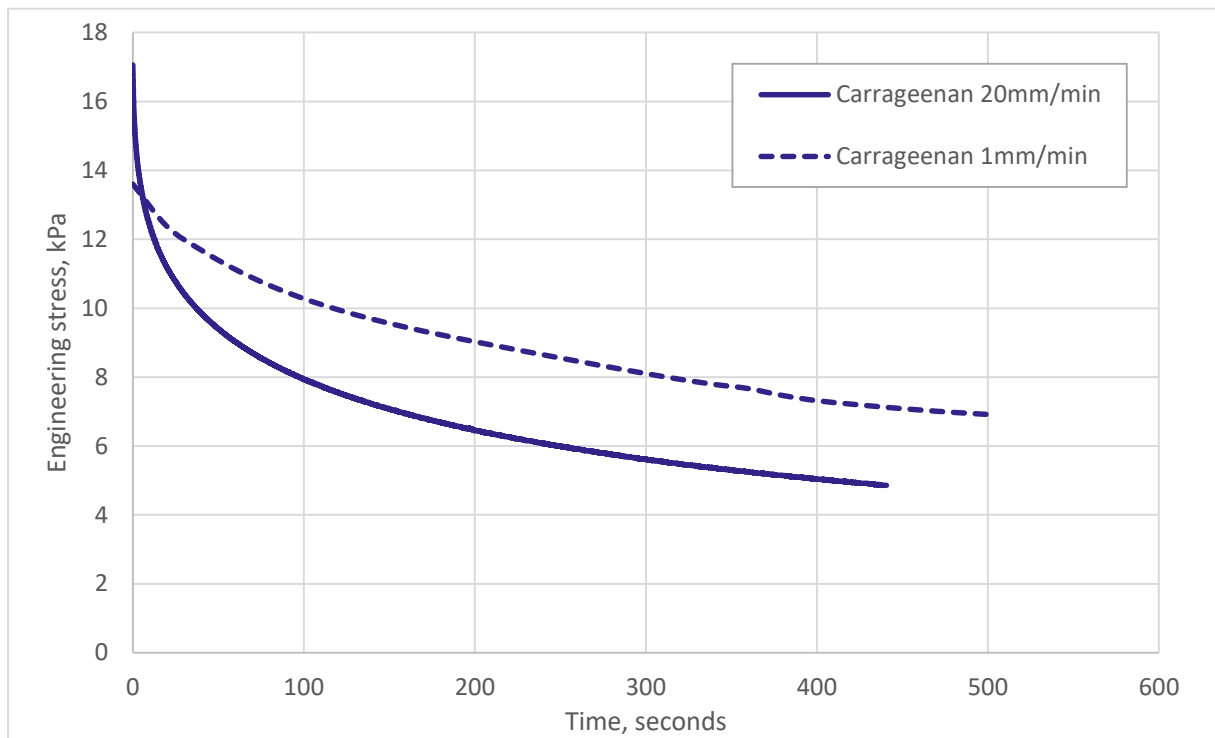


Figure 2-13 Stress relaxation response of carrageenan at 0.25 strain after loading rates of 1 mm/min and 20 mm/min

Four samples were tested at a loading rate of 20 mm/min and 3 samples at 1 mm/min, the average response of the samples tested has been plotted in Figure 2-13. It can be seen that carrageenan exhibits a more severe stress-relaxation response than gelatine. The initial drop in force response, or stress, is significant.

The difference in stress relaxation rates between the samples loaded at different rates is also significant. It was expected that the gels which reached a higher stress would relax quicker at the start, and then both curves would follow the same pattern, as observed with the gelatine samples. It is unclear why stress-relaxation paths for carrageenan crossed.

Hysteresis loop

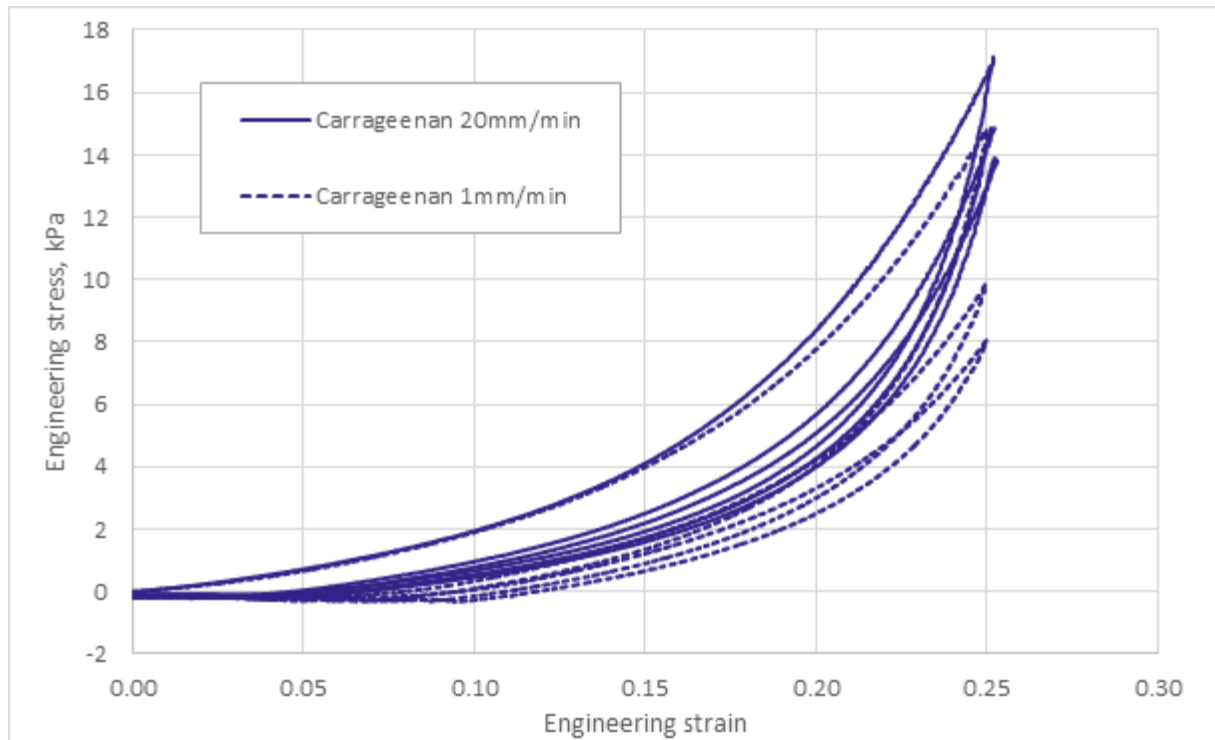


Figure 2-14 Cyclic compression response of carrageenan at 1 mm/min and 20 mm/min

In this analysis four samples were tested at 20 mm/min, and two samples at 1 mm/min. The average response is plotted in Figure 2-14. With initial comparison to the cyclic assessment of gelatine in Figure 2-11 and carrageenan in Figure 2-14; it can be seen that carrageenan exhibits a more significant pre-conditioning effect. A similar response is found with human skin tissue in a study by Remache et al [49], where the “hysteresis loops shifted down and became increasingly narrow as a function of the number of cycles”.

2.3.7 Compression test results: Konjac

Compressive response

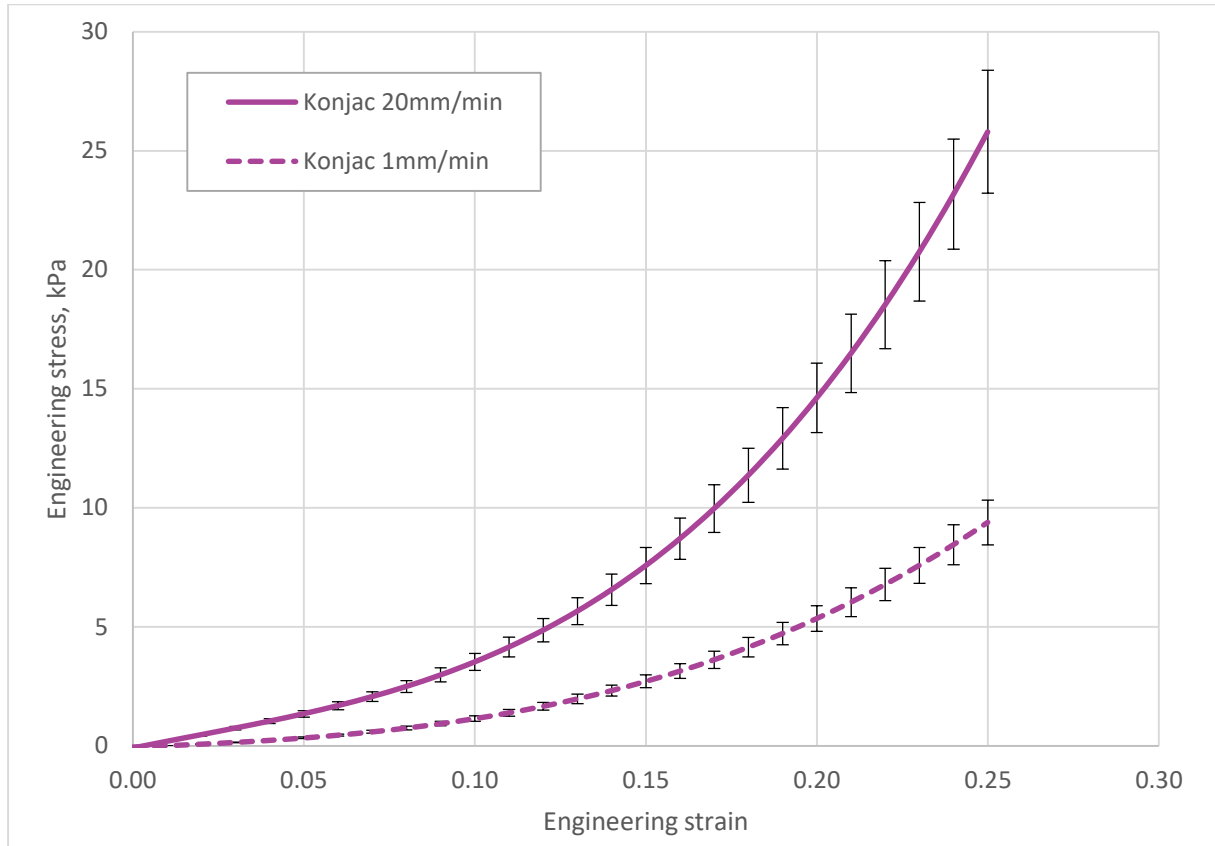


Figure 2-15 Compression of konjac jelly to 0.25 strain at 1 mm/min and 20 mm/min loading rate

Seven samples were tested at 20 mm/min, and five samples at 1 mm/min, and the average response at each loading rate is plotted in Figure 2-15. It can be seen that konjac jelly exhibits much higher load rate-dependence than the previous two gels. This compares favourably with the strong load rate-dependence also exhibited by human skin [104, 106, 112-119].

Stress-relaxation observation

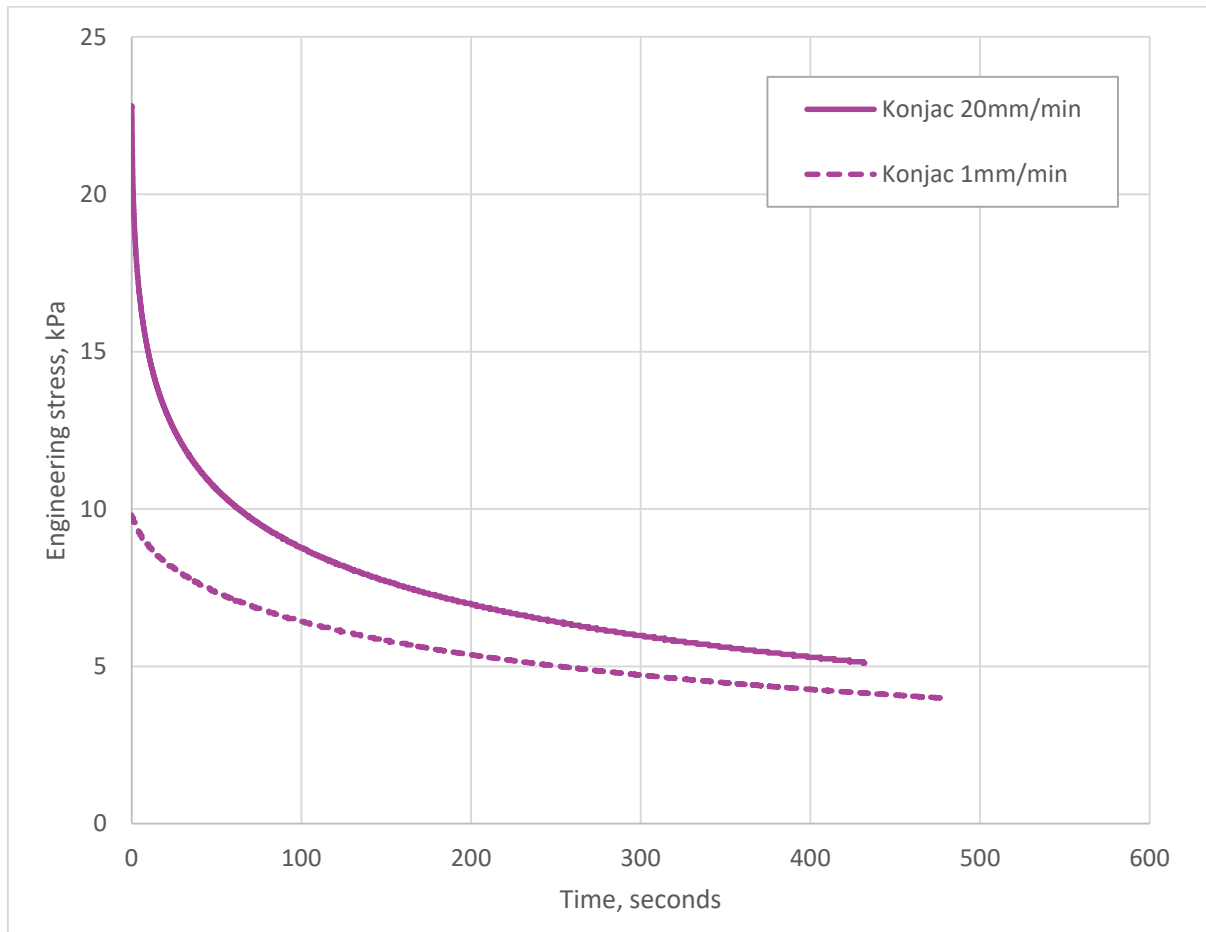


Figure 2-16 Stress relaxation response of konjac jelly at 0.25 strain after loading rates of 1 mm/min and 20 mm/min

Seven samples were tested at 20 mm/min, and five samples at 1 mm/min; Figure 2-16 contains the average stress relaxation response at the different speeds. Konjac jelly exhibits a similar stress relaxation response as carrageenan, where the drop in force from the samples loaded at 20 mm/min is significantly higher than the drop from the 1 mm/min loaded samples. However, with comparison to the carrageenan result in Figure 2-13, the stress relaxation paths do not cross.

Hysteresis loop

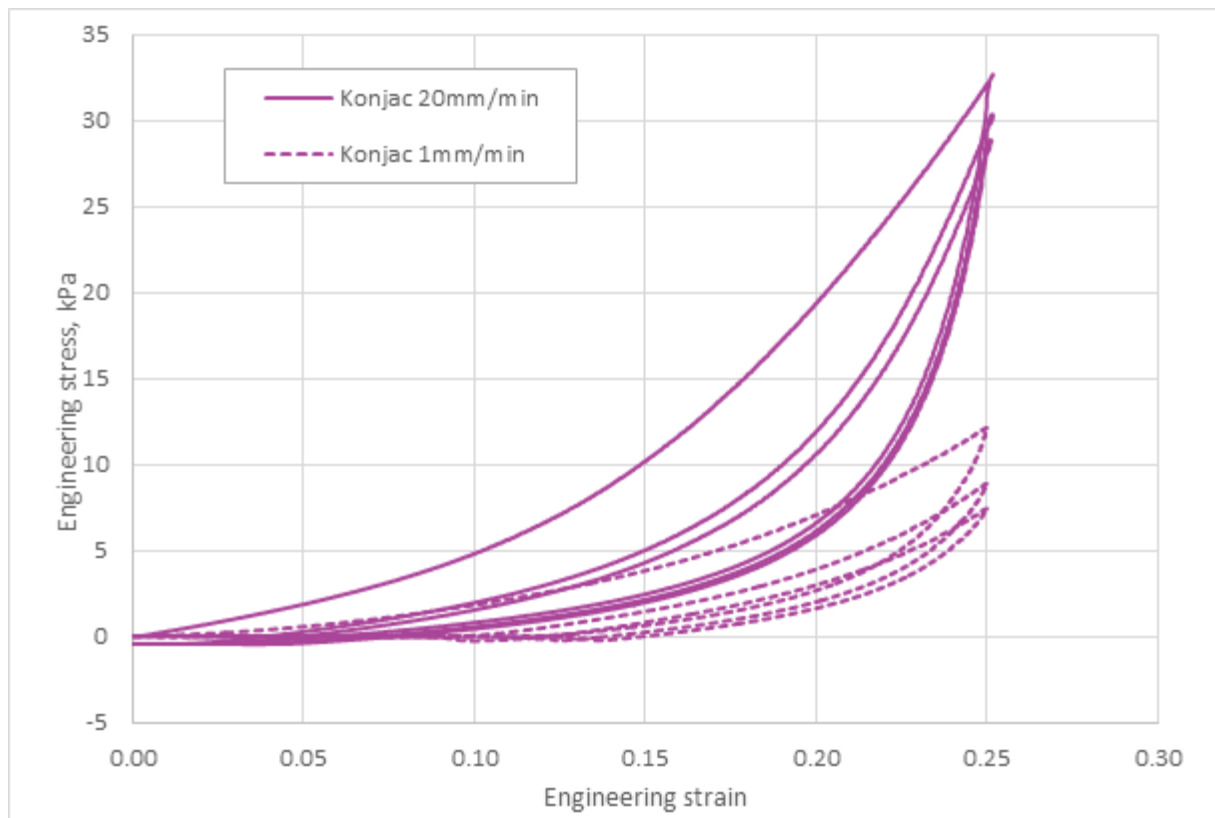


Figure 2-17 Cyclic compression response of konjac jelly at 1 mm/min and 20 mm/min

For this cyclic analysis eight samples were tested in total, with four at each loading rate. Figure 2-17 shows the average response of the gels during the three cycles. It can be seen that the konjac jelly undergoes a clear preconditioning cycle, and the subsequent cycles adhere to a tighter sequence and appear to start converging. A similar behaviour has been observed in porcine skin in a study by Remache et al [49], and in a study testing human skin by S. Diridollou *et al.* [57].

2.3.8 Compression Results: Comparison

In this sub-section the results for the three gels compressed to a strain of 0.25 at different loading rates have been combined for comparison.

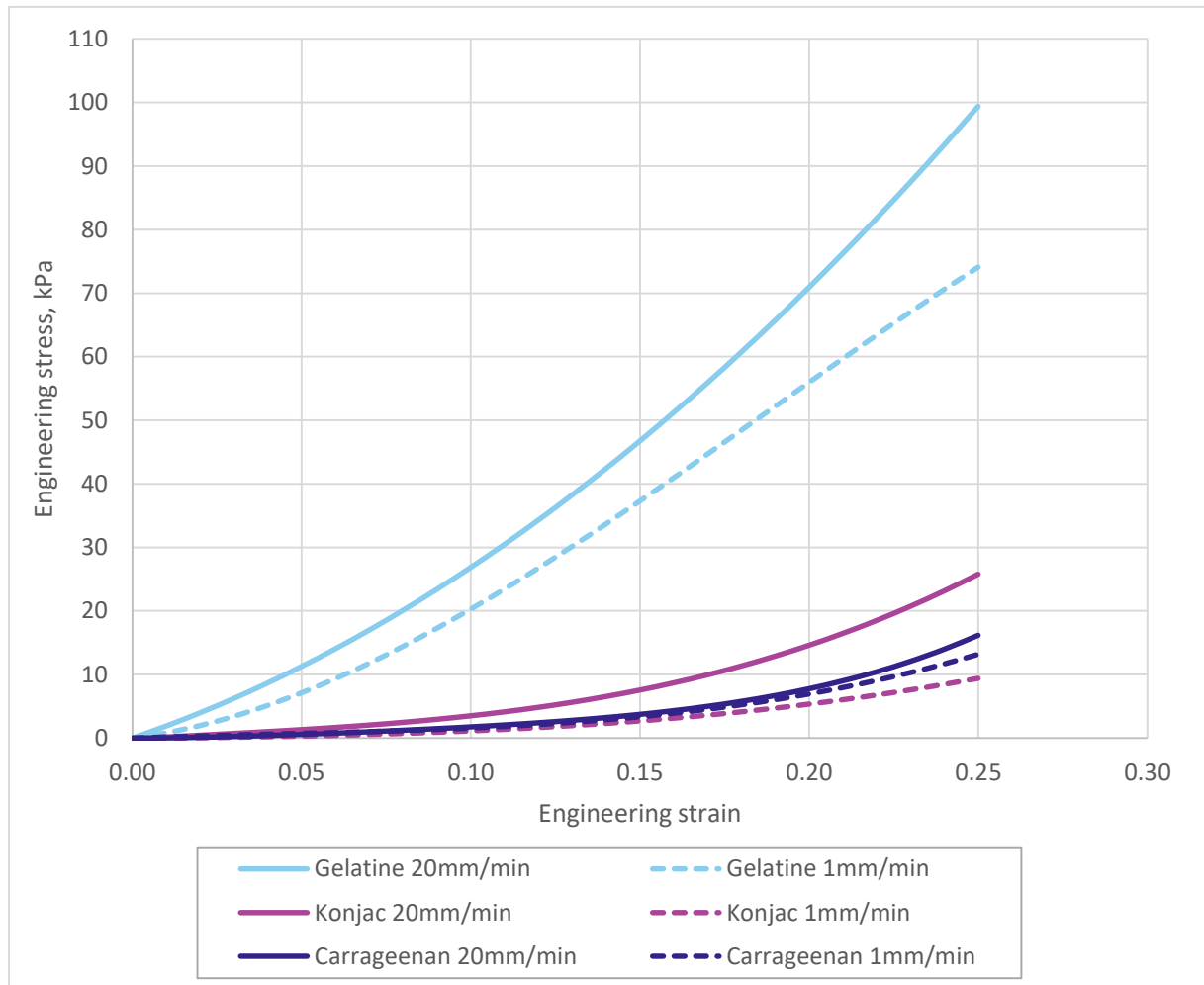


Figure 2-18 Comparison of the compressive responses of the various gels at 1 mm/min and 20 mm/min

The elastic modulus was calculated using the gradient of the curves in the approximately linear region between 0.20 and 0.25 strain. The modulus was calculated in this region as this research is concerned with the crack development around the needle tip, which is associated with larger strains. Therefore, using the material properties at this point is more meaningful.

Table 2-3 contains the results for elastic modulus in compression of the three gels at the varying loading rates.

	Elastic modulus at varying loading rates, kPa		Percentage difference between loading rates
	1 mm/min	20 mm/min	
Gelatine	362.8 ± 18.1	569.4 ± 28.5	44 %
Carrageenan	124.2 ± 6.2	167.9 ± 8.4	30 %
Konjac	80.7 ± 4.0	223.5 ± 11.2	94 %

Table 2-3 Results for elastic modulus in compression of the various gels at 1 mm/min and 20 mm/min

It is evident that all three gels respond with an increased stiffness as the loading rate is increased, yet the amount that they change varies. Konjac jelly performs significantly differently between loading rates, with a percentage difference of 94%. This is approaching results in the study by Remache *et al.* which tested the response of porcine skin at various loading rates [49]. They found a percentage difference of 147% between samples tested at 6 mm/min and 60 mm/min.

The results for elastic modulus in compression for gelatine are far greater than the desired range. The concentration of the gelatine gel used to simulate skin tissue is normally between 10% and 20% to water weight ratio [122]. However, it was recommended to tailor the percentage for that specific batch of gelatine powder as results change from batch to batch. This percentage of 20% was chosen as it was successfully used in previous research [7, 19, 80]. Clearly if gelatine was taken forward for use in needle insertion investigation the concentration would need to be lowered.

The elastic modulus results for carrageenan at a concentration of 1.5% powder to water by weight fit perfectly within the stated range of elastic modulus for human tissue *in vivo*. As can be seen in Table 2-3 konjac jelly almost perfectly fits the desired range for elastic modulus.

However, further investigation is required if the carrageenan or konjac gels are taken forward for needle insertion investigation to assess how they respond under a greater range of speeds used in needle insertions, and how the gels perform in tension.

2.4 Tensile testing

Tensile testing was conducted to determine the gels toughness and elastic modulus in tension. The gel's toughness was measured using the area under the engineering stress strain curve.

2.4.1 Moulding of tensile specimens

No international test standards could be found for tensile testing or testing resistance to crack growth of soft, non-rubber, materials. Therefore standards for similar tests were researched and used as concepts for a suitable tear test for gel materials.

In section 1.2.2 it was mentioned that most soft tissue surrogates do not accurately emulate the resistance to crack growth that skin tissue exhibits. Therefore, each tensile specimen was punctured with a biopsy needle in its centre prior to testing. This made it possible to monitor the crack propagation from a crack caused by a needle insertion, thus allowing the tensile results to be linked to resistance to crack growth.

The ISO 34 – 2 standard was investigated as it is used for testing the tear strengths of rubbers [123]. The standard requires a simple rectangular specimen with a slit in the centre. During testing this slit was replaced with a needle puncture hole in order to assess how the hole propagates. This specimen shape appeared to be advantageous as it avoided cutting complex geometries out of gel sheets. However, when the gel specimens were subjected to tensile loading they failed in inconsistent locations, which led to a lot of scatter within the results. Consequently, alternative sample shapes were researched.

The standard ASTM D-412-F is for testing rubbers and elastomers in tension [124], it requires a slender dogbone sample with large grip sections. This type of shape was thought to be advantageous as the large grip sections will make the sample easier to attach to the grips with glue, and the slender mid-section will ensure the sample fractures in the centre. The samples have a thickness of 8 mm, and the mid-section width was increased slightly from the standard suggestion from 6 mm to 8 mm to allow for a needle puncture hole to be added. This puncture allowed for the assessment of the material's resistance to crack growth. The puncture was applied after the samples were loaded in the grips in order to avoid increasing the puncture size when handling the sample. The needle used to create the puncture hole was a 14 gauge Tru-cut bevel tipped biopsy needle with an external diameter of 2.1 mm; model # 2N2704X.



Figure 2-19: Dimensions of dogbone tensile sample

When testing the new sample shape the gel specimens consistently failed in the mid-section by the needle puncture, as desired. Therefore, this sample shape was used for all future tests. Initially the samples were cut from gel sheets, but this was inaccurate due to the complex sample shape. Therefore, moulds were created which the gel could be poured into.

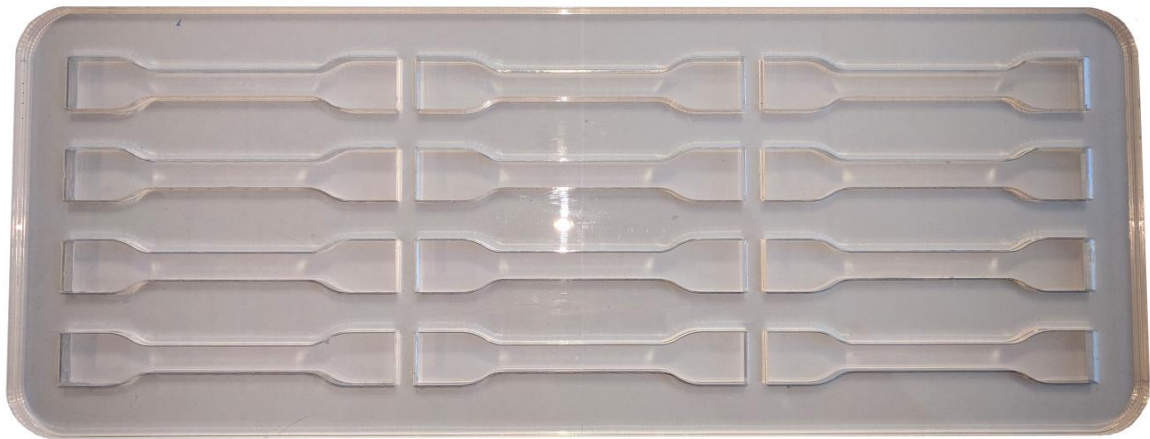


Figure 2-20: Mould used for tensile samples

The moulds were made by laser cutting a PVC sheet. Two sets of the moulds were made, with each containing twelve holes to create the tensile samples. The full capacity of the moulds was used for each batch of testing, as it was easy to damage the samples when removing from the moulds.

2.4.2 Tensile test setup

Since the gel specimens were so fragile conventional grips couldn't be used, as securing the samples with pressure would destroy them. The carrageenan and konjac samples were also quite slippery to touch which added an extra difficulty in securing the specimens.

It was decided to glue the samples to grips as Miller *et al.* did for testing brain tissue in tension [125]. Tensile grips were designed to fit the specimen for maximum adhesion area; these can be seen in Figure 2-21.

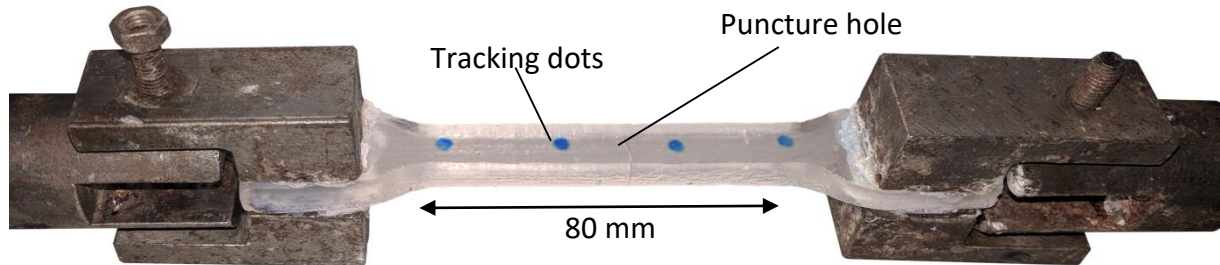


Figure 2-21: Sample glued between grips with visible needle puncture and tracking dots, image rotated by 90° for display purposes.

Loctite superglue was applied to the grips and the tensile samples were loaded in one grip section at a time. The samples were left to settle for a minute to allow the glue to dry completely before testing.

As can be seen in Figure 2-21, the samples had opaque ink dots drawn on prior to testing. These dots were spaced at uniform intervals, with 20 mm between each. The gradual change in spacing between the dots and the change in width allowed for estimation of the principal strain development. The test was filmed and the estimation was performed using the data from recordings. These data were used later in the optical analysis to calculate the strain optic coefficient of the material in chapter 3.

As with the compression tests, all samples were tested on a Tinius Olsen 5 kN benchtop tester using a 250 N load cell. New samples were used for each test, and the number of samples used for each experiment will be stated with the data. The numerous results from each test set were combined to show the average result; this is the data that is presented in this section. The full results will be available in the appendix.

The tests were performed at an ambient temperature of $24\pm 1^{\circ}\text{C}$. The samples were refrigerated at $4\pm 1^{\circ}\text{C}$ until they were required for testing. Once removed, they were quickly loaded into the grips and testing began to prevent heat absorption.

2.4.3 Range of tensile tests

The samples were loaded until completely fractured across the needle insertion point in the mid-section. If the glue was incorrectly applied, or too much applied, the samples sometimes broke in another location. These results were not used for the analysis.

Material additives

In section 1.4.6 it was hypothesized that adding sugar to the samples may increase their resistance to crack growth. Therefore, sugar was added during preparation of some of the samples.

Loading rate analysis

Mirroring the compression tests, the tests were conducted at loading rates of 1 mm/min and 20 mm/min. The two speeds were selected to see whether an increase in loading rate affected the recorded results, which is a common observation in skin tissue [104, 106, 112-119].

2.4.4 Tensile test results: Sugar addition

In section 2.3.4.2 it was suggested that the sugar requirement in konjac jelly could contribute to notable resistance to crack growth. Therefore, in this section the effect of adding sugar to carrageenan gel is presented. This assessment was done using carrageenan and not konjac, as if the carrageenan does not resist crack growth when sugar is added then the resistance to crack growth must be a property of the konjac jelly alone.

Carrageenan samples of 1.5% concentration were made with and without the addition of sugar. The samples were extended at 1 mm/min until they completely fractured across the mid-section. The position and force response were recorded and used to calculate the engineering stress and engineering strain for each preparation. The results are plotted in Figure 2-22.

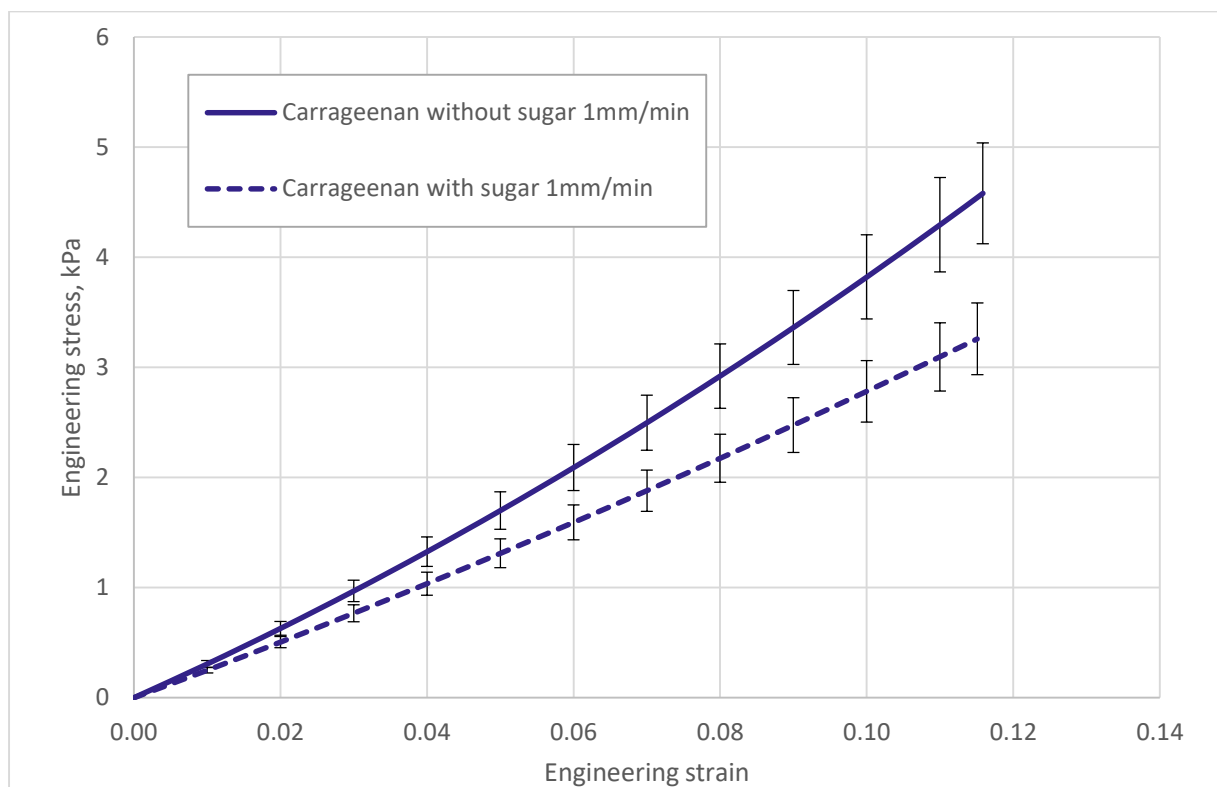


Figure 2-22: Graph displaying the effect of adding sugar to 1.5% concentration carrageenan

The toughness of the different gels was calculated by measuring the area under the curves; results are presented in Table 2-4.

Material	Toughness, kJm^{-3}
Carrageenan without sugar	0.27 ± 0.01
Carrageenan with sugar	0.19 ± 0.01

Table 2-4: Toughness results for carrageenan with and without sugar

It can be seen that the sugar addition does not increase the carrageenan gel's resistance to crack growth; in fact it reduces it. In Figure 2-22 it can be seen that the two variations broke at similar strains, this shows that sugar does not increase resistance to crack growth.

Material	Elastic modulus, kPa
Carrageenan without sugar	50.6 ± 2.5
Carrageenan with sugar	32.0 ± 1.6

Table 2-5: Results for elastic modulus in tension for carrageenan with and without sugar

It is also evident from Figure 2-22 that sugar reduces the stiffness of the gel, as the slope of the graph is reduced with sugar addition. Results of the two stiffness's are presented in Table 2-5. Since the addition of sugar to carrageenan gel does not contribute to a resistance to crack growth, the subsequent gel preparations will not contain sugar.

2.4.5 Tensile test results: Gelatine

In this assessment the tensile samples were extended at rates of 20 mm/min and 1 mm/min until they fractured across the needle puncture hole. The force and displacement were recorded and used to calculate the engineering stress and strain for each sample. The average results of each gel type were calculated and plotted for analysis.

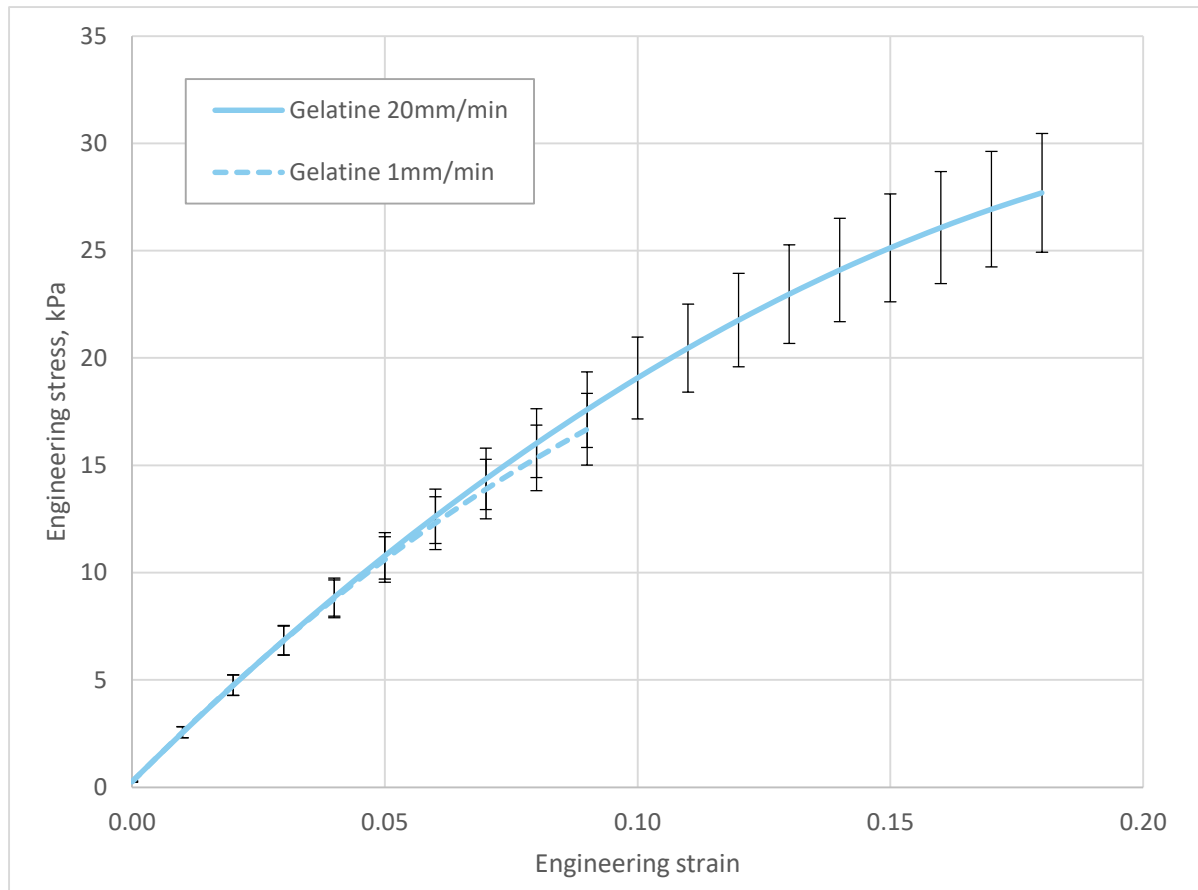


Figure 2-23 Tensile response of gelatine tested at 20 mm/min and 1 mm/min until break

Six samples were tested at 1 mm/min and four samples at 20 mm/min, the averages of these results are displayed in Figure 2-23. It can be seen that the gradient of the curves didn't vary much between the different loading rates; this behaviour was also observed for the samples compression in Figure 2-9. However, the samples loaded at 20 mm/min reached greater extension before fracture than the samples loaded at 1 mm/min.

2.4.6 Tensile test results: Carrageenan

The carrageenan samples were tested in the same manner as the gelatine samples presented.

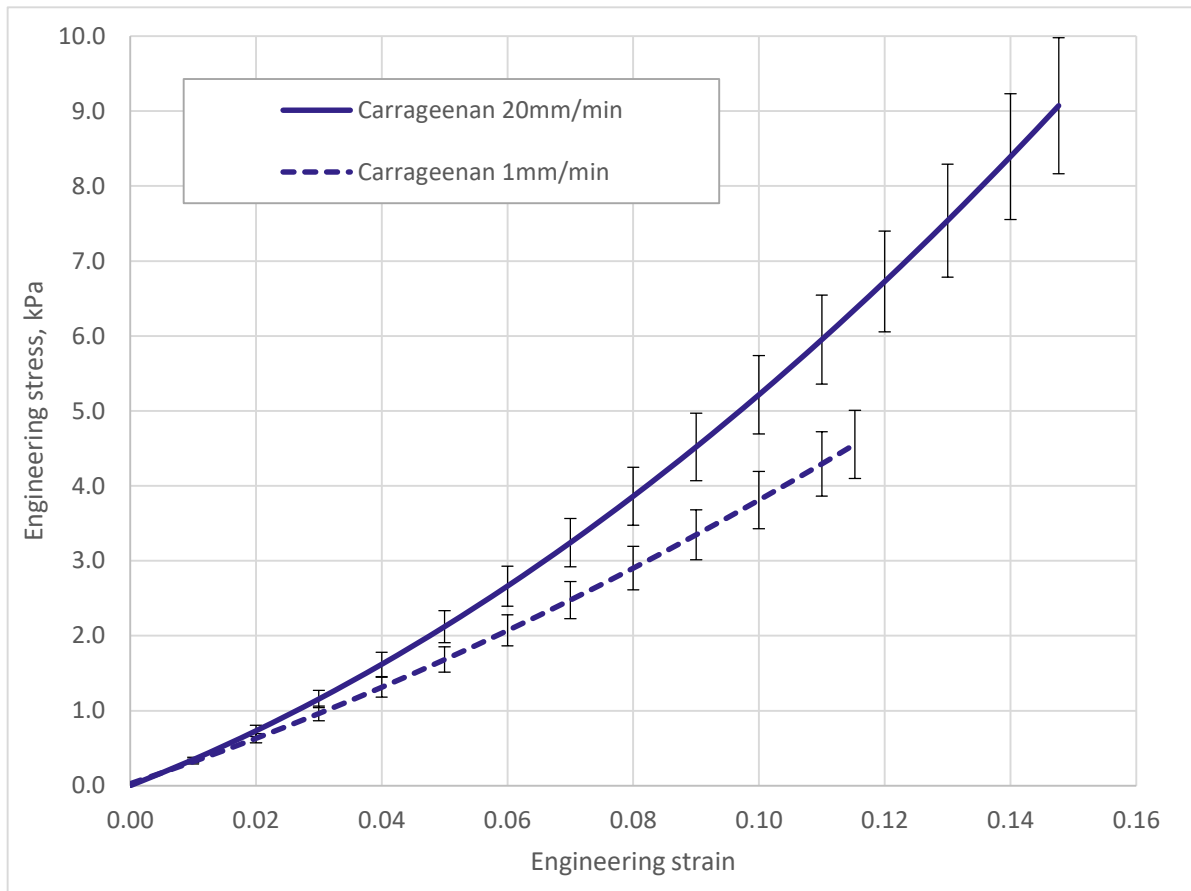


Figure 2-24 Tensile response of carrageenan tested at 20 mm/min and 1 mm/min until break

Four samples were tested at 1 mm/min and six samples were tested at 20 mm/min, the averages of these results were calculated and plotted in Figure 2-24. As with the previous carrageenan analysis in compression the responses didn't vary much with increasing loading rate. Similarly to the tensile results for gelatine, the samples loaded at 20 mm/min reached a greater extension before failure than the samples loaded at 1 mm/min.

2.4.7 Tensile test results: Konjac

The konjac samples were tested in the same manner as the previous gels.

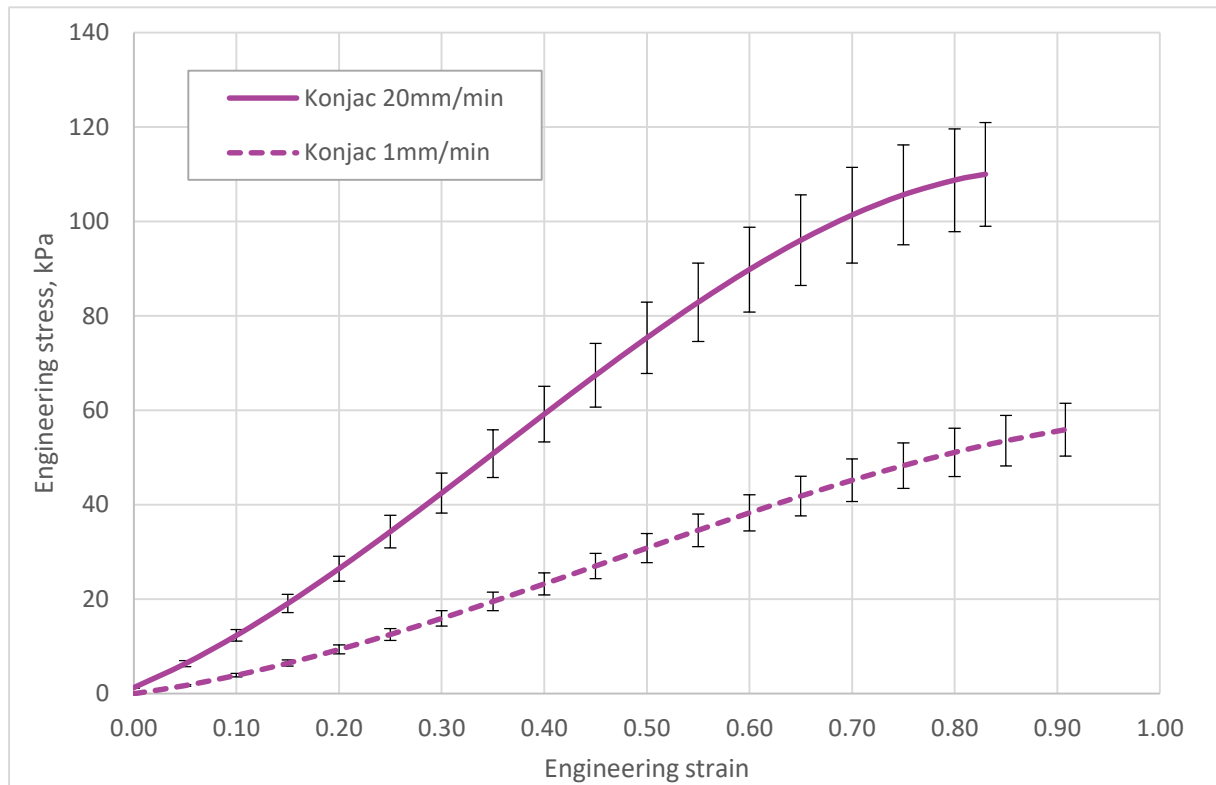


Figure 2-25 Tensile response of konjac jelly tested at 20 mm/min and 1 mm/min until break

Five samples were tested at 1 mm/min and six samples at 20 mm/min, the averages of each loading rate are plotted in the Figure 2-25. It can be seen in Figure 2-25 that konjac jelly increases stiffness response with increasing loading rates in tension; this behaviour is consistent with its performance in compression.

Previously it was shown that the gelatine and carrageenan samples failed at the 1 mm/min loading rate at lower extensions than at 20 mm/min. However, the opposite is shown for the konjac tensile samples.

In section 1.2.3 tensile experiments on skin tissue *ex vivo* resulted in a failure strain between 0.27 – 1.13 [50, 52-54]. The results for konjac jelly in tension produced a range of failure strain between 0.83 – 0.97 at 1 mm/min, and 0.66 – 0.98 at 20 mm/min. These two intervals for konjac are within the range reported for skin tissue, whereas the other two gels are not.

2.4.8 Tensile test results: Comparison

In this sub-section the average tensile responses of all three gels at the different loading rates have been combined into one figure for ease of comparison. The elastic moduli of the gels have been calculated using the same steps outlined in the compression section.

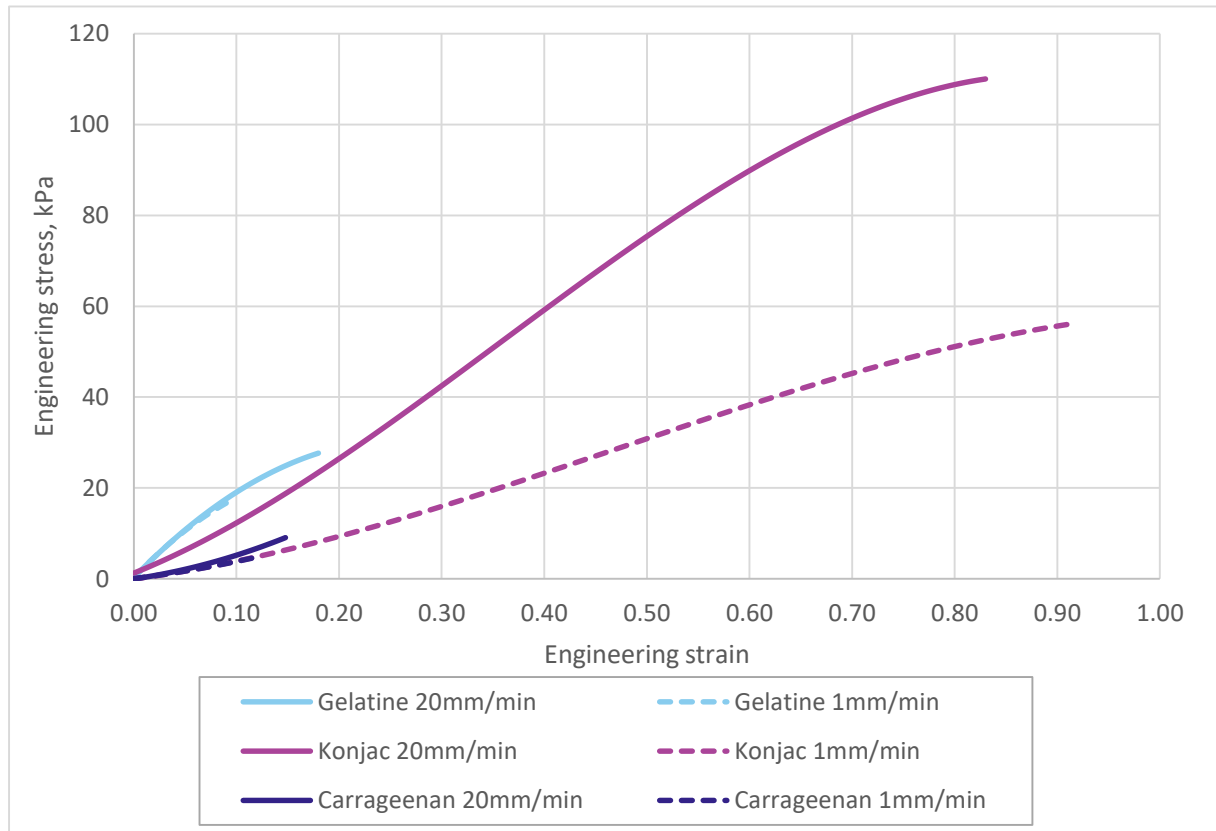


Figure 2-26 Comparison of the tensile responses of the various gels at 1 mm/min and 20 mm/min

In Figure 2-26 the effect of the resistance to crack growth (or tearing) is reflected in this curve by the differences in fracture location. In a previous study by Tomlinson *et al.* it was shown through qualitative analysis that gelatine exhibits little resistance to crack growth compared to konjac jelly [4], and this has been quantified here.

The gelatine samples fractured at very low average strains of 0.08 and 0.18. They exhibited very little resistance to crack growth, and it was observed that the crack propagated very quickly from the initial needle puncture hole. It was hoped that since carrageenan is the gelling agent in konjac jelly it would exhibit some resistance to crack growth but that is not the case. A chemical or composition analysis of konjac jelly should be completed if the reason for this increased crack resistance is required to be understood further. However, that is outside the scope of this project but could be explored in future work.

The toughness of each of the gels was measured using the area underneath the curves, and the results have been presented in Table 2-6.

	Toughness at varying loading rates, kJm^{-3}	
	1 mm/min	20 mm/min
Gelatine	0.8 ± 0.1	2.5 ± 0.4
Carrageenan	0.3 ± 0.1	0.7 ± 0.1
Konjac	25.4 ± 3.6	50.7 ± 7.6

Table 2-6 Results for toughness in tension of the various gels at 1 mm/min and 20 mm/min

When comparing the gelatine results to the carrageenan response it can be seen that the carrageenan samples reached a greater strain before fracturing completely. Despite this, the results for toughness for carrageenan are much lower due to the lower stiffness. The konjac samples reached a significantly higher strain than the other gels before fracturing. This caused the toughness to be substantially larger than the toughness of gelatine and carrageenan.

Accounting for puncture hole

Calculations for elastic modulus assume a constant cross section of the specimens, yet the samples used in the tensile tests included a needle puncture hole in order to assess how the crack propagated. This hole caused the recorded stiffness of the samples to be less than the actual stiffness. The magnitude of this difference was tested by testing some carrageenan samples with and without a puncture hole.

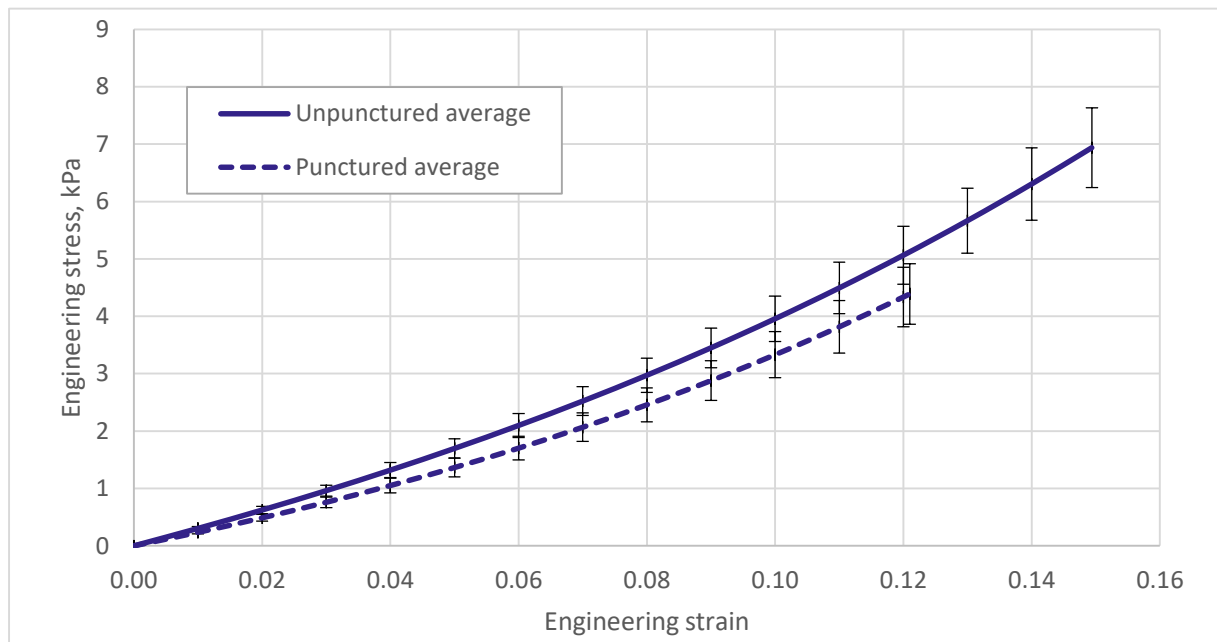


Figure 2-27 Tensile response of carrageenan tested with and without a puncture hole

Nine samples were tested with needle puncture hole, and five successful samples without a puncture; the samples without a puncture hole consistently failed in other locations so it was problematic to gather data. All the samples were tested at a loading rate of 1 mm/min. The results show that the puncture hole does have an effect on the gels stiffness, and the hole also causes the samples to fail prematurely. The elastic modulus was calculated using the data in the near-linear region between 0.1 and 0.12 strain.

	Without puncture	With puncture
Elastic modulus, kPa	55.2 ± 5.8	50.3 ± 6.1

Table 2-7 Results for elastic modulus in tension of carrageenan tested with and without a puncture hole

Results in Table 2-7 show the difference in elastic modulus when the puncture is included. Ideally, this experiment would have been conducted for all three of the gels. However, when both gelatine and konjac samples were extended without a puncture hole they would fail in inconsistent locations. If an experimental setup is required without a puncture hole the sample shape should be revisited.

Elastic modulus

Table 2-8 contains the results for elastic modulus in tension of the three gels at the varying loading rates. Mirroring the method in the compression test section, the elastic modulus was calculated using results between a strain of 0.2 and 0.25. However, the gelatine and carrageenan samples did not achieve this amount of strain before fracturing. Therefore, the elastic modulus was calculated using the results in the last 0.5 strain amount ahead of fracture.

	Elastic modulus at varying loading rates, kPa		Percentage difference between loading rates
	1 mm/min	20 mm/min	
Gelatine	157.8 ± 7.9	174.7 ± 8.7	10 %
Carrageenan	49.6 ± 2.5	77.0 ± 3.9	44 %
Konjac	63.6 ± 3.2	156.9 ± 8.0	85 %

Table 2-8 Results for elastic modulus in tension of the various gels at 1 mm/min and 20 mm/min

Once again the gels all perform differently at the varying loading rates. Konjac jelly performs significantly differently between the two rates, with a percentage difference of 85% for elastic modulus. As with the compression results, this percentage difference is approaching the percentage difference of elastic modulus for porcine skin at various loading rates [49]; which had a percentage difference of 147% between samples tested at 6 mm/min and 60 mm/min.

2.5 Compressive and tensile summary

Table 2-9 contains all results for elastic modulus gathered during the material analysis. This was prepared as the results in compression and tension for the gels have been different throughout.

	Elastic modulus at varying loading rates, kPa			
	1 mm/min		20 mm/min	
	Compressive	Tensile	Compressive	Tensile
Gelatine	362.8 ± 18.1	157.8 ± 7.9	569.4 ± 28.5	174.7 ± 8.7
Carrageenan	124.2 ± 6.2	49.6 ± 2.5	167.9 ± 8.4	77.0 ± 3.9
Konjac	80.7 ± 4.0	63.6 ± 3.2	223.5 ± 11.2	156.9 ± 8.0

Table 2-9 Comparing results for elastic modulus in compression and tension of the various gels at 1 mm/min and 20 mm/min

It is interesting to note that all gels produced a lower stiffness in tension than compression. As discussed in section 1.2.3, tension-compression asymmetry has also been observed in skin tissue *in vivo*, though in that case with higher tensile stiffness than compressive. This difference in response for konjac jelly could be due to fluid dispersion during the experiments.

The konjac samples consistently fractured at strains over 0.8 whereas the other gels barely reached a strain of 0.3 before failing. It is clear that konjac jelly is the only gel that exhibits the important resistance to crack growth. The desired range for elastic modulus for skin tissue *in vivo* is 81.8 – 226.2 kPa. When comparing this range to the results in Table 2-9 it is clear that konjac jelly is the best fit. Therefore, konjac jelly was chosen for use in further analysis for needle insertion investigation in chapter 4.

2.6 Continued assessment with konjac glucomannan

Results from sections 2.3 and 2.4 show that konjac jelly is the most suitable gel for use as a skin tissue surrogate in this study. Before any needle insertion experiments began the gel was tested further in order to get a more comprehensive understanding of its behaviour.

2.6.1 Effect of loading rate on mechanical properties

Earlier experiments tested the response of konjac jelly at loading rates of 1 mm/min and 20 mm/min. It was found that increased loading rates led to an increase in stiffness, which is consistent with skin tissue [104, 106, 112-119]. In this section a greater range of loading rates between 1 mm/min and 600 mm/min will be explored which represent loading rate during needle insertion.

The same test setup was used as described in section 2.4.2, where samples were glued to the grips and extended until failure. A needle puncture hole was initiated across all samples so that the developing crack could be observed; all the samples failed across this section. The force and displacement were recorded for all samples and used to calculate engineering stress and strain, the averages of these plots are combined in Figure 2-28.

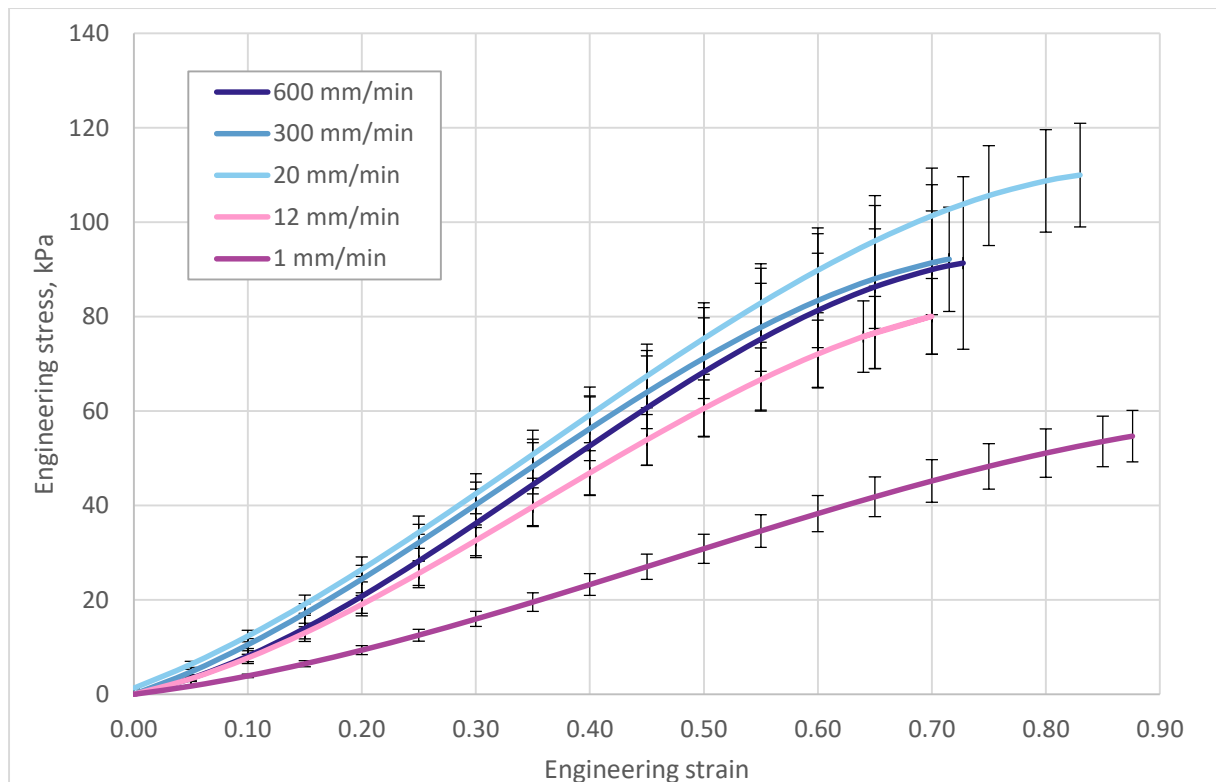


Figure 2-28: Stress strain graph comparing the average tensile responses from konjac gel at varying loading rates.

Figure 2-28 compares the average response of konjac gel in tension at varying loading rates; at least four samples were completed at each loading rate and used to calculate the average. When the standard deviation and errors are considered, the results between loading rates of 20 mm/min and 600 mm/min do fall within the same population. The experiments at 300 mm/min and 600 mm/min were from the same batch and have similar results, but the other experiments were from different batches of gel. The spread of data for all the experiments is presented in the appendix in section 8.1.

A study by Rahedi demonstrated how small modifications to the gel manufacturing process led to variations in mechanical properties for ballistic gelatine [126]. It is probable that the differences in mechanical properties between loading rates of 20 mm/min and 600 mm/min could be from slight, unintentional, variations during the gel manufacturing process. Rahedi noted that variations in the heating temperature had a significant effect on the final results. It is therefore assumed that the difference in mechanical properties between the range of loading rates of 20 mm/min and 600 mm/min may just be batch to batch discrepancies. With this consideration it can be deduced that as the loading rate is increased so does the stiffness response, which can be seen by the slope of the curve.

Table 2-10 contains the calculated values for elastic modulus for konjac jelly in tension at the different loading rates. This was calculated using the slope of the curve between the strain values of 0.2 and 0.25, which mimics the method used in sections 2.3 and 2.4.

Speed, mm/min	Elastic modulus, kPa
1	63.6 ± 3.2
12	131.8 ± 7.6
20	157.0 ± 9.9
300	154.9 ± 17.6
600	153.4 ± 19.7

Table 2-10: Results of elastic modulus for konjac jelly at varying loading rates.

The stiffness increases up to the loading rate of 20 mm/min; after this the results for elastic modulus do not change significantly. In section 1.1.4 the average speed for a biopsy procedure was found to 600 mm/min. However, this speed varies significantly through the procedure. During the needle insertion investigation in chapter 4, the effect of insertion speed will be investigated for the range of speeds explored in the material analysis.

2.6.2 Assessing konjac jelly's birefringence and clarity

In order to use konjac in photoelasticity it needs to be clear, and it must exhibit temporary birefringence. Figure 2-29 shows a photograph of a konjac sample deforming under its own weight (a), and the same sample under load (b).

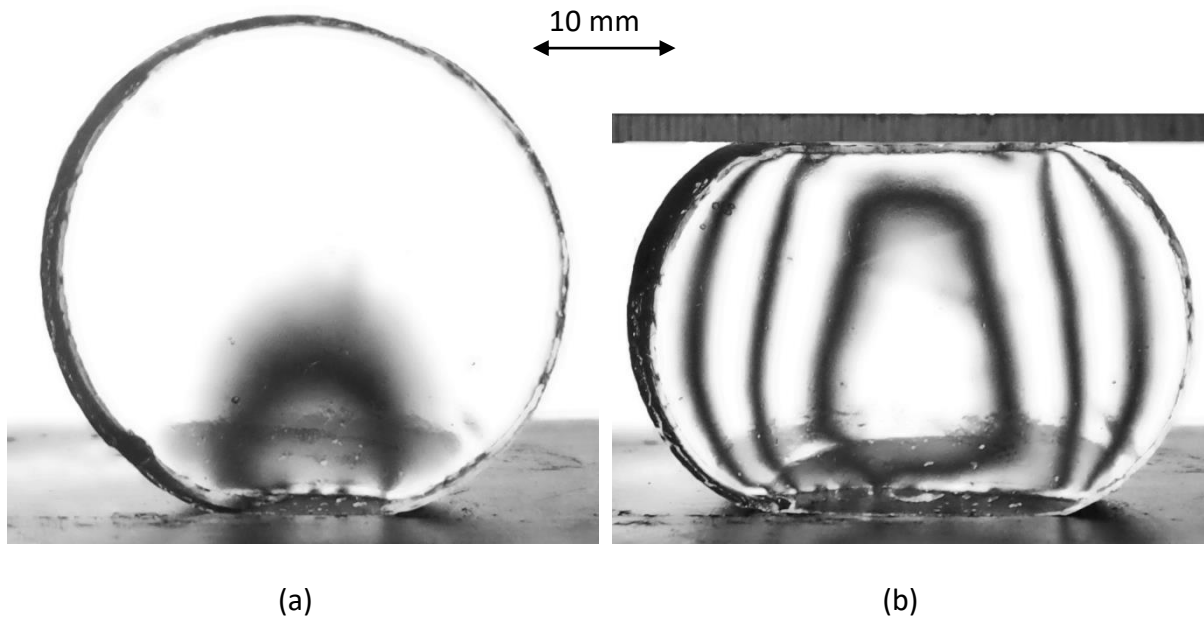


Figure 2-29: Konjac sample (a) unloaded (b) under compressive load

It can be seen that the gel is clear and colourless. The gel also exhibits temporary birefringence, where fringes appear when the gel is under load. In chapter 3 the strain optic coefficient will be determined; this constant relates the optical behaviour to the strain experienced by the material.

2.6.3 Conclusion

At the start of this section three criteria were presented which the developed gel would have to satisfy in order to be used as a skin tissue surrogate for needle insertion experiments.

Stiffness: A stiffness ranging between 81.8 kPa – 226.2 kPa was required to reflect the elastic modulus of skin tissue *in vivo*. Compression experiments were conducted to determine an appropriate concentration of konjac powder to water; it was found that a concentration of 1.5% konjac powder was suitable. Further mechanical assessments showed that konjac jelly exhibits time dependant and loading rate dependant behaviour, similar behaviour was also found for skin tissue [104, 106, 112-119]. Konjac jelly also produced a range of elastic modulus at varying loading rates which matched the desired range.

Tear Resistance: It was discussed that the gel should exhibit tear resistance. Tensile samples of the three gels were created with a needle puncture hole in the centre. This allowed for the resistance to crack growth to be assessed. It was found that only konjac exhibited a tear resistance; producing a range of failure strains between 0.66 – 0.98, comparable to the failure strains of 0.27 – 1.13 found for human skin tissue *ex vivo* [50, 52-54].

Optical Properties: In order to use the gel for photoelastic analysis it must be clear, and it must exhibit temporary birefringence. It was found that with careful preparation konjac jelly produces a clear gel, and a brief analysis shows that it exhibits temporary birefringence. Further optical analysis is required to determine the materials strain optic coefficient, which will be presented in chapter 3.

3 OPTICAL CHARACTERISATION

In chapter 2 the mechanical properties of the gels were assessed and compared to the published mechanical properties of skin tissue. It was found that konjac jelly exhibited similar mechanical behaviour to skin tissue and it was the only gel which exhibited a resistance to crack growth. Therefore, all further work involves the use of konjac jelly as the skin tissue surrogate.

In order to use the gel in photoelastic analysis the strain optic coefficient of the gel needs to be determined; an optic coefficient is a material property which is used to link the optical behaviour to the stress or strain experienced by the material. Zhao and Huang found that the optic coefficient for their soft birefringent material was strain rate and temperature sensitive under dynamic conditions [111]. More recently, Atenaga and Tomlinson found that the optic coefficient for konjac may be dependent on loading rate [127]. In their assessment the konjac samples were elongated at loading rates of 20 mm/min and 40 mm/min, and the percentage difference between the two optic coefficients was 27%. However, Atenaga went on to discuss that the different results could be from temperature discrepancies. Furthermore, when errors are accounted for the optic coefficients do fall into the same population for both loading rates.

The temperature dependencies of konjac gel were discussed within chapter 2, and it was resolved by ensuring all gel samples are stored in a temperature controlled fridge prior to testing. However, the possibility of konjac gel exhibiting a loading-rate-dependant optic coefficient needs to be investigated. Therefore a range of loading rates will be used to determine an optic coefficient and the results will be compared to assess whether any differences are significant.

In this chapter the calculations behind the strain optic coefficient are described, and the experimental setup used to gather the optical data is presented. The strain optic coefficient was calculated at loading rates of 20 mm/min, 300 mm/min, and 600 mm/min to assess whether it depended on loading rate.

3.1 Strain optic coefficient theory

In chapter 2 it was shown that konjac jelly exhibited stress-relaxation and non-linear behaviour. Therefore, the strain optic coefficient was calculated, instead of the more commonly presented stress optic coefficient.

In the GFP 2500 operator manual the signal returned by the camera is described by [128]:

$$S \propto K_{\varepsilon S} h (\varepsilon_1 - \varepsilon_2) \quad \text{Equation 3.1}$$

where S is the signal in camera units which corresponds to the retardation δ , $K_{\varepsilon S}$ is the strain optic coefficient specific to the software, h is the thickness of the specimen, and ε_1 and ε_2 are the principal strains.

The strain optic law in Equation 3.2 can be used to find the strain optic coefficient:

$$(\varepsilon_1 - \varepsilon_2) = \frac{N\lambda}{hK_{\varepsilon}} \quad \text{Equation 3.2}$$

where N is the fringe order, λ is the wavelength of light used, and K_{ε} is the strain optic coefficient. Usually when working in photoelasticity the output variable is fringe order, whereas the poleidoscope software returns the output as retardation, δ . This can be later converted to fringe order using the following equation.

$$N = \frac{\delta}{2\pi} \quad \text{Equation 3.3}$$

Combining and rearranging Equation 3.3 and Equation 3.2 the following equation is produced and can be used to find the optic coefficient.

$$K_{\varepsilon} = \frac{\lambda \delta}{(\varepsilon_1 - \varepsilon_2) 2\pi h} \quad \text{Equation 3.4}$$

However, in the software manual the equation for the optic coefficient is given as Equation 3.5, which is different to Equation 3.4.

$$K_{\varepsilon S} = \frac{\delta}{(\varepsilon_1 - \varepsilon_2) h} \quad \text{Equation 3.5}$$

This difference between Equation 3.4 and Equation 3.5 is because the calculations in the software automatically include the 2π and wavelength values, and the user manually enters the thickness of the specimen for each experiment. The optic coefficient $K_{\varepsilon S}$ which is used in the software can be related to K_{ε} using the following equation:

$$K_{\varepsilon S} = \frac{K_{\varepsilon} 2\pi}{\lambda} \quad \text{Equation 3.6}$$

K_{ε} should not be confused with the more commonly referenced optic coefficient f_{ε} which is specific to a certain wavelength of light. The two can be related through the following equation:

$$f_{\varepsilon} = \frac{\lambda}{K_{\varepsilon}} \quad \text{Equation 3.7}$$

3.2 Experimental setup

A GFP 2500 poleidoscope, as described in the literature review in section 1.3.7, was used for the tests described in this section. It allowed for continuous capture of full field retardation data from the developed birefringent material.

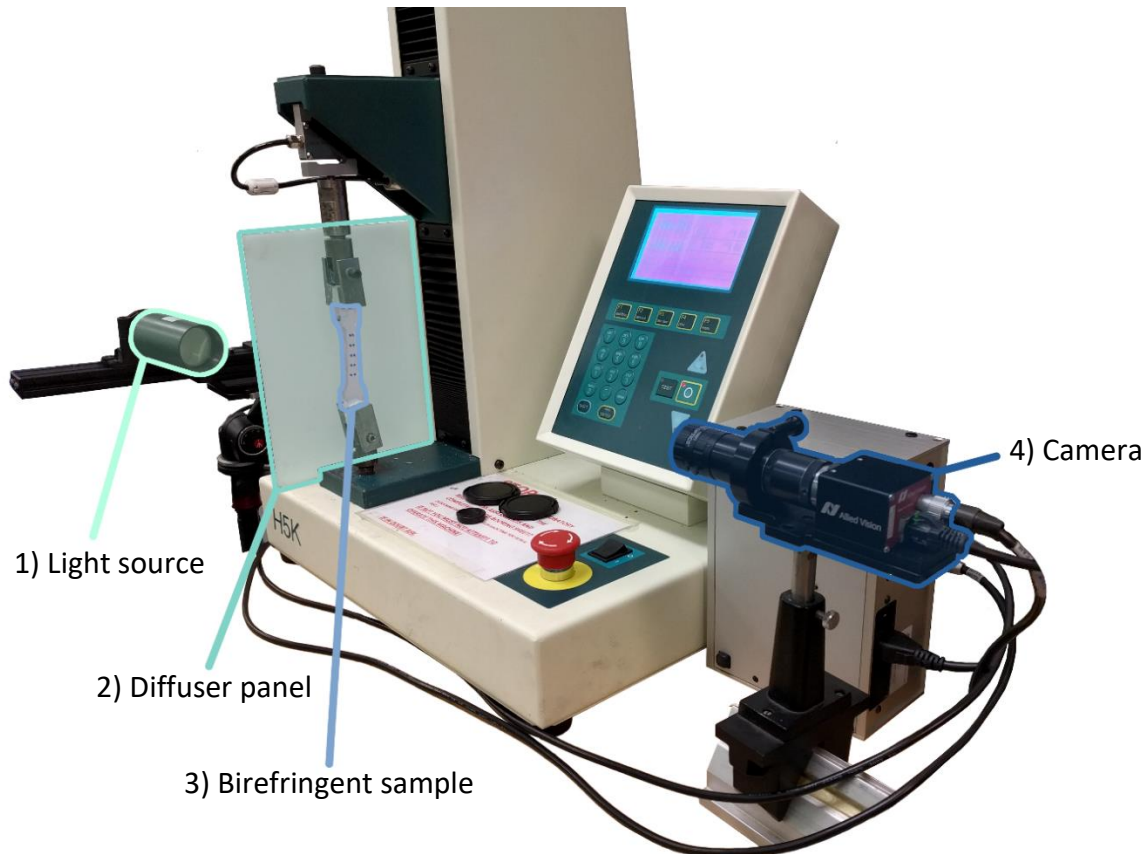


Figure 3-1: Photograph of setup for strain optic coefficient analysis.

The experimental setup for assessing the materials strain optic coefficient is shown in Figure 3-1. The components of interest are highlighted and labelled as follows:

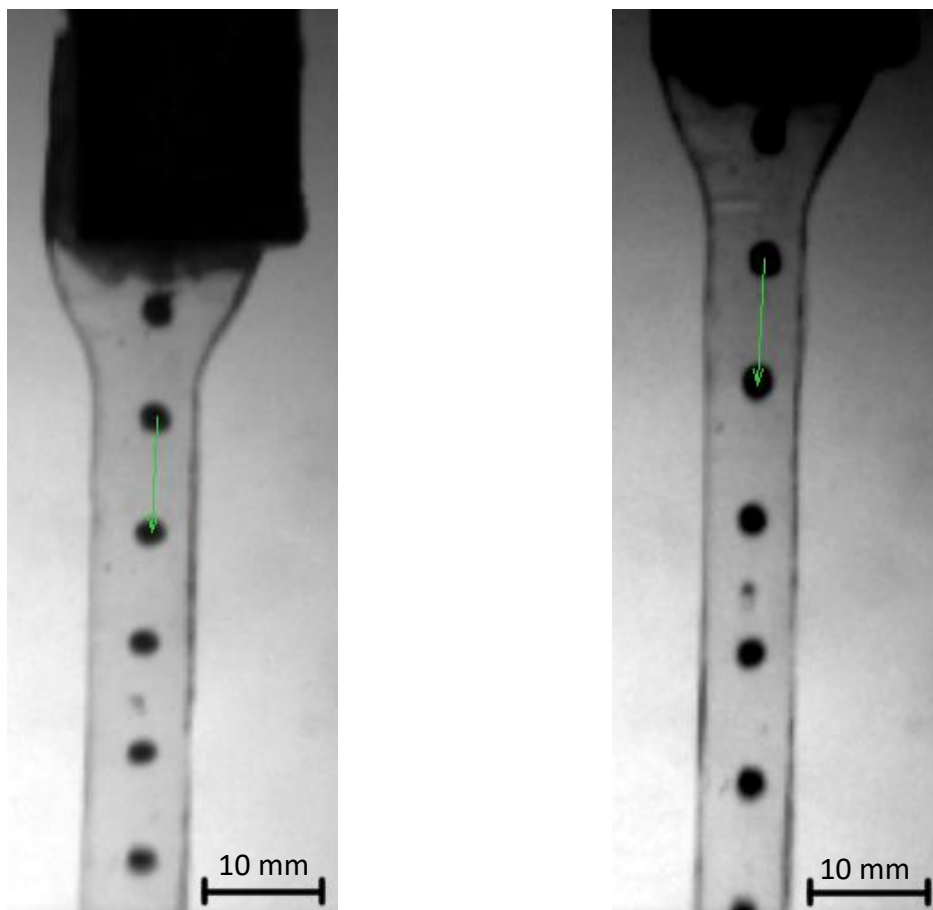
- 1) Light source, which emitted linearly polarised light.
- 2) Diffuser panel; a plastic sheet which ensured the light was evenly distributed.
- 3) Birefringent sample; a konjac dog-bone sample loaded in the test machine. The gel's concentration was 1.5% powder to water; as developed in chapter 2.
- 4) GFP2500 poleidoscope camera; the camera which captured the intensity of light exiting the specimen, and split the image into four sections at the four polarisation angles. Further descriptions on the mechanisms used in the GFP2500 poleidoscope are presented in section 1.3.7.

3.2.1 Tensile optical experiments

Uniaxial tensile tests were performed in the same way as described in section 2.4. Tensile samples were elongated until they failed at loading rates of 20, 300, and 600 mm/min, and intensity maps were recorded using the GFP2500 poleidoscope kit shown in Figure 3-1.

With reference to Equation 3.5 the values required to calculate the software optic coefficient are both principal strains, specimen thickness, and retardation due to strain:

Principal strains: Within the Deltavision analysis software there is an option to view the recorded light intensity, described in the manual as the transmission of light averaged over all polarization orientations [128]. In this view the change in distance between the opaque ink dots was evident, as shown in Figure 3-2. The local longitudinal and lateral strains were calculated at chosen intervals by measuring the change in distance between the opaque ink dots and the change in width during extension.

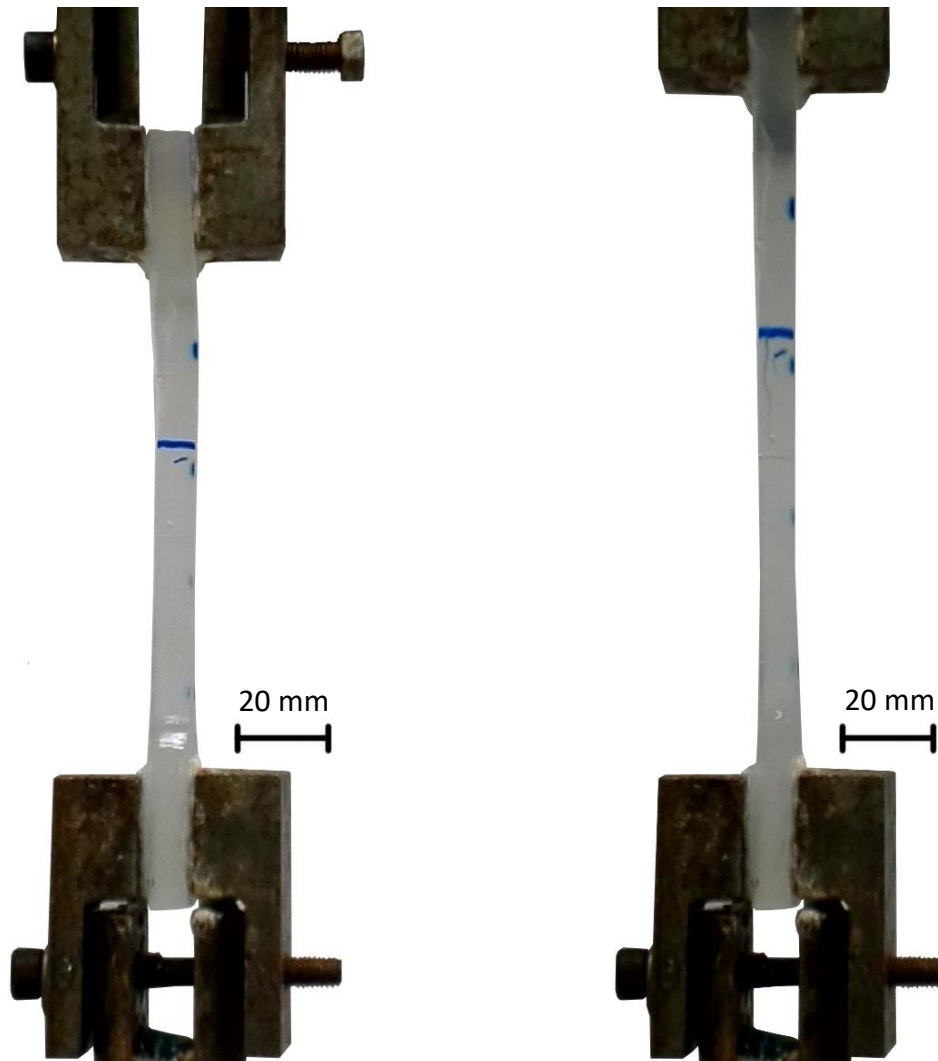


a) Tensile sample at 0 mm extension

a) Tensile sample at 15 mm extension

Figure 3-2: Figures showing the length measurement in light intensity view of a tensile sample during extension.

Thickness: As the samples were elongated their thickness reduced. The change in thickness was tracked using an additional camera directed at the out of plane sample surface. The sample thickness was measured prior to loading, and a ruler was visible behind the sample in the test machine in order to track the change in width. Figure 3-3 shows frames of the recorded video where the sample was at 0 mm extension, and 30 mm extension.



a) Tensile sample at 0 mm extension

a) Tensile sample at 30 mm extension

Figure 3-3 Photographs showing the change in width of a tensile sample during extension

Retardation: The poleidoscope camera captured four different intensity images and converted them into retardation. These data was then processed within the GFP2500c software to produce a continuous retardation map [90].

Within the poleidoscope analysis software there is an option to subtract one retardation map from another. Therefore, the retardation map of the sample at zero extension was subtracted from all succeeding images to return a retardation amount solely due to the applied extension, and not from residual strain or stress from loading the sample; demonstrated in Figure 3-4:

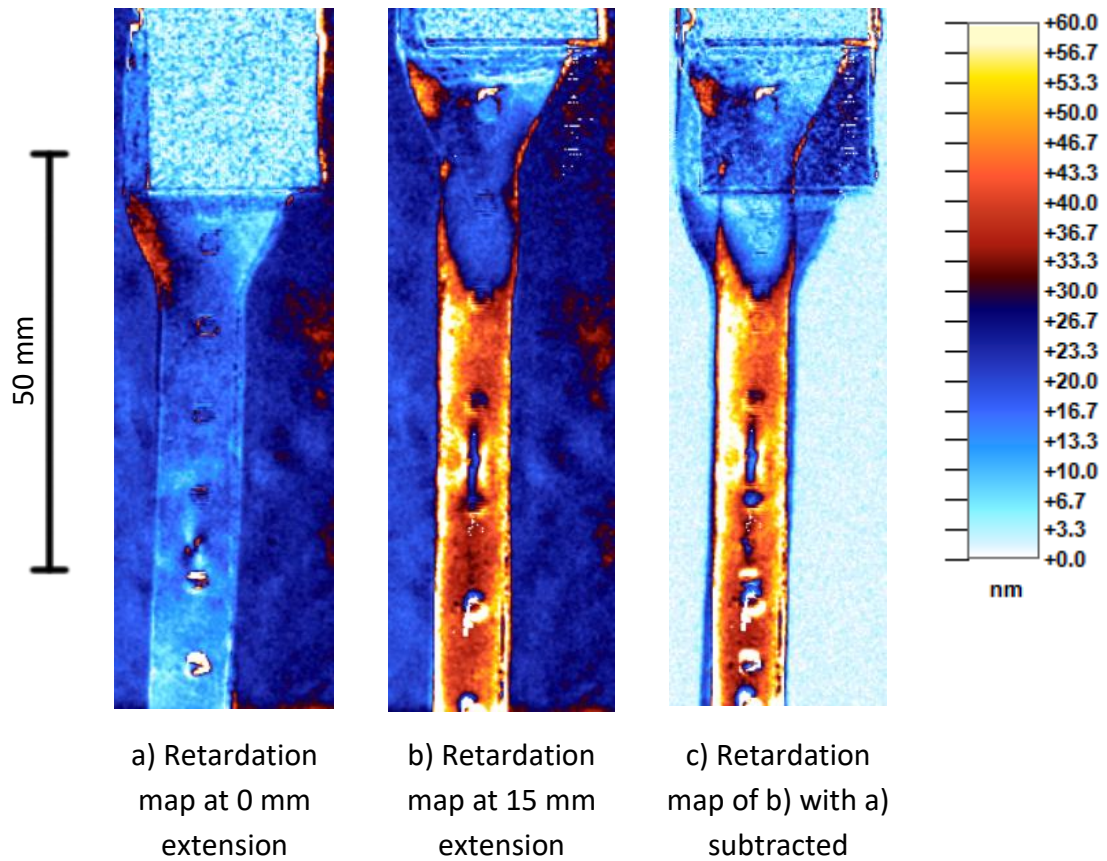


Figure 3-4: Figures displaying the effect of subtracting one retardation map from another retardation map.

The retardation magnitude was obtained using data from the “shear 45” images, rather than the “shear max” images. The retardation in the “shear 45” images correspond to the direct strain changes in the x and y directions and exclude any retardation from strain changes at 45° to the horizontal. This was done as only the change in strain in the x and y directions was measured using the ink dots on the sample.

The poleidoscope was used to record the development of retardation due to extension from zero deflection until the samples fractured. The video data was then processed to get continuous retardation data, and frames were saved at 3 mm intervals between extensions of 0 mm and 24 mm. The images showed a map of the retardation due to extension, and a selection of images showing the progression of the retardation is shown in Figure 3-5.

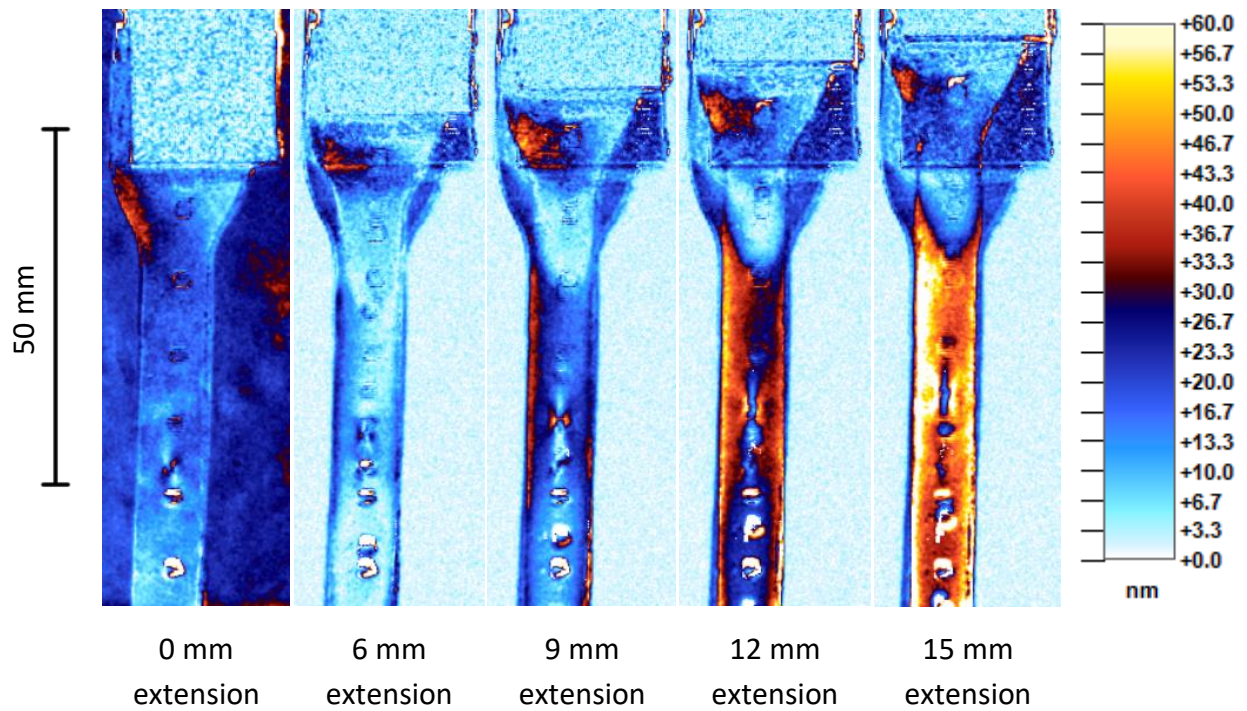


Figure 3-5 Processed results showing the development of retardation during extension

The optic coefficient was calculated at all the intervals to ensure that it remained consistent at increasing strains. The optic coefficient was also calculated for specimens extended at three loading rates to assess whether it changed for different loading rates, a phenomenon which both Zhao and Huang, and Atenaga and Tomlinson experienced with their materials [111, 127]. Six samples were tested at 20 mm/min, and four samples for each loading rate of 300 mm/min and 600 mm/min. Full numerical results and calculations of the strain optic coefficient are presented in the appendix, and a summary of the results are presented in Table 3-1.

Figure 3-6, Figure 3-7, and Figure 3-8 display the results for the software strain optic coefficient, K_{ϵ_S} , at increasing strains for each sample at the various loading rates. The erratic nature of the curves shows that each calculation is subject to large errors. There were some difficulties with processing the results which likely caused the errors; these will be discussed in section 3.3.

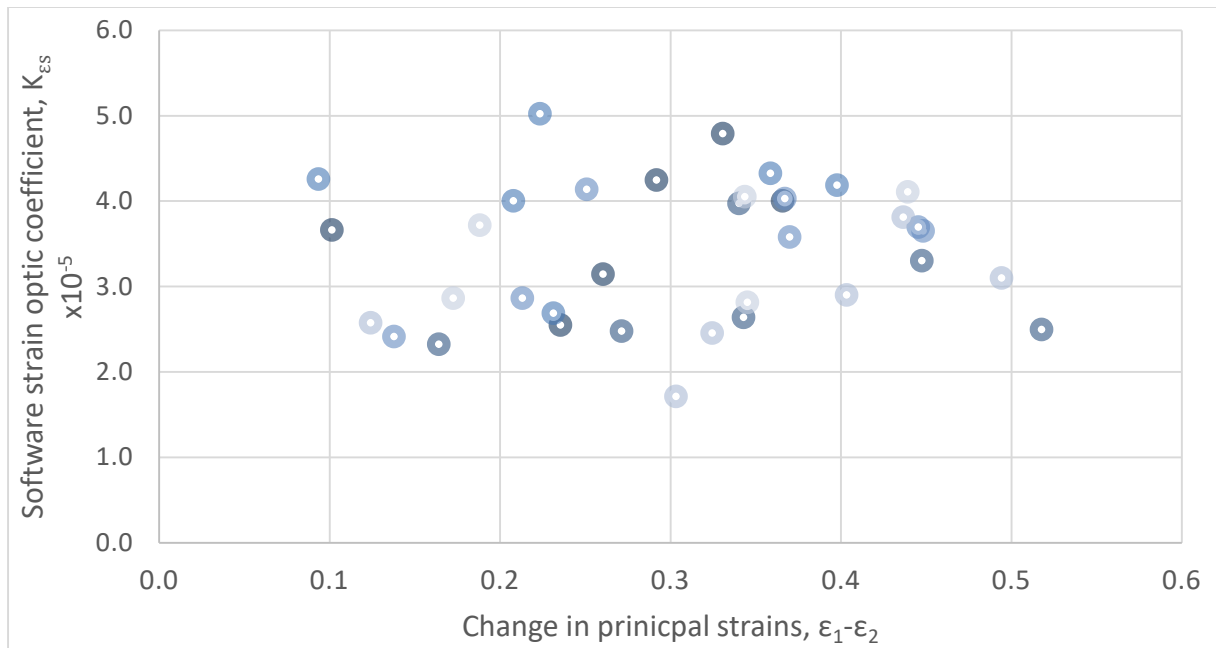


Figure 3-6: Strain optic coefficient through increasing strains at a loading rate of 20 mm/min

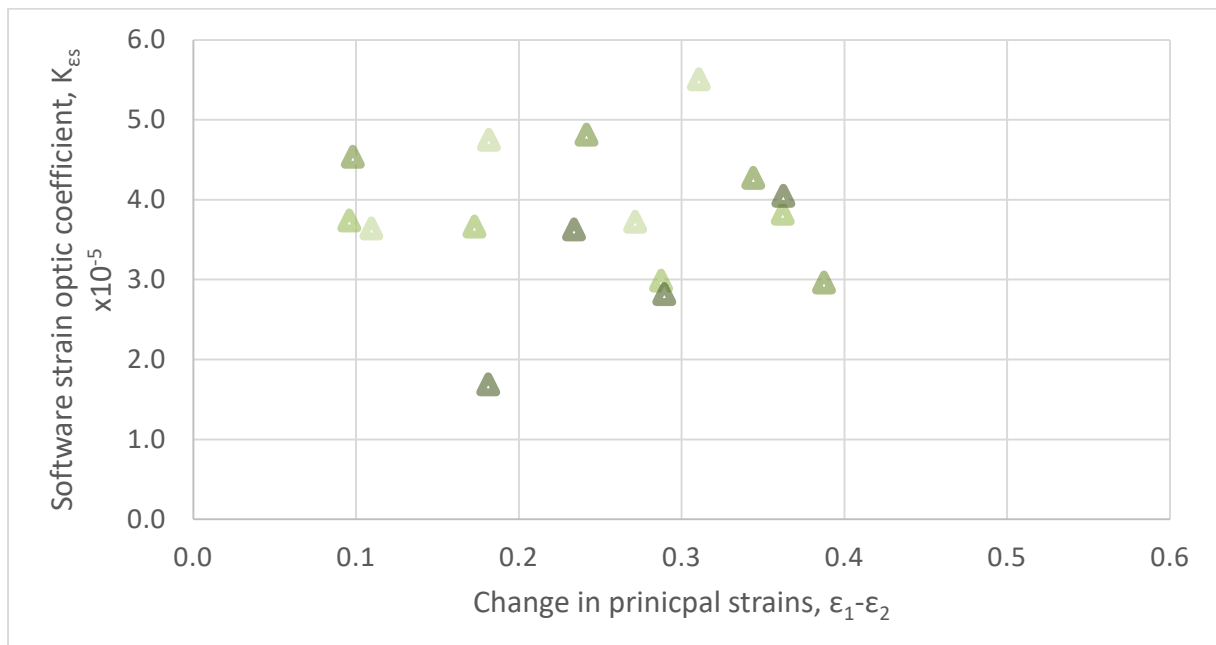


Figure 3-7: Strain optic coefficient through increasing strains at a loading rate of 300 mm/min

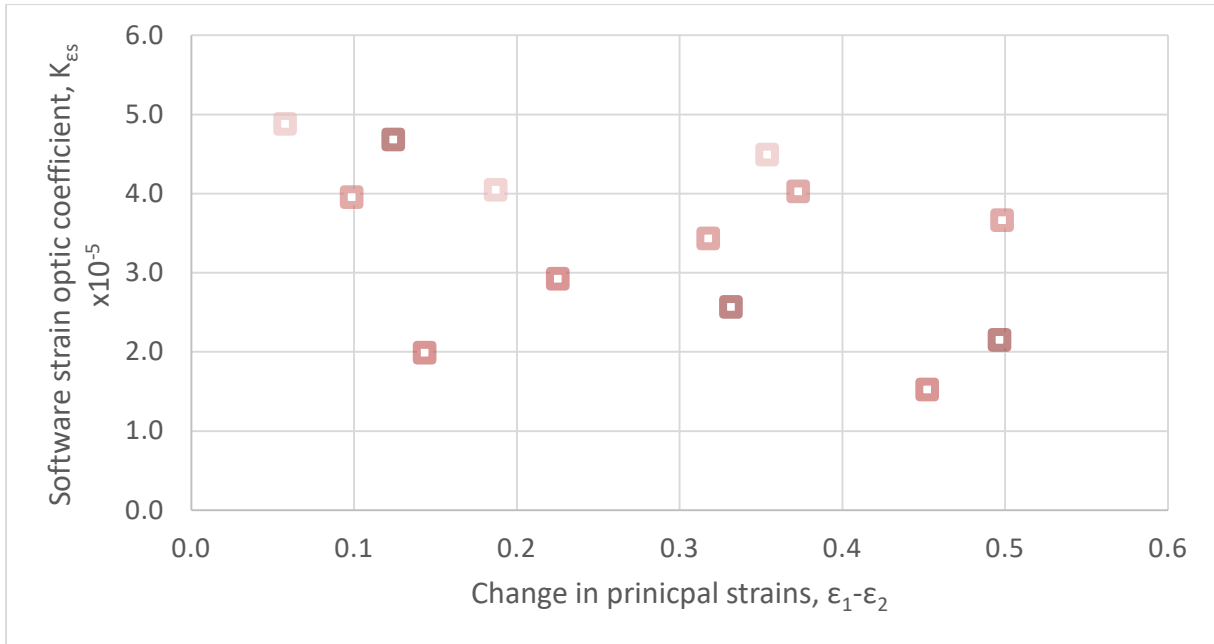


Figure 3-8: Strain optic coefficient through increasing strains at a loading rate of 600 mm/min

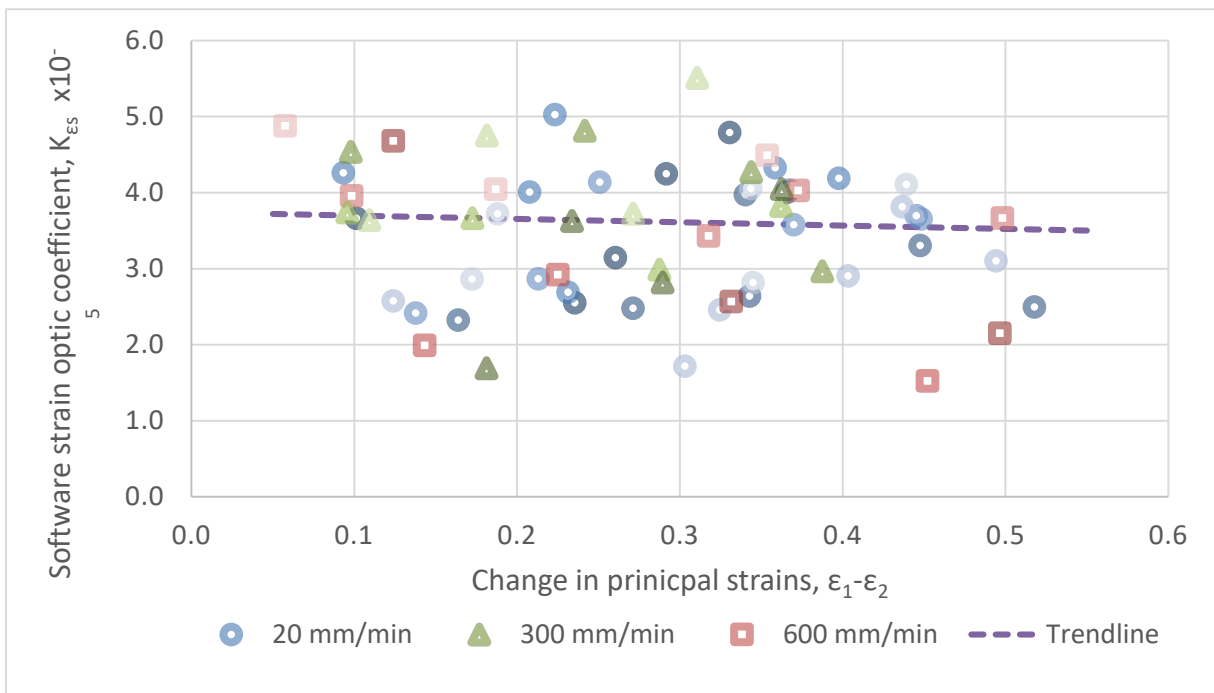


Figure 3-9: Strain optic coefficient through increasing strains at various loading rates

Combining all the results for the software optic coefficient in Figure 3-9 shows that all the results do stick to a general trend, however there is large scatter. One reason for the scatter was due to the variability with the principal strains; the magnitude of change in ϵ_1 was not always the same as the magnitude of change in ϵ_2 . This meant that the result for optic

coefficient would appear to increase while the change in principal strains remained constant, which is prevalent in Figure 3-6. This only occurred for a limited number of samples, and it appeared to be due to the samples ‘settling’ into the grips.

Loading rate, mm/min	Software strain optic coefficient, $K_{\epsilon S}$
20	$3.31 \times 10^{-5} \pm 0.22 \times 10^{-5}$
300	$3.78 \times 10^{-5} \pm 0.31 \times 10^{-5}$
600	$3.38 \times 10^{-5} \pm 0.49 \times 10^{-5}$

Table 3-1: Results for strain optic coefficient specific to the software at various loading rates

Table 3-1 contains the averaged results for the optic coefficient specific to the software at the three loading rates. In order to assess whether the difference in the results were statistically significant an “Anova: Single Factor” statistical analysis test was conducted. The variation of results between the three groups is statistically insignificant if a P-value is greater than 0.05. When comparing the three groups a P-value of 0.57 was obtained, so it has been concluded that the optic coefficient is independent from loading rate

Using all the optical data at the three loading rates returns an average software strain optic coefficient of $K_{\epsilon S} = 3.47 \times 10^{-5} \pm 0.18 \times 10^{-5}$ for konjac jelly at 1.5% concentration gel powder to water. Applying this data into Equation 3.6 returns an optic coefficient of $K_{\epsilon} = 3.03 \times 10^{-9} \pm 0.16 \times 10^{-9}$ for konjac jell at 1.5% concentration gel powder to water for a wavelength of 550 nm.

3.3 Processing limitations

In Figure 3-6, Figure 3-7, and Figure 3-8 the inconsistency of the results for optic coefficient was observed within each test. These inconsistencies could be due to a variety of factors which will be discussed in this sub-section.

3.3.1 Motion

Normally, as the sample approached an extension of 50 mm the recorded images showed processing errors. An example of these processing errors is shown in Figure 3-10 as the white patches, which returned an implausible retardation value over 200 nm. As a result of this, the optic coefficient was calculated using results at lower extensions. During the training sessions with this kit it was said that the software experiences processing difficulties if the sample moves greatly during the test [129]. At the extension in Figure 3-10 the sample has moved significantly from the starting point, and the software has had clear difficulty in processing.

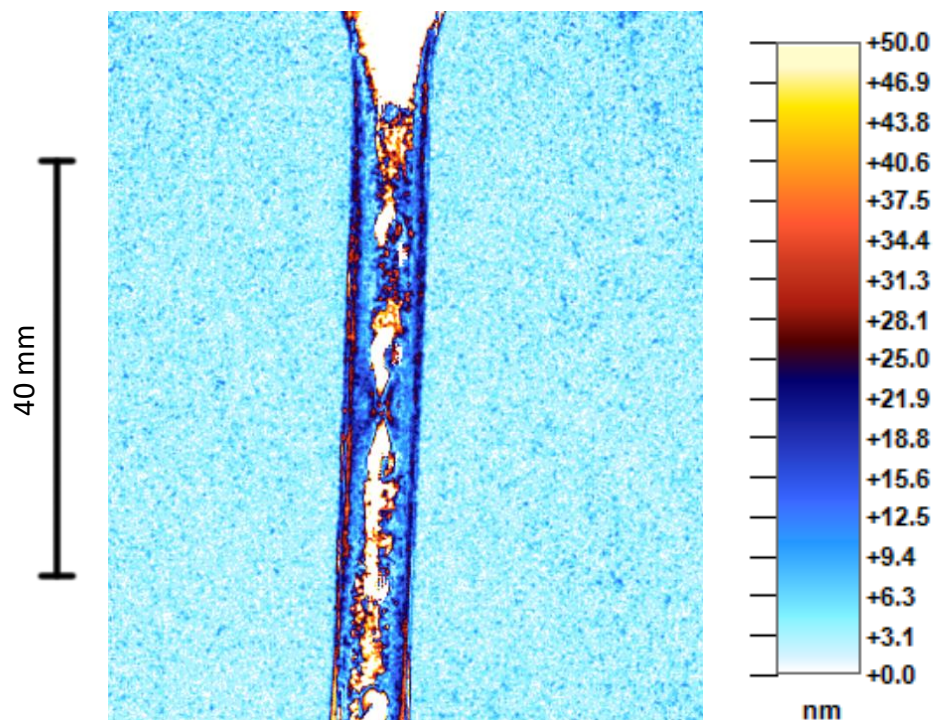


Figure 3-10 Example of processed image deteriorating at 50 mm extension

The software also had some difficulty processing data around the opaque ink dots, and this became worse at higher extensions. As the extension increased the whole mid-section of the sample returned fluctuating retardation amounts between 0 nm or over 300 nm.

3.3.2 Heat errors

Within the processing software there is an option to subtract the retardation map of one image from another. In Figure 3-10 the background retardation was subtracted to produce an image without background noise. Figure 3-11 is an example of the 'background image' where the poleidoscope camera is returning retardation data from the diffuser panel, which is not under any residual or applied stress.

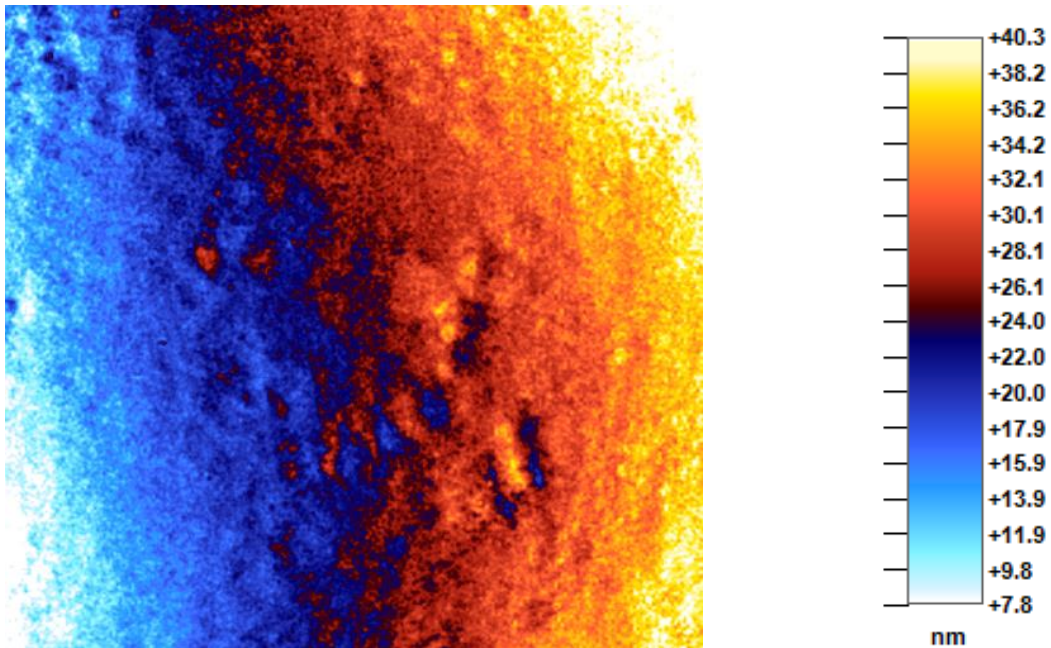


Figure 3-11 Processed background image

When the camera was recording data it would gradually increase in temperature. This temperature increase was worse during tests in the summer months when the temperature in the lab exceeded 28°C. It was noted that this background retardation data became more extreme as the camera temperature increased. A correlation of data errors was noted on days where the temperature of the lab was significantly higher than usual and errors occurring partway through the recorded data. The data file could be loaded but the software crashed when frames at the later section of the video were selected. This also caused problems with processing, as the software could not load the frames to process them. It was evident that the camera sensor was temperature sensitive.

In subsequent experiments a cooling block was placed on the camera prior to each test to prevent it from heating up and causing errors. However, longer tests were still producing errors; all the experiments at 1 mm/min were unfortunately unusable.

3.3.3 Uneven retardation maps

Cylindrical samples of diameter 50 mm and thickness 20 mm, as presented in section 2.3, were also created in an attempt to assess the optic coefficient through compression. However, when the data was processed using the processing tool it was observed that it did not result in a continuous retardation map. Comparisons between the unprocessed and processed data are shown in Figure 3-12.

The poleidoscope software does not work for fringes over 2.5, and using the fringe counting method described in the literature review in section 1.3.7, the maximum fringe order in the data map in Figure 3-12 is slightly over 1.75.

With comparison of the retardation maps and graphs in Figure 3-12 it appears that the data has not been processed at all. Furthermore, with reference to the retardation results for the tensile samples the retardation does not exceed 100 nm before errors were encountered. Shortly after 100 nm is reached it is expected that the gradient of the retardation map would change signs, signalling the fringe order reaching 0.25. It is postulated that none of the data has actually been processed, and this was only observed in the compression samples as they were thicker and therefore produced fringe orders greater than 0.25.

Examples of unprocessed retardation graphs were presented in the literature review in section 1.3.7 in Figure 1-17. This example retardation result is smooth and continuous, whereas the graphs in the compression samples show an uneven result. It is assumed that the processing tool within the software is incorrectly identifying the uneven retardation result as the gradient changing sign. It is assumed that this would lead to processing errors and it is incorrectly identifying fringe orders much greater than 2.5. This issue was discussed with StressPhotonics; however, no solution has been achieved at this time.

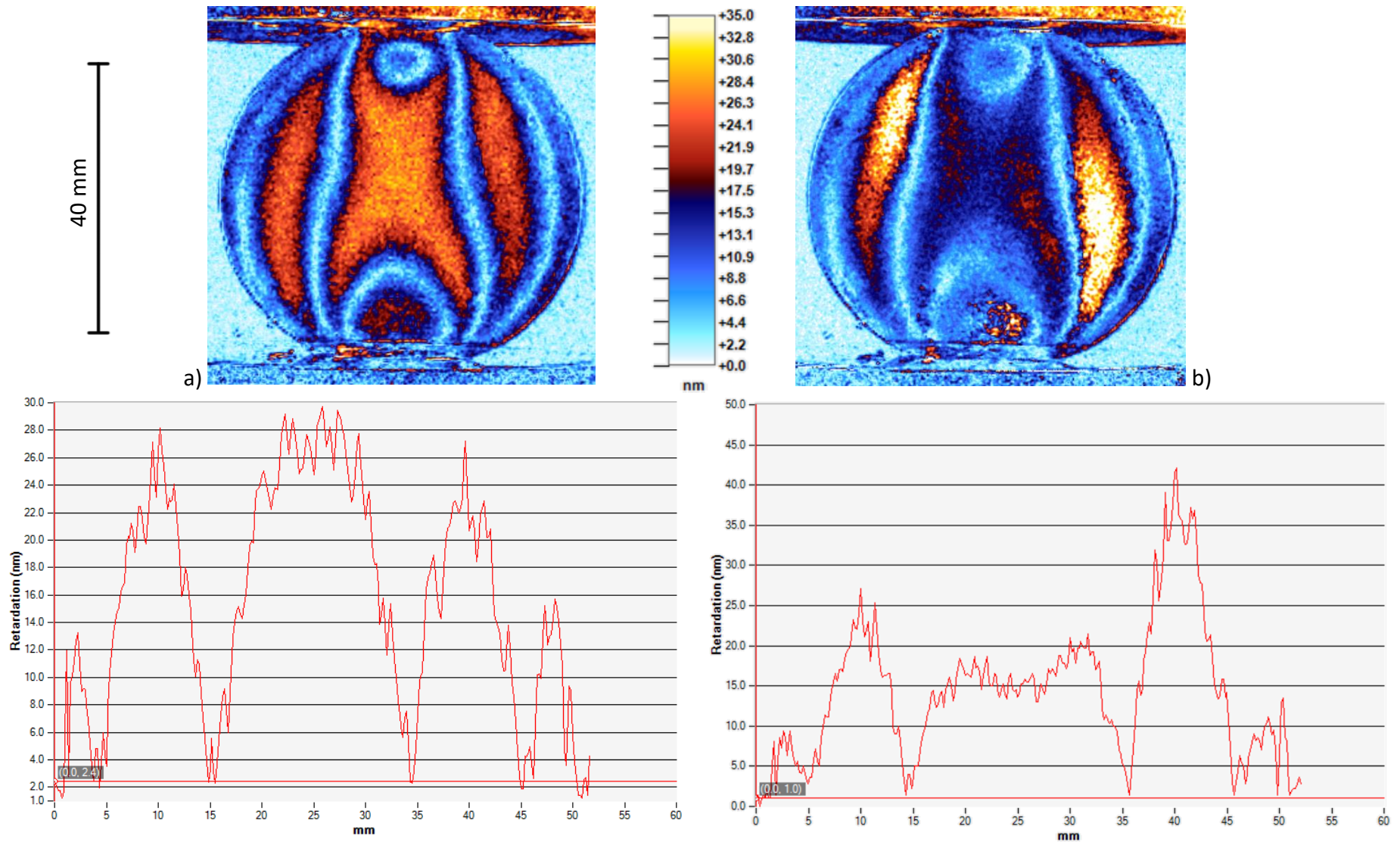


Figure 3-12: Comparisons of unprocessed (a) and processed retardation data (b) for a disk in compression.

3.4 Strain optic coefficient validation

The optic coefficient was applied to random tensile samples to assess how the calculated strain from the strain optic coefficient compared to the measured strain. This was done to verify the accuracy of the coefficient when considering the inconsistencies discussed in section 3.3. Random tensile samples were selected for the range of loading rates, and images at random extensions were saved. The optic coefficient of $K_{\epsilon_s} = 3.47 \times 10^{-5}$ was applied, along with the thickness of the specimen at that extension. Figure 3-13 shows an example of the input panel within the “Deltavision v2” software including optic coefficient and thickness parameters [91].

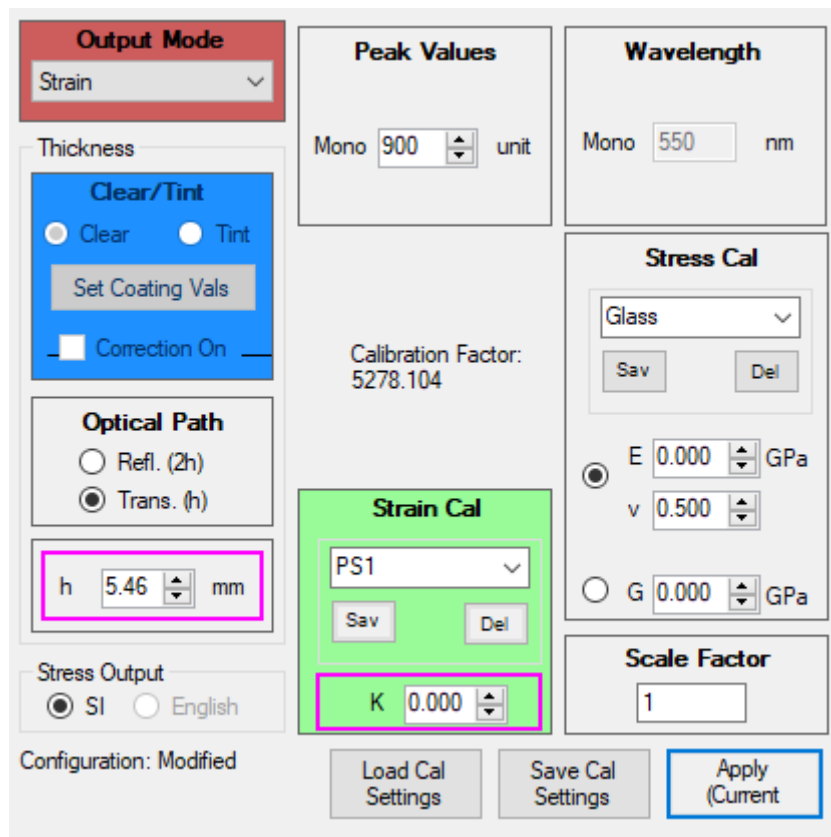


Figure 3-13: Screenshot showing calibration panel with required input values highlighted

The software is originally designed for stiff materials like glass, which have a higher elastic modulus and optic coefficient. Therefore, all the units are presented at awkward magnitudes for this material, such as stiffness in gigapascal and strain in micro-strain. Some values also appear to be zero in Figure 3-13; in actuality their values are simply too small to be presented in the default calibration units.

The local strain was calculated using the change in distance between the ink dots, and the change in width. Recording the change in distance between two dots, and the change in width between the two elongations returned a difference in principal strain of 0.4 for the example sample in Figure 3-14.

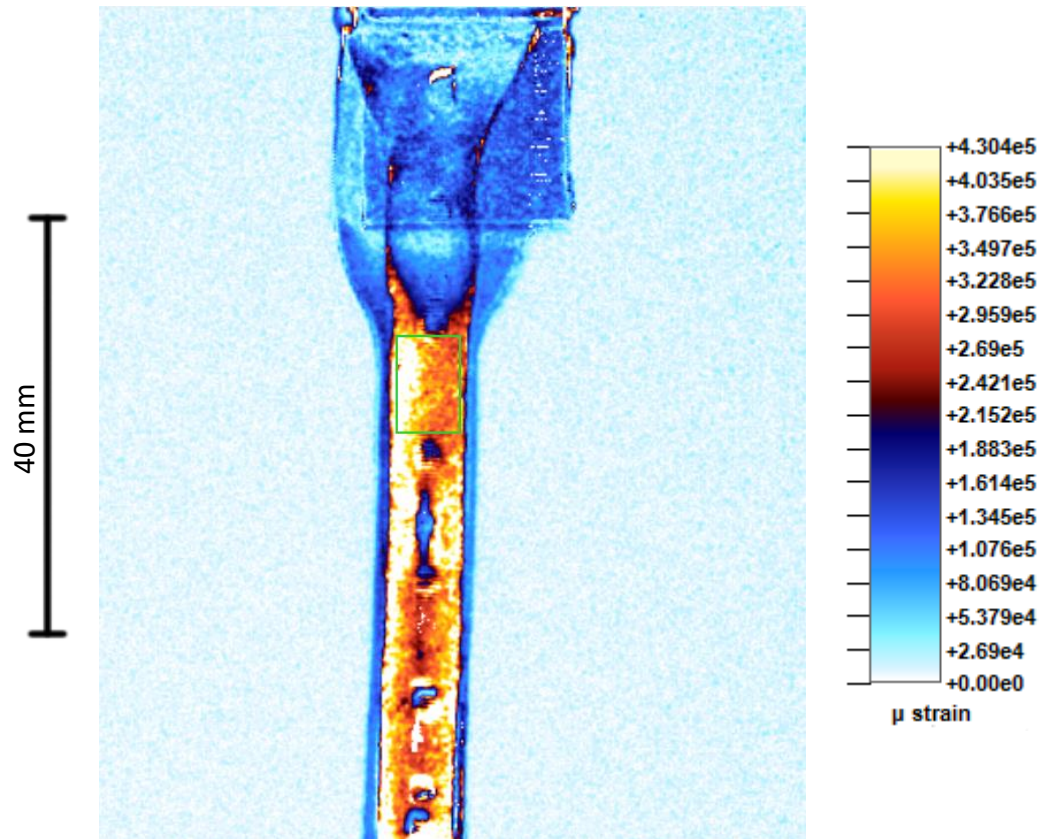


Figure 3-14: Processed strain of a random sample at 7 mm elongation with 0 mm elongation subtracted

Figure 3-14 shows the strain map due to extension along the tensile sample. The retardation image at zero elongation has been subtracted from this image, thereby returning the retardation due to extension only.

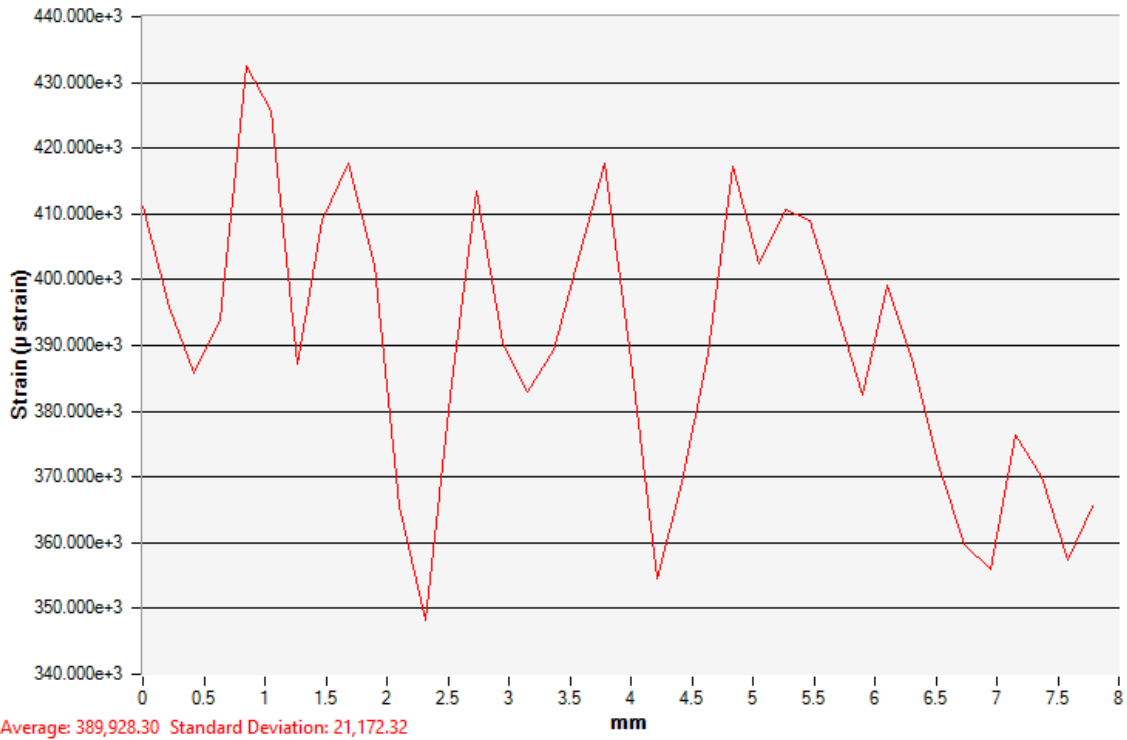


Figure 3-15: Strain along the dotted segment used to calculate observed strain

Figure 3-15 shows the software-calculated strain from the optic coefficient at a section between two dots, highlighted in Figure 3-14. The average strain between the dots was calculated to be 389,928.30 micro strain, which corresponds to 0.39 strain. The strain value obtained from measuring the change between the dots returned a value of 0.4 strain. This was repeated for a number of tensile samples at the various loading rates, and a comparison of all the results is presented in Table 3-2.

Measured $\epsilon_1 - \epsilon_2$	Software $\epsilon_1 - \epsilon_2$
0.40	0.39
0.10	0.11
0.16	0.13
0.36	0.40
0.25	0.24
0.30	0.26
0.17	0.13
0.21	0.19

Table 3-2: Comparison between measured principal strain, and calculated principal strain

This result shows that the optic coefficient is valid as the results for the software strain calculation and physical strain calculation have an average percentage difference of 12.2%.

3.5 Conclusion

The strain optic coefficient of konjac gel at 1.5% concentration of gel powder to water was calculated using tensile experiments. The change in principal strains was measured using marker dots on the samples, and the retardation due to extension was recorded using the GFP2500 poleidoscope. The coefficient was calculated for three different loading rates, at 20 mm/min, 300 mm/min, and 600 mm/min. It was found that the optic coefficient does not depend on loading rate. Using all the optical data at the three loading rates returned an average software strain optic coefficient of $K_{\varepsilon S} = 3.47 \times 10^{-5} \pm 0.18 \times 10^{-5}$

The software optic coefficient was applied to random tensile samples to compare the software calculated strain to the measured strain using the marker dots. The results were similar between the two and it was concluded that the optic coefficient is valid.

4 NEEDLE INSERTION EXPERIMENTS

During the literature review three possible variables were discussed which could affect the strain profile in the region of a needle insertion, and the needle trajectory through skin tissue. These are as follows:

- Various speeds; It was found that soft tissue surrogates generally produced higher reaction forces at higher insertion speeds [26-30], yet the opposite was found for the soft tissues tested *ex vivo* [8, 31-35]. This difference was hypothesised to originate from the different crack profiles, or the tribological differences between tissue surrogates and real tissue.
- Various needle shapes; changes in the needle tip shape, tip angle, and needle gauge have all been shown to affect the force response, and overall deflection of the needle [4, 11, 14, 15, 95, 107, 130].
- Homogenous or inhomogeneous tissue; previous studies have mainly involved homogenous tissue as it is easier to produce consistent imitations [4, 130]. However, the inhomogeneity of skin tissue may increase the resultant deflection of the needle [131]. Therefore, simple inhomogeneous surrogates will be created to assess if there is any difference between both types of surrogates.

Within this section the skin tissue surrogate will be subjected to various needle insertions to assess the impact of changing the aforementioned variables has on the needle's trajectory, and how they affect the stress and strain profile in the region of a needle insertion.

Previously, in section 2.6.1, it was found that the difference in material properties of konjac jelly between loading rates of 20 mm/min and 600 mm/min were minimal. As a result of this finding, needle insertion can be tested within this range of speeds without assuming that the material properties of the gel are changing due to the different insertion rates.

In the preceding chapter 3 it was found that the optical coefficient did not vary with increased loading rate. Therefore, the optical coefficient will remain constant for all of the tests involving varying speeds.

4.1 Experimental Setup

4.1.1 Tanks

Previous work at The University of Sheffield used a large glass tank to house the surrogate [4]. The tank was constructed using two sheets of stress free glass which the sample was viewed through, and the sides and base was made using clear Perspex. The tank was water-tight and could be filled with molten gel which solidified in the tank. As the tank was large a number of needle punctures could be carried out on the surrogate block. However, it was difficult to keep the gel a consistent temperature between tests as it had to be refrigerated between each test. Concerns were also raised on the distance between each puncture and whether previous insertions would affect results on subsequent insertions nearby.

Therefore, five smaller tanks were created for the following experiments. The tanks were made out of 5 mm thick panes of stress free glass for the viewing panes and clear Perspex for the sides and base. The gap between the stress free panes was 12 mm, the same as the large tank. The tanks were designed to be large enough to house one needle insertion test without experiencing any effects from the glass boundaries.

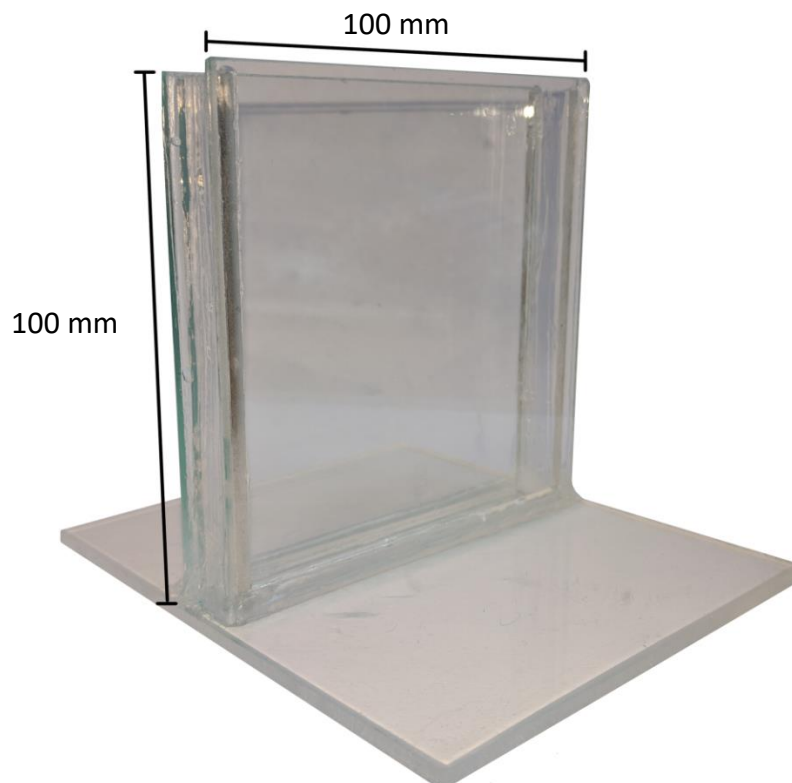


Figure 4-1: New tanks for housing the gel surrogate for needle insertion testing

4.1.2 Needle Setup

Figure 4-2 below shows how a biopsy needle was secured in the test rig for the needle insertion testing. The needle was secured in a vertical position in standard tensile clamping grips which prevented the needle from moving during the test.

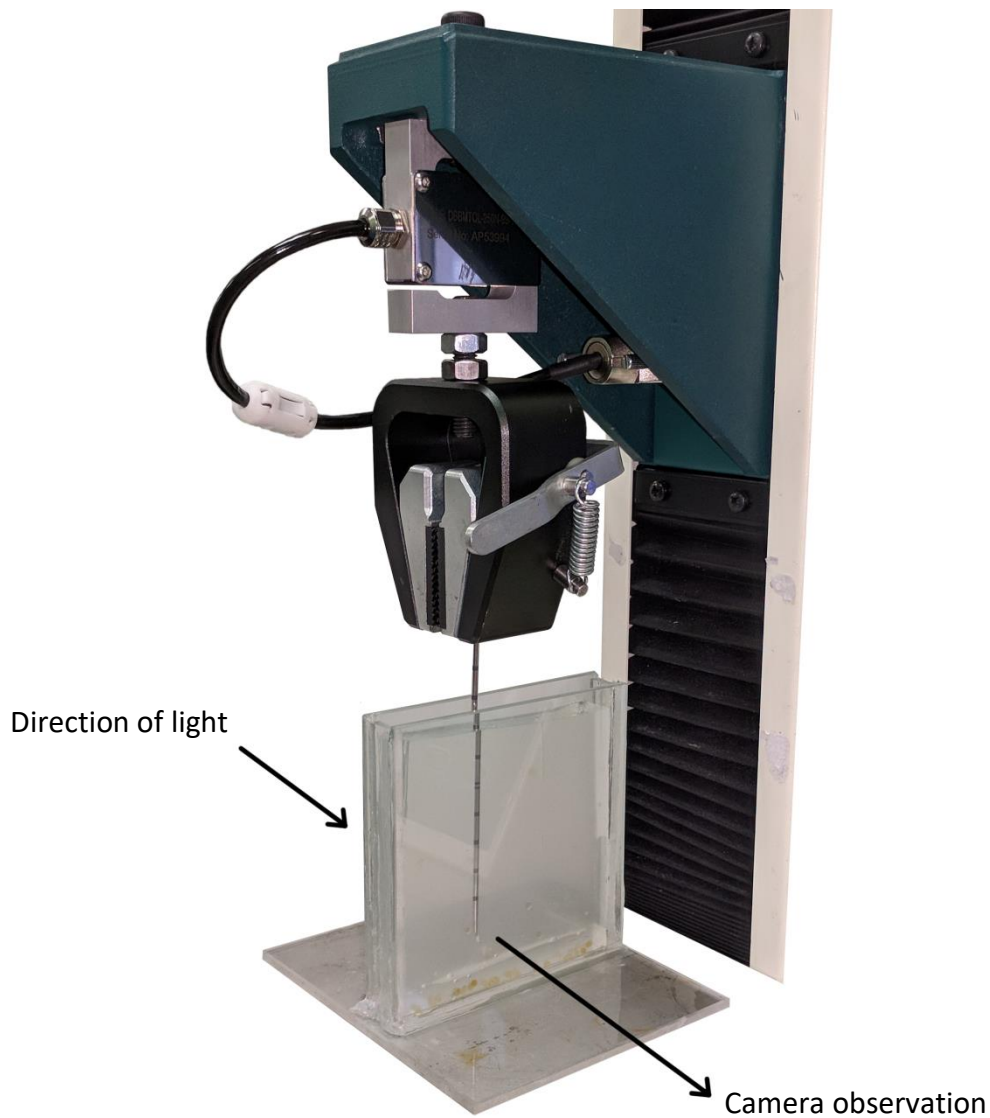


Figure 4-2: Photograph showing setup for needle experiments

A layer of thick plastic tape was wrapped around the gripped end of the biopsy needle; this ensured the needle did not slip in the grips. The other needles used were secured with the same grips, but did not require the addition of the tape as they had plastic ends which were easy to grip. The GFP2500 poleidoscope was set up in the same way as shown in section 3.2, and used to capture the retardation caused by changes in strain within the surrogate material.

4.1.3 Measurement of deflection

The needles were held rigidly between the grips during testing. This was done to create a consistent testing environment; it is assumed that a human operator would not be able to produce consistent speeds and would likely impact the final results. However, this meant that the motion of the needle was limited and the needle could not deflect freely.

Nevertheless, after the experiment was concluded the needle's path through the surrogate was visibly slanted. It appeared that the gel surrogate moved as the rigid needle was inserted.

Original measurement method

After each insertion experiment the gel tank was removed from the testing platform and examined. It was found that the needle path was visible with the naked eye but it was not clear in photographs. Attempts were made to augment the visibility of the needle path by adding dye to the puncture location in hopes that the dye would bleed down, but the dye remained on the top surface.

A further attempt to make the needle path visible to the camera involved re-inserting the needle into the original path. The needle was no longer secured in the testing grips and was carefully guided along the initial puncture path post-test. When the needle was fully inserted photographs were taken which clearly illustrated the needle deflection, as shown in Figure 4-3.

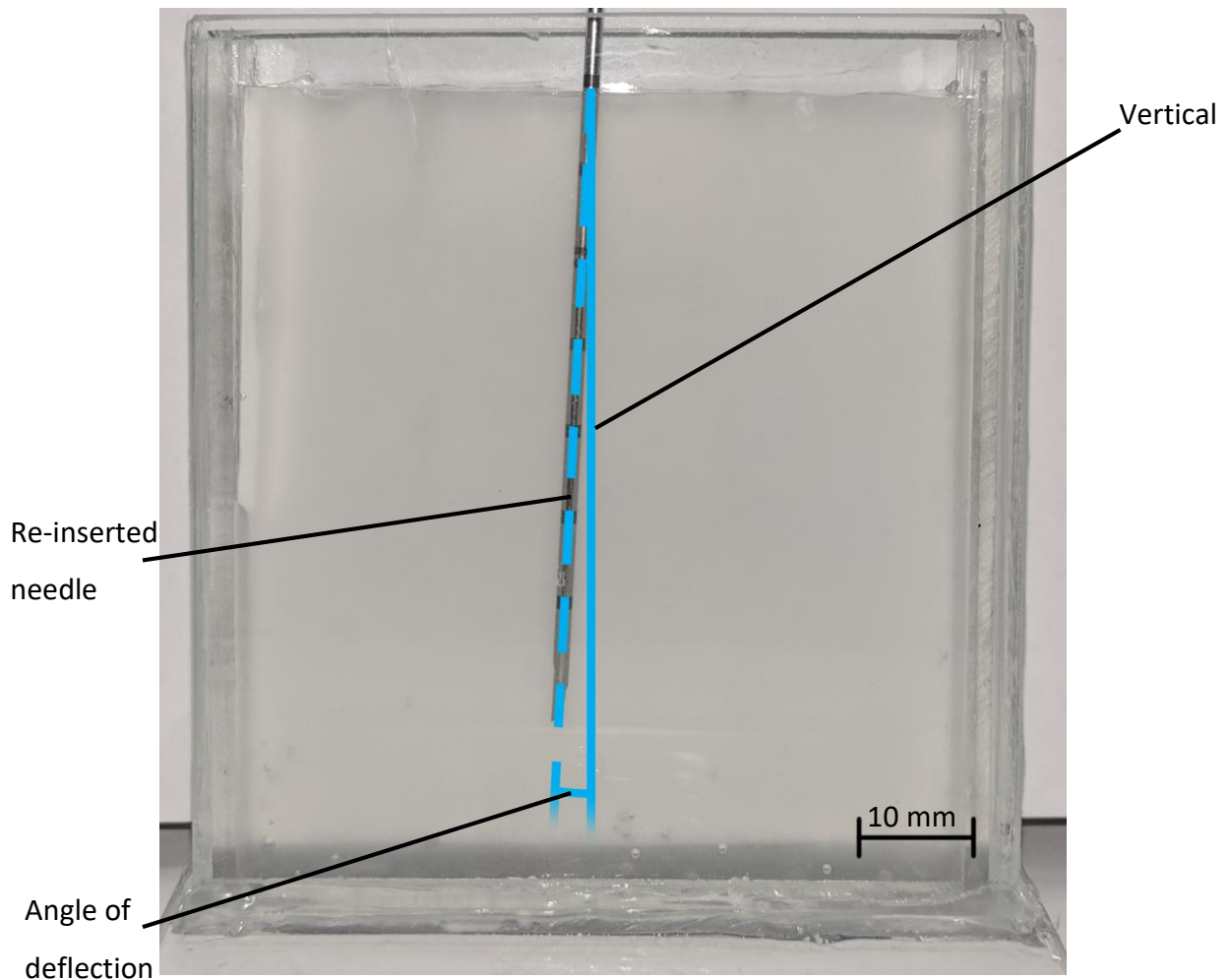


Figure 4-3: Example image showing the final deflection of a needle at 3°

However, after the results were gathered there was significant scatter within deflection results for the same needle, at the same insertion speed, within the same batch. It is assumed that when the needle was re-inserted it may have moved the surrogate material, thus altering the result. Or the material may have moved slightly as it was transported from the testing apparatus to the benchtop. It was therefore decided to re-evaluate the method for analysing the deflection amount.

Modified method

With re-evaluation of the optical results it was found that the needle path was visible through the GFP2500 poleidoscope camera as a dark line, which is highlighted in Figure 4-4 as a dotted line.

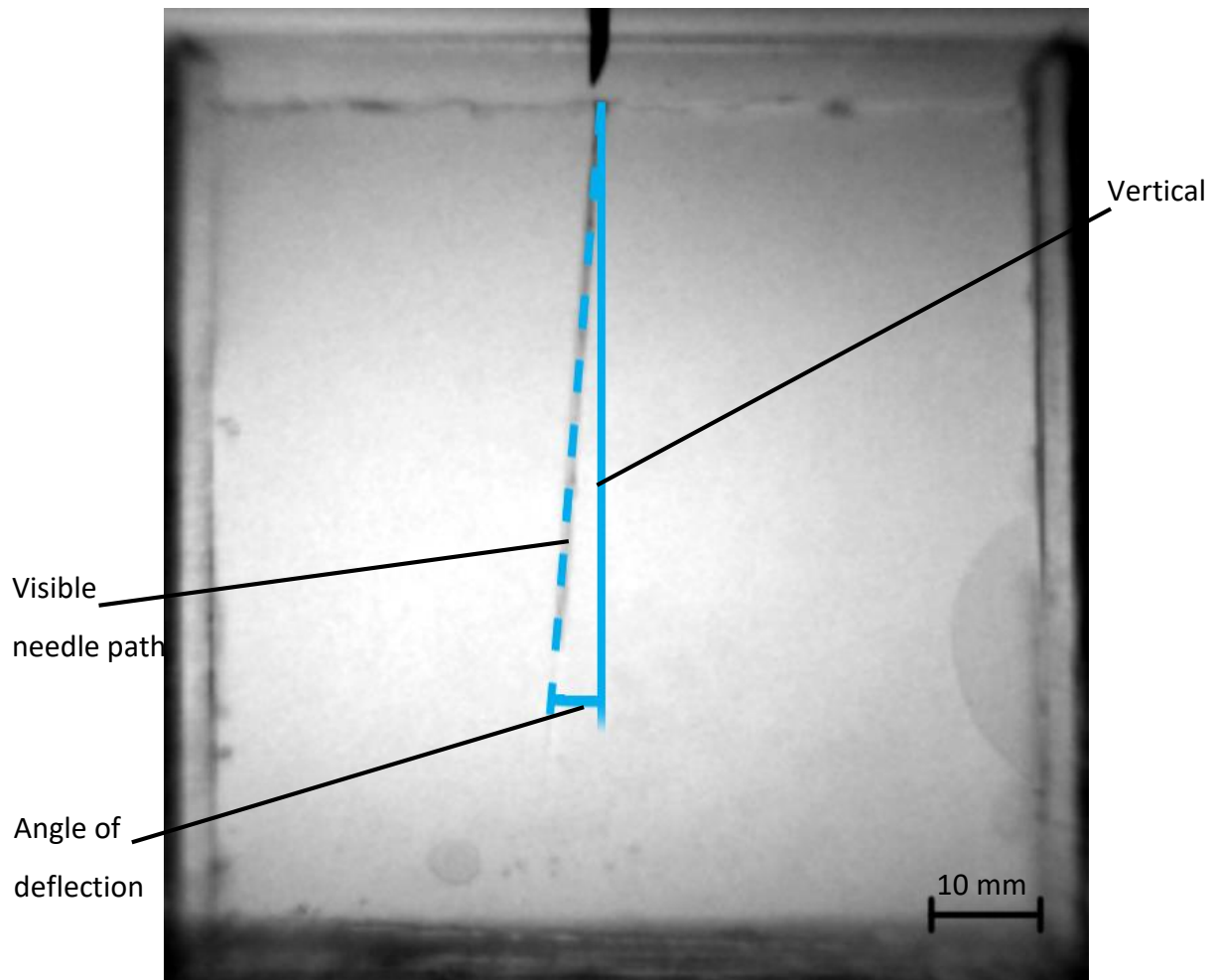


Figure 4-4: Example image from GFP2500 poleidoscope showing the final deflection of a needle at 4.6°

Images were saved at the end of each individual test when the needle had been completely removed from the gel surrogate. As with the original method, the deflection amount was measured from the needle insertion point to the end of the needle path with reference to the vertical. Both Figure 4-3 and Figure 4-4 are of the same tank and needle insertion. It can be seen that the deflection recorded in the original method was 3°, whereas the new method returned 4.6°. The results from the new method produced much less scatter, but the results were generally greater amounts of deflection. It is assumed that the change in results is because of unintended interference with the sample when re-inserting the needle, or when transporting the tank.

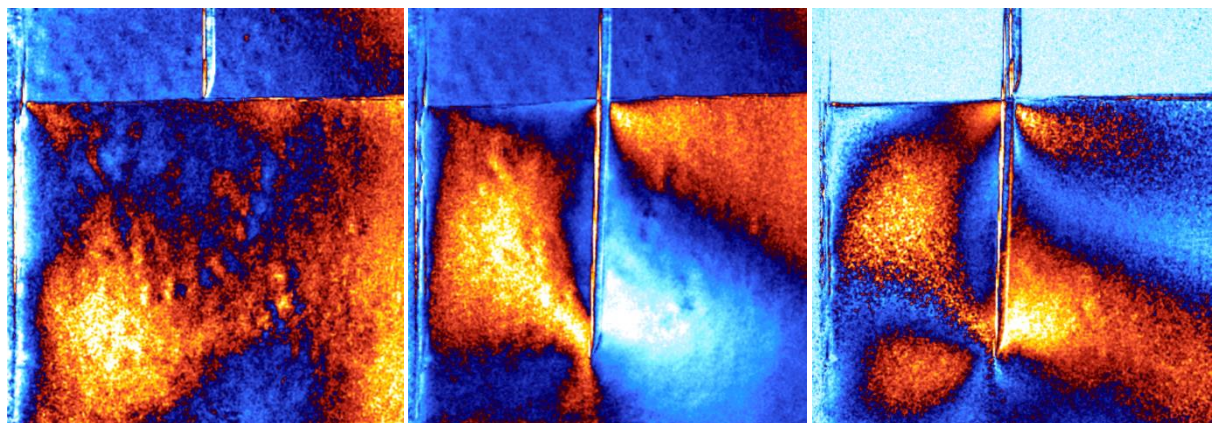
The deflection results for each variation of needle inserted will be presented within this chapter, and the original deflection measurements for the speed assessment using the re-insertion method are presented in the appendix in section 8.3.

4.1.4 Optical analysis method

The GFP2500 poleidoscope, described in section 1.3.7, was used to record all the needle insertions. The camera captured the retardation due to load in the konjac jelly, and with use of the optic coefficient this retardation could be converted to strain. Two separate retardation maps in the recorded video were collected for each needle insertion:

- One retardation map was saved at the start of the experiment before the needle had come into contact with the material; shown in Figure 4-5 a).
- Another retardation map was saved where the needle was almost at the maximum insertion point but still moving down; shown in Figure 4-5 b).

The image of the retardation map at zero insertion was subtracted from the retardation map at max insertion, to return Figure 4-5 c). This was done to ensure any recorded retardation was only a result of the needle insertion, and not any residual loads on the konjac jelly.



a) Retardation map at 0 insertion

b) Retardation map at max insertion

c) Retardation map of b) with a) subtracted

Figure 4-5: Figures displaying the effect of subtracting one retardation map from another retardation map.

This process was applied to all the needle insertions. The optic coefficient, which was calculated in chapter 3, was then used to determine the strain in the material.

4.2 Homogenous surrogate: Biopsy needle insertion at various speeds

The initial set of experiments assessed whether a change in the needle insertion speed affected the needle's response. A 14 gauge "Tru-Cut" biopsy needle, shown in Figure 4-6, was inserted into tanks containing gel with 1.5% concentration konjac jelly, as developed in chapter 2. The needle was inserted up to 50 mm depth at a range of speeds between 20 mm/min and 600 mm/min. The insertion depth and force response was recorded using the Tinius Olsen 5 kN benchtop tester with a 250 N load cell. The force response was used to calculate the puncture force, and the energy absorbed in the needle insertion at the varying speeds. The change in retardation due to loading was captured using the GFP2500 and was used to assess the strain field around the needle.



Figure 4-6: Tru-cut biopsy needle

4.2.1 Overall force response during needle insertion and removal

Figure 4-7 through Figure 4-14 show the complete force response when the 14-gauge biopsy needle was inserted and removed from the konjac surrogate at the varying speeds. Each figure contains results from two separate needle insertions at the same speed to show the consistency between the results.

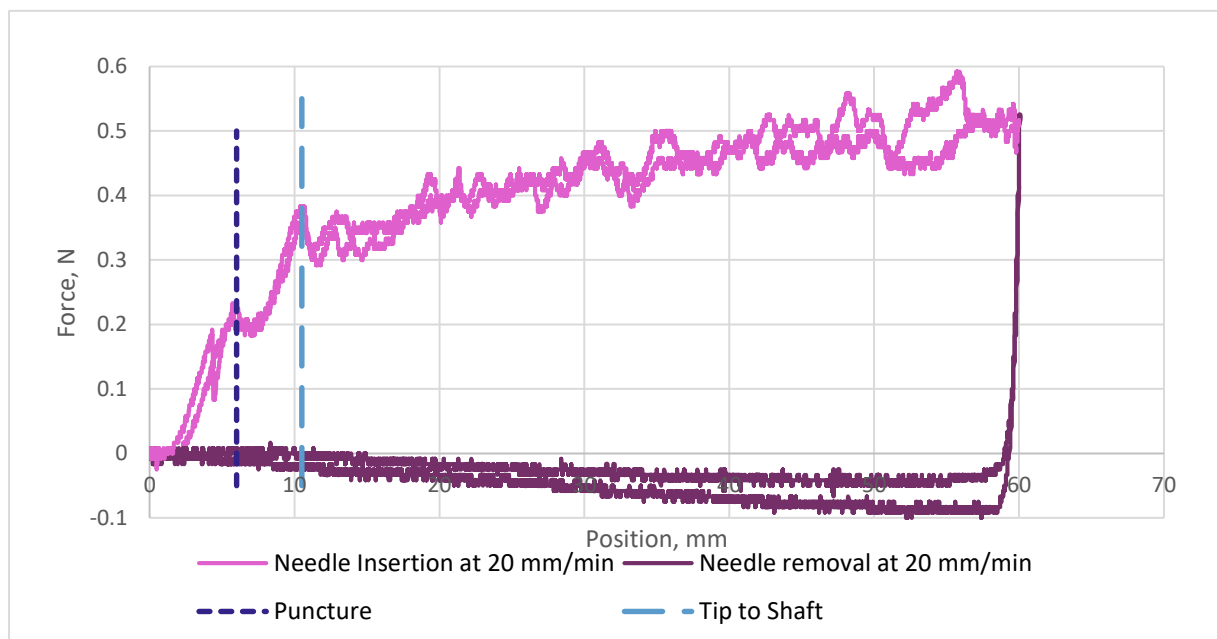


Figure 4-7: Force profile during needle insertion and removal at 20 mm/min

As the needle contacted the material the force gradually increased until a puncture occurred; at this point the force dropped suddenly. The puncture is highlighted in Figure 4-7 by the dark dotted line. The force response then began to increase again and a second, smaller, force drop occurred when the material moved from around the needle tip to the needle shaft. This is highlighted in Figure 4-7 by the blue dashed line. After this point any force increase was normally due to an increase in frictional resistance from more of the needle shaft passing through the material. As the needle was removed the force response dropped to a negative value, indicating the frictional force to remove the needle. As the needle was removed the magnitude of this force decreased.

The response observed mimics the force responses during needle insertions described by Mueller and Stellman who used polyurethane membranes [10, 132, 133], and further descriptions and depictions of a needle force profile through soft tissue *in vivo* [2, 8, 9, 134].

All the insertions follow the same pattern, however at higher speeds the recorded value for force frequently undulates, as seen in Figure 4-13 and Figure 4-14.

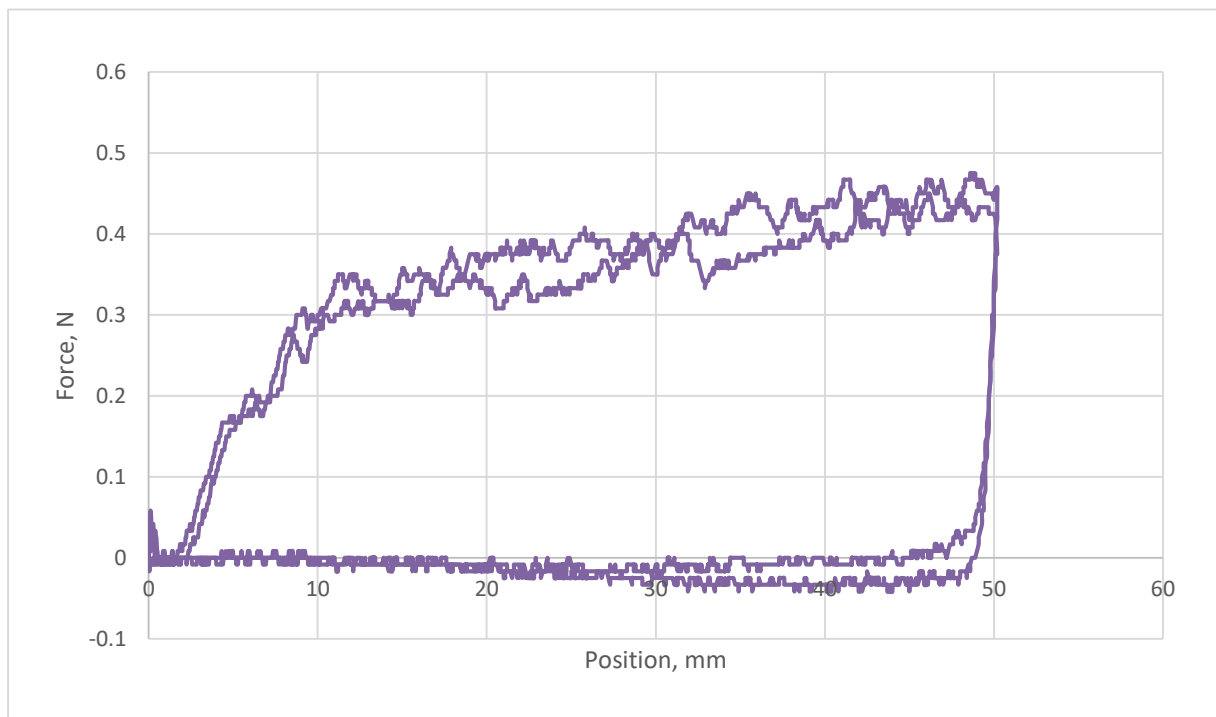


Figure 4-8: Force profile during needle insertion and removal at 100 mm/min

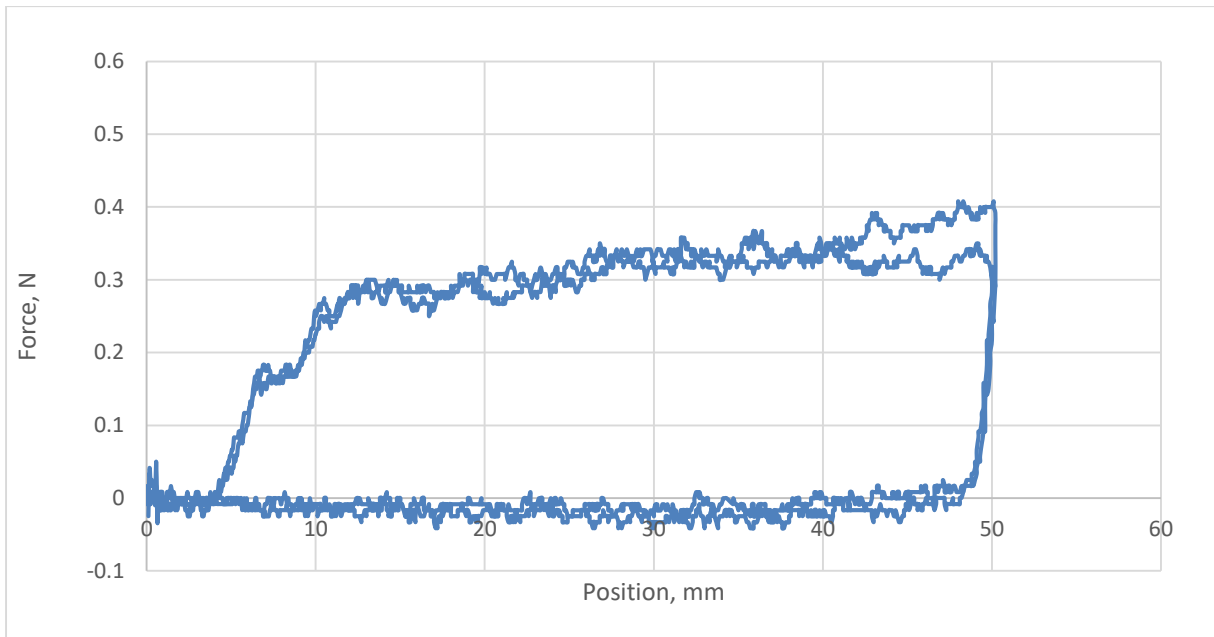


Figure 4-9: Force profile during needle insertion and removal at 150 mm/min

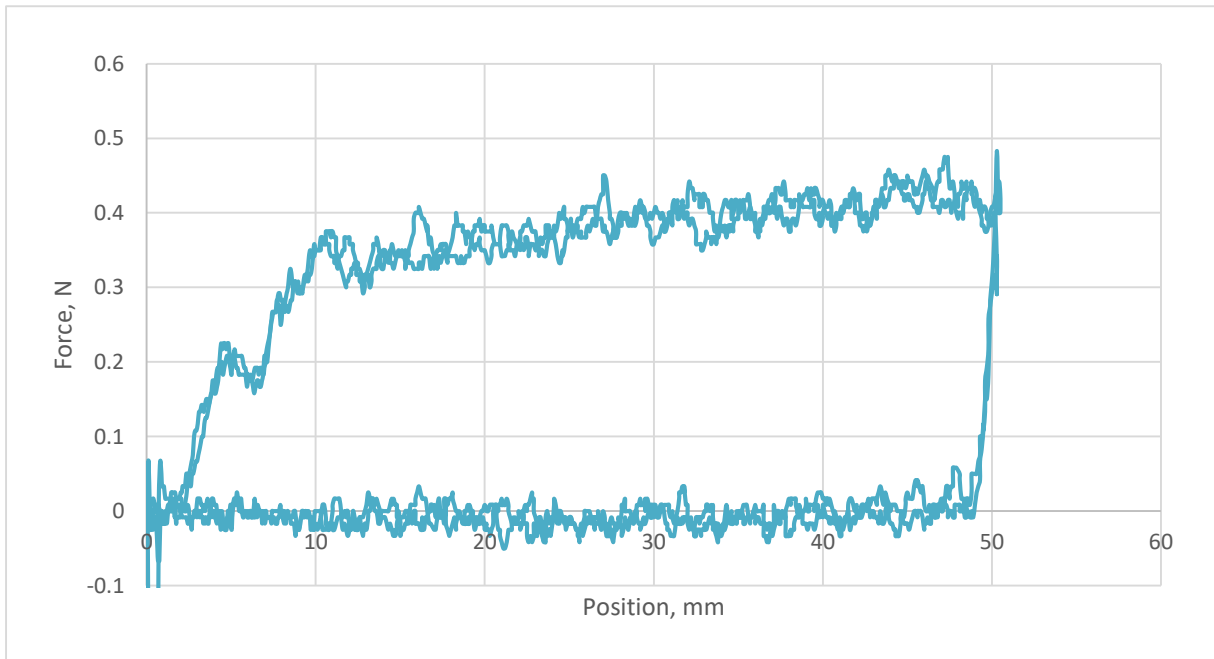


Figure 4-10: Force profile during needle insertion and removal at 200 mm/min

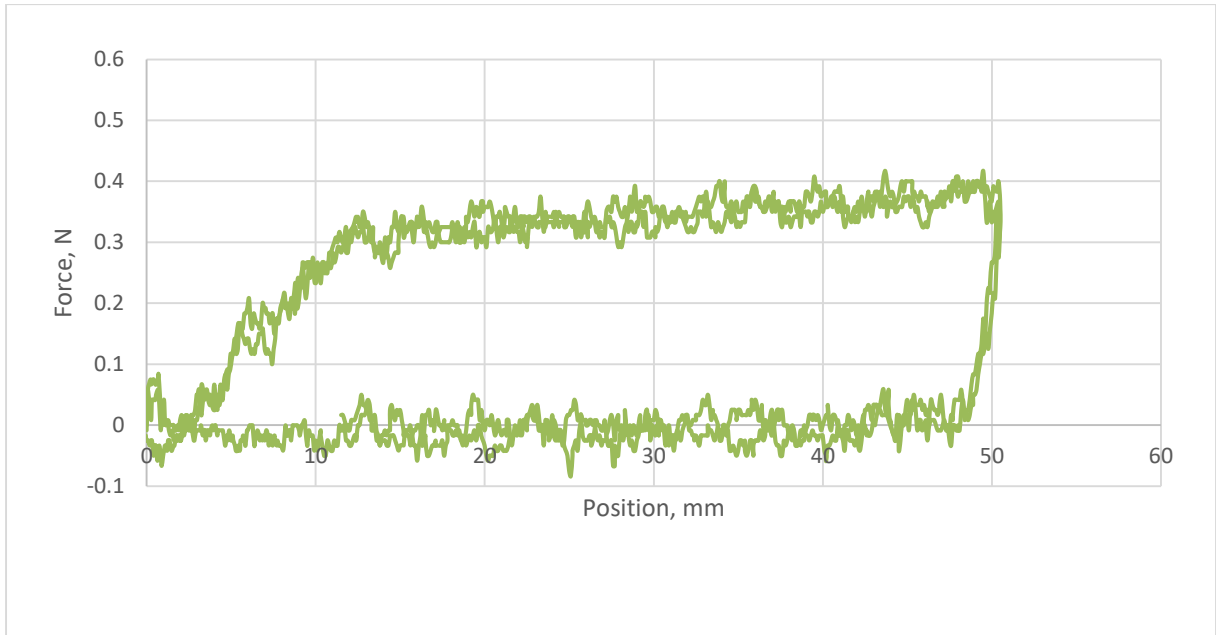


Figure 4-11: Force profile during needle insertion and removal at 250 mm/min

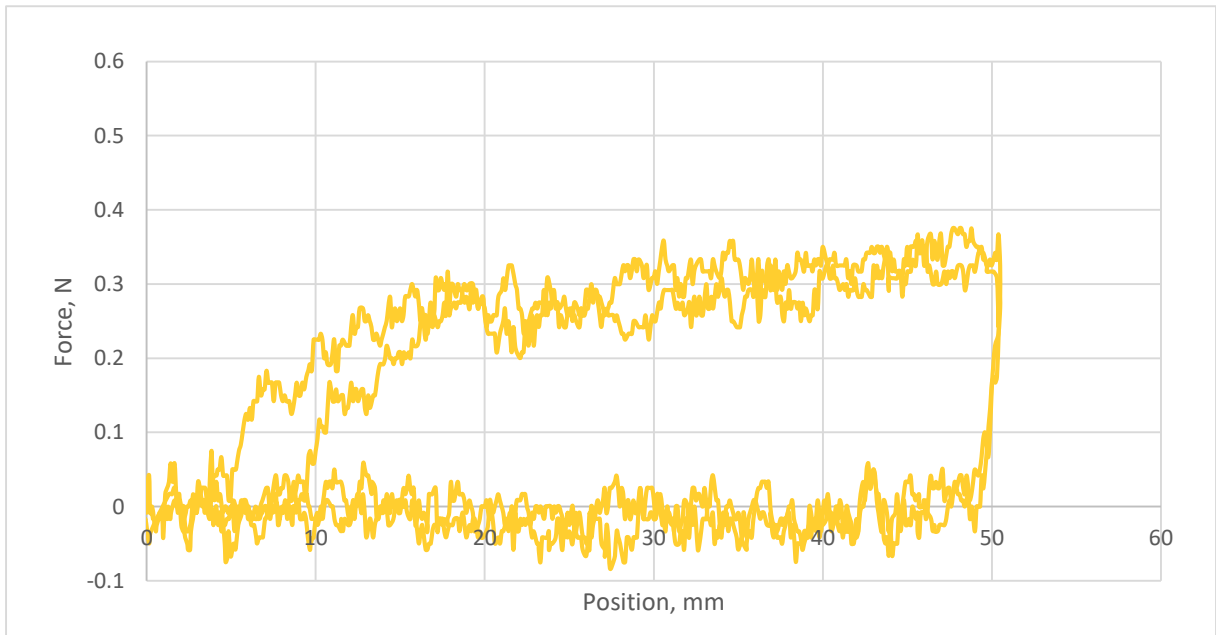


Figure 4-12: Force profile during needle insertion and removal at 300 mm/min

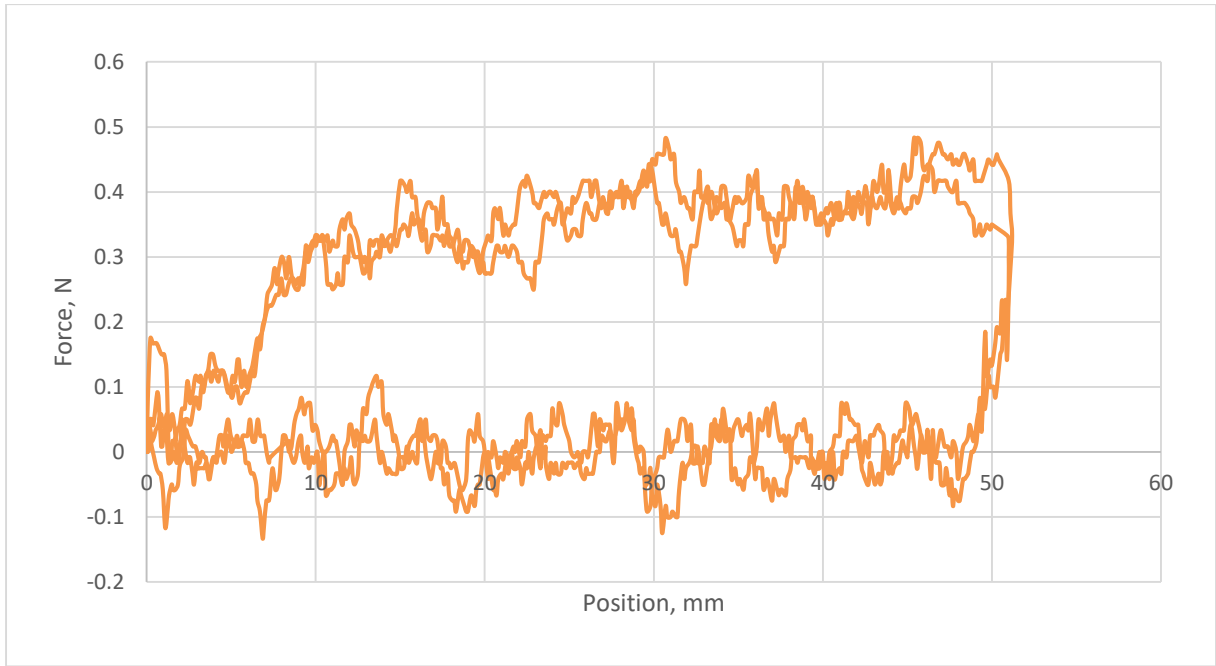


Figure 4-13: Force profile during needle insertion and removal at 400 mm/min

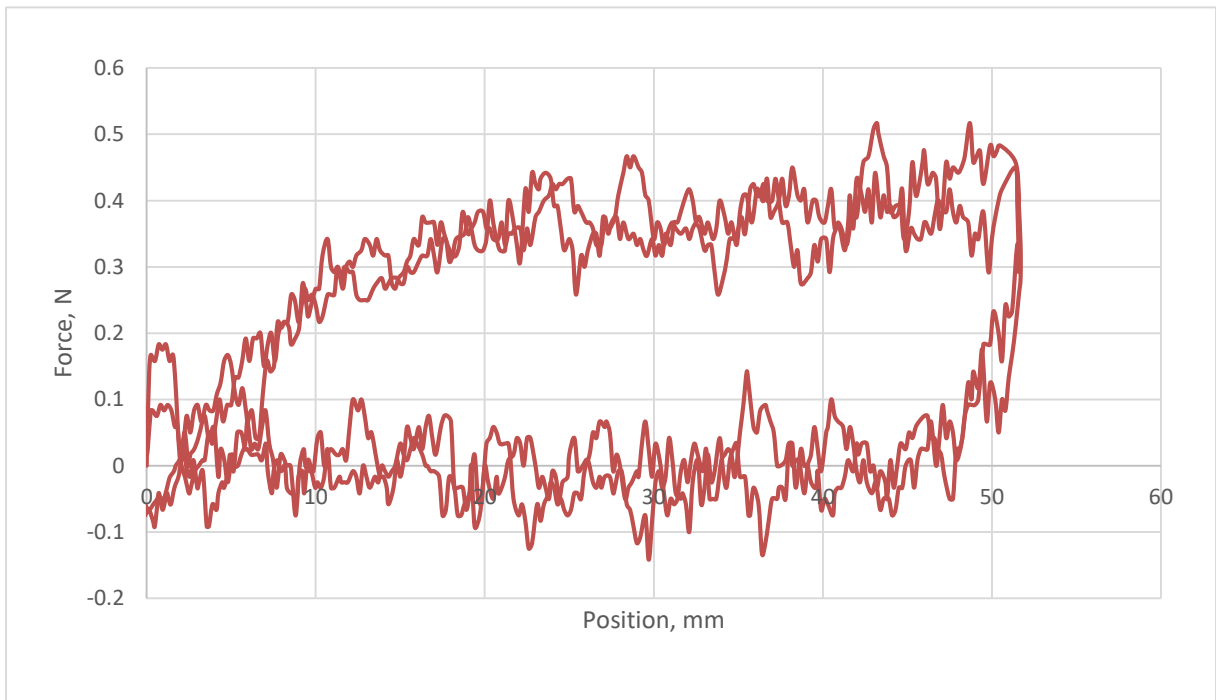


Figure 4-14: Force profile during needle insertion and removal at 600 mm/min

Speed assessment

As discussed in section 1.1.4, the average needle insertion speed during a medical procedure is 600 mm/min. Therefore, the experimental setup should involve needle insertions at this speed to provide an accurate comparison, especially since the results in Figure 4-15 and Figure 4-16 showed that insertion speed does affect the force response. However, at speeds above 200 mm/min the force results fluctuated significantly. This fluctuation could be due to feedback from the measurement apparatus, or the needle could be slipping through the material. In order to replicate the force response from typical needle insertions then a higher speed should be used, but experiments at higher speeds had decreased clarity of the results.

With analysis of the results at varying needle insertion speeds it was decided to conduct future experiments at an insertion speed of 150 mm/min. The force response at this insertion speed is similar to the response at 600 mm/min, and the results are legible and consistent between each test. This will offer greater confidence that any change in force response, strain field, or final needle deflection was a result of applied changes to the test setup rather than random noise response from the testing apparatus.

4.2.2 Puncture force with biopsy needle

The puncture force is the force required for the needle to form a crack initiation and breach the surrogate boundary. It is identified as the force peak after a gradual force increase caused by the needle pushing against the tissue boundary. The puncture force peak is immediately followed by a sudden drop in force response, which signals where the needle has breached the tissue boundary. The puncture force at the various insertion speeds was recorded and plotted in Figure 4-15.

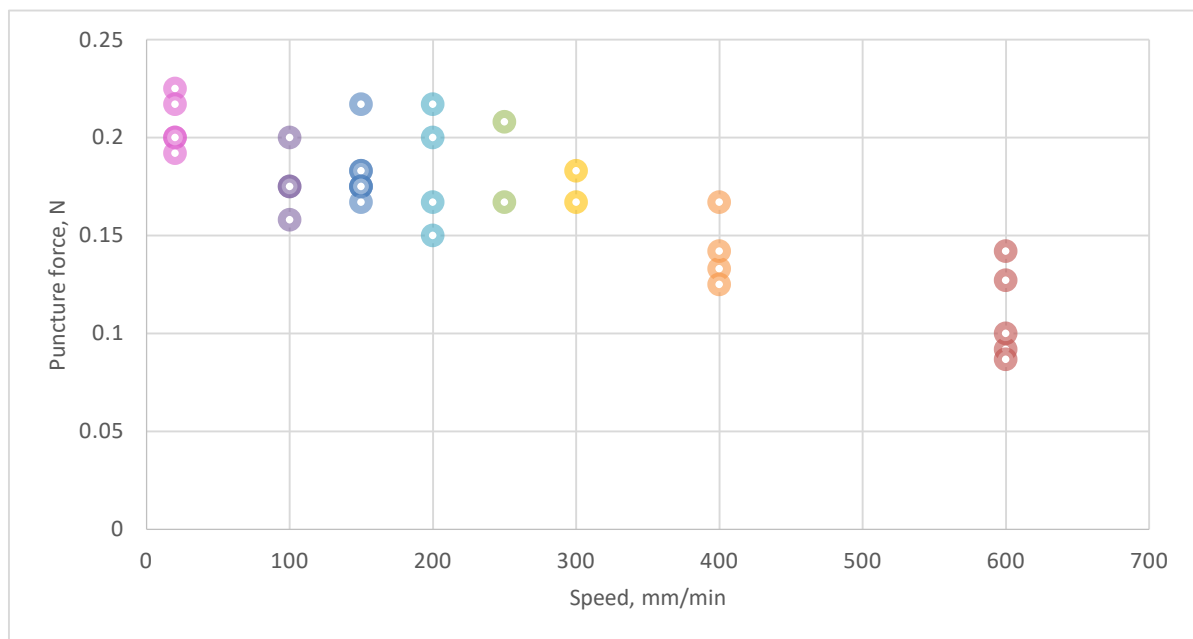


Figure 4-15: Relationship between needle insertion speed and puncture force

A total of 33 insertions were completed using the same Tru-cut gauge 14 biopsy needle; five at 600 mm/min, four at 400 mm/min, two at 300 mm/min, two at 250 mm/min, four at 200 mm/min, seven at 150 mm/min, four at 100 mm/min, and five at 20 mm/min.

The results in Figure 4-15 show that as the needle speed increases, the force required to puncture the material decreases. These results are similar to results from Mahvash and Dupont, who investigated the effect of robotically controlled needle velocity on puncture force into porcine heart muscle [32]. Their study involved needle insertions at speeds of 60 mm/min to 15,000 mm/min, and showed that the mean rupture force at lower insertion speed was greater than the mean rupture force at higher insertion speed.

Hing *et al.* also assessed the effect of human controlled needle velocity on puncture force into porcine liver. They used an 18 gauge prostate steering needle at a range of speeds between

60 mm/min to 1500 mm/min [34]. Their results also showed that puncture force decreases at increasing speeds.

Possible causes for different responses between konjac and conventional surrogates

The results show that konjac jelly responds similarly to real tissue, where an increase in insertion speed caused a decrease in puncture force [8, 31-35]. It was discussed in section 1.1.4 that conventional tissue surrogates return higher puncture force responses at higher insertion speeds [26-30]. This difference in response could be a result of the different crack profile observed which konjac exhibits when punctured with a needle, as discussed in 1.2.2. This result demonstrates that konjac jelly more accurately represents skin tissue than existing surrogates.

4.2.3 Average insertion force

The effect of insertion velocity on the average force response was also assessed. The average force was calculated using the force results between 10 mm insertion and 50 mm insertion. This was done to avoid any contributions from the puncture force, as this was shown to depend on insertion speed and would skew the results.

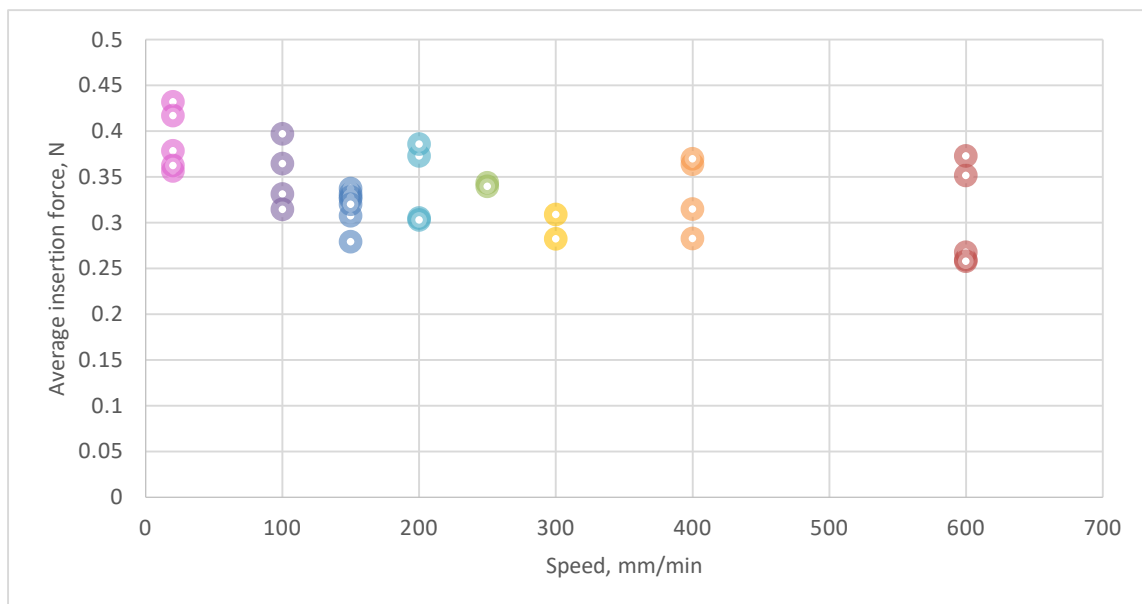


Figure 4-16: Relationship between needle insertion speed and average insertion force

In section 1.1.1, it was discussed that Okamura *et al.* demonstrated that the overall force response that a needle experiences during a needle insertion is a combination of three forces [11]:

$$F_{needle}(x) = F_{cutting}(x) + F_{stiffness}(x) + F_{friction}(x) \quad \text{Equation 4.1}$$

The results in Figure 4-16 are a combination of all three separate forces and are from the same needle insertions described in Figure 4-15. It can be seen that there is a relationship between insertion speed and force response, where the faster speeds return a lower average force. As the insertion speed increased from 20 mm/min to 600 mm/min the average insertion force reduced by under 0.1 N.

An ANOVA single factor statistical analysis was conducted on the results in Figure 4-16 to determine if the differences were statistically significant. The result returned a P-value of 0.029, which is less than 0.05, showing that the results are significantly different for the different groups.

Comparing results to responses from conventional surrogates

The effect of changing needle insertion speeds was discussed in section 1.1.4. It was shown that needle insertions into tissue surrogates returned a higher average value for insertion force at higher speeds [2, 26-30]. Whereas insertions into tissue surrogates *ex vivo* showed that insertion speeds had little to no effect on the force response [8, 31-35].

The different responses between the konjac surrogates and conventional surrogates could also be a result of the tissue tribology. In section 1.1.4, it was discussed that a needle insertion into human tissue will be lubricated from the moisture within the skin tissue, whereas rubber tissue surrogates are dry and would grip the needle. The surrogate tissues used in the needle speed studies were all dry gels: PVC gel, silicone rubber, and porcine gelatine. These gels do not have any lubrication, so it is likely that the gels gripped the needle as it was inserted and this gripping was more noticeable at higher speeds. Konjac jelly has a wet surface, and this wetness could be simulating the lubrication in real tissue *in vivo*, thus allowing the needle to glide more freely through the tissue. Once again, this result shows that konjac jelly represents the response from skin tissue better, and more realistically, than existing surrogates.

4.2.4 Work done at varying insertion rates

The effect of insertion velocity on the work done (energy absorbed) was also assessed. This was calculated using the area underneath the force vs position curves for each needle

insertion. Similar to the force response, the work was calculated between an insertion of 10 mm and 50 mm. This was done to avoid any contributions from the puncture force.

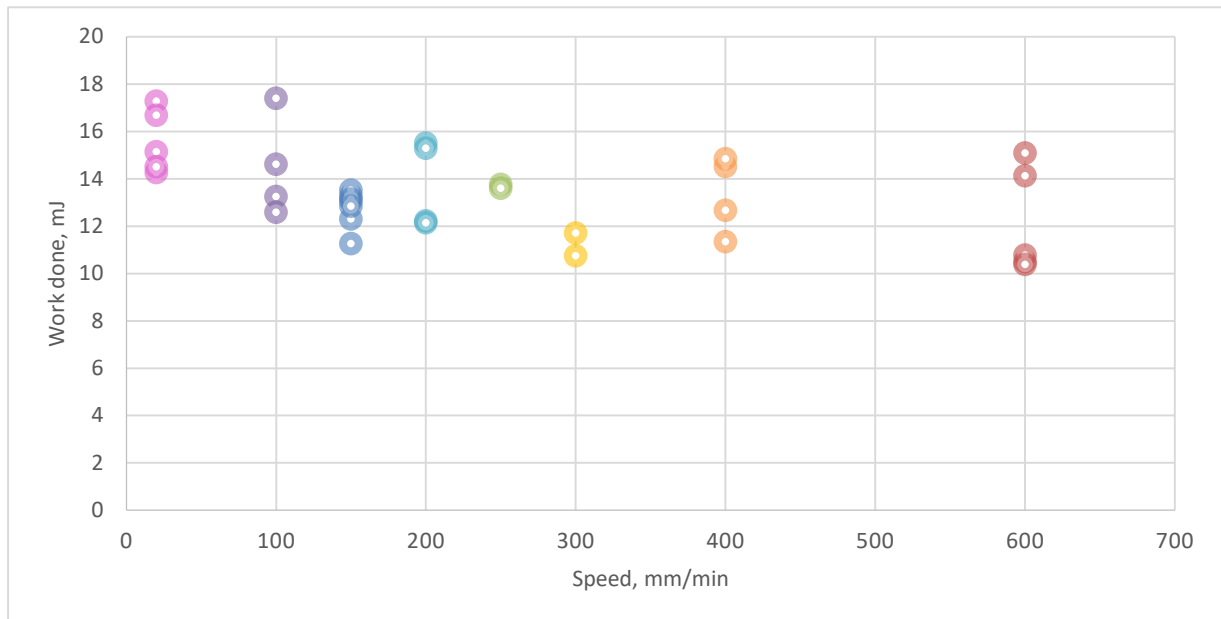


Figure 4-17: Relationship between needle insertion speed and work done

The results in Figure 4-17 mirror the results presented in Figure 4-16, where the faster insertion speed produced a lower result.

It is considered that the measurement of energy consumed, or work done, by the needle when being inserted into tissue is a more meaningful measure of the process than the average force. However, plotting average force allows for comparison with previously published research, and the trends are the same in Figure 4-16 and Figure 4-17.

4.2.5 Deflection angle at various insertion speeds

The deflection angles were measured using the method described in section 4.1.3. One plane image of the needle and tank was captured from the GFP2500 poleidoscope footage at the end of the experiment when the needle was fully removed. Within this image the track of the needle insertion was visible, and the deflection angle with respect to the vertical could be determined from the insertion point to the end of the needle track. The results at the various insertion speeds were gathered in Figure 4-18.

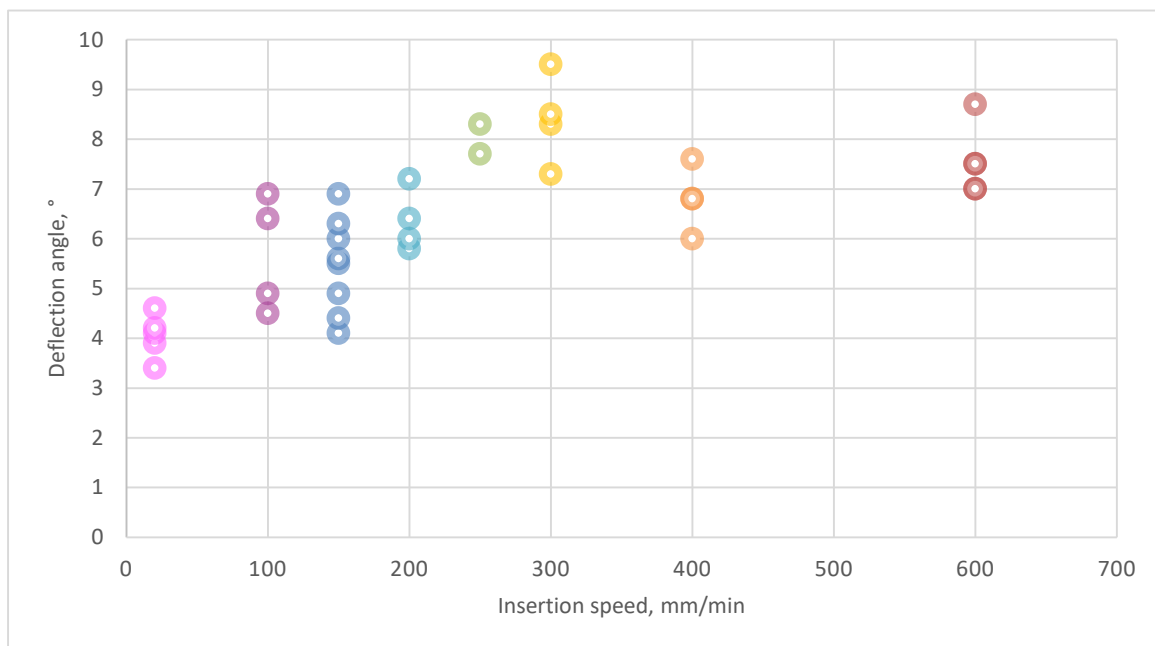


Figure 4-18: Relationship between needle insertion speed and deflection angle

The results show that the deflection amount is dependent on the insertion speed, where increased insertion speeds led to an increased needle deflection. This is synonymous with results by Hing *et al.*, who showed that in a human operated needle insertion the deflection increased with increasing speed [34].

However, the results Hing *et al.* presented show significantly lower amounts of deflection, with values lower than 0.1 degrees at 1,500 mm/min. Lehmann *et al.* also produced similar results to Hing *et al.* with a deflection amount of under 0.1 degrees when an 18 gauge needle was inserted into porcine loin tissue [103].

Movement of tissue surrogate

It is assumed that the greater deflection in this study is a result of the observed free movement of the konjac samples. As described in the chapter 2, the konjac jelly shrinks slightly as it sets. As a result of this the material could move slightly within the tank. The needle was rigidly secured within the grips so the deflection observed was only due to the material moving around the needle as it was inserted. The experimental method used by Hing *et al.* and Lehmann *et al.* ensured that their subject material was rigidly constrained and was not permitted to move.

Robotically controlled vs human controlled experiments

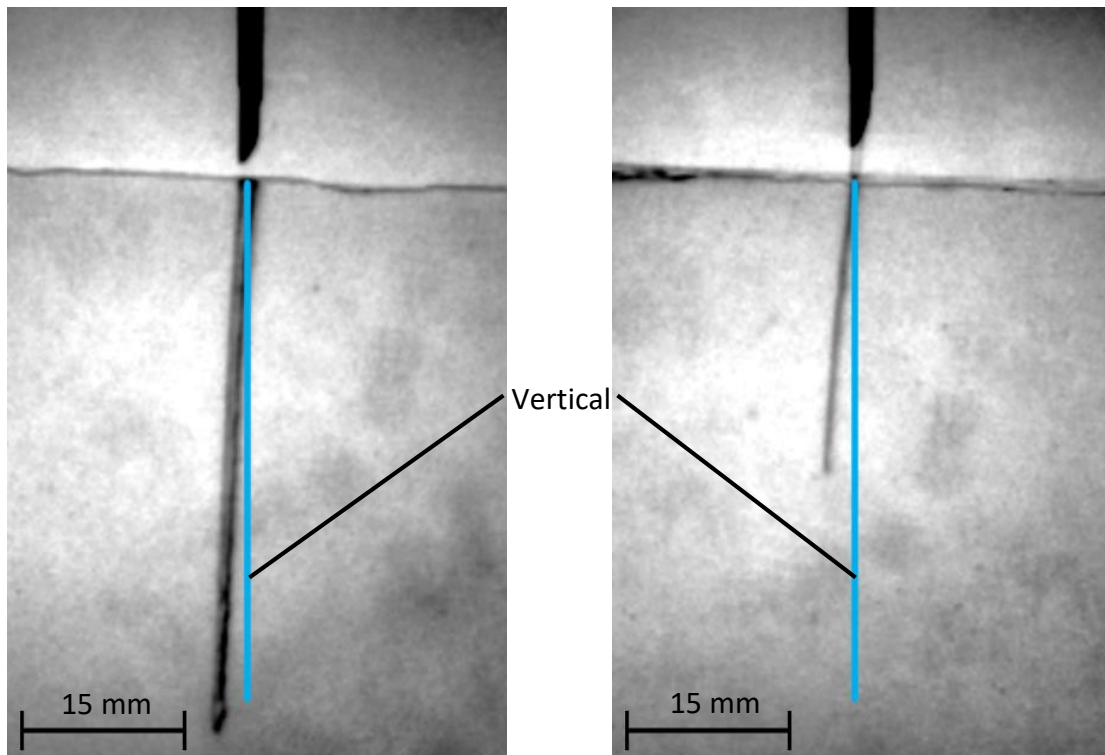
There is a noticeable difference between human operated and robotically controlled needle insertion. Logically, the insertion speed will not be as consistent for a human operated needle insertion. This was shown by Podder *et al.* from needle insertions through real tissue; a robotically operated needle moved at a constant speed of 0.1 m/s, and a human operated needle moved at an average of 0.1 m/s within a range of 0.01 m/s to 0.5 m/s [23]. A human controlled needle insertion will also be affected by the haptic feedback experienced.

Anecdotal evidence within this research found that inserting the needle at faster speeds resulted in a greater deflection. When the needle was inserted at slower speeds it was possible to 'correct' the deflection from the force response experienced, and at higher insertion speeds it was difficult to apply this correction. A robotically operated needle insertion experiment was not able to simulate this feedback correction.

It would be interesting to measure the difference in deflection amounts between a human controlled needle insertion, and a robotically controlled insertion at the same insertion speeds. This would be an interesting topic to cover in future studies within this body of research.

Needle deflection path

A difference in deflection path was observed for the needles inserted at the different speeds. Figure 4-19 shows the insertion paths when the needle was inserted at 20 mm/min, and at 600 mm/min. The path at 20 mm/min is more visible as the needle was in the material for a greater period of time, thus allowing the material to settle around the needle.



a) Insertion path at 20 mm/min

b) Insertion path at 600 mm/min

Figure 4-19: GFP2500 poleidoscope images of the deflection tracks at the different insertion speeds.

The notable observation is the difference in needle path shape between the two speeds of insertion. At a slower speed the needle path is straight, whereas at the faster insertion speed the path has a slight curve. This difference in insertion path could be a cause for the greater deflection amount at higher speeds.

Another cause for the difference in deflection could be due to the tissue relaxing. At 20 mm/min the needle is in the surrogate for a longer period of time. The duration of an insertion experiment was 300 seconds for 20 mm/min, and only 10 seconds for 600 mm/min. During this time difference the material may have ‘settled’ around the needle. This is evident with the larger, more visible needle path at the slower insertion rate.

In order to test this hypothesis photographs of the needle path could be taken after the surrogate has had a chance to relax, e.g. 10 minutes. If there is any change between the images taken straight after the needle was removed, and after the rest period then it is likely the different deflection angles are just from material relaxing during the slower test.

4.2.6 Deflection angle at various insertion depths

It was assumed that if more of the needle was inserted then the deflection amount would increase. This was measured by inserting the biopsy needle at various depths at an insertion speed of 150 mm/min. The deflection angles were measured using the method described in section 4.1.3.

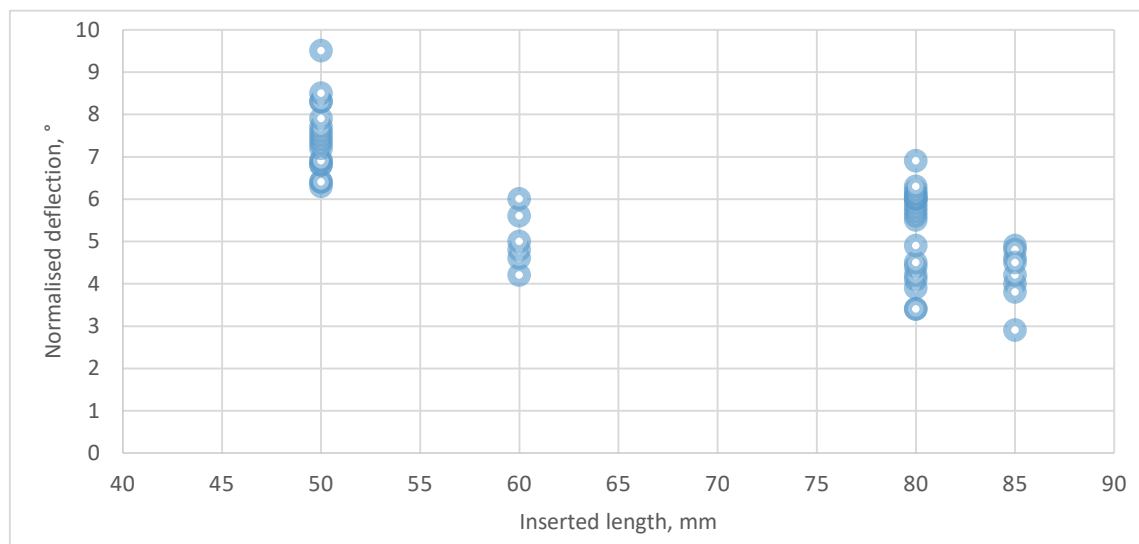


Figure 4-20: Relationship between needle insertion depth and deflection angle

The results show that the deflection angle actually decreased as more of the needle was inserted. However, as mentioned in section 4.2.5, as the needle is fixed the deflection measured is actually the deflection due to the material moving. If the needle was secured in a flexible grip which allowed some rotation and the material was fixed, then the results may be different.

4.2.7 Optical analysis at the varying insertion speeds

Optical data for the needle insertions at various speeds was gathered and processed using the experimental method described in section 4.1.4. The images in Figure 4-21 show the magnitude and direction of the principal strain through the different insertion speeds.

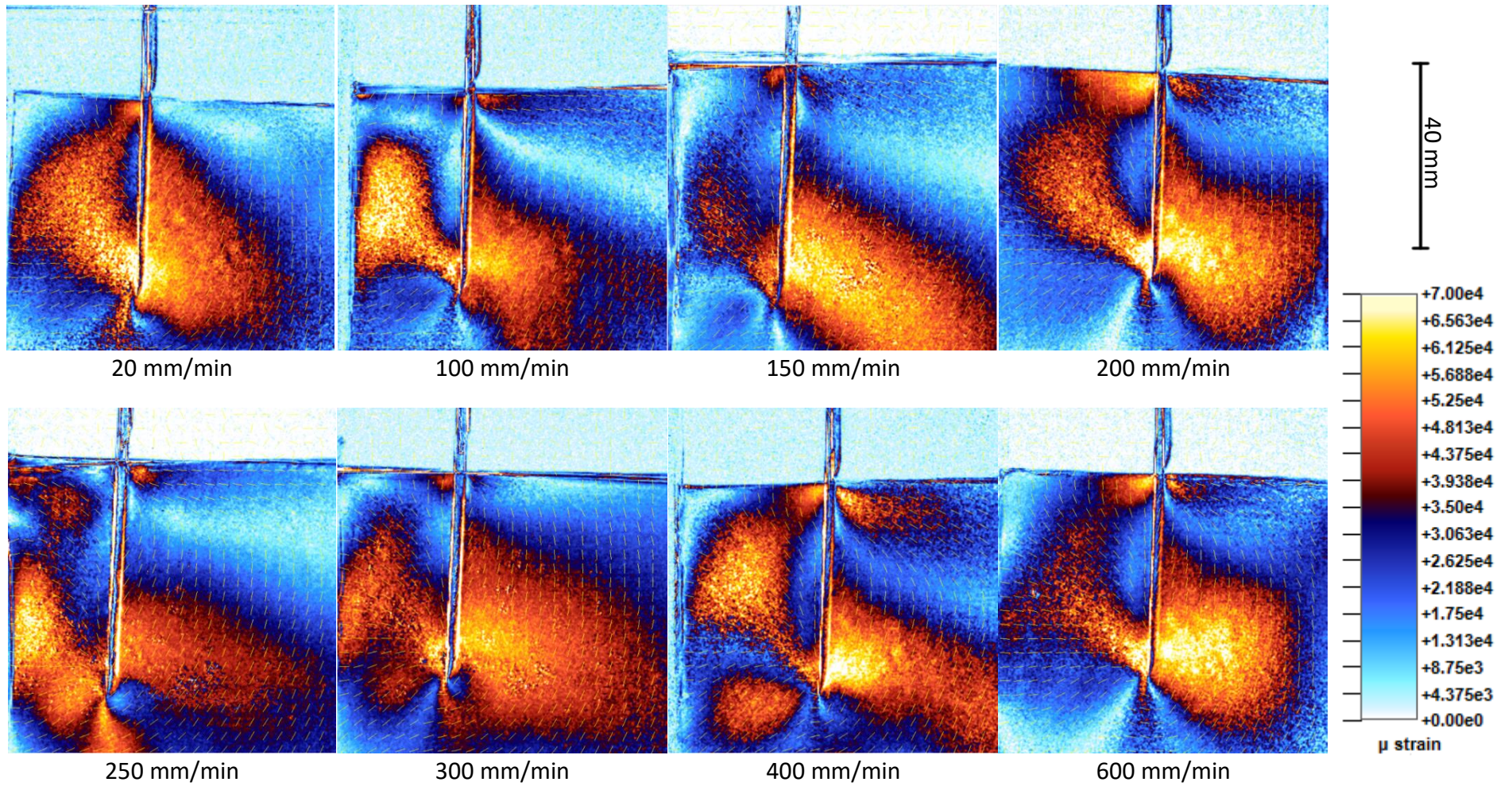


Figure 4-21: Principal strain maps of biopsy needle insertion at various speeds

The strain results show that there is consistency in the needle insertions at the various speeds. All the results show an area of maximum strain in the tissue surrogate on the angled tip of the needle. It is assumed that this large deformation on only one side is causing the needle deflection. It is interesting to note the increased strain around the puncture location. This area is resisting the deflection of the needle; and acting like a pivot location. The images in Figure 4-21 also contain the directional vectors; shown as yellow dotted lines. The combination of the force magnitude and direction vectors reveal a moment acting on the needle, as highlighted in Figure 4-22 by a yellow arrow.

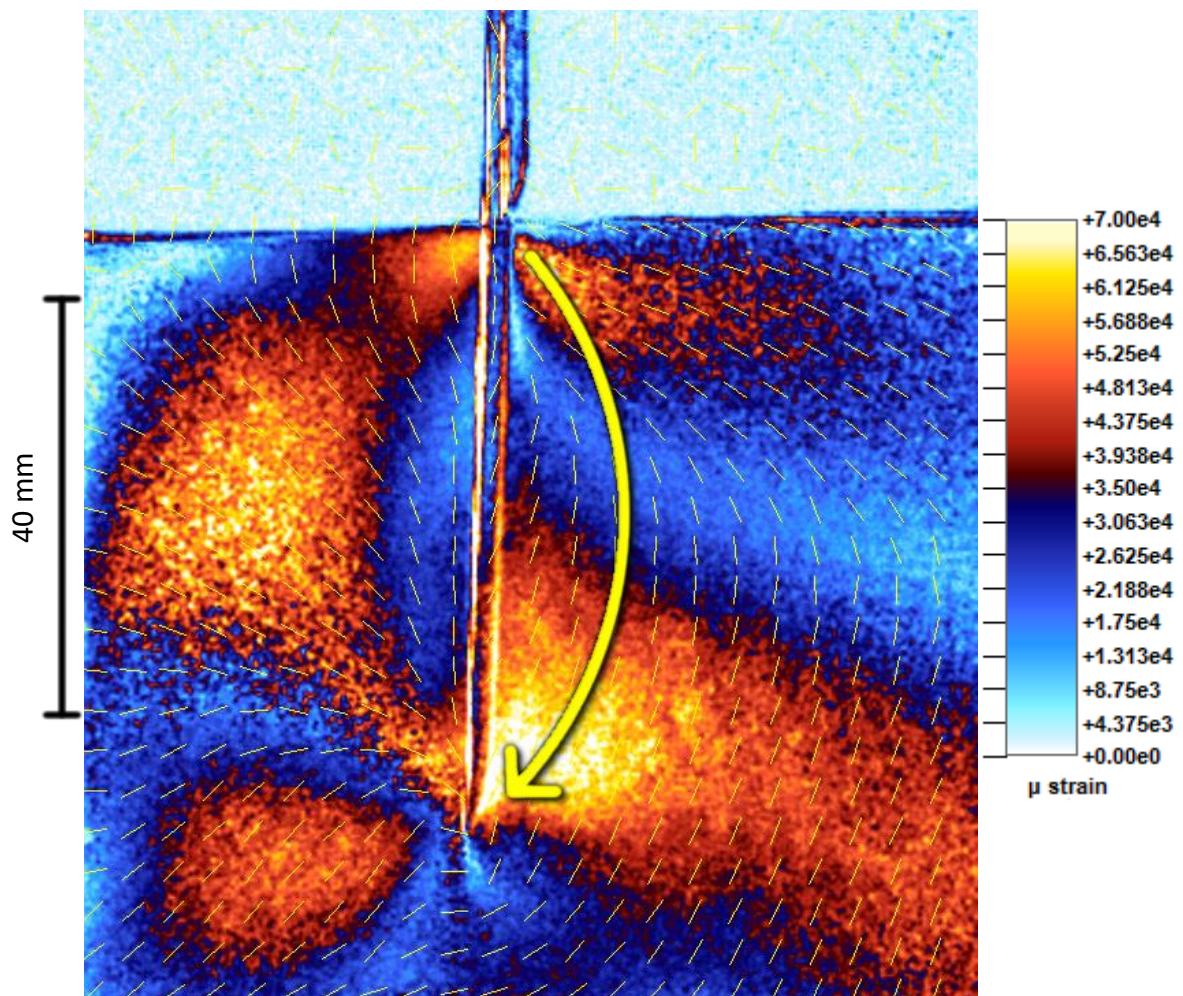


Figure 4-22: Illustrated principal strain diagram of needle insertion

Previous research within this area has not demonstrated the direction of the forces during the needle insertion. Some studies speculate the distribution of the forces, but most expect the force distribution on the bevel side of the needle to be reducing towards the puncture location [2, 103, 135]. However, for the first time, the GFP2500 poleidoscope images in Figure 4-21 have revealed a consistent load around the needle entry point, which resist the bending

moment. This directional information also reveals how the surrogate material rotates during a needle insertion, showing that both needle and tissue deflect during an insertion.

4.2.8 Conclusion

Suitability of konjac jelly as a skin tissue surrogate

In section 1.1.4 it was discussed that existing soft tissue surrogates generally produced higher reaction forces at higher insertion speeds [26-30], yet the opposite was shown for the soft tissues tested *ex vivo* [8, 31-35]. In this section it was found that konjac jelly replicates the same force response development at varying insertion speeds as soft tissues tested *ex vivo*. Therefore, konjac jelly accurately replicates needle insertion responses through soft tissue better than existing surrogates.

It is assumed that the more accurate response is due to a combination of the different crack profile that konjac displays when punctured with a needle, and the lubricated texture observed in konjac jelly. These differences produce a more realistic soft tissue surrogate compared to conventional, rubbery tissue surrogates.

Needle deflection discussion

The recorded results for needle deflection were significantly higher than results for needle deflection through real tissue using similar gauge needles. It was discussed that this difference could be due to the free movement of the gel observed in the tanks, where the konjac jelly was able to move slightly as it shrank as it cooled. The comparative studies involved tissue samples which were securely constrained in all directions [34, 103].

It was found that the deflection amount increases at increasing insertion speed, which was also reported for real tissue tested *ex vivo*. It was also noted that the needle path appeared to change when the speed of the insertion was increased. The faster insertions followed a curved path, and the slower insertions had a straighter path. It is assumed that this trajectory change contributed to the increased needle deflection at greater insertion speeds.

It was also found that the deflection angle decreased when the needle was inserted further into the tissue surrogate at the same speed. This was an unexpected outcome, as it was assumed that when the needle is inserted further it will deflect more. However, it is assumed that this outcome is due to the relatively free movement of the tissue surrogate.

Contributing factors for needle deflection

In a real needle insertion, the needle deflection will be a combination of the tissue moving around the needle and the asymmetrical forces on the needle tip causing the needle to divert from a straight path. In this research the needle was constrained within the grips, so the needle was unable to divert. However, even with the rigidly gripped needle, a significant amount of relative deflection between tissue and needle was observed. It is clear that the flexible tissue surrogate moves during the needle insertion, and the deflection is not just due to the needle moving. The needle is significantly stiffer than the surrogate tissue so it is unsurprising that the tissue deforms before the needle begins to bend. Within section 6 a range of new experiments have been proposed which could quantify the amount of deflection between needle bending, needle deflection, and tissue motion.

Anecdotal evidence revealed that during a human-steered needle insertion it was possible to correct the needle deflection at slow insertion speeds, but this became difficult at faster insertion speeds. It was noted that it would be interesting to assess the different magnitudes of deflection when inserting an electronically controlled needle compared to a human controlled needle into a soft tissue surrogate. It is expected that the human controlled insertion may result in a lower amount of deflection as haptic feedback will allow for trajectory corrections.

GFP2500 Poleidoscope data

With use of the GFP2500 poleidoscope apparatus it was possible to acquire full field, directional data during the needle insertions. The principal strain maps at the different insertion speeds all displayed similar results. The principal strain maps also showed an increased strain at the needle puncture location, and a significant strain concentration on the side of the needle bevel tip. The directional data revealed a bending force acting on these two strain concentrations, which is assumed to causes the needle deflection.

4.3 Homogenous surrogate: Various needles at the same insertion speed

In this sub-section a range of needles were inserted into tanks containing gel with 1.5% concentration konjac jelly at 150 mm/min. The experimental setup used for testing the biopsy needles at various speeds has been repeated, where the insertion depth and force response were recorded using the Tinius Olsen 5 kN benchtop tester with a 250 N load cell. The force response was used to calculate the puncture force for the various needles. The change in retardation due to loading was captured using the GFP2500 poleidoscope and was used to assess the strain field around the needles. The responses were compared to assess whether different needle gauges and tip angles had an effect on the overall force response and deflection. All needles are made out of stainless steel with an elastic modulus of 200 GPa, and details on the needles dimensions and tip geometries are found in Table 4-1.

Needle Make	Gauge	Outer diameter, mm	Length, mm	Flexural stiffness, Mpa.mm ³	Tip Angle, °	Tip Type
Tru-cut Biopsy	14	2.1	140	21821	45	Back Bevel S'
BD Blunt Fill	18	1.2	40	6206	30	Bevel C'
Agani Needle	19	1.1	38	5137	14	Back Bevel C'
Agani Needle	21	0.8	38	1405	14	Back Bevel C'
Agani Needle	23	0.6	32	573	14	Back Bevel C'
Agani Needle	25	0.5	25	364	14	Back Bevel C'
BD Eclipse Needle	21	0.8	40	1334	14	Back Bevel C'
BD Eclipse Needle	25	0.5	16	569	14	Back Bevel C'

Table 4-1: Details of needle tip shapes and dimensions

In section 1.1.2 and 1.1.3, studies were presented which showed that changing the needle geometry has an effect on both the forces experienced during needle insertion, and the deflection angle. A number of studies showed that the shape of the needle tip can affect the puncture force and the deflection of the needle [11, 14-17, 95]. Studies also showed that needles with a smaller diameter experience greater bending, and thus were susceptible to greater deflection amounts [11].

All the needles in Table 4-1 have a form of bevel tip. The biopsy needle has a solid back bevel tip, known as a stylet. The remaining needles all have hollow tips as they are used for delivering or removing fluids. The BD Blunt fill needle has a bevel tip, whereas the others have a back bevel tip which has a more tapered point. The difference between a back bevel tip and a bevel tip is minimal, and is illustrated in Table 4-2, which was also presented in section 1.1.2 in literature review.



Table 4-2: Examples of common needle tip types [12]

Studies showed that different tip types had a large effect on the deflection and force response from a needle insertion [11, 95]. Since the tip types are relatively consistent in this study it is expected that the similar tip types will produce similar principal strain maps.

Some of the needles available have different tip angles, and studies have shown that the tip angles can affect the overall deflection of the needle [14]. However, the needles available all have variabilities between gauge, length, and tip angle. These attributes all affect the needle deflection. Therefore, any apparent difference in results can't be linked to one unique feature of the needle. Ideally, to assess the effect of changing needle gauge the different needle lengths and tip shapes should be the same, and vice versa. However, the needles presented are real needles used in hospitals today, so an understanding on the current performance is still advantageous.

4.3.1 Optical analysis of needle insertions

Optical data for the different needle insertions was gathered and processed using the experimental method described in section 4.1.4. The images in Figure 4-23 through Figure 4-38 show a photograph of the needles described in Table 4-1, followed by a principal strain map of that needle inserted into the konjac surrogate.

Tru-cut biopsy needle: gauge 14



Figure 4-23: Tru-cut biopsy needle

Figure 4-23 shows the biopsy needle used for the insertion experiments. The biopsy needle usually has a handle which is used to manipulate the inner and outer sections of the needle to gather the biopsy sample, but this was removed in order to grip the needle.

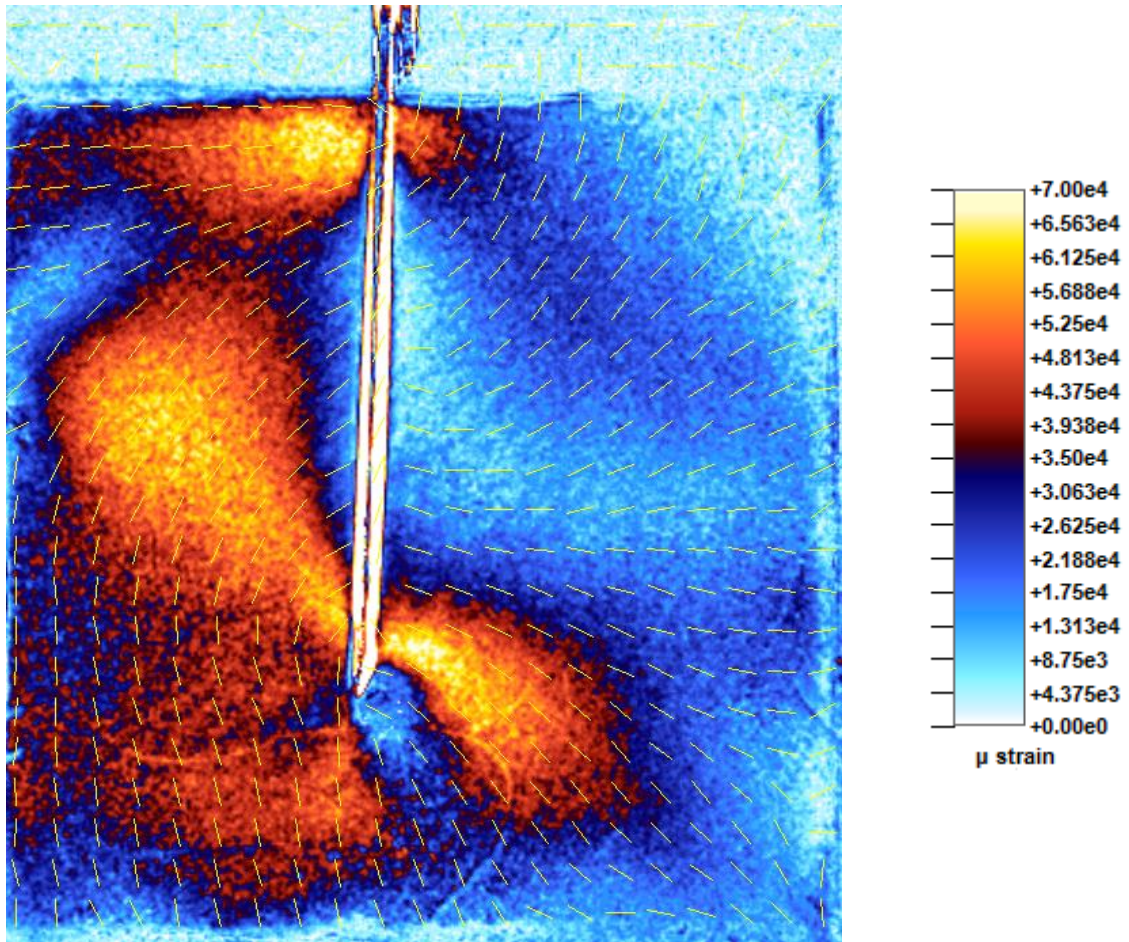


Figure 4-24: Principal strain map of biopsy needle insertion at 150 mm/min

Figure 4-24 shows the principal strain map with directional information of the biopsy needle insertion at 150 mm/min. This map shows the same characteristic patterns observed in Figure 4-19 when the needle was inserted at various speeds. There is an increased strain magnitude on the side of the bevel tip and at the insertion point. Directional information indicates how the tissue surrogate is moving.

BD blunt fill needle: gauge 18

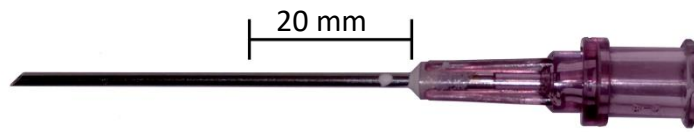


Figure 4-25: BD blood fill needle

Figure 4-25 shows the BD blunt fill needle, it has a hard plastic head which was trimmed to enable it to be secured within the grips. This type of needle is used for taking blood.

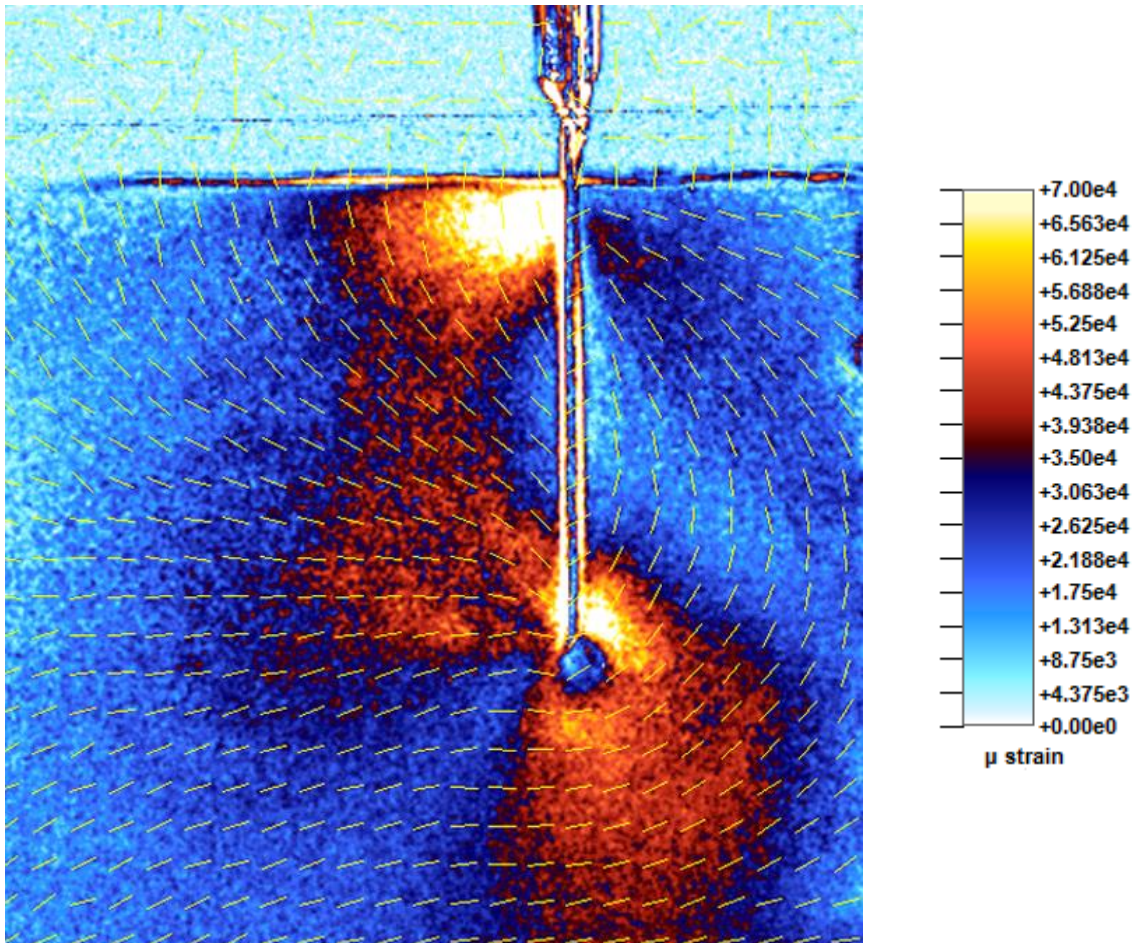


Figure 4-26: Principal strain map of BD blunt fill needle insertion at 150 mm/min

Figure 4-26 shows that the principal strain map for the blunt fill needle mimics the principal strain map for the biopsy needle. There is increased strain magnitude on the side of the needle tip and on the opposite side at the insertion point. The directional information also reveals a similar pattern.

Agani needle: gauge 19

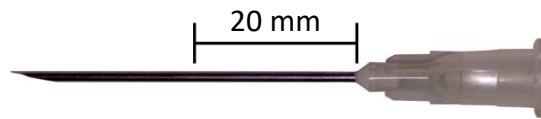


Figure 4-27: Agani needle; gauge 19

Figure 4-27 shows the gauge 19 Agani needle; this style of needle is used for drug delivery. All the Agani needles have a softer plastic head than the BD blunt fill needle. This meant that the plastic head could be easily trimmed and deformed to fit securely within the grips.

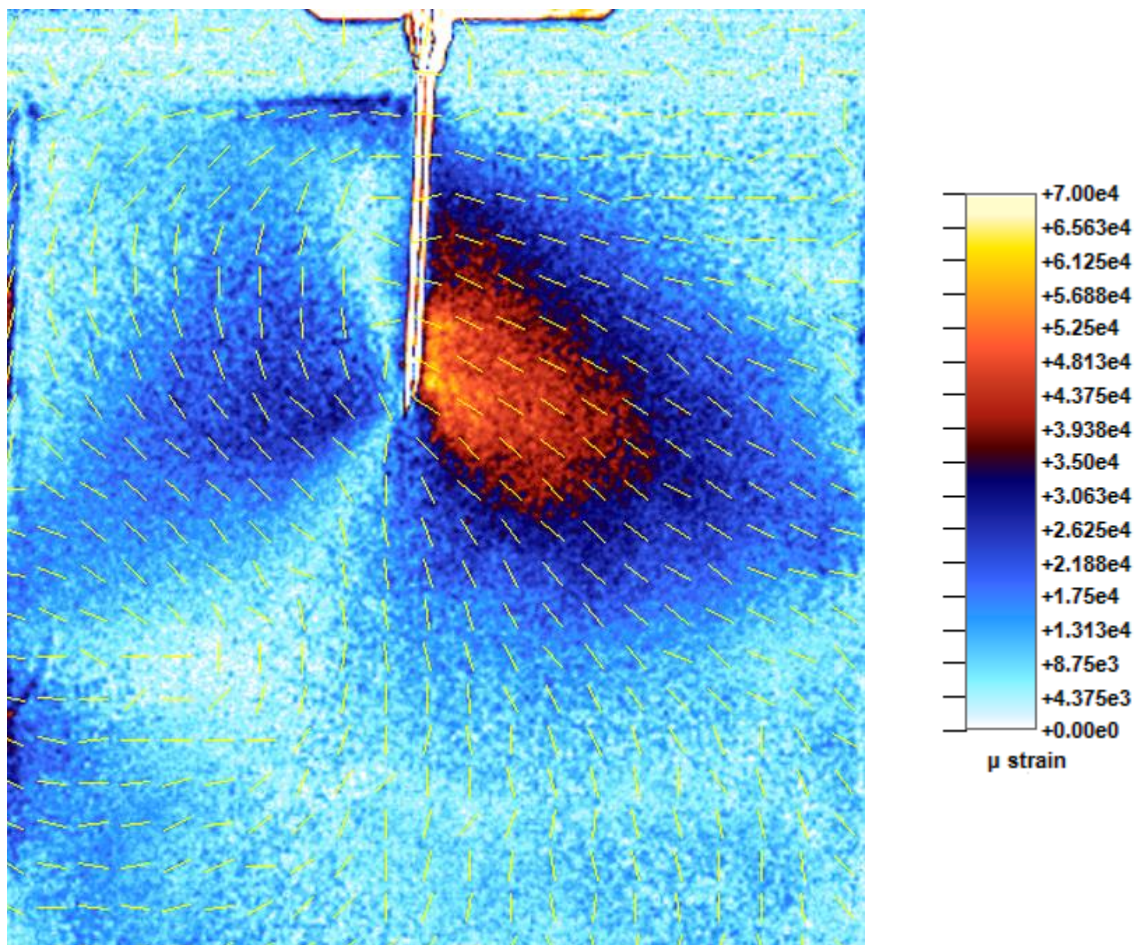


Figure 4-28: Principal strain map of Agani needle gauge 19 insertion at 150 mm/min

The strain and directional map in Figure 4-28 has comparable features to the principal strain maps of the biopsy and BD blunt fill needle. However, this needle has not been loaded perfectly straight, and increased strain is visible as a result of this. This error is discussed later on in this section.

Agani needle: gauge 21

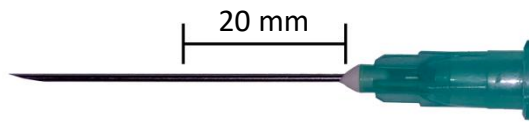


Figure 4-29: Agani needle; gauge 21

The remainder of the Agani needles all have the same plastic head shape which didn't vary with the different needle gauges.

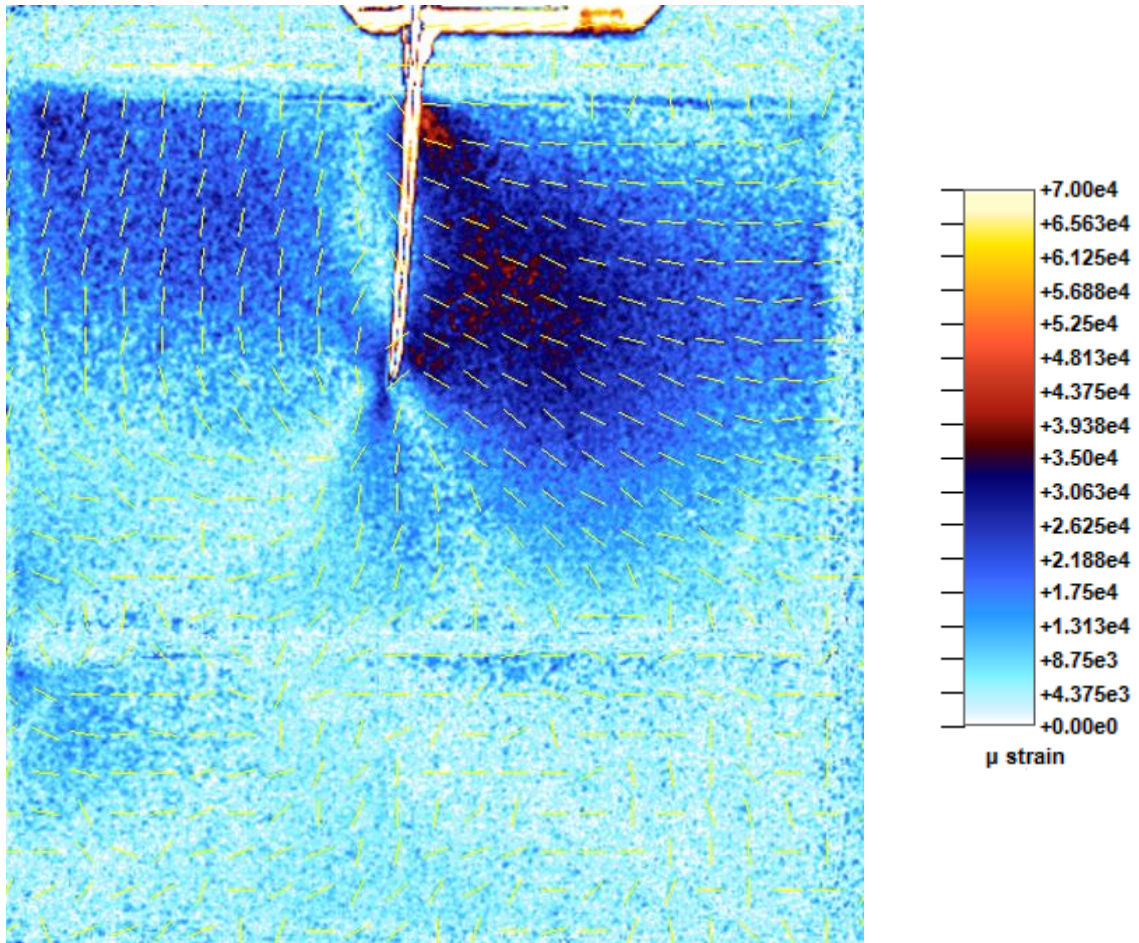


Figure 4-30: Principal strain map of Agani needle gauge 21 insertion at 150 mm/min

In Figure 4-30 it can be seen that once again the needle was loaded at a slight angle, and has an increased strain on one side. However, the characteristic features are still visible, with an increased strain on the side of the bevel tip and at the puncture point.

Agani needle: gauge 23

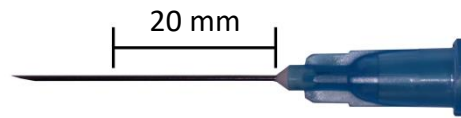


Figure 4-31: Agani needle; gauge 23

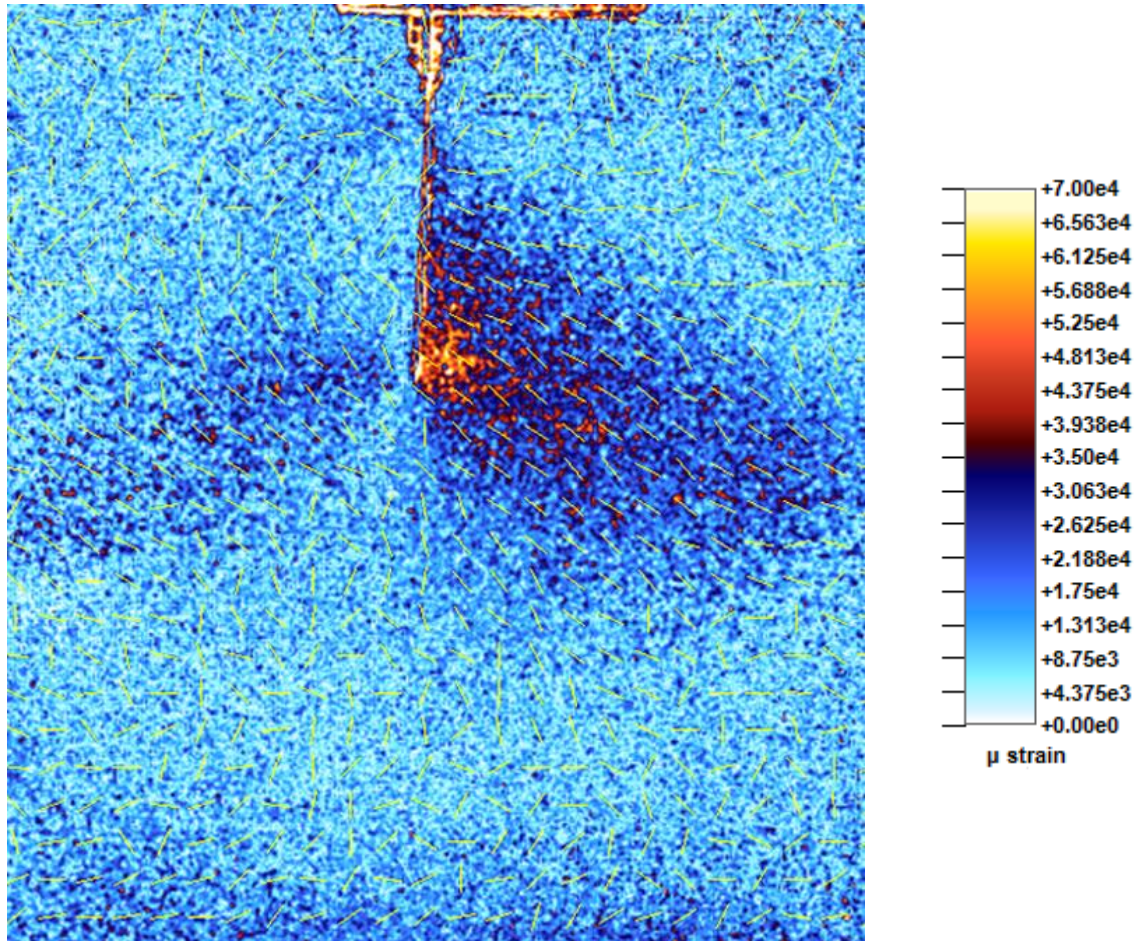


Figure 4-32: Principal strain map of Agani needle gauge 23 insertion at 150 mm/min

The needles in Figure 4-28 and Figure 4-30 were both loaded at a slight angle, which caused inaccuracy within the results. Consequently, significant care was taken to ensure this needle was secured vertically at the start of the test. However, in Figure 4-32 it can be seen that the needle is still at a slight angle from the vertical. The change in direction in this experiment is from the needle bending. With reference to Table 4-1 it can be seen that the flexural stiffness of this needle is significantly lower than the previously presented needles. As a result of this the gauge 23 needle has a lower resistance to bending, which is observed with the visible bending in Figure 4-32.

Agani needle: gauge 25

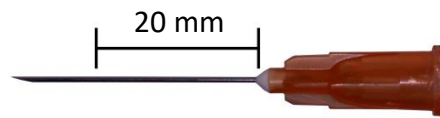


Figure 4-33: Agani needle; gauge 25

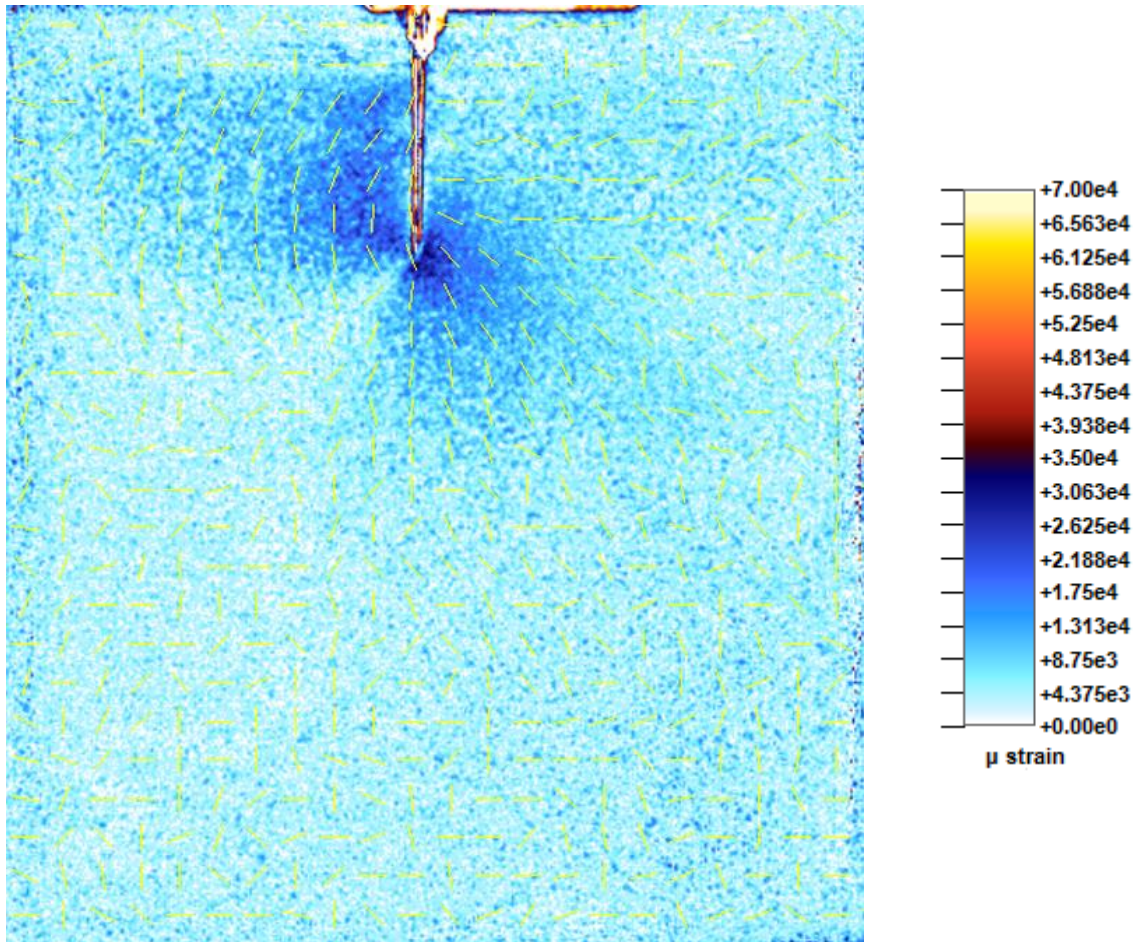


Figure 4-34: Principal strain map of Agani needle gauge 25 insertion at 150 mm/min

The difference in flexural stiffness between the gauge 25 and gauge 23 Agani needles is minimal. However, no significant bending is observed in Figure 4-34 compared to Figure 4-32. It is assumed that the insertion depth also plays a factor in the deflection, where needles inserted to greater depths will experience greater bending. In section 4.2.6 it was shown that the deflection decreased with greater needle insertion, however, that was a stiffer needle which did not show signs of bending. Thinner, flexible needles may experience greater bending loads if inserted further, and subsequently deflect further.

BD eclipse needle: gauge 21

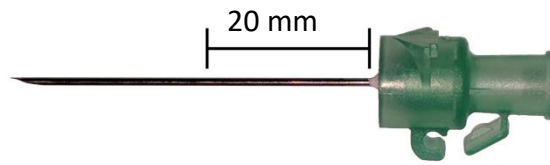


Figure 4-35: BD eclipse needle; gauge 21

The BD eclipse needles are another type of drug delivery needle. The needles have the same tip types as their Agani counterparts, and the dimensions are the same through the different gauges. The only change in the geometry between the BD eclipse needles and the Agani needle shafts is a slight difference in the needle lengths.

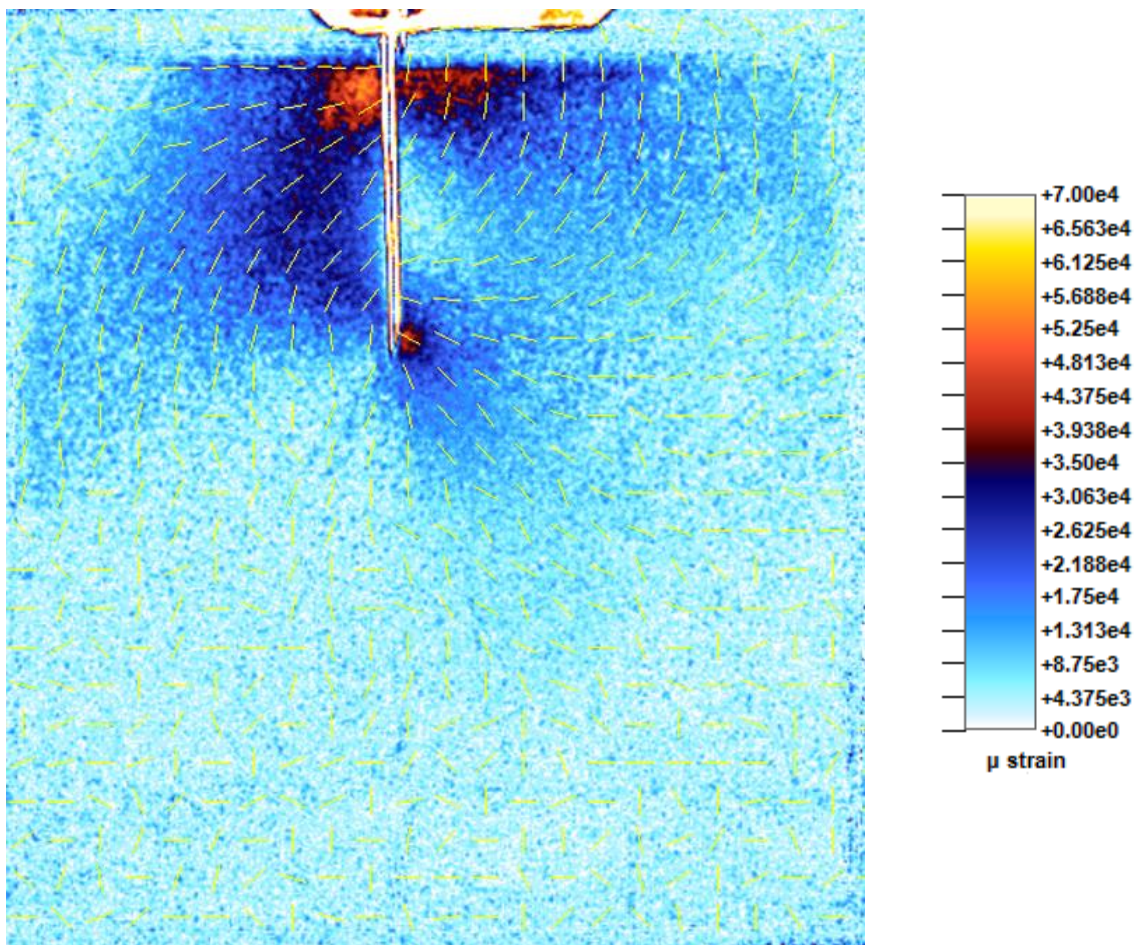


Figure 4-36: Principal strain map of BD eclipse gauge 21 insertion at 150 mm/min

Once again the typical areas of max strain magnitude are located at the needle tip at the side of the bevel angle, and around the puncture location.

BD Eclipse needle: gauge 25

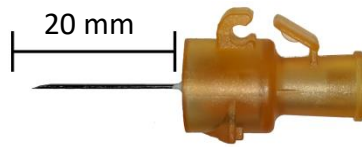


Figure 4-37: BD Eclipse needle; gauge 25

The needle in Figure 4-37 is only 16 mm long, and could therefore not be inserted far into the surrogate material. The reduced length and the high gauge resulted in an unclear result from the GFP2500 poleidoscope. It appears that this needle is too small for the resolution capabilities of the poleidoscope, as the principal strain map in Figure 4-38 is largely unreadable.

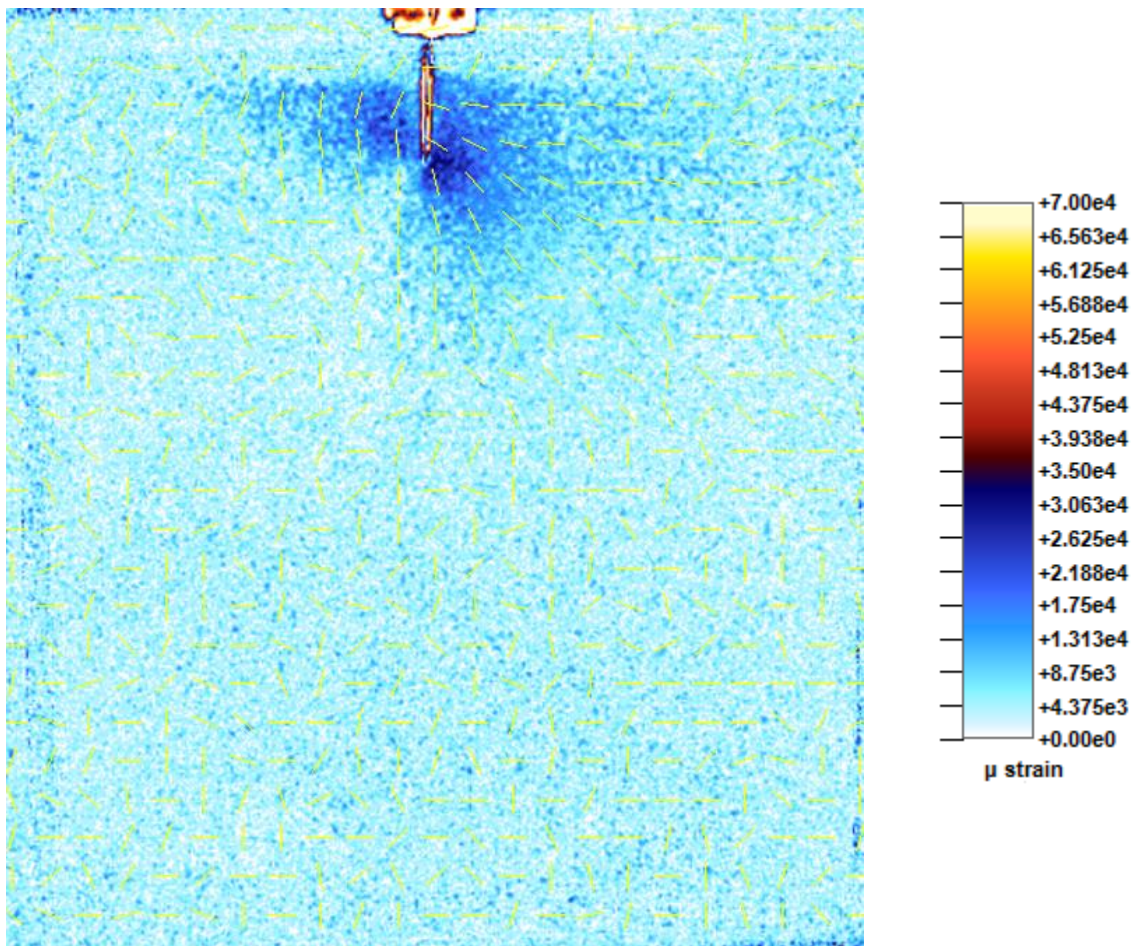


Figure 4-38: Principal strain map of BD eclipse gauge 25 insertion at 150 mm/min

However, even if the resolution is limited the characteristic areas of maximum strain still appear to be in the usual location at needle tip at the side of the bevel angle.

Discussion of GFP2500 poleidoscope results

The results in Figure 4-24 through Figure 4-38 show that there is a consistent pattern for the locations of maximum strain magnitude during a needle insertion, irrespective of gauge size. It is relevant to note that all the needles tested had either a bevel tip, or a back bevel tip. Many studies suggest that the tip shape is the main contributor to needle puncture force and deflection [11, 14-17, 95], so it is therefore unsurprising that needles of the same tip shape responded with analogous results. It may be revealing to assess the strain fields during needle insertion of other tip shapes in order to further understand the cause for needle deflection.

Loading errors

This study was interested in assessing the changes in the strain field around the needle tip during a normal insertion, as such all needles needed to be loaded vertically into the grips. The GFP2500 poleidoscope results in Figure 4-28 and Figure 4-30 revealed that the needle was incorrectly loaded into the grips, where the needle had a slight angle to the vertical. This led to the results showing a higher strain distribution on one side than the typical strain pattern observed. Figure 4-39 shows the difference between optical results when the Agani needle (gauge 23) was inserted at a slight angle, and when it was inserted vertically.

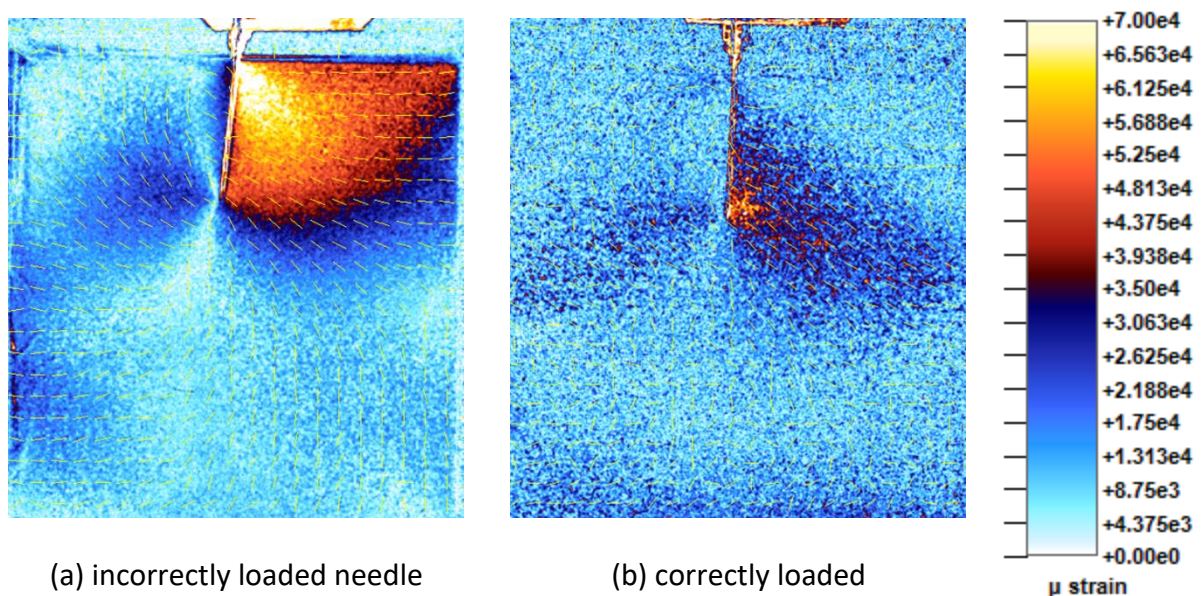


Figure 4-39: Comparative principal strain maps of Agani needle gauge 23 insertions at 150 mm/min a) needle loaded at a slight angle, b) correctly loaded needle

Both images in Figure 4-39 have been adjusted to use the same scale. It can be seen that the strain magnitude for the incorrectly loaded needle is significantly higher. However, this does

show how the strain field would change during a needle insertion if the needle was inserted at a slight angle instead. The insertion angle in Figure 4-39 a) was 2° off the vertical; which is within the bounds of human error. The difference in the strain magnitudes in Figure 4-39 show how such a small degree of error could lead to greater bending forces along the length of the needle, and lead to greater overall deflection.

Resolution limitations

With analysis the optical principal strain map images presented in Figure 4-24 through Figure 4-38 it can be seen that the detail in the images decreases as the needle size decreases. The average maximum retardation due to the biopsy needle insertion was 35 nm, which corresponds to 0.06 of a fringe order. The average maximum retardation due to the smallest BD eclipse gauge 25 needle was only 6 nm, corresponding to 0.01 of a fringe. The GFP2500 poleidoscope works best between a fringe order of 0.25 and 0.5 [92]. It would therefore be recommended that the konjac jelly mixture is modified to increase the strain optic coefficient. This would cause for greater retardation magnitudes at the same loads, and would likely produce images with greater detail.

The strain optic coefficient could be enhanced by adding glycerol or sugar. Tomlinson and Taylor showed that glycerol could increase the optic coefficient of gelatine [4]. In section 2.4.4, it was observed that sugar addition also increased the number of fringes displayed per load; thus increasing the optical sensitivity. In section 2.4.4, it was also shown that sugar addition modified the mechanical response of the material for carrageenan. In order to enhance the optic coefficient further material tests will also be required to re-produce a gel with optimal mechanical and optical properties.

It is also noted that the resolution of the camera is 256 x 256. This is sufficient for larger scale analysis but did not provide enough detail for the smaller images, as shown in Figure 4-38. A potential solution to this was to use a camera with a higher resolution instead of the standard GFP2500 camera. This will be discussed further in section 6.1.2.

4.3.2 Puncture force results for range of needle gauges

The puncture force is the force required for the needle to form a crack initiation and breach the surrogate boundary. It is identified as the force peak after a gradual force increase caused

by the needle pushing against the tissue boundary. The puncture force peak is immediately followed by a sudden drop in force response, which signals where the needle has breached the tissue boundary. The puncture forces for the various needles were recorded and are plotted in Figure 4-40.

A total of 23 punctures were identified: ten for the biopsy needle, and three for each of the remaining needles. Puncture forces for the BD Eclipse needles could not be identified as the force reading was so low.

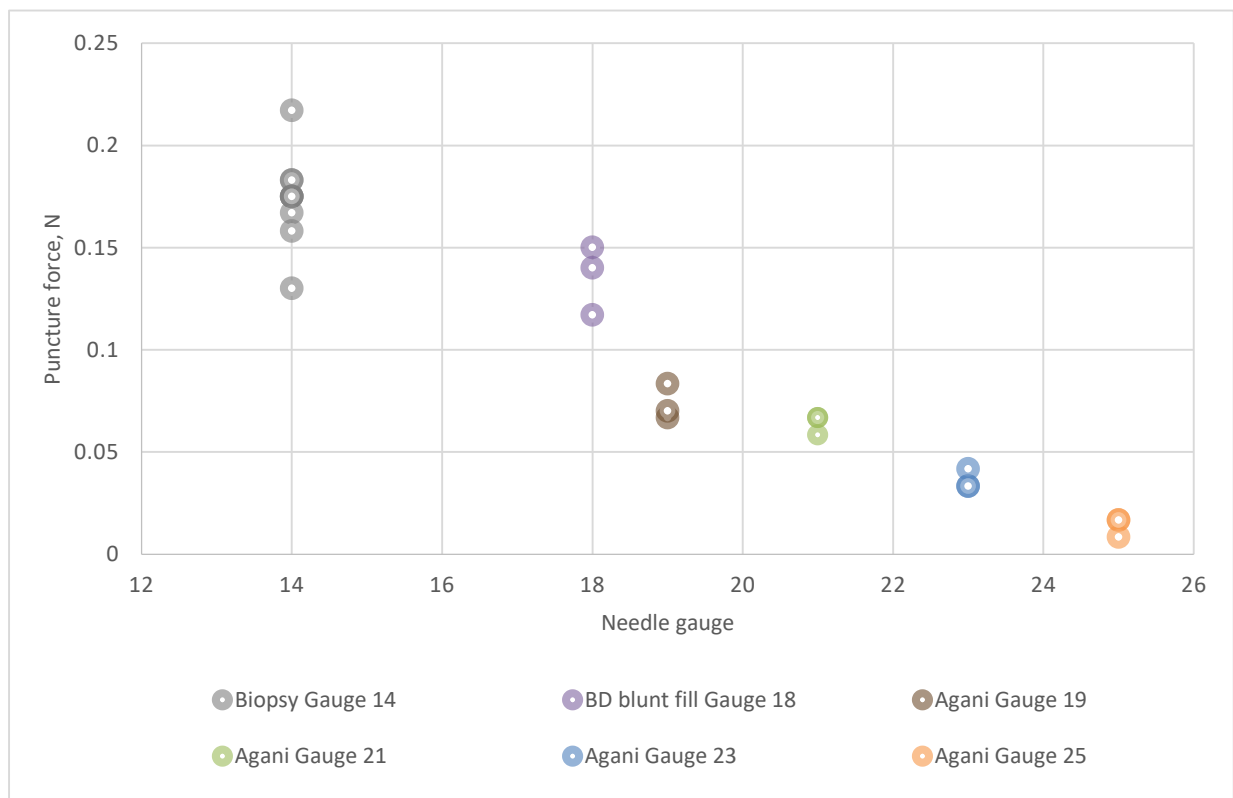


Figure 4-40: Relationship between needle gauges and puncture force

Figure 4-40 shows the relationship between the needle gauge, or size, and the puncture force. Understandably, as the needle size decreases the puncture force decreases. This reflects results presented by Okamura *et al.*, who also showed that increasing needle size caused an increase in force response [11].

4.3.3 Deflection results for range of needle gauges

The deflection angles were measured using the method described in section 4.1.3. One plane image of the needle and tank was captured from the GFP2500 poleidoscope footage at the end of the experiment when the needle was fully removed. Within this image the track of the needle insertion was visible, and the deflection angle could be determined from the insertion point to the end of the needle track. The deflection results for the varying needle types are shown in Figure 4-41.

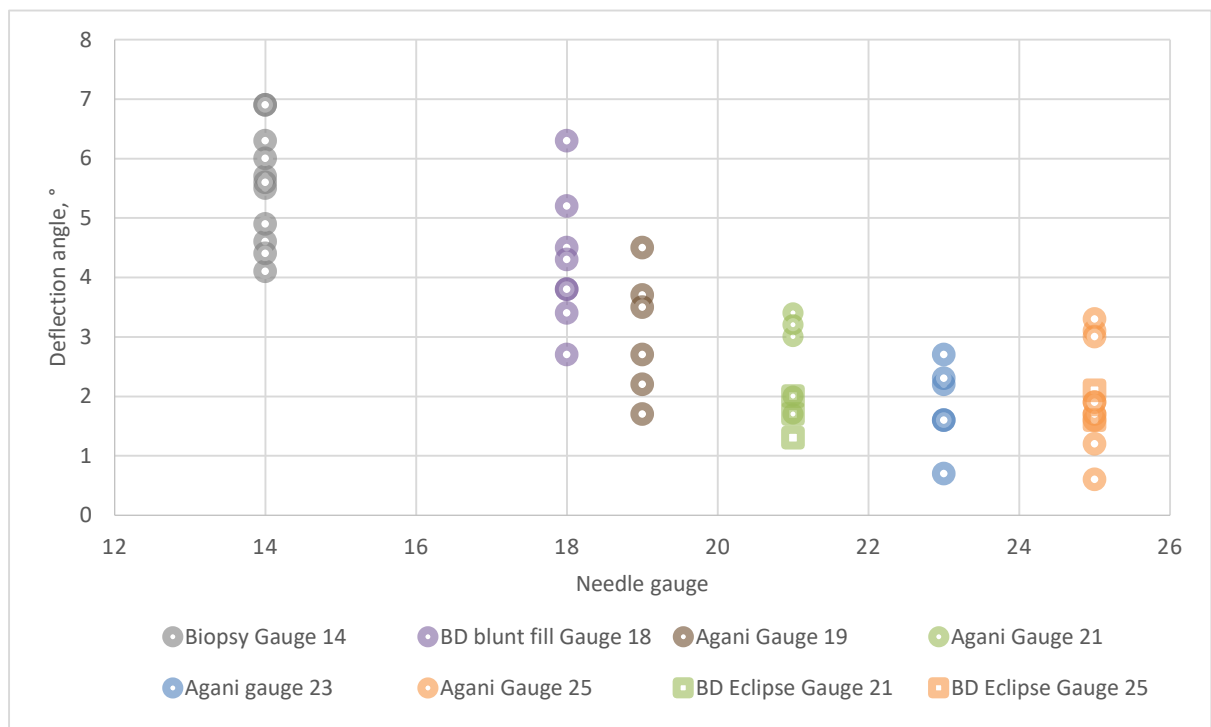


Figure 4-41: Relationship between needle gauge and deflection angle

It was previously assumed that the thinner needles would deflect more than their thicker counterparts, yet the results in Figure 4-41 demonstrate the opposite effect [18]. This contradicts the anecdotal evidence presented in the literature, and results presented by Okamura *et al.* [11]. However, as discussed in section 4.2.8, the values recorded here are mostly due to the material deflecting, not the needle. The needles were held rigidly within the grips and their movement was constrained, whereas the material had some room to move within the tanks. It is possible that the lower gauge needles are causing the surrogate to move more as they are able to exert a higher force on the surrogate. This deformation is then recorded as needle deflection when it is actually tissue movement.

It was previously assumed that the needles with greater lengths would deflect more, as they have a lower flexural stiffness. However, the opposite was presented in section 4.2.6, where biopsy needles inserted at increasing depths resulted in decreased deflection angles. A similar finding is presented in Figure 4-41 with the two types of gauge 21 needle; the Agani needle had a length of 38 mm and the BD Eclipse with a length of 40 mm. There appears to be no trend for the two types of gauge 25 needle, where the Agani needle had a length of 25 mm and the BD Eclipse with a length of 16 mm.

However, the accuracy of the measurement technique is also unknown. The smaller needles could not be inserted a large amount, and as such, their visible needle track was small. This highlights another scenario where an apparatus with a higher resolution camera would be useful.

Furthermore, as stated previously, the deflection measured here is actually the tissue motion rather than needle deflection. As needles are inserted further the material may shift and 'settle' into the new position, causing the deflection reading to be lower. Different results may be presented if the konjac jelly was secured and the needle was secured in grips which allowed some degree of freedom.

4.3.4 Conclusion

GFP2500 poleidoscope data

The results from the GFP2500 poleidoscope showed consistent locations of strain magnitude irrespective of the geometric parameters of the needle. The principal strain maps revealed similar directional patterns as well, where all visible directional data showed a bending moment as highlighted in section 4.2.7 in Figure 4-22.

As the needle size decreased the quality of the poleidoscope images declined. The poleidoscope camera does not have a high enough resolution to capture precise retardation data from the small needle insertions. This issue could be solved with the suggested development of a higher resolution poleidoscope camera. This would allow for more detailed images around the locations of interest during the needle insertion, such as the shape of the strain distribution during a needle puncture. The development and advantages of a new poleidoscope are discussed in section 6.1.2.

It was also discussed that the surrogate could be modified to amplify its optic coefficient, such that it produces more fringes per unit load. This could be done by adding sugar or glycerol to the mixture [4]. These additions do alter the mechanical properties of the surrogate, and therefore if this suggestion is followed then further mechanical tests are required for the improved surrogate.

Needle deflection discussion

Deflection results showed that higher gauge needles, which have a thinner needle shaft and lower flexural stiffness, produced lower deflection angles than their thicker counterparts. This result conflicts with results in the literature. However, this result could be due to the observation that the measurement taken is actually the material motion and not the needle motion. The needles with a lower flexural stiffness are unable to move the material as much as their thicker, stiffer, counterparts.

Nevertheless, the GFP2500 poleidoscope images did reveal that some of the thinnest needles did begin to bend. There must be a threshold to which deflects first depending on the relative flexural stiffness.

4.4 Inhomogeneous laminate surrogate: Biopsy insertion at same speed

In the previous sections, the various needles were inserted into a homogenous skin tissue surrogate to see the effects of changing needle shape and insertion speed on the strain field around the needle tip, and the trajectory of the needle. Within the literature review it was discussed that skin tissue is not a homogenous material, but a complex fibre matrix with three distinct but variable layers; the epidermis, dermis, and hypodermis. Studies showed that asymmetrical needles are more susceptible to changes in the material as they experience greater bending loads than their symmetrical counterparts. This was found during studies where the surrogate material was mostly homogenous. It was assumed that this effect would only increase when tested on inhomogeneous materials [11, 15, 95]. It was therefore decided to create simple, inhomogeneous gel surrogates. Needles were inserted into the inhomogeneous samples at a constant speed, and results will be compared to the experiments from homogenous samples.

4.4.1 Surrogate structure

Gel surrogates were created which had three distinct layers, to mirror the layers found in skin tissue. In section 1.2.3, mechanical properties of the three layers in skin tissue were presented, and this data has been repeated in Table 4-3 for ease of reference.

	Elastic modulus, MPa	Thickness, mm	References
Epidermis	265.2 (1.5 – 1,000)	0.256 (0.032 – 1.5)	[37-39, 66-68]
Dermis	0.02 (0.008 – 0.035)	1.68 (0.95 – 4)	[37, 43, 60, 62, 66, 67]
Hypodermis	0.0034 (0.00002 – 0.0082)	3.95 (0.8 – 7.1)	[37, 38, 46, 60]

Table 4-3: Copy of summary of average values for thickness and separate elastic moduli of human skin tissue

The results in Table 4-3 show that there is a large range for the elastic modulus of the different skin layers. In section 2.3.4 the ratio of konjac powder to water was modified to produce a gel which represented the overall stiffness of skin tissue. However, the possibility of modifying the concentration to mimic different mechanical properties is limited. When too little gel powder was added the gel would not solidify, and when too much powder was added the result was an intractable gel.

Therefore, numerous gel batches were made to assess the limits of the concentration which produces a usable gel. It was found that a gel of 1% konjac powder to water ratio was the lower limit, and 2.5% konjac powder to water ratio was the upper limit. Table 4-4 contains the results for the elastic modulus for the various concentrations in compression.

Concentration, %	Elastic modulus, kPa
2.5	145.4 ± 8.9
1.5	80.7 ± 4.0
1.0	60.3 ± 3.0

Table 4-4: Elastic modulus of konjac gel at the various concentrations

Comparing the results for elastic modulus between Table 4-4 and Table 4-3 shows that there is a significant difference between the surrogate and real properties. However, comparisons between the needle insertions through the layered surrogate and homogenous surrogate will still show if inhomogeneity has an effect on the response.

The results in Table 4-3 also contain the average thickness of the individual layers. It was impractical to create such thin layers for this experiment, and therefore the thicknesses for each layer was chosen and shown in Table 4-5.

Concentration, %	Elastic Modulus, kPa	Thickness, mm
2.5	145.4 ± 8.9	20
1.5	80.7 ± 4.0	40
1.0	60.3 ± 3.0	40

Table 4-5: Elastic modulus of konjac gel at the various concentrations

A photograph of the layered gel surrogate with a biopsy needle inserted is shown in Figure 4-42. The boundaries between the layers were visible with the human eye, but for presentation purposes they were marked using blue markers.

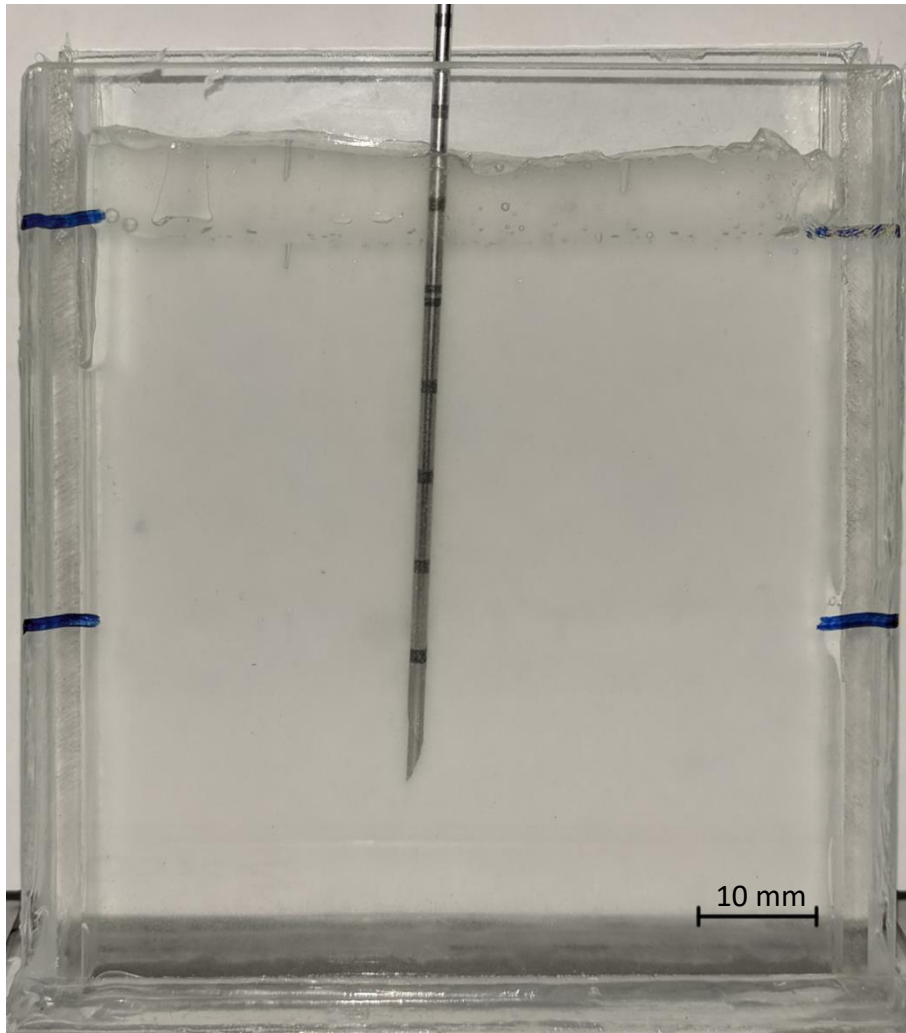


Figure 4-42 Example of tank containing layers of konjac at different concentrations

In Figure 4-42 it can be seen that the top surface, which was constructed with the stiffer gel, is uneven. At a concentration of 2.5% the gel was very difficult to work with and it solidified within minutes after being removed from heat.

4.4.2 Overall force response during needle insertion and removal

Figure 4-43 shows the complete force response when a 14-gauge biopsy needle was inserted and removed from the laminate konjac surrogate at 150 mm/min. The figure contains results from two separate needle insertions to show the consistency between the results. Further figures of the same experiment are displayed in the appendix in section 8.3.

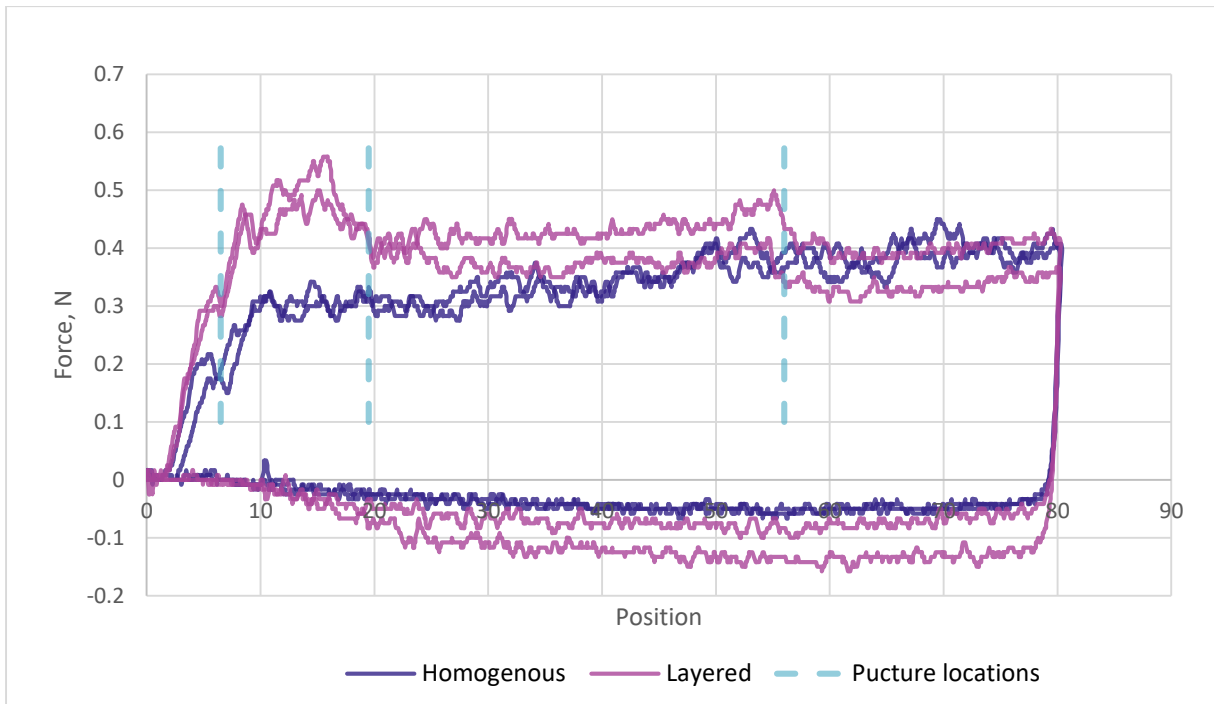


Figure 4-43: Force profile of needle insertion and removal at 150 mm/min through layered sample

In section 4.2.1 the identification of the puncture location was described and highlighted for the needle insertions at various speeds. In Figure 4-43 three distinct puncture locations are indicated with the dotted lines; these are related to the three different layers in the sample.

In the first stage the force response is greater as the needle is travelling through the stiffer gel. As the needle transitions from each section there is a puncture peak followed by a decrease in force response. The observation of a puncture peak through material transitions reflects results in the literature during a needle insertion through biological tissue *ex vivo* and *in vivo* [9, 136, 137].

4.4.3 Deflection angle through different surrogate types

The deflection angles were measured using the method described in section 4.1.3. One plane image of the needle and tank was captured from the GFP2500 poleidoscope footage at the end of the experiment when the needle was fully removed. Within this image the track of the needle insertion was visible, and the deflection angle could be determined from the insertion point to the end of the needle track. The results for the deflection amount through the homogenous surrogate and the layered surrogate are presented in Figure 4-44.

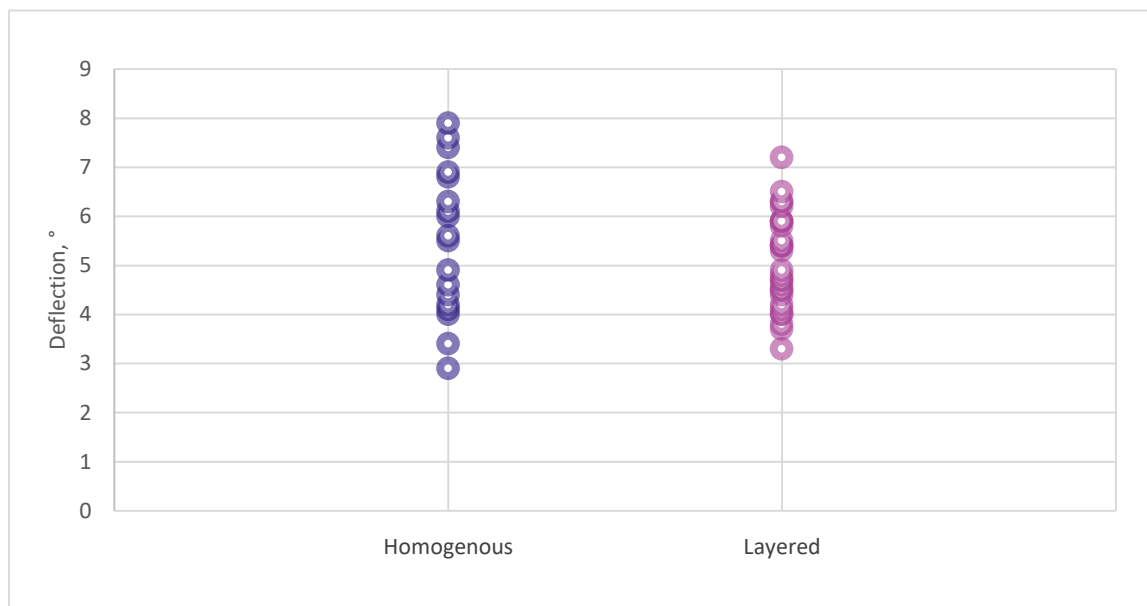


Figure 4-44: Relationship between surrogate type and deflection angle at 150 mm/min

Figure 4-44 shows the recorded deflection angles for the homogenous surrogate sample and the layered sample. The average deflection through the homogenous surrogate was 5.47°, and 5.07° for the layered surrogate. An ANOVA single factor analysis was conducted which produced a P value of 0.27; a P value over 0.05 indicates that the difference between the two sets of results is not statistically significant. There is greater variance in the results for the homogenous needle insertions. However, this could be because the homogenous results were taken over a number of tests, whereas the layered results came from just three batches of surrogate preparation. The results in Figure 4-44 show that the needle deflection is not affected by material inhomogeneity. This aligns with work in the literature which assume and predict that the needle deflection is largely due to the shape and sharpness of the needle, rather than the tissue's structure [14, 107].

4.4.4 Optical analysis of the layered samples

Optical data for the needle insertions through the layered surrogate was gathered and processed using the experimental method described in section 4.1.4. The images in Figure 4-45 show the strain development through the different layers. It is important to note that the images in Figure 4-45 have been processed but the optic coefficient has not been applied, so the values are displayed in terms of retardation. This is because different concentrations of gel have been used, and the different concentrations will have different optic coefficients.

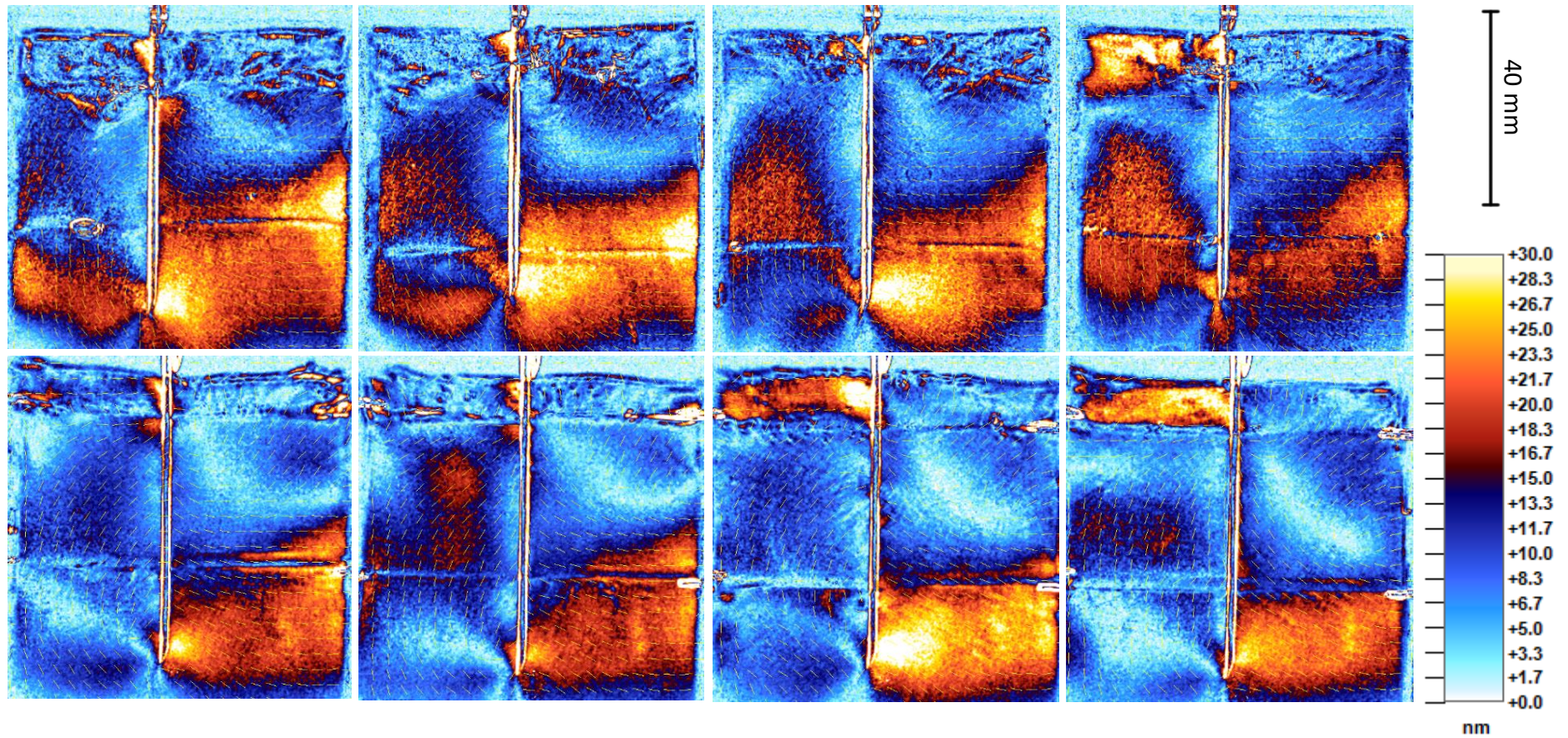


Figure 4-45: Principal strain maps of biopsy needle insertion into laminate surrogates at 150 mm/min

The images in Figure 4-45 all show a biopsy needle at max insertion for eight individual insertions. The method for processing the GFP2500 poleidoscope images, as presented in section 4.1.4, has been applied; thus the retardation is solely due to the needle insertion. It can be seen that the characteristic locations of maximum retardation are located in the same places in both layered and homogenous surrogates.

4.4.5 Conclusion

Structure of konjac surrogate

Within this section it has been shown that it is possible to build a layered skin tissue surrogate out of konjac gel. However, as discussed in section 4.4.1, the mechanical properties of the three layers in the gel surrogate do not match the mechanical properties of the layers in human skin tissue.

It is possible that a stiffer puncture surface, as found in human skin tissue, may influence the needle deflection. Significant reaction forces were recorded at the surface of the surrogate tissue during all needle insertions, as shown in Figure 4-45. However, the mechanical properties of the gel surrogate cannot be altered further by increasing or decreasing the concentration of gel powder to water; the concentrations are already at the limitations for creating a workable, solid, gel surrogate. Other gels could be used to simulate the epidermis, but they do not exhibit the resistance to crack growth that konjac has been shown to have. Therefore, additives could be used to increase the stiffness of the gel, or the gel's manufacturing process could be revisited to assess a way to make solid gel at concentrations lower than 1% gel powder to water ratio, and higher than 2.5% gel to water ratio.

Needle deflection discussion

The results for the deflection angles do not show any significant change when the needle is inserted through the homogenous or the layered surrogate. This aligns with work by Kataoka *et al.* and Alterovitz *et al.*, who discussed that the needle deflection is generally due to the bevel tip and diameter of the needle, and not influenced greatly by material inhomogeneity [16, 17]. However, as discussed within this chapter, it has been noted that the surrogate material moved during the needle insertion. It is possible that if the material was constrained from moving and the needle was allowed some degree of freedom the results may be different between the different types of surrogate.

GFP2500 poleidoscope data

The optical images illustrated that the locations of maximum strain magnitude are in the same locations within the layered tissue surrogate as in the homogenous tissue surrogate. The data could not be processed as the optical coefficient for the two of the three layers had not been identified. Furthermore, the software does not permit the option for using more than one value for optic coefficient. This could be circumvented by applying the three different optic coefficients and isolating each of the layers in a separate image.

4.5 Inhomogeneous particulate surrogate: Biopsy insertion at same speed

In 1.4.6 it was discussed that beads could be added to a homogenous surrogate to mimic a biopsy target. The strain field ahead of the needle could be analysed as it approaches the biopsy target to assess how material inconsistencies could affect the needle trajectory. Clear, tinted beads were added to the konjac gel of 1.5% concentration gel powder to water. The beads were added when the molten gel had cooled slightly, but while it was still liquid, to avoid them all sinking to the bottom. Figure 4-46 contains a photograph of a tank of gel with the beads suspended.

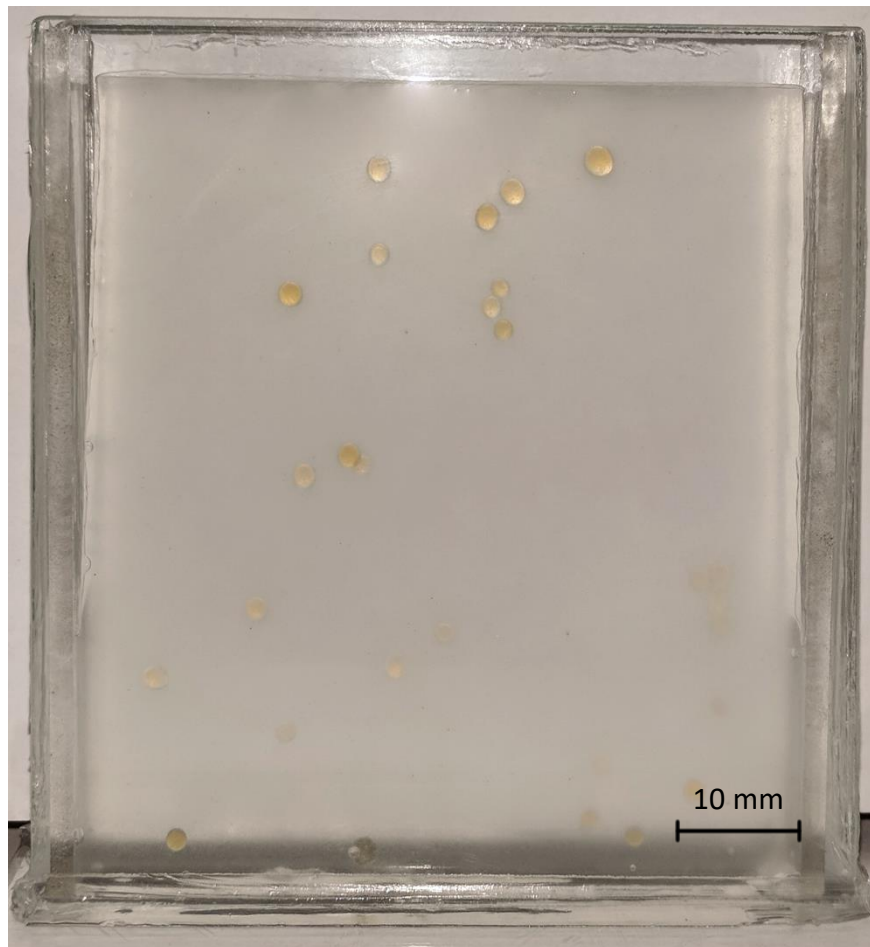


Figure 4-46 Example of tank containing konjac jelly with beads suspended

A large number of beads were added to each tank as it made it easier to locate a path for the needle insertion where it would interact with the beads. However, the beads also distributed within the thickness of the tank, and many tended to drift towards the glass edges.

4.5.1 Overall force response during needle insertion and removal

Figure 4-47 shows the complete force response when a 14-gauge biopsy needle was inserted and removed from the particulate konjac surrogate at 150 mm/min. The figure contains results from two separate needle insertions to show the consistency between the results. Further figures of the same experiment are displayed in the appendix in 8.3.

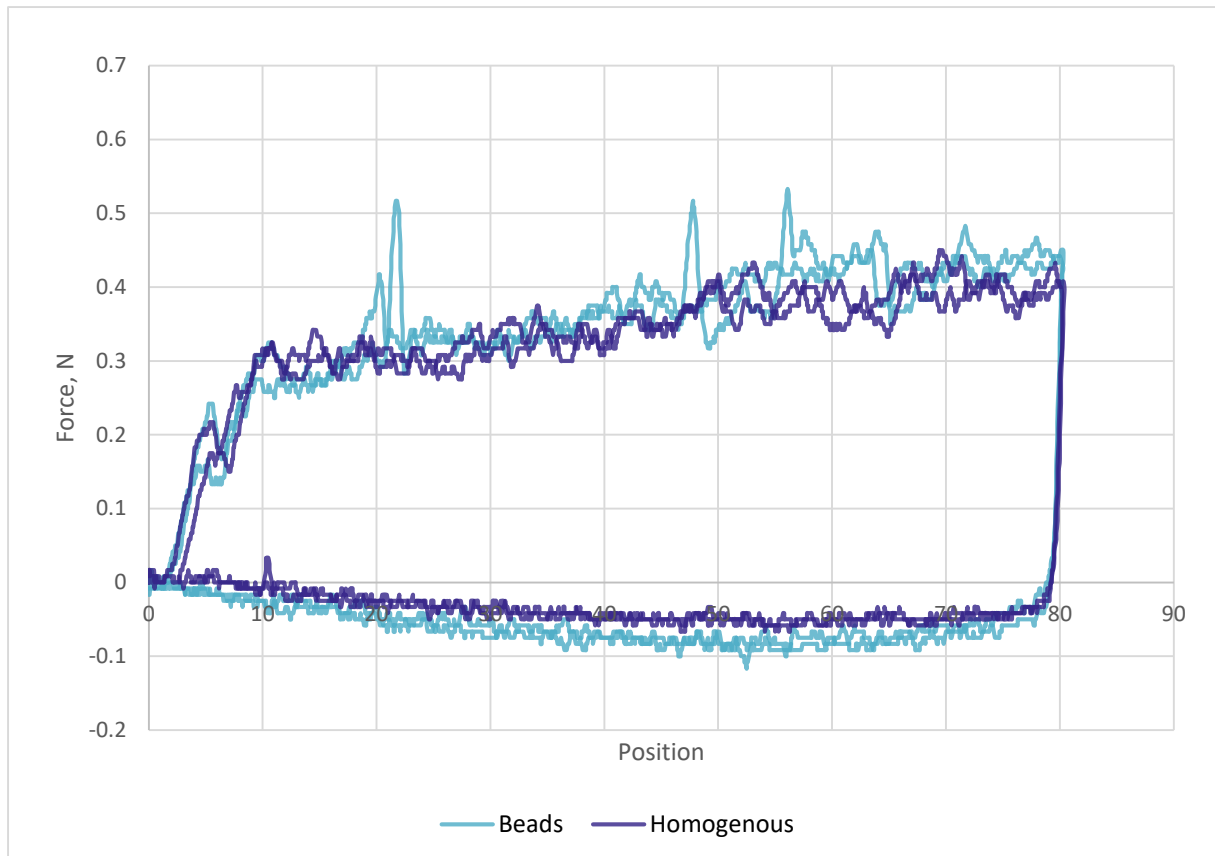


Figure 4-47: Force profile of needle insertion and removal at 150 mm/min through particulate sample

The points where the needle interacts with the beads is visible from the steep force peaks. When these peaks are ignored, the response is comparable to the force response through the homogenous surrogate.

4.5.2 Deflection angle through different surrogate types

The deflection angles were measured using the method described in section 4.1.3. One plane image of the needle and tank was captured from the GFP2500 poleidoscope footage at the end of the experiment when the needle was fully removed. Within this image the track of the needle insertion was visible, and the deflection angle could be determined from the insertion point to the end of the needle track. The results for the deflection amount through the different surrogate types are presented in Figure 4-48.



Figure 4-48: Relationship between surrogate type and deflection angle at 150 mm/min

There appears to be no significant change for the deflection amount between the homogenous surrogate and the inhomogeneous surrogates. An ANOVA single factor analysis was conducted which produced a P value of 0.38; which indicates that the difference between the three sets of results is not statistically significant. The average deflection angles for the three surrogates are presented in Table 4-6.

Surrogate	Average deflection, °
Homogenous	5.48 ± 0.35
Laminate	5.07 ± 0.18
Particulate	4.98 ± 0.24

Table 4-6: Deflection amount for the different surrogates

4.5.3 Optical analysis of the particulate surrogate

Optical data for the needle insertions through the particulate surrogate was gathered and processed using the experimental method described in section 4.1.4. The images in Figure 4-49 show the principal strain maps where the biopsy was at max insertion through the particulate surrogate. It can be seen that the characteristic areas of maximum strain are in the same places as the needle insertions through the other surrogates.

Figure 4-49 shows that the beads have caused some areas of increased localised strain, and do appear to affect the overall strain distribution. In section 4.3 it was shown that the thinner needles experienced bending when inserted into the homogenous konjac surrogate. It would be interesting to insert the higher gauge, more flexible needles into this surrogate to assess whether the beads affect the needle insertion.

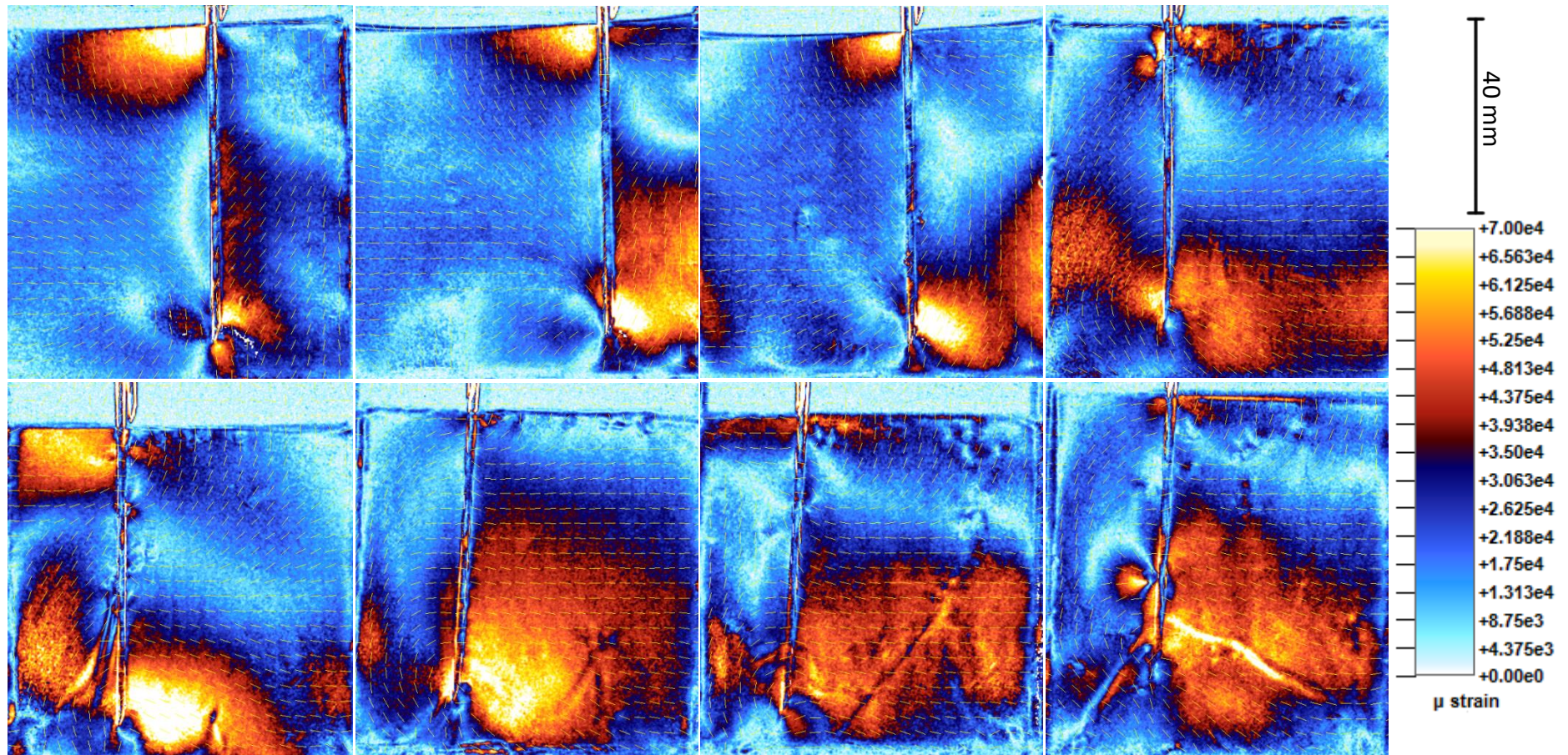


Figure 4-49: Principal strain maps of biopsy needle insertion through inhomogeneous sample with biopsy beads at 150 mm/min

Sequential analysis

The images in Figure 4-51 show the progression of the needle insertion in the light view, and the principal strain map view. When the needle is not in contact with the bead, in Figure 4-51 (a), there is no strain concentration. As the needle contacts the bead, in Figure 4-51 (b), the instantaneous development of increased strain is observed. As the needle travels further into the material it continues to interact with the bead causing a concentration of maximum strain around the bead.

Figure 4-50 shows an enlarged version of the final image in Figure 4-51. It can be seen that the needle interacting with the bead has caused a change in the typical directional pattern observed in previous needle insertion experiments.

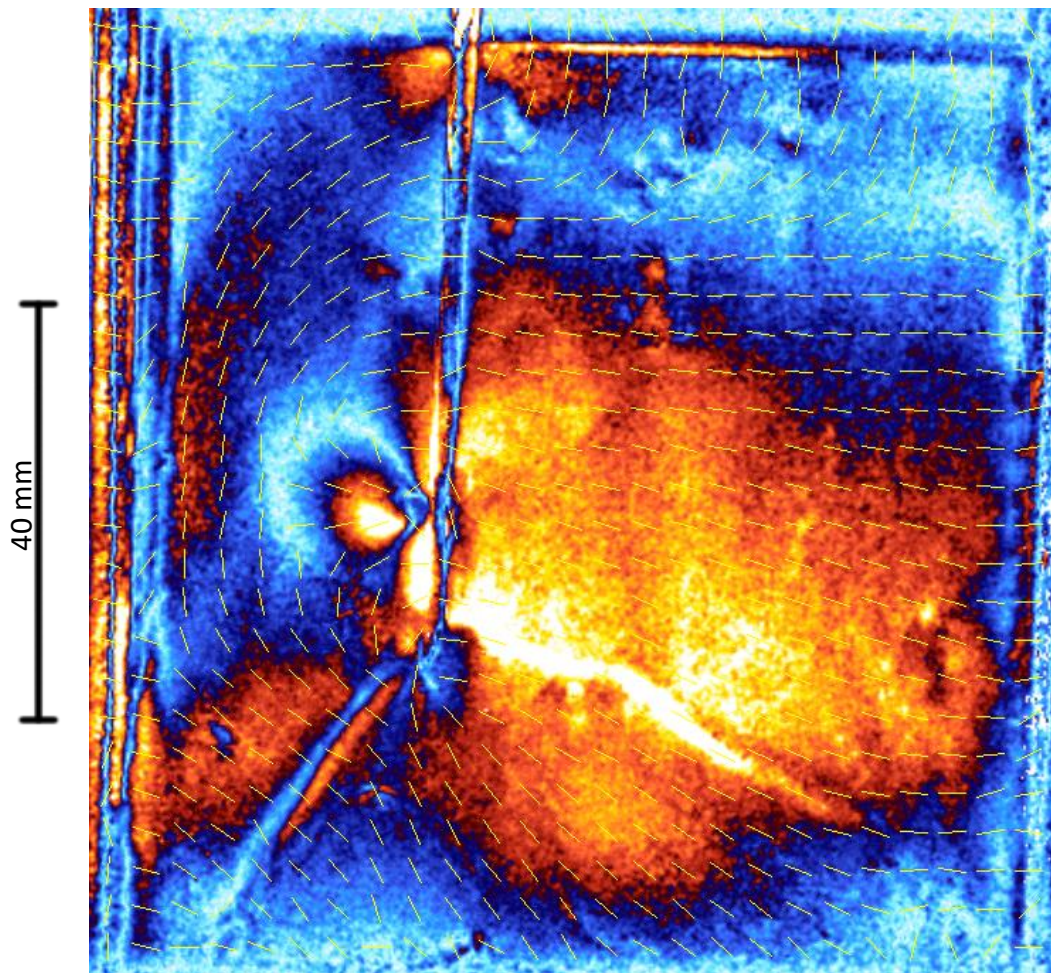


Figure 4-50: Principal strain map of biopsy needle insertion through particulate inhomogeneous surrogate

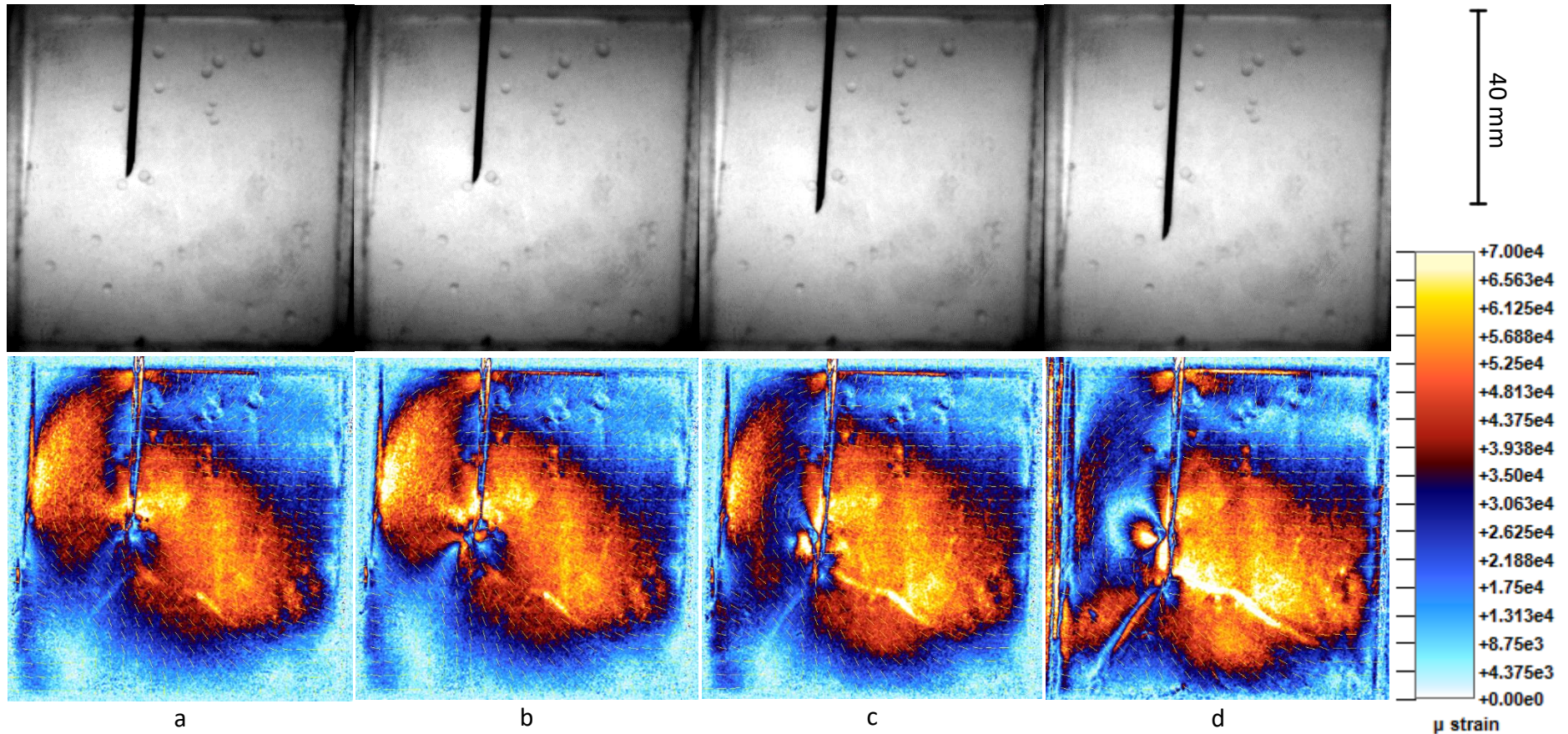


Figure 4-51: Progression of light maps and principal strain maps of biopsy needle insertion through inhomogeneous sample with biopsy beads

The images in Figure 4-51 show the progression of the strain map during a single needle insertion as the biopsy needle is inserted further and interacts with one of the beads. The top row of images show the light view, and the bottom row of image show the corresponding principal strain map.

4.5.4 Conclusion

Structure of konjac surrogate

A number of studies have already included beads within their tissue surrogate, either to act as tracking markers or obstacles to avoid during the needle insertion [26, 99, 102, 138]. The addition of beads for material tracking purposes was not required as the GFP2500 poleidoscope already shows the direction of material motion. The beads were added to show how material inclusions of different properties to the surrounding tissue affect the principal strain field during a needle insertion. The ability to add beads to this surrogate also shows possible development of more complex surrogates for future experiments.

Needle deflection discussion

As with the layered surrogate, the results for deflection angles do not show any significant change between needle insertions through the beaded samples compared to needle insertions through the homogenous surrogates. This still holds true for the insertions where the needle interacted with one or more of the hard beads.

GFP2500 poleidoscope data

Once again, the optical images illustrated that the locations of maximum strain magnitude are in the same locations within the beaded tissue surrogate as in the homogenous and layered tissue surrogates.

It was also shown that the stiff beads affected the overall direction of the tissue motion when interacting with the needle. The beads also caused areas of increased strain magnitude when in contact with the needle. However, unless the needle contacted the hard beads, they had little to no effect on the overall magnitude and direction of the principal strain.

4.6 Conclusion

Suitability of konjac as a skin tissue surrogate

Within this chapter it was found that konjac jelly replicates the force response for needle insertions into soft tissue better than conventional surrogates. Konjac jelly replicated the same force response development at varying insertion speeds as soft tissues tested *ex vivo* for both puncture force, and overall needle insertion force.

Inhomogeneous surrogates were also constructed out of konjac jelly: laminate surrogates and particulate surrogates. While no significant results were found using these inhomogeneous surrogates, they do highlight the possibility of creating more complex skin tissue surrogates out of konjac jelly for future work.

Experimental considerations

During a needle insertion the needle experiences bending, which leads to deflection. The insertion material also moves during the needle insertion, which increases the deflection magnitude. It is difficult to quantify both material movement and needle bending in the same test, and most existing experimental setups have both needle and material securely gripped so any deflection is solely due to needle bending [11, 14, 16, 17, 95].

The experiments presented in this chapter involved a securely gripped needle, and a surrogate with some degree of freedom. It was found that the surrogate moved significantly before the needle began to bend, and only needles with high gauge (small diameters) showed signs of bending.

It would be beneficial to conduct further experiments where the material is constrained and the needle is relatively unconstrained; e.g. held in a ball and socket type grip. This would show how the needle tip type and gauge dictates the deflection. Combining this data with the data on the material motion from different tip types and gauge could reveal how both material motion and needle deflection affect the overall deflection.

Optical analysis

The optical analysis of the needle insertions revealed never-before-seen information about the force distribution during a needle insertion. Two locations of increased strain magnitude were identified during a needle insertion, one near the needle tip along the bevel side, and one on the opposite side near the puncture hole. The area of strain magnitude around the puncture hole has not been identified before this research.

The optical analysis also revealed full field directional information of the tissue surrogate during the needle insertion. Most research regarding needle insertion investigation focuses on the magnitude of the forces, and neglects the directions of those forces. The directional information revealed how the needle affects the surrogate as a whole, and bending patterns were visible as the needle was inserted.

5 DISCUSSION

5.1 Summary

This research aimed to develop a new soft tissue surrogate suitable for needle insertion investigation, and to use the surrogate in conjunction with photoelastic analysis to assess the causes for needle deflection through soft tissue.

An investigation into the current literature showed that existing skin tissue surrogates did not perform similarly to real skin tissue *in vivo* during needle insertions. This study focused on developing a surrogate for human skin tissue, as current surrogates did not accurately replicate the fracture mechanism when a needle is inserted.

A GFP2500 poleidoscope was used for the photoelastic analysis; it is a digital polariscope which allowed for the capture of instantaneous, dynamic, full field data using one piece of photoelastic apparatus [6].

A variety of needle insertion experiments were conducted to assess how changing the insertion speed and needle shape affected the overall deflection and principal strain field. Existing research in this area has focussed on discrete points of data; such as the force response at the needle tip or tracking the motion of individual tracking markers. The photoelastic analysis revealed never-before-seen full field directional and principal strain maps of the needle insertions.

5.2 Overall impact

Conventional gel surrogates fracture in a fundamentally different way to human skin tissue *in vivo* when punctured with a needle. Konjac glucomannan gel has been developed as a new surrogate which fractures in the same way as skin tissue. This surrogate and experimental techniques used within this research could be taken forward for numerous applications as follows.

5.2.1 Robotic surgery

The experimental setup described in section 4.1 which was used for the needle insertion research mimicked a robotic needle insertion, where the needle speed and direction was controlled by a machine rather than a human operator. Further research with similar experimental parameters could be used to develop and program robotic surgery methods.

Research into using robots for surgeries which require high level of precision has been developing through recent years [139-143]. Konjac could be used as a new surrogate for testing and refining the computer programs used to control a needle insertion. Konjac is an accurate tissue surrogate while remaining transparent, which would allow for easy analysis on the location of the needle with reference to the computer controller.

5.2.2 Training physicians

It was found that konjac replicates the needle response through real tissue *in vivo* better than existing surrogates. Therefore, konjac could be used to develop more realistic training models for new physicians.

5.2.3 Further needle development experimentations

Since konjac better replicates the needle response through soft tissue it should be used for further needle experimentations. A number of different experiments have been designed and discussed in section 6 which would be a good starting point for future work.

5.3 Behaviour of developed surrogate

It was found that conventional gel surrogates fracture in a fundamentally different way to human skin tissue *in vivo* when punctured with a needle. Within this research konjac gel was developed as a surrogate which fractures in the same way as skin tissue. The reasons for the similarities between konjac and skin tissue will be discussed in this sub-section.

Biological tissue is made up of a collection of cells. Each cell is independent, but bonded to adjacent cells to create a biological structure. The bonds between each cell are weaker than the cell wall. Thus, when skin is punctured with a needle, the bonds between the cells are broken, and not the cells themselves, and the cells move around the needle as it is inserted.

Polymer gels are made up of polymer chains, which form when the molten gel is solidifying. Different polymers have different lengths of polymer chains. An indicator for the length of the polymer chain is the time it takes to set from a molten gel to a solid gel, where longer chains take longer to form and solidify. Gelatine takes hours to set and become a solid gel, whereas konjac gel sets in minutes. This difference in setting time indicates that gelatine has longer polymer chains than konjac. Long polymer chains will fracture when punctured with a needle, rather than the chains moving around the needle. Since konjac chains are short the chains will move during a needle insertion, which better replicates what happens during a needle insertion into biological tissue.

5.3.1 Experimental comparison

One comparative method to test a materials' suitability as a skin tissue surrogate is to conduct a stress-strain test where the material is extended and returned to the original position. If the gel mimics the collagen rearrangements observed in skin tissue, there will be plastic deformation. This was shown in a study by Remache *et al.* who conducted cyclic tensile tests on porcine skin [49], the results of one cyclic test are shown in Figure 5-1. With each cycle the response of the skin varies, and plastic deformation is observed as the collagen in the skin is rearranged.

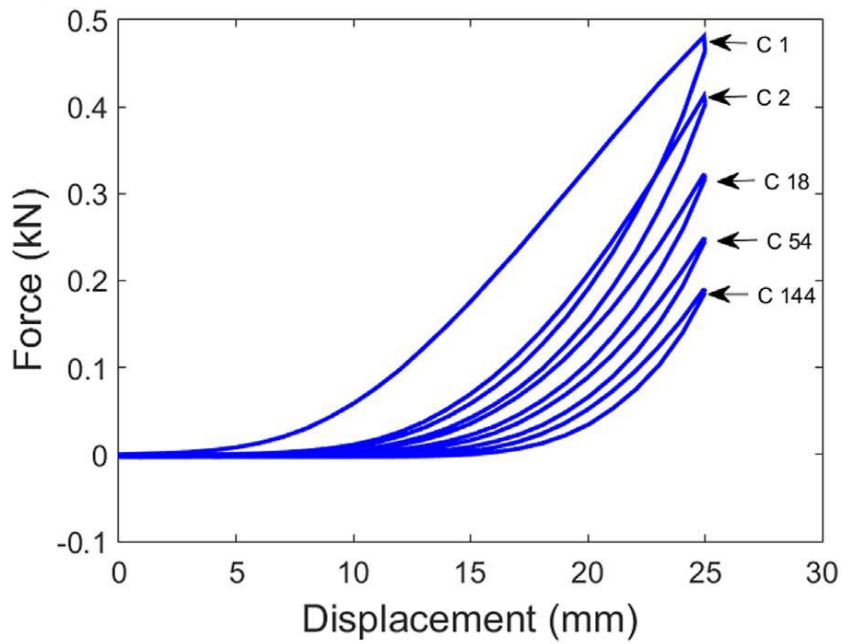


Figure 5-1 Hysteresis loops obtained from cyclic test performed on porcine skin at 1 mm/s [49]

In this thesis similar experiments were conducted on potential and existing tissue surrogates. Figure 5-2 shows the response of konjac jelly under cyclic compression, it can be seen that both konjac and porcine skin show similarities in the shape of the hysteresis curve. The konjac also shows plastic deformation, mimicking the response of the collagen in the porcine skin.

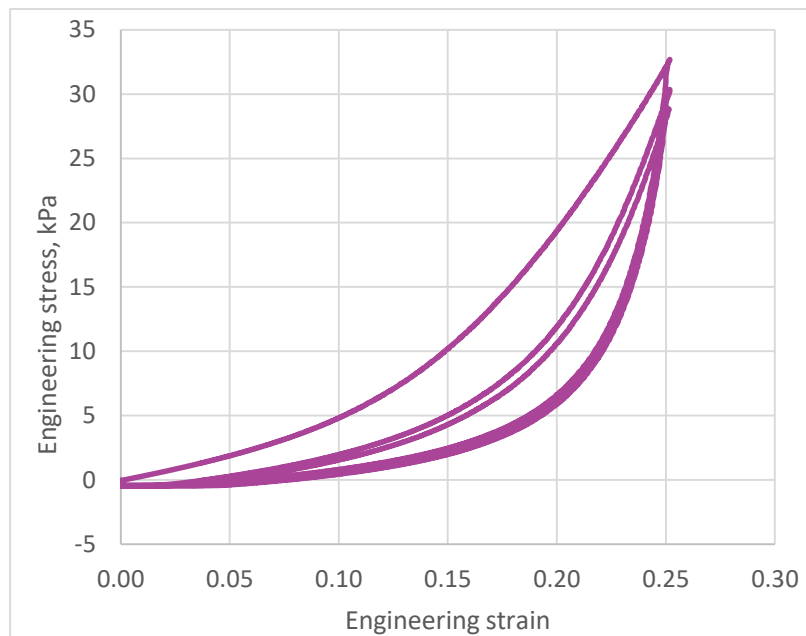


Figure 5-2 Hysteresis loops obtained from cyclic test performed on konjac at 20 mm/min

Figure 5-3 shows the hysteresis response for gelatine. The loading response is near linear, and no plastic deformation is observed. Comparison between Figure 5-3 and Figure 5-1 highlights

gelatine's unsuitability as a tissue surrogate as it is less able to mimic the response from the collagen rearranging.

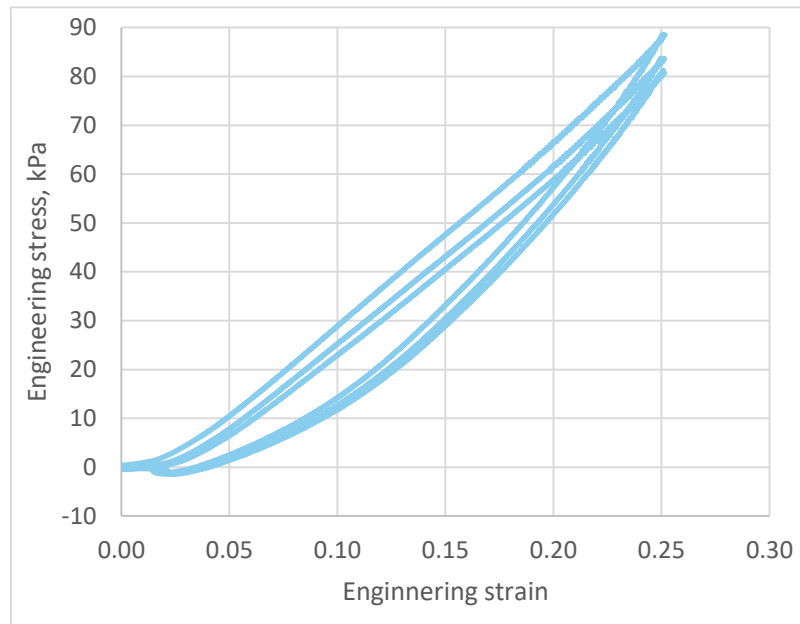


Figure 5-3 Hysteresis loops obtained from cyclic test performed on gelatine at 20 mm/min

5.4 Theoretical Modelling

The research presented in this thesis has developed an experimental model for assessing needle deflection through soft tissue. The impact of the results could be maximised by incorporating theoretical modelling.

The experimental results could be used to develop and validate a finite element model. Parameters in the model such as the needle shape and size could be easily modified to allow for in depth analysis into factors which affect a needle insertion.

5.5 Discussion of main results

5.5.1 Development of a new skin tissue surrogate

Conventional gel surrogates fracture in a fundamentally different way to human skin tissue *in vivo* when punctured with a needle [4]. Konjac glucomannan gel has been developed as a new soft tissue surrogate which fractures in the same way as skin tissue. This was demonstrated by photographing a BD blood fill needle insertion into human skin tissue *in vivo*, and comparing the crack profile to the same needle insertion into konjac gel, as shown in Figure 5-4.

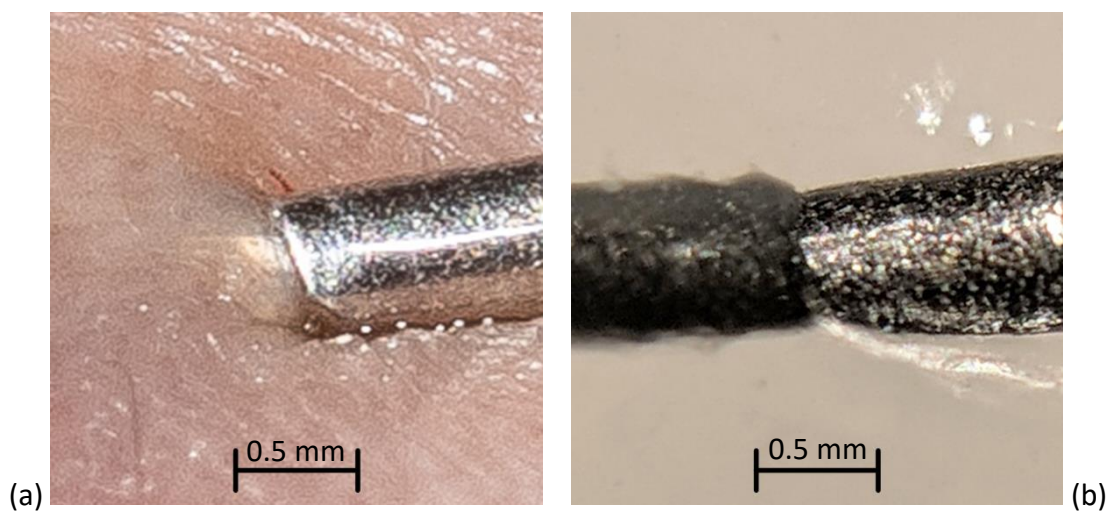


Figure 5-4: Figure displaying the similar crack profile for a needle insertion into skin tissue (a) and konjac (b)

Mechanical analysis of konjac gel was conducted to determine whether its mechanical properties would make it a viable skin tissue surrogate. Using results from various papers the desired range for elastic modulus was found to be 81.8 kPa – 226.2 kPa from experiments *in vivo* [50-63]. A concentration analysis showed that 1.5% konjac powder to water weight resulted in an elastic modulus within this range. Cyclic experiments showed that konjac exhibited non-linear behaviour and plastic deformation when under load, shown in Figure 5-2. The response of konjac is comparable to work by Remache *et al.* who analysed the response of porcine skin, shown in Figure 5-1.

5.5.2 Needle insertion experimentation

All the needle insertion experiments were recorded using a GFP2500 poleidoscope, as well as recording the force reactions from the needle through a Tinius Olsen 5 kN test machine with a 250 Newton load cell.

5.5.2.1 Insertion forces

In section 1.1.1 it was discussed that the needle force response can be split into three components; frictional force, cutting force, and the resultant force from tissue deformation which is dependent on stiffness [11]. Figure 5-5 contains the force response of a needle insertion through the konjac surrogate at 20 mm/min. As the needle is inserted it is affected by all of the three forces. As it is removed, only the frictional force is recorded, as the needle is no longer cutting the surrogate or deforming it.

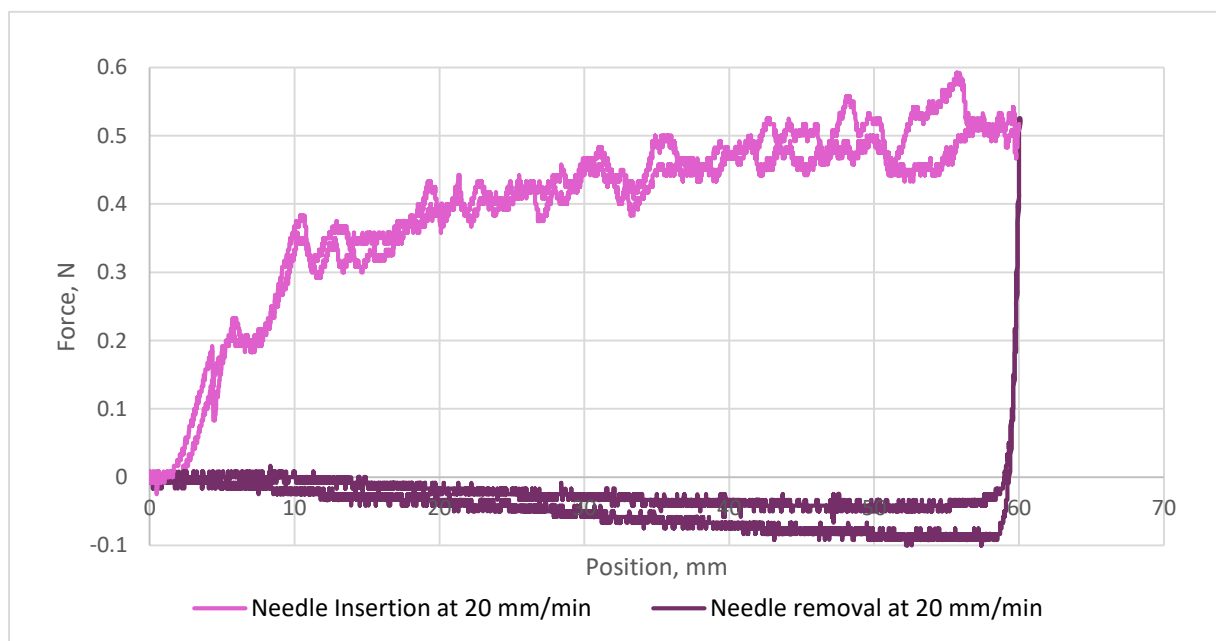


Figure 5-5: Force profile during needle insertion and removal at 20 mm/min

It was found that the frictional force increases by an average 1 mN for each millimetre of needle insertion for the 14-gauge biopsy needle at insertion and removal rates of 20 mm/min and 100 mm/min. This analysis could be repeated for the other insertion speeds, but significant noise was evident at higher insertion speeds so it isn't possible to isolate the friction forces. If this noise is reduced in future experiments a more thorough analysis on the effect of insertion speed and friction force is possible.

5.5.3 Speed assessment

The effect of insertion speed on puncture force was recorded for biopsy needle insertions inserted between 20 mm/min and 600 mm/min. It was found that puncture force decreases with increasing insertion force, which mimics results in the literature which were conducted on real tissue *ex vivo* [8, 31-35].

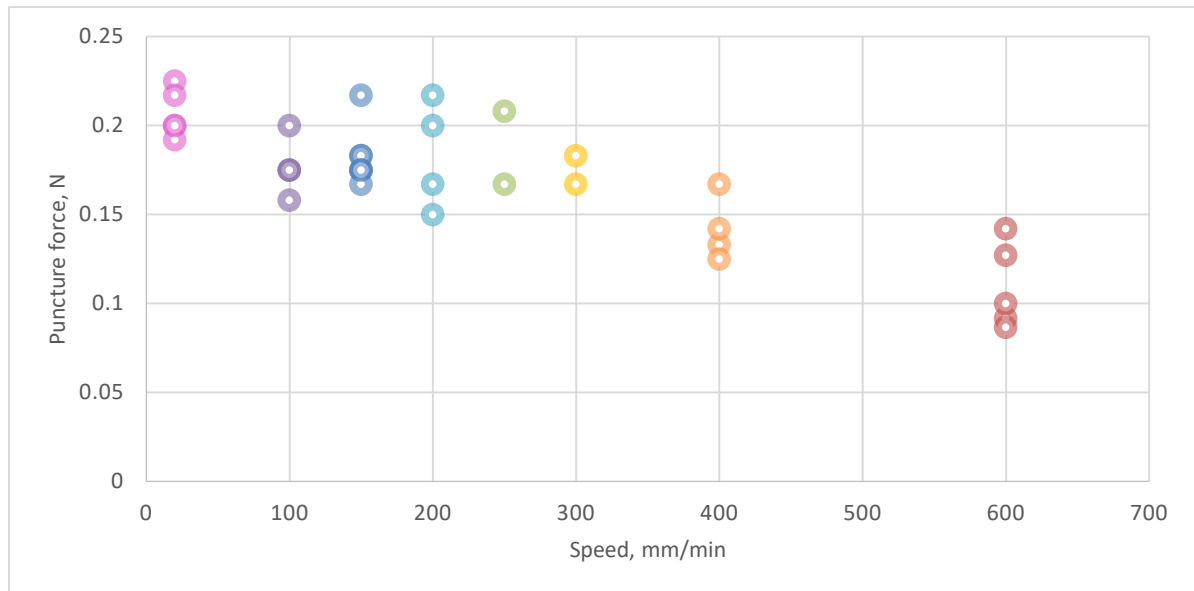


Figure 5-6: Relationship between needle insertion speed and puncture force

In the literature it was found that conventional surrogates responded with an increase in puncture force at increasing insertion speeds [26-30]. The surrogate tissues used in the needle speed studies were all dry gels: PVC gel, silicone rubber, and porcine gelatine.

This result was re-iterated with assessing the average force response at different insertion speeds after the puncture had occurred, and the result is presented in Figure 5-7.

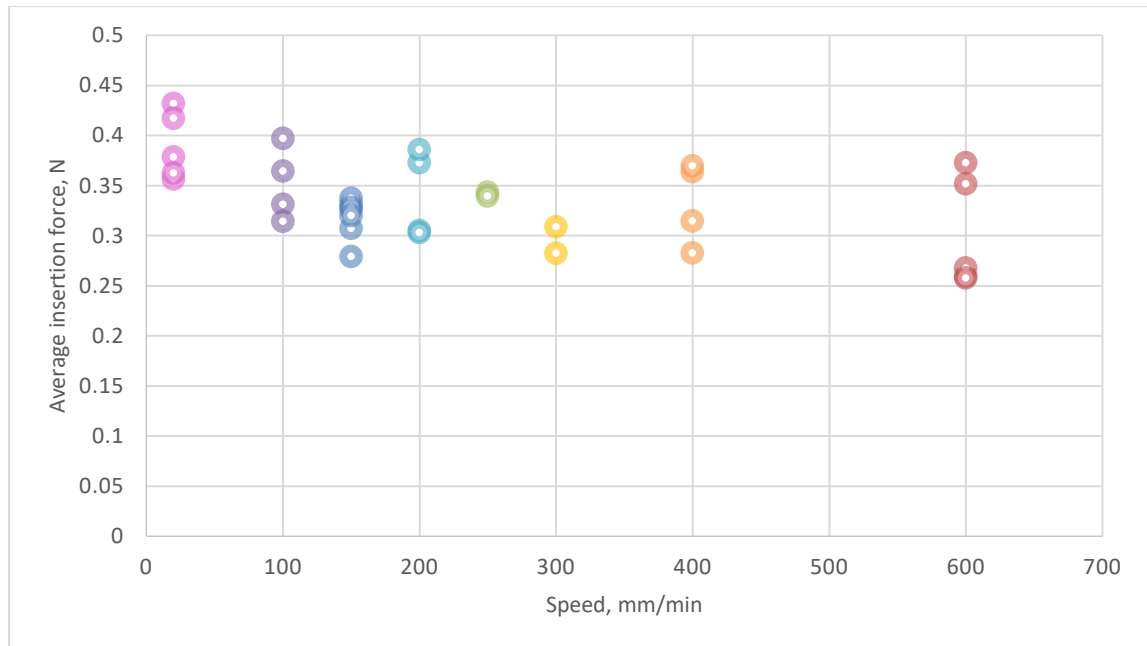


Figure 5-7: Relationship between needle insertion speed and average insertion force

In section 4.2.1 it was discussed that the magnitude of frictional force can be isolated for each insertion speed by analysing the force response when the needle is removed. If this is conducted the frictional force component can be isolated from the results presented in Figure 5-7. This would show whether the change in force response is dependent on friction, or whether the cutting force and stiffness response are changing with increasing insertion speed. The forces should be analysed separately as previous research showed that existing surrogates do not accurately replicate a needle response through soft tissue *ex vivo* [8, 26-35]. An in depth analysis could reveal what is causing the differences, and how to ensure any further surrogate development continues to emulate the response from real soft tissue.

5.5.3.1 Poleidoscope data

The results from the GFP2500 poleidoscope in chapter 4 returned a visual representation of the principal strain map during a needle insertion. The poleidoscope was used to record the insertions of various needles with outer diameters ranging from 0.5 mm to 2.1 mm. It was also used to record the insertions at different insertion speeds. It was found that the loading pattern was consistent irrespective of needle diameter or insertion speed. Existing research tends to assume that a bevel needle experiences one of two loading patterns during a needle insertion [2, 10, 105, 144]:

1. A constant distributed load along the length of the needle.
2. An increasing distributed load along the side of the needle with the bevel tip, which is near zero at the entry point and maximum at the needle tip.

However, the photoelastic data revealed that the loading pattern is a lot more complicated, and is demonstrated in Figure 5-8.

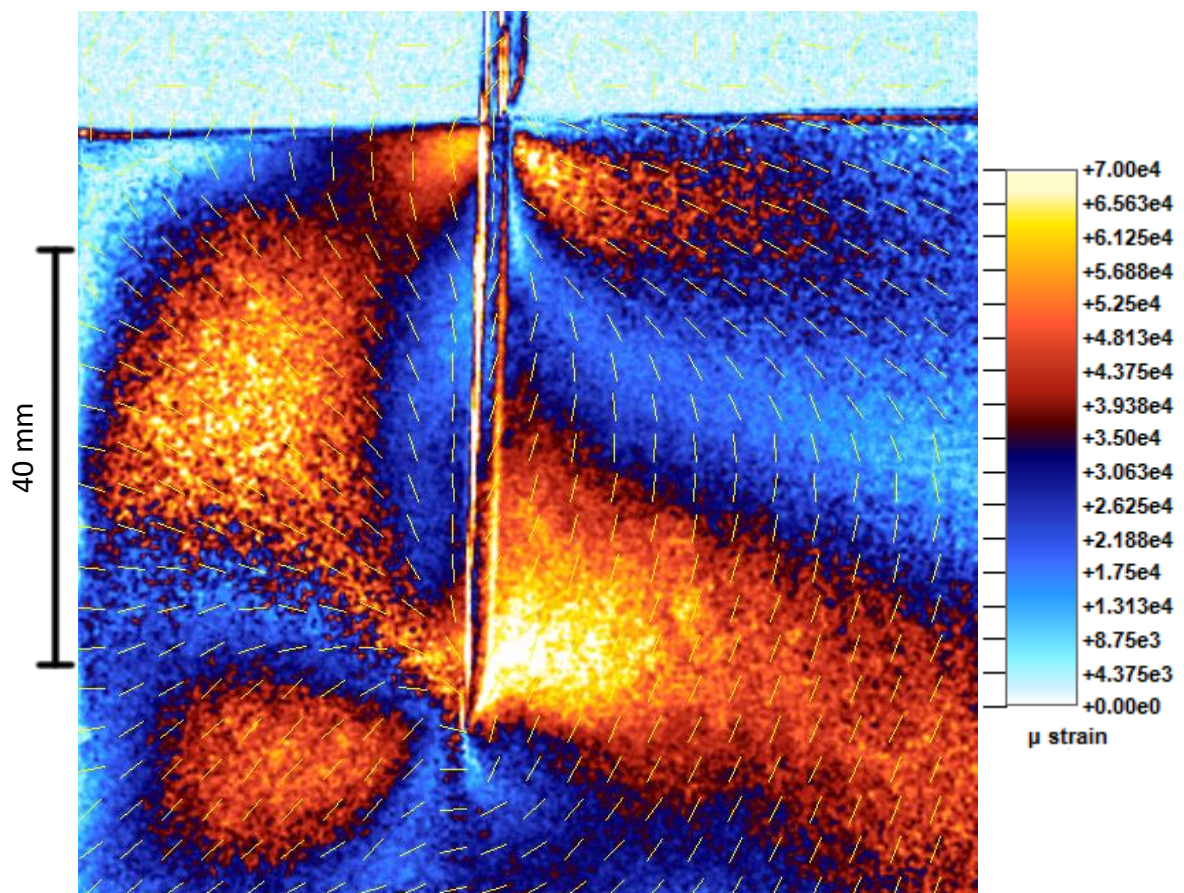


Figure 5-8: Principal strain difference diagram of needle insertion

It should be noted that the poleidoscope integrates the retardation through the thickness of the birefringent konjac gel. Therefore, it is likely that the local maximum around the needle is lower than the presented value.

Throughout the needle insertion experiments the needles have been inserted in the same orientation for ease of comparison, where the bevel tip is along the right edge when viewing through the poleidoscope. To ensure that the results were not dictated by this orientation a further experiment was conducted where the needle was inserted in the opposite orientation with the bevel tip on the left edge, as shown in Figure 5-9.

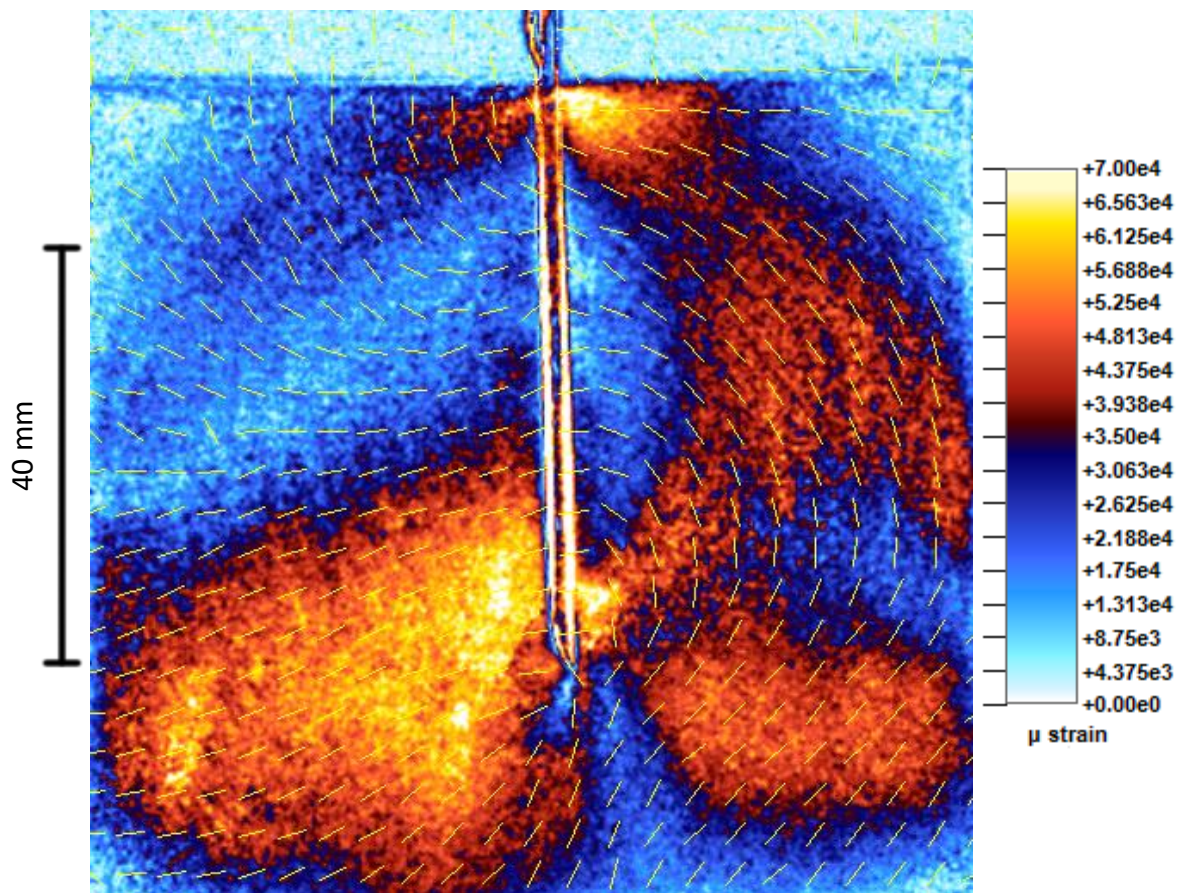


Figure 5-9: Principal strain difference diagram of needle insertion with flipped needle

The strains in Figure 5-9 mirror those in Figure 5-8, thus displaying that the locations of maximum strain are consistent irrespective of needle orientation. Further experiments could be conducted with the bevel tip facing the poleidoscope, to see the effect of the overall results on the principal strain map.

6 FUTURE DEVELOPMENT

The experimental analysis techniques used in this research have not been used for non-linear materials before, and have not been used for dynamic needle insertion analysis. As a result of this many areas for development have been identified. This section will discuss areas for future development within this research topic.

6.1.1 Modifying konjac surrogate

In chapter 4 it was discussed that the optic coefficient of konjac jelly could be amplified to produce more fringes per unit load. The GFP2500 poleidoscope works best between fringes of 0.25 and 0.5 [92], but the maximum fringe order recorded for the needle insertions was between 0.01 and 0.06 fringes. The optic coefficient could be modified by adding sugar or glycerol. However, this would modify the stiffness of the gel, as shown in section 2.4.4. If this modification is made, then the mechanical assessment of konjac jelly would have to be revisited.

This modification would provide more detailed principal strain maps of the needle insertions. However, it is suggested that the processing issues described in chapter 3 are resolved first before the optical coefficient is modified. It was postulated that the processing software was not processing the results correctly over a fringe order of 0.25. If the optic coefficient is modified to produce fringe orders over 0.25 for a needle insertion and the processing error is not fixed, then results may be unusable. A new version of the GFP2500 poleidoscope apparatus and software has recently been released, and it is hoped that the updates have corrected the aforementioned processing issues.

In section 4.4 an inhomogeneous laminate surrogate was developed which had three distinct layers to mimic the three layers of skin. It was not possible to modify the concentration of the konjac gel to match the varying mechanical properties of skin tissue. If further development of the layered surrogate is required it is suggested that the top surface of the gel is made with a stiffer material which is able to mimic the puncture toughness of the epidural layer. A few suggestions could be cling film or layers of spray paint.

6.1.2 Microscopic analysis of needle insertion

In chapter 4 the requirement for higher resolution analysis of needle insertion was identified. The highest gauge needle used in this investigation had an outer diameter of 0.5 mm, and the current optical setup did not have the resolution to capture the response in detail. This is highlighted in Figure 6-1, which shows the initiation of a 14 gauge biopsy needle puncturing the konjac surrogate. The outer diameter of the biopsy needle is 2.1 mm, but the resolution of the image is still inadequate.

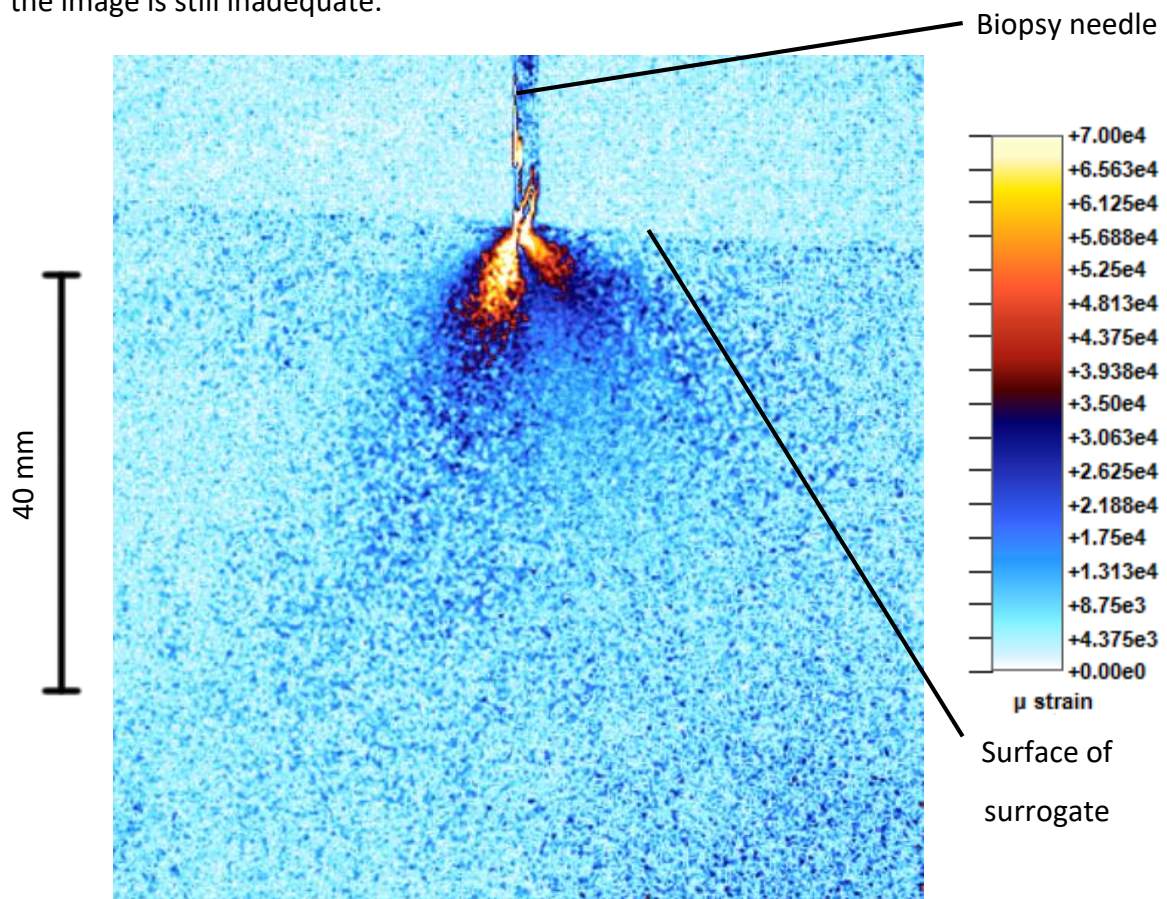


Figure 6-1 Principal strain map of a biopsy needle puncturing the konjac surrogate

The image in Figure 6-1 is not clear due to the low resolution of the GFP2500 poleidoscope camera. This is a situation where a higher resolution, or magnified image is required. The system is capable of obtaining full field magnitude and direction data, but it is limited by the resolution. It is suggested that future work within this area use a higher resolution camera instead of the standard resolution comes with the poleidoscope setup.

6.1.3 Range of needles

A range of real needles currently used in medicine were used for the needle insertion analysis within this research. However, many of the needles had variations between gauge, length, and tip angle. External research has shown that these all individually affect the needle response through soft tissue, and it was therefore difficult to conclude which geometric differences caused variations in the needle deflection and principal strain map in this thesis.

It is therefore suggested that a set of needles is gathered which only have one shape variable, between: needle length, gauge (thickness), tip angle, and tip type. Existing research has conducted experiments on isolated aspects of needle geometry [11, 14, 15, 18, 95], but not using the newly developed konjac surrogate. Within chapter 4 it was shown that konjac replicates the needle response through skin tissue *in vivo* better than existing surrogates, and it is possible that the effects of changing needle geometry may be different, and more accurate, with the new surrogate.

6.1.4 Modified experimental setup

In chapter 4 it was discussed that the deflection measurements were actually mostly due to the surrogate moving within the tanks. The higher gauge needles did show signs of bending, but the amount was minimal.

It is suggested that a range of experiments are conducted with different boundary conditions in order to assess how needle bending, needle deflection, and surrogate motion all contribute to the overall direction of the needle insertion:

a) Surrogate and needle fixed:

This experimental setup involves fixing the tissue surrogate and needle in place, such that any recorded deflection is solely due to needle bending. This could be done by clamping the needle securely within grips which prevent any movement. Securing the gel would be more difficult due to it shrinking in the cooling process, and the gel surface is also slippery so it cannot be easily secured in grips. Soft fillers could be added in the shrinkage void between gel and tank, or a smaller set of tanks could be crafted which are slightly smaller than the original and the surrogate could be transferred.

Existing work within this body of research tends to stick to the above boundary conditions, where both needle and tissue surrogate are fixed. However, this type of experiment has not been conducted with konjac jelly as the tissue surrogate.

b) Needle fixed and surrogate free:

This setup would mimic the setup used within this section of research, where the needle is securely clamped but the surrogate is permitted to move.

c) Surrogate fixed and needle in flexible grip:

It is suggested that a new experiment is designed where the needle is held in a flexible clamp or pivot grip, and the surrogate is secured. This could show how the needle tip shape dictates the insertion path.

Anecdotal evidence within this research revealed that the needle tip shape dictated the path through the surrogate material in a hand-held insertion. The haptic feedback from the insertion allowed for the direction of the needle to be corrected. It is assumed that the deflection from a human controlled needle insertion will be different than the deflection from a simple robotically controlled insertion, due to the haptic feedback. Hence, the experiment in point c) could be repeated for a human operated needle insertion. The comparisons of the results between a human operated needle insertion, and a robotically controlled insertion would quantify the magnitude of trajectory correction during a human-operated insertion.

6.1.5 Measurement of deflection

Throughout this research the optical results have been presented with the background image subtracted; such that any presented retardation was due to the needle insertion and applied load rather than residual stresses or strains in the material. A similar subtraction method could also be utilized for measuring the needle deflection. Instead of subtracting the images to remove residual retardation, the images are subtracted to show the amount of deflection or bending of the needle:

- a) Capture image where the needle has been lowered to maximum insertion depth.
- b) Retract the needle

- c) Capture image where the needle has been inserted to maximum depth into tissue surrogate
- d) Subtract image (a) from image (b).

The subtracted image would show the difference between the uninhibited needle 'insertion' to the insertion through the tissue surrogate. The differences would show the overall deflection from the vertical path, and highlight any bending of the needle.

6.1.6 Three-dimensional analysis

This research, and similar research in this area, has been concerned with two dimensional deflection analysis. Three-dimensional analysis could be conducted with two GFP2500 poleidoscopes; where one camera is set up viewing the needle motion out of plane, and another viewing the motion in plane. The surrogate shape would have to be modified from a thin square sheet to a rectangular column, and thus the thickness through the in plane and out of plane would be greater. This would be more representative of a mass of tissue, where the material is constrained in all directions, and potentially reveal further insight into needle-tissue interaction.

This suggested setup is essentially tomographic photoelasticity. However, it is difficult to quantify the principal strain field as it is tensor tomography rather than scalar tomography; which has not yet been resolved for non-asymmetric problems [145]. During the experiment the principal strain field is changing with time, and therefore multiple data sets are required. If two GFP2500 poleidoscopes are used for two simultaneous viewing directions then multiple data sets will be acquired, which would be a start to developing this analysis technique.

6.1.7 Modifying angle of insertion

Throughout this research the needle was inserted vertically into the soft tissue surrogate. However, the needle is inserted at an angle for medical procedures where blood is taken or drugs are delivered. Therefore, further experiments could be conducted where the needles are inserted at varying angles into the tissue surrogate. This would show how insertion angle affects the bending, and deflection of the needle.

6.1.8 Mechanical characterisation

In chapter 2 the reasons behind characterising konjac jelly with elastic modulus were discussed. Konjac jelly is not a linear-elastic material, and it experienced stress-relaxation. Future work within this area should include the measurement of the viscoelastic modulus for konjac jelly. There should be emphasis on the time domain component on the viscoelastic modulus, to allow for a quantitative investigation on how the material degrades or creeps over time.

It is suggested that future work within this area could work on the development of a photoviscoelastic analysis technique, where a dynamic modulus can be used to describe the material. The Stress Photonics software is not currently equipped to handle a varying material property like viscoelastic modulus. It would be beneficial to work with the developers to incorporate an option for non-linear and viscoelastic materials. This would allow for more rigorous analysis in this topic and increase the analysis possibilities with this experimental method.

7 CONCLUSION

7.1 Surrogate development

Conventional gel surrogates fracture in a fundamentally different way to human skin tissue *in vivo* when punctured with a needle. The author has **developed a novel surrogate**, konjac glucomannan gel, and has demonstrated that it **fractures in the same way as skin tissue**. The photographs in Figure 7-1 highlight the similarities between the crack profile between skin tissue and konjac when punctured with a BD Blood Fill needle.

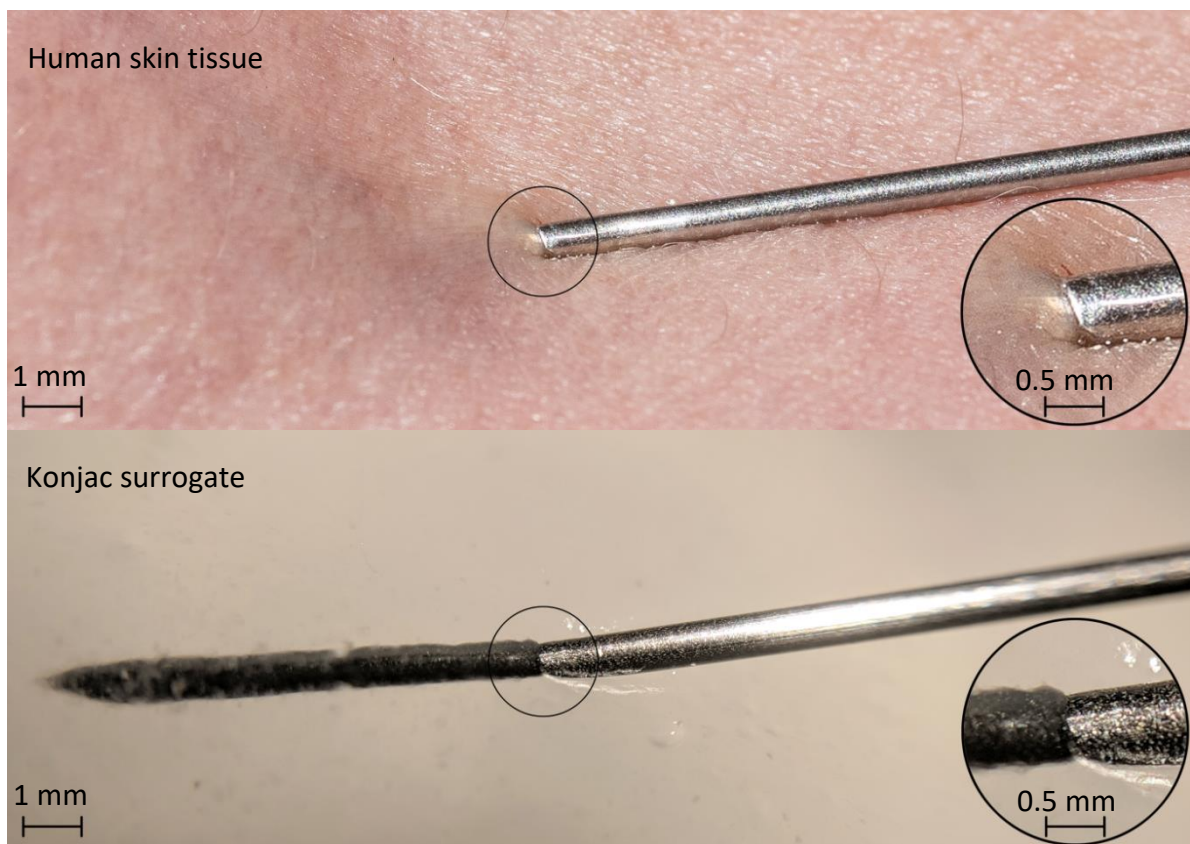


Figure 7-1: Figure displaying the similar crack profile for a needle insertion into skin tissue and konjac

Mechanical analysis of konjac glucomannan was conducted to determine whether it would create a suitable gel surrogate for needle insertion investigation using photoelastic optical analysis. **Results from compression and tensile experiments showed that its elastic modulus at 1.5% concentration was comparable to the elastic modulus of skin tissue *in vivo***. The tensile experiments also revealed that **konjac exhibited better tear resistance than conventional gel surrogates**; with konjac producing a range of failure strains between 0.66 –

0.98, comparable to the failure strains of 0.27 – 1.13 found for human skin tissue *ex vivo* [50, 52-54].

7.2 Optical analysis

It was demonstrated that with careful preparation konjac jelly produced a clear gel, which also exhibited temporary birefringence; two qualities which are required for photoelastic optical analysis. Tensile experiments were conducted to determine the gels **strain optic coefficient** for use with the GFP2500 poleidoscope software; which was found to be $K_{\epsilon S} = 3.47 \times 10^{-5} \pm 0.18 \times 10^{-5}$.

7.3 Needle insertion experiments

7.3.1 Varying insertion speed

Needle insertion experiments were conducted using konjac jelly as the skin tissue surrogate. Biopsy needles were inserted at varying speeds to assess the force response development at varying insertion speeds. Previous research showed that existing surrogates produced higher reaction forces at higher insertion speeds [26-30], yet the opposite was shown for the soft tissues tested *ex vivo* [8, 31-35]. The data showed that that **konjac jelly accurately replicates needle insertion responses through soft tissue better than existing surrogates**, where the insertion and puncture force reduced as the insertion speed increased. It was also shown that needle insertions through konjac followed the same force pattern as insertions through skin tissue; where force peaks before puncture, and force troughs after puncture were clearly visible [2, 8-10].

It is assumed that the different response between the konjac surrogate and existing surrogates was due to the different fracture mechanisms. Konjac fractures in a similar way to human skin tissue when punctured with a needle, whereas existing surrogates tore. It is also assumed that the observed tribological similarities between konjac and real skin tissue amplified its suitability as a skin tissue surrogate. Existing surrogates are dry and rubbery; unlike skin tissue. It was observed that konjac had a lubricated surface, and when needles were inserted they were also lubricated by the gel. **This tribological similarity between konjac and skin tissue produced a more realistic surrogate.**

Additional analysis with biopsy needles revealed that **insertion speed affected the deflection angle, where faster insertion speeds led to greater deflection**. It was also shown that **greater insertion depth reduced the overall deflection angle**.

7.3.2 Various needle geometries

Further needle insertion experiments were conducted using a range of real needles with various gauges and lengths. It was found that **higher gauge needles, which have a smaller diameter, produce lower force responses**. The results for the deflection analysis conflicted with results in the literature. It was found that the higher gauge needles deflected less in this study than their thicker, lower gauge counterparts. However, this result could have been due to the different lengths of the needles tested, and the surrogate material moving within its container. It was shown that insertion length led to reduced deflection, and the higher gauge needles also had reduced length. It was shown that the thicker needles moved the tissue surrogate more, but the thinner needles exhibited bending due to their lower flexural stiffness.

7.3.3 Inhomogeneous analysis

Inhomogeneous surrogates were also prepared using konjac jelly. Layered surrogates were created which had three distinct layers; to mimic the layers in human skin tissue. Particulate surrogates were created which included suspended beads; to mimic the response from a biopsy target. It was shown that **biopsy needles deflected the same amounts through the homogenous surrogates as through the inhomogeneous surrogates**. This agrees with discussions from Kataoka *et al.* and Alterovitz *et al.*, who argued that the needle deflection is generally due to the bevel tip and diameter of the needle, and not influenced greatly by material inhomogeneity [16, 17].

7.4 Optical analysis of needle insertions

All the needle insertion experiments were recorded using the GFP2500 poleidoscope. It is a digital polariscope that allows for instantaneous, dynamic, full-field data to be captured using one piece of photoelastic apparatus [6]. This apparatus captured the magnitude of principal strain, and the direction of surrogate movement due to the needle insertion. The **directional**

information has never been seen before for a full field analysis, as conventional analysis focuses on the motion of discrete points. An example of the typical response from a needle insertion is shown in Figure 7-2.

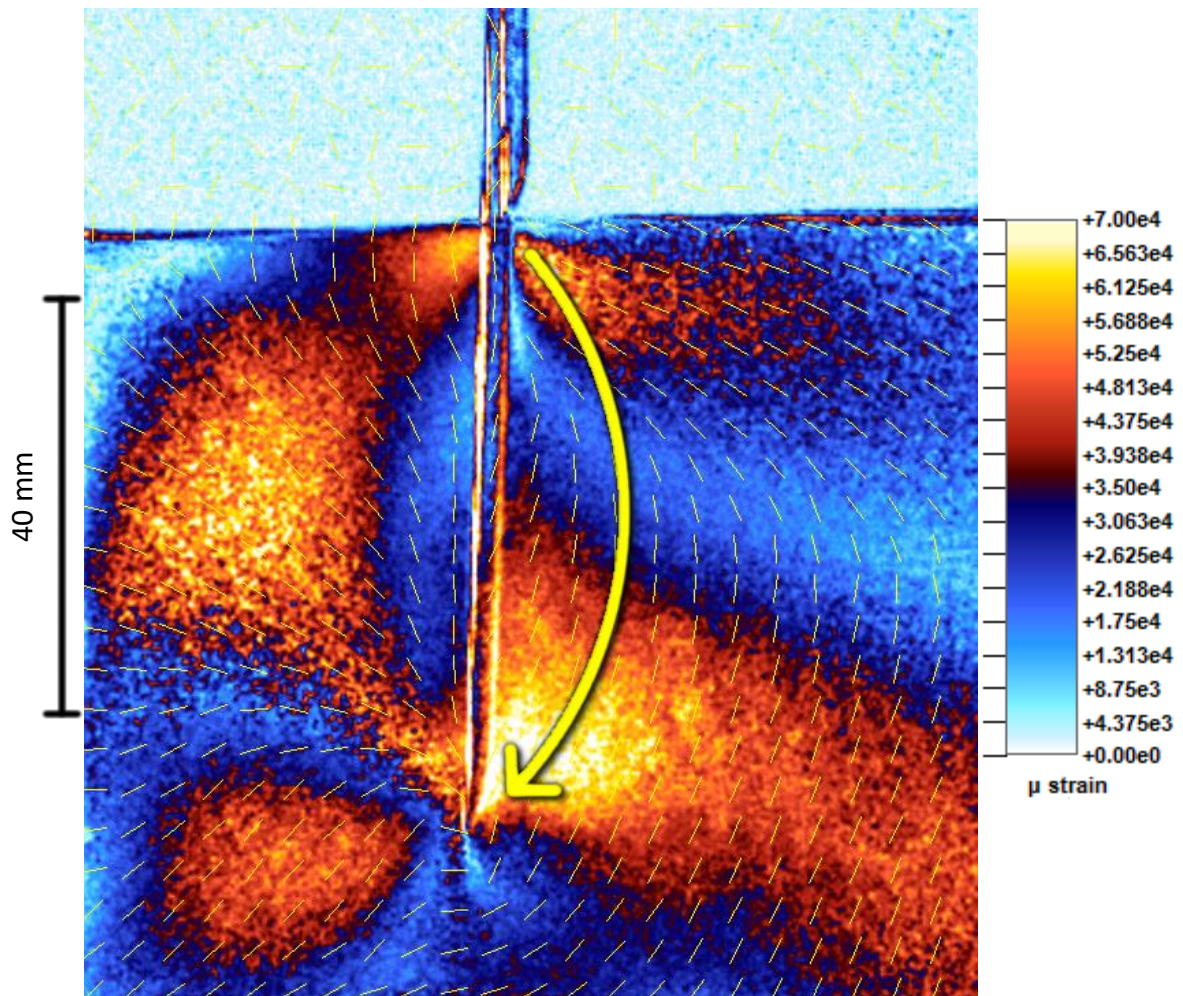


Figure 7-2: Illustrated principal strain difference diagram of needle insertion

The GFP2500 poleidoscope data revealed never-before-seen data regarding the strain distribution during a needle insertion. Locations of maximum principal strains were identified against the side of the bevel tip, and at the entry point; which has not been reported before. These locations of maximum principal strain difference were consistent across the range of needle experiments, for all the insertion speeds and range of needles tested. The **new directional information** visualised the bending pattern as the needle was inserted, which is highlighted in Figure 7-2. The utilisation of the GFP2500 poleidoscope with the newly developed skin tissue surrogate revealed how the needle affected the surrogate as a whole.

REFERENCES

- [1] N. Abolhassani, R. Patel, and M. Moallem, "Needle insertion into soft tissue: A survey," *Medical Engineering & Physics*, vol. 29, pp. 413 - 431, 2007.
- [2] D. J. van Gerwen, J. Dankelman, and J. J. van den Dobbelsteen, "Needle-tissue interaction forces – A survey of experimental data," *Mechanical Engineering and Physics*, vol. 34, pp. 665-680, 2012.
- [3] R. A. Mrozek, Y. R. Sliozberg, J. W. Andzelm, and J. L. Lenhart, "Polymer Gels for Defense Applications," *Mechanics of Biological Systems and Materials*, vol. 7, pp. 47 - 51, 2014.
- [4] R. Tomlinson, and Z. Taylor, "Photoelastic materials and methods for tissue biomechanics applications," *Optical Engineering*, vol. 54, no. 8, pp. 081208, 2015.
- [5] H. Aziz, "Optical experimental stress analysis of needle tissue interaction using surrogate gel materials," *Mechanical Engineering*, The University of Sheffield, 2016.
- [6] J. Lesniak, S. J. Zhang, and E. A. Patterson, "Design and Evaluation of the Poleidoscope A Novel Digital Polariscopes," *Society for Experimental Mechanics*, vol. 44, no. 2, pp. 128-135, 2004.
- [7] G. Morton, "Needle Insertion: Experimental Modelling," *Mechanical Engineering*, University of Sheffield, Sheffield, 2014.
- [8] Y. Kobayashi, T. Sato, and M. G. Fujie, "Modeling of Friction Force based on Relative Velocity between Liver Tissue and Needle for Needle Insertion Simulation," in 31st Annual International Conference of the IEEE EMBS, Minneapolis, Minnesota, USA, 2009, pp. 5274-5278.
- [9] B. Morin, "In vivo study of forces during needle insertions," *Proceedings of the scientific workshop on medical robotics, navigation and visualization*, pp. 415 - 422, 2004.
- [10] N. Abolhassani, R. Patel, and M. Moallem, "Needle insertion into soft tissue: A survey," *Medical Engineering & Physics*, vol. 29, pp. 413 - 431, 2007.
- [11] A. M. Okamura, C. Simone, and M. D. O'Leary, "Force Modeling for Needle Insertion Into Soft Tissue," *Transactions on Biomedical Engineering*, vol. 51, pp. 1707-1716, 2004.
- [12] P. Han, D. Che, K. Pallav, and K. Ehmann, "Models of the cutting edge geometry of medical needles with applications to needle design," *International Journal of Mechanical Sciences*, vol. 65, pp. 157 - 167, 2012.
- [13] M. D. O'Leary, C. Simone, T. Washio, K. Yoshinaka, and A. M. Okamura, "Robotic needle insertion: effects of friction and needle geometry," *IEEE International conference on robotics and automation*, pp. 1774 - 1780, 2003.
- [14] R. J. Webster, J. Memisevic, and A. M. Okamura, "Design considerations for robotic needle steering.." pp. 3599 - 3605.

- [15] S. Misra, K. B. Reed, A. S. Douglas, K. T. Ramesh, and A. M. Okamura, "Needle-Tissue Interaction Forces for Bevel-Tip Steerable Needles," in Conference on Biomedical Robotics and Biomechatronics, Scottsdale, 2008, pp. 224-231.
- [16] H. Kataoka, T. Washio, M. Audette, and K. Mizuhara, "A model for relations between needle deflection, force, and thickness on needle insertion," *Proceedings of the medical image computing and computer assisted intervention*, pp. 966 - 974, 2001.
- [17] R. Alterovitz, K. Goldberg, and A. Okamura, "Planning for steerable bevel-tip needle insertion through 2D soft tissues with obstacles." pp. 1652 - 1657.
- [18] R. J. Falconer, "Personal communication," S. E. Falconer, ed., 2017.
- [19] A. Thompson, "Needle Insertion," Mechanical Engineering, University of Sheffield, Sheffield, 2015.
- [20] L. Hiemenz, A. Litsky, and P. Schmalbrock, "Puncture mechanics for the insertion of an epidural needle," *21st annual meeting of the American society of biomechanics*, pp. 36 - 37, 1997.
- [21] A. E. Healey, J. C. Evans, M. G. Murphy, S. Powell, T. V. How, and D. Groves, "In vivo force during arterial intervention radiology needle puncture procedures," *Westwood Journal*, vol. 13, pp. 178 - 184, 2005.
- [22] N. Abolhassani, R. Patel, and M. Mollem, "Control of soft tissue deformation during robotic needle insertion," *Minimal Invasive Theory*, vol. 15, pp. 165 - 176, 2006.
- [23] T. K. Podder, J. Sherman, D. P. Clark, E. M. Messing, D. J. Rubens, and J. G. Strang, "Evaluation of robotic needle insertion in conjunction with in vivo manual insertion in the operating room," *International workshop on robots and human interactive communication*, pp. 66 - 72, 2005.
- [24] T. Podder, D. Clark, J. Sherman, D. Fuller, E. Messing, and D. Rubens, "In vivo motion and force measurement of surgical needle intervention during prostate brachytherapy," *Journal of Medical Physics*, vol. 33, pp. 2915 - 2922, 2006.
- [25] T. Podder, J. Sherman, L. Li, J. Joseph, D. R. Rubens, and E. M. Messing, "Mechanical properties of human prostate tissue in the context of surgical needle insertion," *International journal of computer assisted radiology and surgery*, vol. 2, pp. 82 - 133, 2007.
- [26] J. R. Crouch, C. M. Schneider, J. Wainer, and A. M. Okamura, "A velocity dependant model for needle insertion in soft tissue," *Lecture notes in computer science*, Springer, ed., pp. 624 - 632, Berlin, 2005.
- [27] S. P. DiMaio, and S. E. Salcudean, "Needle Insertion Modeling and Simulation," *Transactions on Robotics and Automation*, vol. 19, pp. 864-875, 2003.
- [28] T. K. Podder, D. P. Clark, D. Fuller, J. Sherman, N. W. S., and L. Liao, "Effects of velocity modulation during surgical needle insertion." pp. 5766 - 5770.
- [29] K. Naemura, Y. Uchino, and H. Saito, "Effect of the needle tip height on the puncture force in a simplified epidural anaesthesia simulator," *29th Annual international conference of the IEEE EMBS*, pp. 3504 - 3507, 2007.

- [30] M. Meltsner, N. Ferrier, and B. Thomadsen, "Observations on rotating needle insertions using a brachytherapy robot," *Physics in Medicine and Biology*, vol. 52, pp. 6027 - 6037, 2007.
- [31] Y. Kobayashi, A. Onishi, T. Hoshi, and K. Kawamura, "Modelling of conditions where a puncture occurs during needle insertion considering probability distribution," in IEEE/RSJ international conference on intelligent robots and systems, 2008, pp. 1433 - 1440.
- [32] M. Mahvash, and P. E. Dupont, "Mechanics of Dynamic Needle Insertion into a Biological Material," *IEEE Transactions on Biomedical Engineering*, vol. 57, no. 4, pp. 934-943, 2010.
- [33] J. T. Hing, A. D. Brooks, and J. P. Desai, "Reality-based needle insertion simulation for haptic feedback in prostate brachytherapy," in IEEE international conference on robotics and automation, 2006, pp. 619 - 624.
- [34] J. T. Hing, A. D. Brooks, and J. P. Desai, "A biplanar fluoroscopic approach for the measurement, modelling, and simulation of needle and soft-tissue interaction.," *Medical Imaging Analysis*, vol. 11, pp. 62 - 78, 2007.
- [35] T. Frick, D. Marucci, J. Cartmill, C. Martin, and W. Walsh, "Resistance forces acting on suture needles," *Journal of biomechanics*, vol. 34, pp. 1335 - 1340, 2007.
- [36] L. Slomianka. "Blue Histology - Integumentary System," January 2020.
- [37] K. Hwang, H. Kim, and D. J. Kim, "Thickness of skin and subcutaneous tissue of the free flap donor sites: A histologic study," *Microsurgery*, vol. 36, 2015.
- [38] A. Delalleau, G. Josse, J. George, Y. Mofid, F. Ossant, and J.-M. Lagarde, "A human skin ultrasonic imaging to analyse its mechanical properties " *European Journal of Computational Mechanics*, vol. 18, pp. 105 - 116, 2009.
- [39] M. J. Koehler, T. Vogel, P. Elsner, K. Konig, R. Buckle, and M. kaatz, "In vivo measurement of the human epidermal thickness in different localisations by multiphoton laser tomography," *Skin Research and Technology*, vol. 16, pp. 259-264, 2010.
- [40] B. W. Barry, "Novel mechanisms and devices to enable successful transdermal drug delivery," *Pharmaceutical Sciences*, vol. 14, pp. 101-114, 2001.
- [41] Y. S. Papir, K.-H. Hsu, and R. H. Wildnauer, "The effect of Water and Ambient Temperature on the Tensile Properties of Newborn Rat Stratum Corneum," *Biochimica et Biophysica Acta*, vol. 399, pp. 170-180, 1975.
- [42] F. H. Silver, J. W. Freeman, and D. DeVore, "Viscoelastic properties of human skin and processed dermis," *Skin Research and Technology*, vol. 7, pp. 18-23, 2001.
- [43] T. L. Moore, M. Lunt, B. McManus, M. E. Anderson, and A. L. Herrick, "Seventeen-point dermal ultrasound scoring system - a reliable measure of skin thickness in patients with systemic sclerosis," *Rheumatology*, vol. 42, pp. 1559-1563, 2003.
- [44] F. H. Silver, L. M. Siperko, and G. P. Seehra, "Mechanobiology of force transduction in dermal tissue," *Skin Research and Technology*, vol. 9, pp. 3-23, 2003.

- [45] I. A. Brown, "Scanning electron-microscope study of effects of uniaxial tension on human skin.," *British Journal of Dermatology*, vol. 89, pp. 383-393, 1973.
- [46] S. Iva, A. Tanabe, T. Maeda, H. Funamizu, and Y. Aizu, "Development of Non-Deterioration-Type Skin Tissue Phantom Using Silicone Material," *Optical Review*, vol. 21, pp. 353-358, 2014.
- [47] K. Comley, and N. A. Fleck, "The toughness of adipose tissue measurements and physical basis," *Journal of Biomechanics*, vol. 43, pp. 1823-1826, 2010.
- [48] M. A. Meyers, and K. K. Chawla, *Mechanical Behaviour of Materials*, Cambridge: University Press, 2009.
- [49] D. Remache, M. Caliez, M. Gratton, and S. Dos Santos, "The effects of cyclic tensile and stress-relaxation tests on porcine skin," *Mechanical Behaviour of Biomedical Materials*, vol. 77, pp. 242-249, 2018.
- [50] L. Jansen, and P. Rottier, "Some mechanical properties of human abdominal skin measured on excised strips," *Dermatologica*, no. 117, pp. 65-83, 1958b.
- [51] M. G. Dunn, and F. H. Silver, "Viscoelastic behaviour of human connective tissues: Relative contribution of viscous and elastic components," *Connective Tissue Research*, vol. 12, no. 1, pp. 59-70, 1983.
- [52] H. Vogel, "Age dependence of mechanical and biochemical properties of human skin," *Bioengineering and the skin*, vol. 3, pp. 67-91, 1987.
- [53] C. Jacquemoud, K. Bruyere-Garnier, and M. Coret, "Methodology to determine failure characteristics of planar soft tissues using a dynamic tensile test," *Journal of Biomechanics*, vol. 40, no. 2, pp. 468-475, 2007.
- [54] A. Ni Annaidh, K. Bruyere, M. Destrade, M. D. Gilchrist, and M. Ottenio, "Characterization of the anisotropic mechanical properties of excised human skin," *Mechanical Behaviour of Biomedical Materials*, vol. 5, pp. 139-148, 2012.
- [55] R. Sanders, "Torsional Elasticity of Human Skin in vivo," *Pflugers Arch*, vol. 342, pp. 255-260, 1973.
- [56] P. G. Agache, C. Monneur, J. L. Leveque, and J. De Rigal, "Mechanical Properties and Young's Modulus of Human Skin in Vivo," *Dermatological Research*, vol. 269, pp. 221-232, 1980.
- [57] S. Diridollou, M. Berson, V. Varbe, D. Black, B. Karlsson, F. Auriol, J. M. Gregoire, C. Yvon, L. Valliant, Y. Gall, and F. Ptat, "An in vivo method for measuring the mechanical properties of the skin using ultrasound," *Ultrasound in Medicine and Biology*, vol. 24, no. 2, pp. 215-224, 1998.
- [58] F. Khatyr, C. Imberdis, P. Vescovo, D. Varchon, and J. M. Lagarde, "Model of the viscoelastic behaviour of skin in vivo and study of anisotropy," *Skin research and Technology*, vol. 10, pp. 96-103, 2004.
- [59] J. Jachowicz, R. McMullen, and D. Prettypaul, "Indentometric analysis of in vivo skin and comparison with artificial skin models," *Skin Research and Technology*, vol. 13, pp. 299-309, 2007.

- [60] C. Pailler-Mattei, S. Bec, and H. Zahouani, "In vivo measurements of the elastic mechanical properties of human skin by indentation tests," *Medical Engineering & Physics*, vol. 30, no. 5, pp. 599-606, 2008.
- [61] G. Boyer, L. Laquieze, A. Le Bot, S. Laquieze, and H. Zahouani, "Dynamic indentation on human skin in vivo: ageing effects," *Skin Research and Technology*, vol. 15, pp. 55 - 67, 2009.
- [62] H. Zahouani, C. Pailler-Mattei, B. Sohm, R. Vargiolu, V. Cenizo, and R. Debret, "Characterization of the mechanical properties of a dermal equivalent compared with human skin in vivo by indentation and static friction tests.," *Skin Research and Technology*, vol. 15, pp. 68-76, 2009.
- [63] X. Liang, and S. A. Boppart, "Biomechanical Properties of In Vivo Human Skin from Dynamic Optical Coherence Elastography," *Transactions on Biomedical Engineering*, vol. 57, no. 4, pp. 953-959, 2010.
- [64] C. Edwards, and R. Marks, "Evaluation of Biomechanical Properties of Human Skin," *Clinics in Dermatology*, vol. 13, pp. 375-380, 1995.
- [65] L. Barbe, B. Bayle, M. de Mathelin, and A. Gangi, "Needle insertions modeling Identifiability and limitations," *Biomedical Signal Processing and Control*, vol. 2, pp. 191-198, 2007.
- [66] C. Pailler-Mattei, S. Pavan, and R. Vargiolu, "Contribution of stratum corneum in determining biotribological properties of the human skin " *Wear*, pp. 1038 - 1043, 2007.
- [67] D. J. Tobin, "Biochemistry of human skin - our brain on the outside " *Chem Soc Rev*, vol. 35, pp. 52 - 67, 2006.
- [68] M. Geerligs, L. van Breemen, and G. Peters, "In vitro indentation to determine the mechanical properties of epidermis " *Journal of biomechanics*, vol. 44, pp. 1176 - 1181, 2011.
- [69] K. Comley, and N. A. Fleck, "A micromechanical model for the Young's modulus of adipose tissue," *Solids and Structures*, vol. 47, pp. 2982-2990, 2010.
- [70] W. L. Wong, T. J. Joyce, and K. L. Goh, "Resolving the viscoelasticity and anisotropy dependence of the mechanical properties of skin from a porcine model," *Biomechanics and Modeling in Mechanobiology*, vol. 15, pp. 433-446, 2016.
- [71] J. van Kuilenburg, M. Masen, and E. van der Heide "Contact modelling of human skin: What value to use for the modulus of elasticity? ," *Journal of Engineering Tribology*, vol. 4, pp. 349 - 361, 2012.
- [72] D. Taylor, N. O'Mara, E. Ryan, M. Takaza, and C. Simms, "The Fracture Toughness of Soft Tissues," *Journal of the Mechanical Behaviour of Biomedical Materials*, vol. 6, pp. 139-147, 2012.
- [73] C. Flynn, M. B. Rubin, and P. Nielsen, "A model for the anisotropic response of fibrous soft tissues using six discrete fibre bundles," *International Journal for Numerical Methods in Biomedical Engineering*, vol. 27, pp. 1793-1811, 2011.

- [74] F. M. Hendriks, D. Brokken, C. W. J. Oomens, and F. P. T. Baaijens, "Influence of hydration and experimental length scale on the mechanical response of human skin in vivo, using optical coherence tomography," *Skin Research Technology*, vol. 10, pp. 231 - 241, 2004.
- [75] A. K. Dabrowska, G. M. Rotaru, S. Derler, F. Spano, S. Camenzind, S. Annaheim, R. Stampfli, M. Schmid, and R. M. Rossi, "Materials used to simulate physical properties of human skin," *Skin Research and Technology*, vol. 22, pp. 3 - 14, 2016.
- [76] P. S. Theocaris, and E. E. Gdoutos, *Matrix Theory of Photoelasticity*: Springer-Verlag, 1979.
- [77] J. W. Dally, and W. F. Riley, *Experimental Stress Analysis*, 4 ed., Knoxville: College House Enterprises, 2005.
- [78] M. L. Williams, and R. J. Arenz, "The engineering analysis of linear photoviscoelastic materials," *Experimental mechanics.*, vol. 4, no. 9, pp. 249-262, 1964.
- [79] Y.-H. Zhao, and J. Huang, "Photoviscoelastic Stress Analysis of a Plate with a Central Hole," *Experimental Mechanics*, vol. 41, pp. 312-318, 2001.
- [80] W. K. Aui Yong, "Experimental Modelling," Mechanical Engineering, University of Sheffield, Sheffield, 2013.
- [81] F. W. Hecker, and B. Morche, "Computer-aided measurement of relative retardation in plane photoelasticity," *Experimental Stress Analysis*, pp. 535 - 542, 1986.
- [82] Z. F. Wang, and E. A. Patterson, "Use of Phase-stepping with Demodulation and Fuzzy Sets for Birefringence Measurement," *Optics and Lasers in Engineering*, vol. 22, pp. 91 - 104, 1994.
- [83] E. A. Patterson, and B. Morche, "Toward full-field automated photoelastic analysis of complex components," *Strain*, vol. 27, pp. 49 - 56, 1991.
- [84] K. Ramesh, T. Kasimayan, and B. Neethl Simon, "Digital Photoelasticity: A comprehensive review," *Journal of Strain Analysis*, vol. 46, pp. 245 - 266, 2011.
- [85] K. Ramesh, *Digital Photoelasticity: Advanced Techniques and Applications*: Springer, 2000.
- [86] J. Lesniak, M. Zickel, C. Welch, and D. Johnson, "An innovative polariscope for photoelastic stress analysis," in *Experimental Mechanics*, Spring Conference., 1997.
- [87] E. A. Patterson, "Digital Photoelasticity Principles, Practice and Potential," *Strain*, vol. 38, pp. 27-39, 2002.
- [88] E. A. Patterson, and Z. F. Wang, "Simultaneous observation of phase stepped images for automated photoelasticity," *The Journal of Strain Analysis for Engineering Design*, vol. 33, pp. 1 - 15, 1998.
- [89] W. Ji, and E. A. Patterson, "Simulation of Errors in Automated Photoelasticity," *Experimental Mechanics*, vol. 38, no. 2, pp. 132 - 139, 1998.
- [90] J. Lesniak, "GFP2500 c," Stress Photonics, 2013.
- [91] J. Lesniak, "DeltaVision v2," Stress Photonics, 2013.

- [92] G. Calvert, "GFP 1200 Benchmarking Tests," 2007, p. 7.
- [93] M. Coppola, M. Djabourov, and M. Ferrand, "Unified phase diagram of gelatin films plasticized by hydrogen bonded liquids," *Polymer*, vol. 53, pp. 1483-1493, 2012.
- [94] Y. Wang, B. L. Tai, H. Yu, and A. J. Shih, "Silicone-Based Tissue-Mimicking Phantom for Needle Insertion Simulation," *Journal of Medical Devices*, vol. 8, pp. 021001-1 - 021001-7, 2014.
- [95] M. D. O'Leary, C. Simone, T. Washio, K. Yoshinaka, and A. M. Okamura, "Robotic needle insertion: effects of friction and needle geometry," in International conference on robotics and automation, 2003, pp. 1774 - 1780.
- [96] O. A. Shergold, and N. A. Fleck, "Experimental Investigation Into the Deep Penetration of Soft Solids by Sharp and Blunt Punches, With application to the Piercing of Skin," *Transactions of the ASME*, vol. 127, 2005.
- [97] D. S. Cronin, and C. Falzon, "Characterization of 10% ballistic gelatin to evaluate temperature, aging and strain rate effects " *Experimental Mechanics*, vol. 51, pp. 1197 - 1206, 2011.
- [98] J. Kwon, and G. Subhash, "Compressive strain rate sensitivity of ballistic gelatin " *Journal of Biomechanics*, vol. 43, pp. 420 - 425, 2010.
- [99] A. Leibinger, A. E. Forte, Z. Tan, M. J. Oldfield, F. Beyrau, D. Dini, and F. Rodriguez Y Baena, "Soft Tissue Phantoms for Realistic Needle Insertion: A Comparative Study," *Biomedical Engineering Society*, vol. 44, no. 8, pp. 2442 - 2452, 2016.
- [100] A. N. Mat Daud, M. S. Rohani, and R. Jaafar, "Acoustic Characterisation of Konjac Glucomannan Gel as a Medical Phantom," *Solid State Phenomena*, vol. 268, pp. 379 - 383, 2017.
- [101] F. S. Agency. "Current EU Approved additives [Online]," February 2, 2016. Available http://www.food.gov.uk/science/additives/enumberlist#h_6.
- [102] Y. Hong, M. Sarntinoranont, G. Subhash, S. Canchi, and M. A. King, "Localized Tissue Surrogate Deformation due to Controlled Single Bubble Cavitation " *Experimental Mechanics*, vol. 56, pp. 97-100, 2016.
- [103] T. Lehmann, C. Rossa, N. Usmani, R. S. Sloboda, and M. Tavakoli, "A real-time estimator for needle deflection during insertion into soft tissue based on adaptive modeling of needle-tissue interactions," *Transactions on Mechatronics*, vol. 2, pp. 2601 - 2612, 2016.
- [104] G. Kang, and X. Wu, "Ratchetting of porcine skin under uniaxial cyclic loading," *J. Mech. Behav. Biomed. Mater.* , vol. 4, pp. 498 - 506, 2011.
- [105] Z. Cheng, M. Chauhan, B. L. Davies, D. G. Caldwell, and L. S. Mattos, "Modelling needle forces during insertion into soft tissue," in EMBC, 2015, pp. 4840-4844.
- [106] O. A. Shergold, N. A. Fleck, and D. Radford, "The uniaxial stress versus strain response of pig skin and silicone rubber at low and high strain rates," *Int. J. Impact Eng*, vol. 32, pp. 1384 - 1402, 2006.

- [107] S. P. Davis, B. J. Landis, Z. H. Adams, M. G. Allen, and M. R. Prausnitz, "Insertion of microneedles into skin measurement and prediction of insertion force and needle fracture force," *Journal of Biomechanics*, vol. 37, pp. 1155-1163, 2004.
- [108] W. K. Aui Yong, "Needle Insertion: Experimental Modelling," Mechanical Engineering, University of Sheffield, Sheffield, 2013.
- [109] A. Franck, "Viscoelasticity and dynamic mechanical testing," TA Instruments, 2002.
- [110] N. Ravikumar, C. Noble, E. Cramphorn, and Z. A. Taylor, "A constitutive model for ballistic gelatin at surgical strain rates," *Mechanical Behaviour of Biomedical Materials*, vol. 47, pp. 87 - 94, 2015.
- [111] Y.-H. Zhao, and J. Huang, "Photoviscoelastic Stress Analysis of a Plate with a Central Hole," vol. 41, pp. 312-318, 2001.
- [112] G. W. Dombi, R. C. Haut, and W. G. Sullivan, "Correlation of high-speed tensile strength with collagen content in control and lathyrus rat skin," *J. Surg. Res*, vol. 54, pp. 21 - 28, 1993.
- [113] L. E. Edsberg, and R. E. Mates, "Mechanical characteristics of human skin subjected to static versus cyclic normal pressures " *J. Rehabil. Res. Dev.*, vol. 36, pp. 2, 1999.
- [114] Y. Fung, *Biomechanics: Mechanical Properties of Living Tissues*, New York: Springer-Verlag, 1993.
- [115] W. Hutton, T. Burlin, and H. Ranu, "An apparatus for measuring the effects of radiotherapy on the elastic properties of human skin in vivo," *Med. Biol. Eng. Comput.*, vol. 13, pp. 584 - 585, 1975.
- [116] J. Lim, J. Hong, W. W. Chen, and T. Weerasooriya, "Mechanical response of pig skin under dynamic tensile loading " *Int. J. Impact Eng.*, vol. 38, pp. 130 - 135, 2011.
- [117] F. H. Silver, G. P. Seehra, J. W. Freeman, and D. DeVore, "Viscoelastic properties of young and old human dermis: a proposed molecular mechanism for elastic energy storage in collagen and elastin " *J. Appl. Polym. Sci.*, vol. 86, pp. 1978 – 1985, 2002.
- [118] H. Vogel, "Influence of age, treatment with corticosteroids and strain rate on mechanical properties of rat skin " *Biochim. Biophys. Acta (BBA)-Gen. Subj.*, vol. 286, pp. 79 - 83, 1972.
- [119] F. Xu, and T. Lu, *Introduction to Skin Biothermomechanics and Thermal Pain*: Springer, 2011.
- [120] SpecialIngredients. "Carrageenan Kappa [Online]," January, 2019. Available <https://www.specialingredients.co.uk/carrageenan-kappa-500g>.
- [121] C. H. Daly, "Biomechanical properties of dermis," *Journal of Investigative Dermatology*, no. 79, 1982.
- [122] J. Jussila, "Preparing ballistic gelatine - review and proposal for a standard method," *Journal of Forensic Science International*, vol. 141, pp. 91 - 98, 2003.
- [123] International-Organization-of-Standardization, "ISO 34 - 2," *Rubber, vulcanized or thermoplastic - Determination of tear strength*, 2015, p. 12.

- [124] ASTM-International, "ASTM D412," *Tension test for rubber and elastomers*, 2015, p. 15.
- [125] K. Miller, "How to test very soft biological tissues in extension?," *Journal of Biomechanics*, vol. 34, pp. 651-657, 2001.
- [126] N. B. Rahedi, "Needle Insertion: Experimental Modelling," Mechanical Engineering, The University of Sheffield, Sheffield, 2017.
- [127] E. Atenaga, "Needle Insertion: Experimental Modelling," Mechanical Engineering, University of Sheffield, Sheffield, 2018.
- [128] Stress-Photonics-Inc., "GFP1400 Operator's Manual," 2014, p. 101.
- [129] G. Calvert, "Personal Communication," S. E. Falconer, ed., 2016.
- [130] A. M. Okamura, C. Simone, and M. D. O'Leary, "Force Modeling for Needle Insertion Into Soft Tissue," *Transactions on Biomedical Engineering*, vol. 51, pp. 1707 - 1716, 2004.
- [131] K. Miller, and K. Chinzei, "Mechanical properties of brain tissue in tension," *Journal of Biomechanics*, vol. 35, pp. 483-490, 2002.
- [132] F. Muller, "Biomechanical test report on hsw fine-ject needles," Mechanical Engineering, Georgia Institute of Technology, 2011.
- [133] J. Stellman, "Development, production, and characterization of plastic hypodermic needles," Georgia Institute of Technology, 2009.
- [134] B. Maurin, "In vivo study of forces during needle insertions," *Proceedings of the scientific workshop on medical robotics, navigation and visualization*, pp. 415 - 422, 2004.
- [135] M. Khadem, C. Rossa, R. S. Sloboda, N. Usmani, and M. Tavakoli, "Mechanics of Tissue Cutting During Needle Insertion in Biological Tissue," *IEEE Robotics and automation letters*, vol. 1, pp. 800 - 807, 2016.
- [136] C. Simone, and A. Okamura, "Modelling of needle insertion forces for robot-assisted percutaneous therapy." pp. 2085 - 2091.
- [137] F. Casanova, P. R. Carney, and M. Sarntinoranont, "In vivo evaluation of needle force and friction stress during insertion at varying insertion speed into the brain," *Journal of Neuroscience Methods*, vol. 237, pp. 79-89, 2014.
- [138] S. DiMaio, and S. Salcudean, "Needle steering and model-based trajectory planning." pp. 33 - 40.
- [139] J. Burgner-Kahrs, C. Rucker, and H. Choset, "Continuum Robots for Medical Applications: A Survey," *IEEE Transactions on Robotics*, vol. 31, pp. 1261 - 1280, 2015.
- [140] J. Peirs, J. Clijnen, D. Reynaerts, H. Van Brussel, P. Herijgers, B. Corteville, and S. Boone, "A micro optical force sensor for force feedback during minimally invasive robotic surgery," *Sensors and Actuators*, vol. 115, pp. 447 - 455, 2004.
- [141] R. H. Taylor, and D. Stoianovici, "Medical Robotics in Computer-Integrated Surgery," *IEEE Transactions on robotics and automation*, vol. 19, pp. 765 - 781, 2003.

- [142] K. Masamune, E. Kobayashi, Y. Masutani, M. Suzuki, T. Dohi, H. Iseki, and K. Takakura, "Development of an MRI-Comparable Needle Insertion Manipulator for Stereotactic Neurosurgery," *Image Guided Surgery*, vol. 4, pp. 242 - 248, 2010.
- [143] R. Taylor, P. Jensen, L. Whitcomb, A. Barnes, R. Kumar, D. Stoianovici, P. Gupta, Z. Wang, E. deJuan, and L. Kavoussi, "A Steady-Hand Robotic System for Microsurgical Augmentation," *The International Journal of Robotics Research*, vol. 18, pp. 1201 - 1210, 1999.
- [144] S. Misra, K. B. Reed, B. W. Schafer, K. T. Ramesh, and A. M. Okamura, "Mechanics of Flexible Needles Robotically Steered through Soft Tissue," *The International Journal of Robotics Research*, vol. 29, no. 13, pp. 1640-1660, 2010.
- [145] S. Abrego, "Experimental Assessment and Implementation of Photoelastic Tomography," Mechanical Engineering, The University of Sheffield, Sheffield, 2019.

8 APPENDIX

8.1 Full results from material development chapter

8.1.1 Concentration Analysis

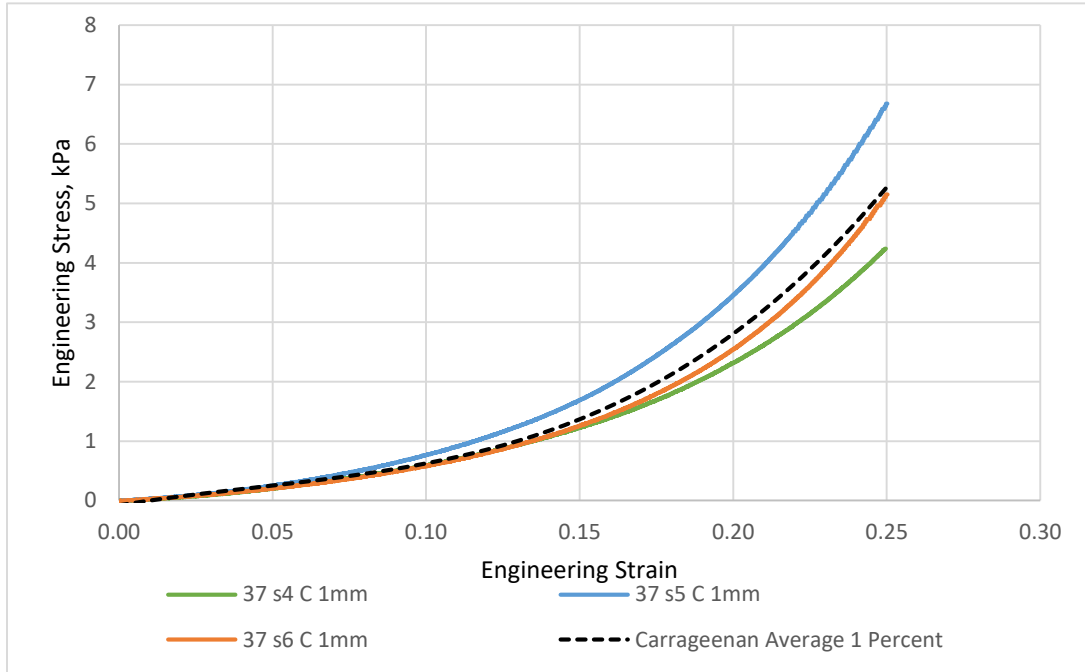


Figure 8-1: Results for carrageenan compression 1mm/min 1% concentration

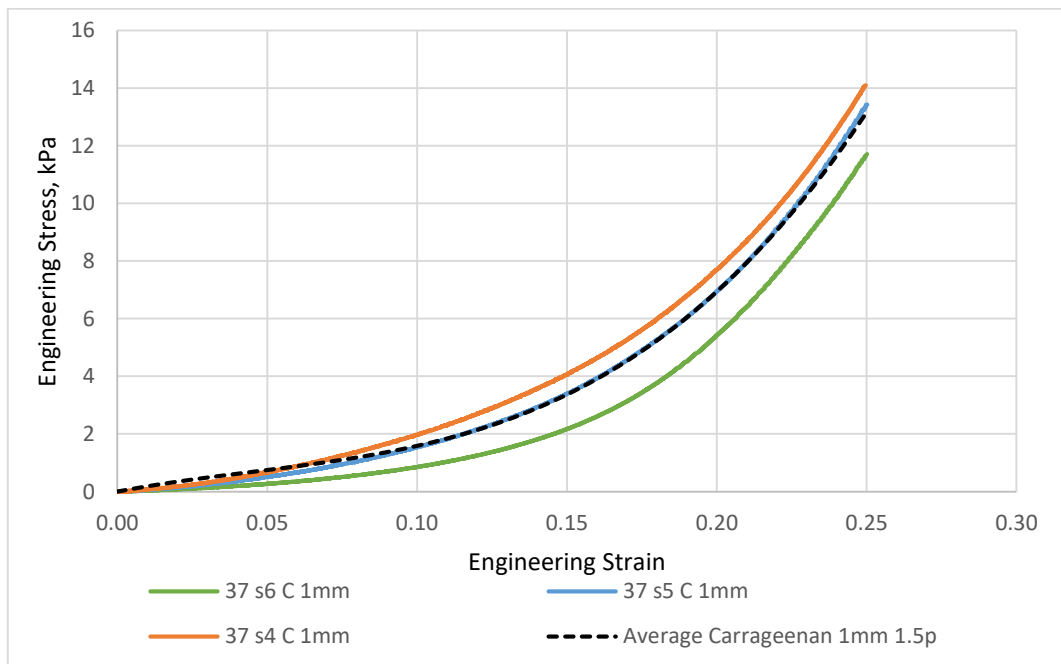


Figure 8-2: Results for carrageenan compression 1mm/min 1.5% concentration

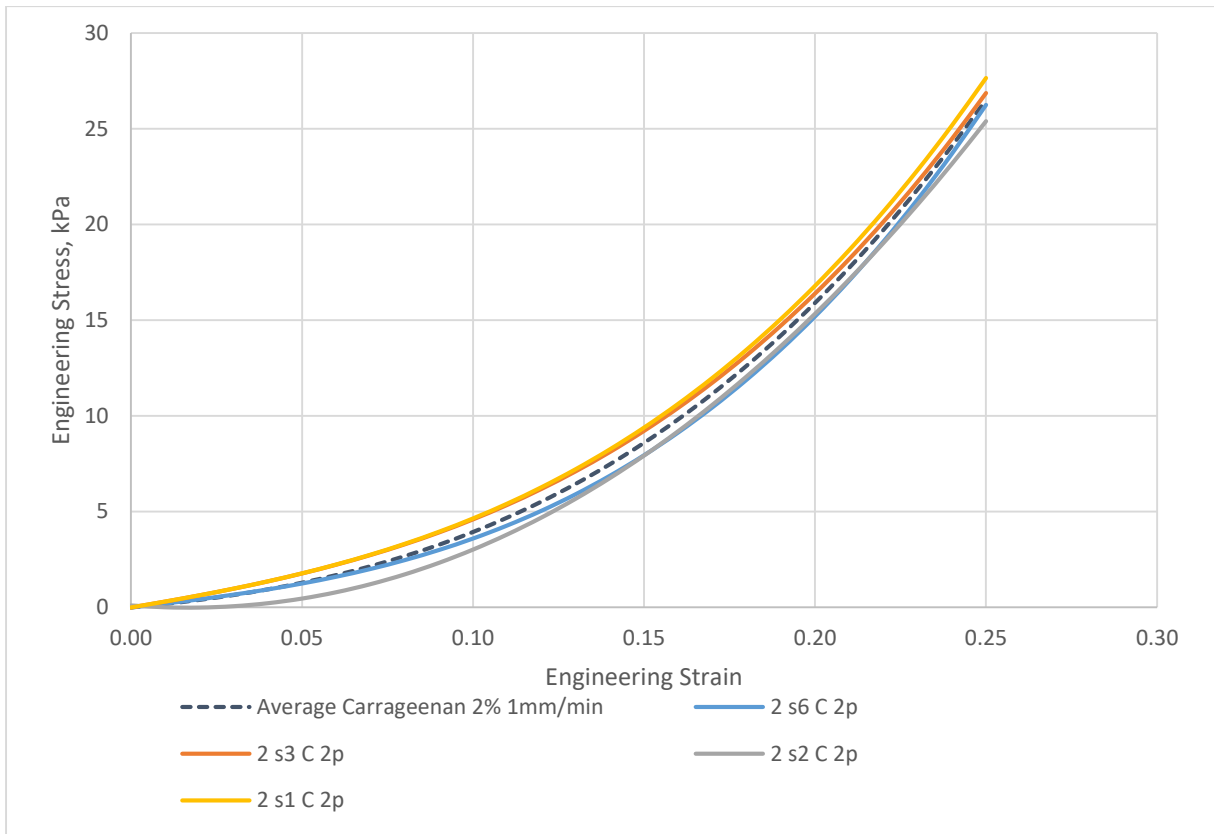


Figure 8-3: Results for carrageenan compression 1mm/min 2% concentration

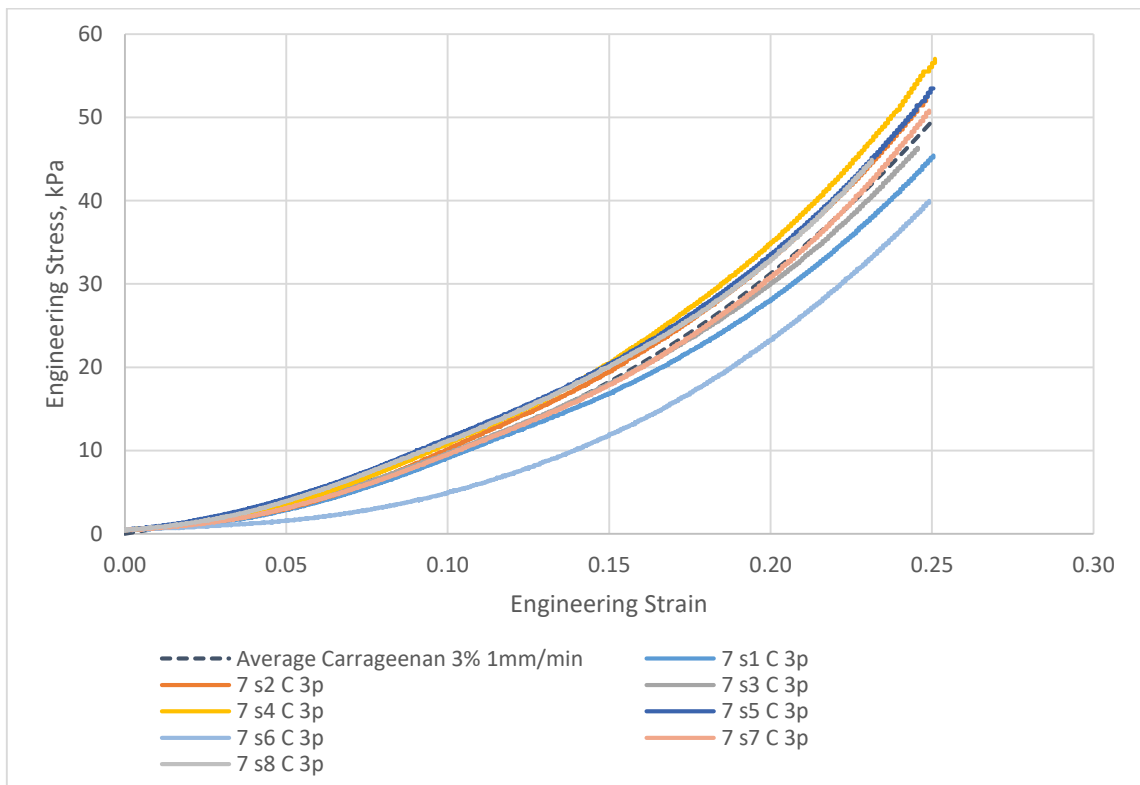


Figure 8-4: Results for carrageenan compression 1mm/min 3% concentration

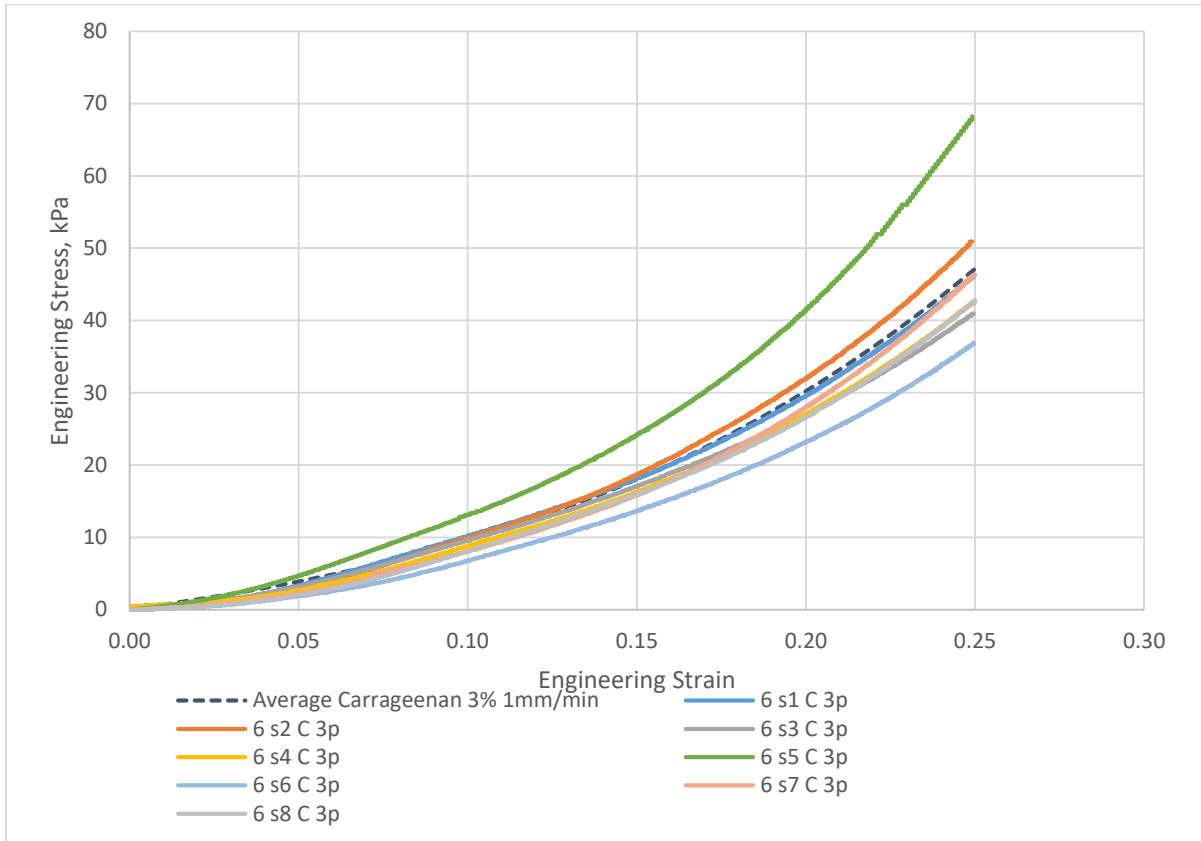


Figure 8-5: Results for carrageenan compression 1mm/min 3% concentration repeats

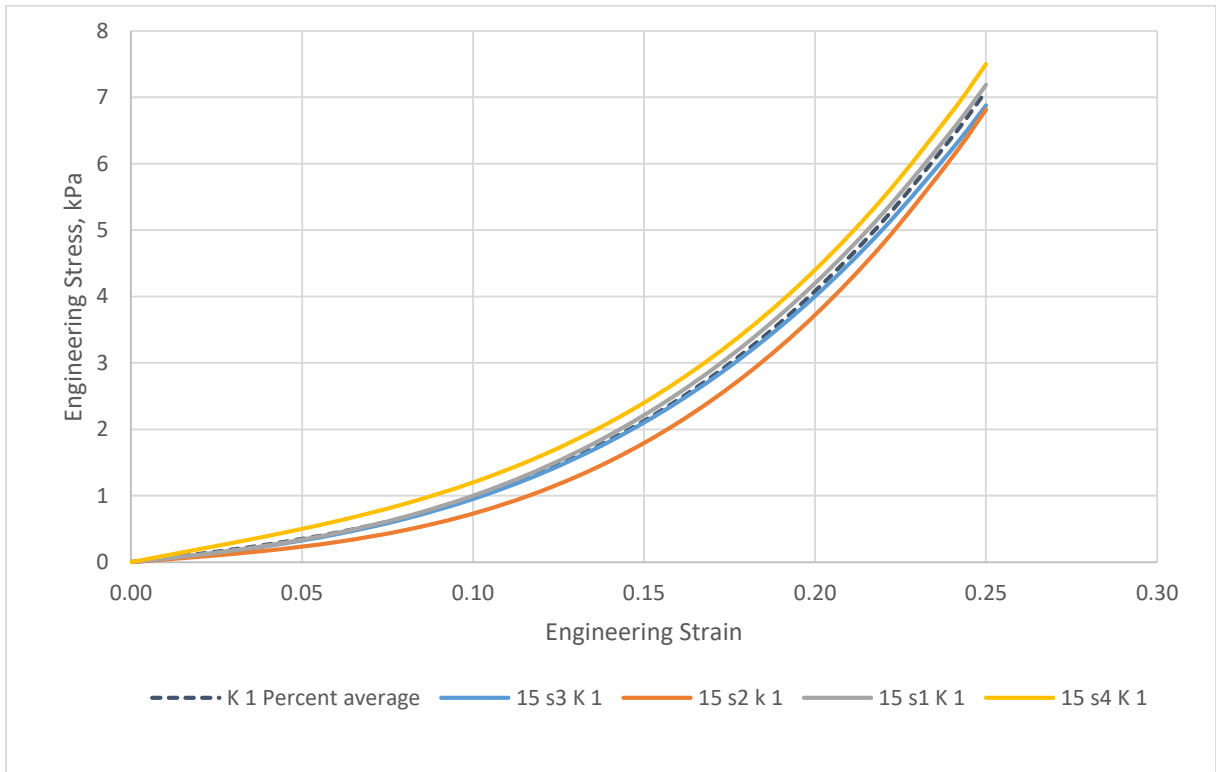


Figure 8-6: Results for konjac compression 1mm/min 1% concentration

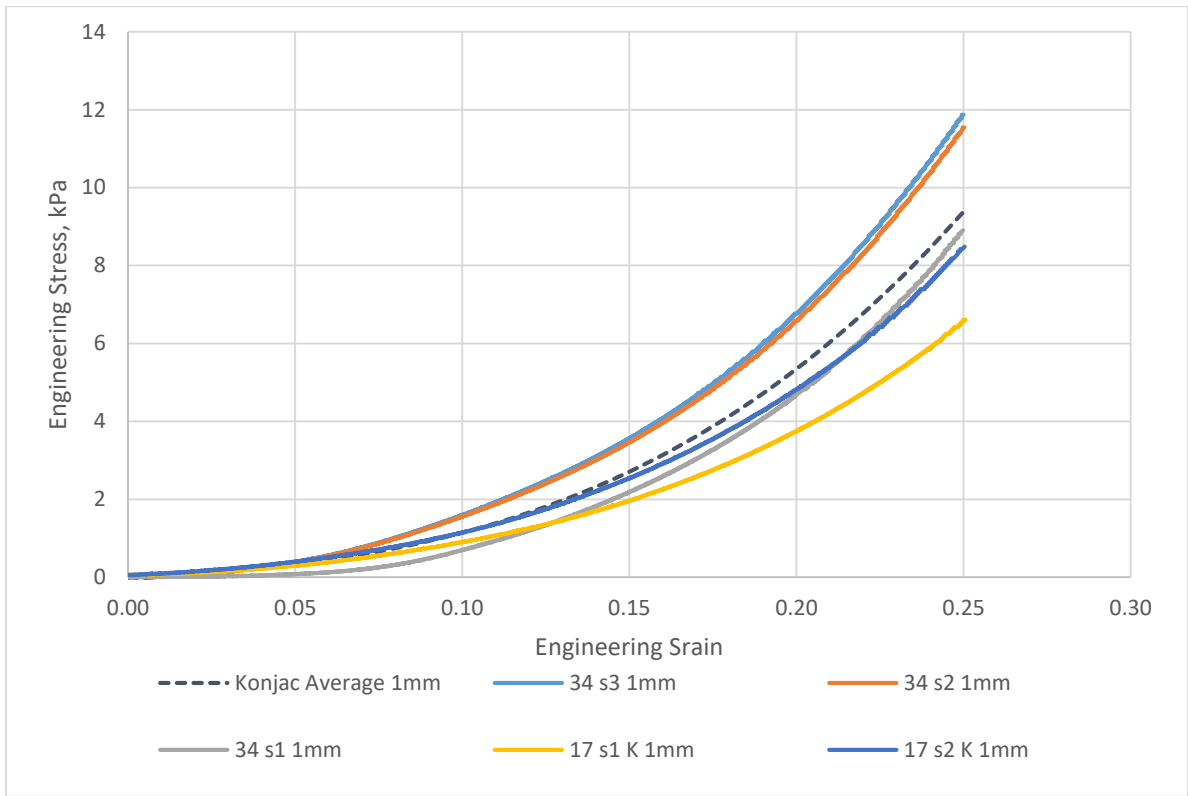


Figure 8-7: Results for konjac compression 1mm/min 1.5% concentration

8.1.2 Compression results: Gelatine

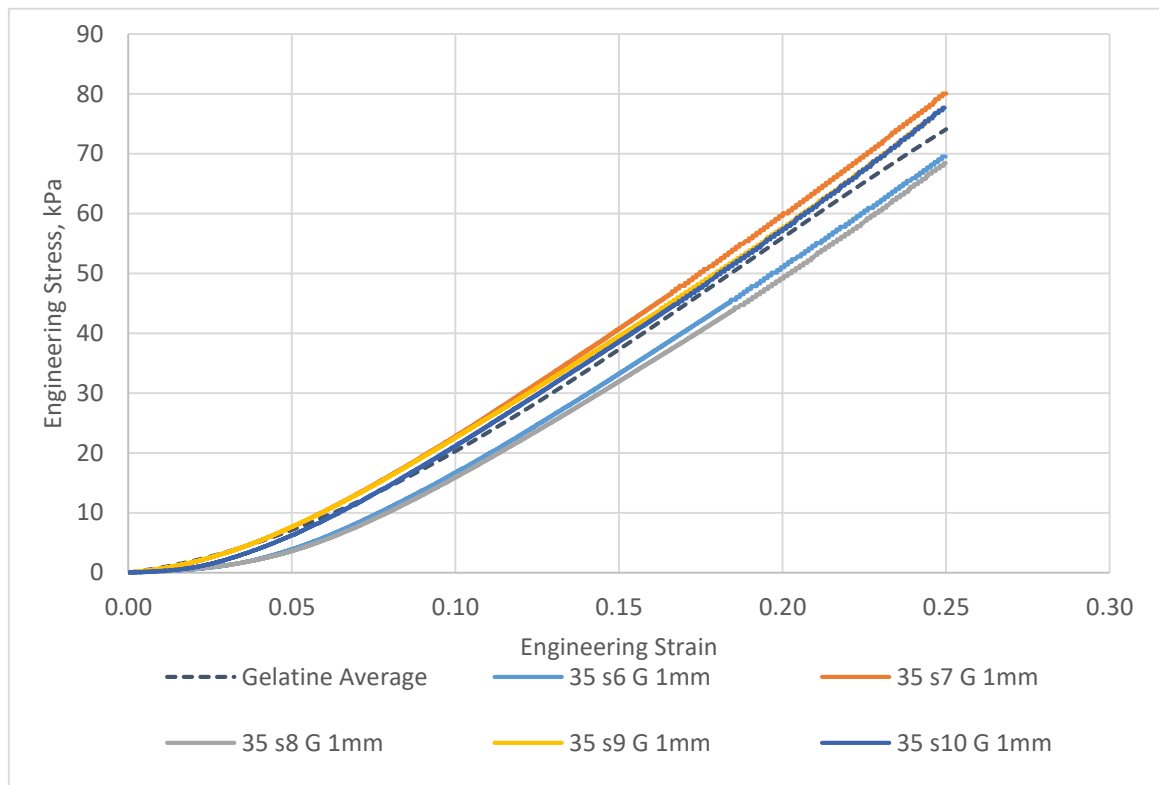


Figure 8-8 Results for compression of gelatine to 0.25 strain at 1mm/min

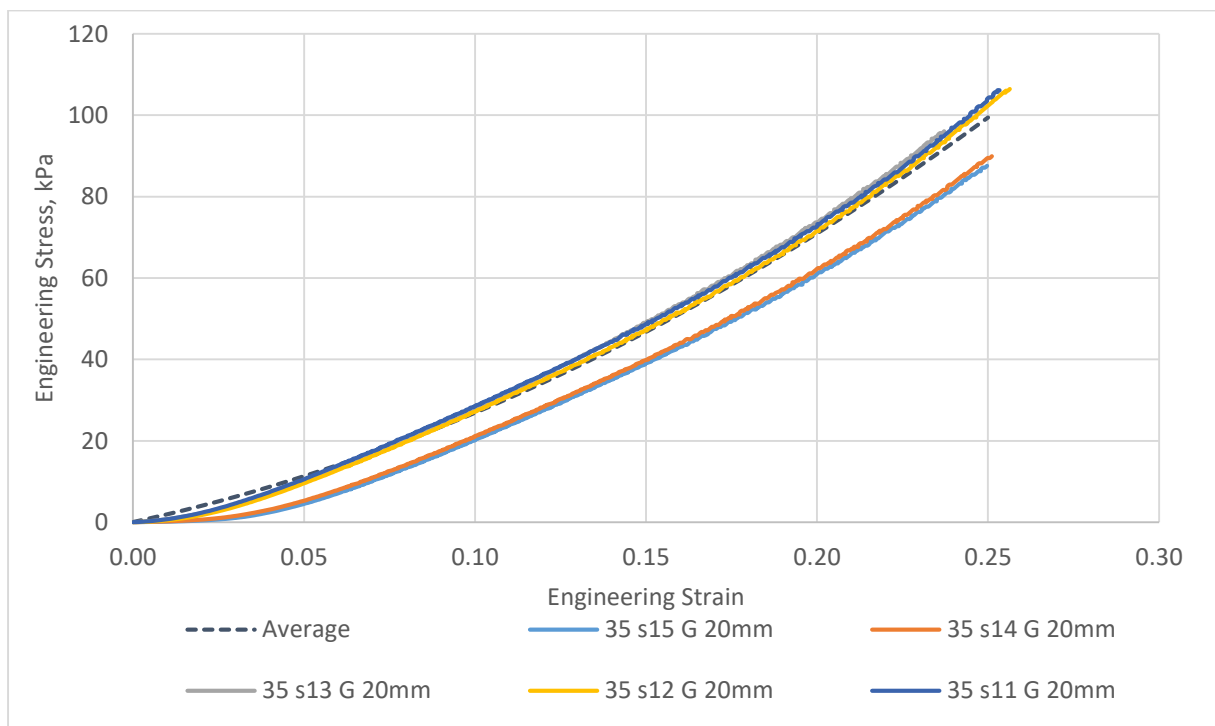


Figure 8-9 Results for compression of gelatine to 0.25 strain at 20mm/min

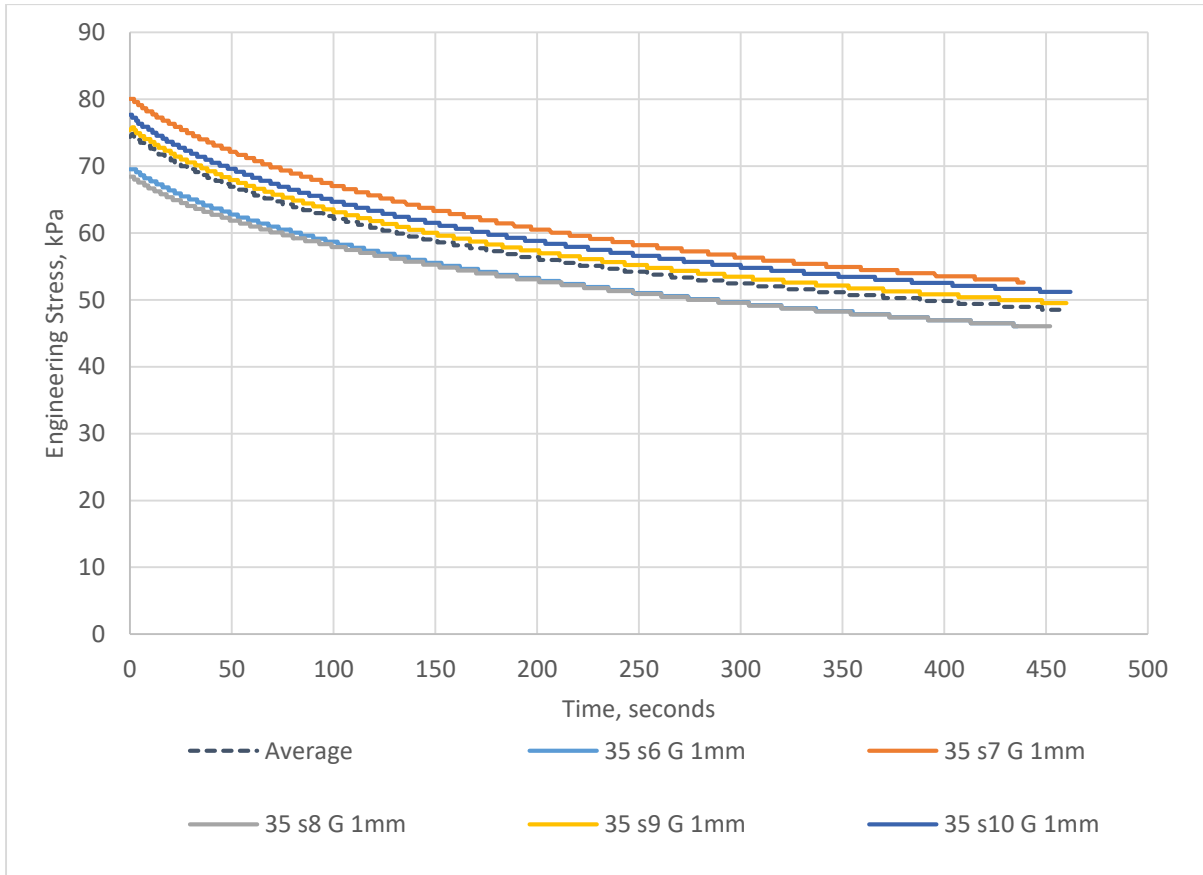


Figure 8-10 Results for creep response of gelatine at 0.25 strain after loading rates of 1mm/min

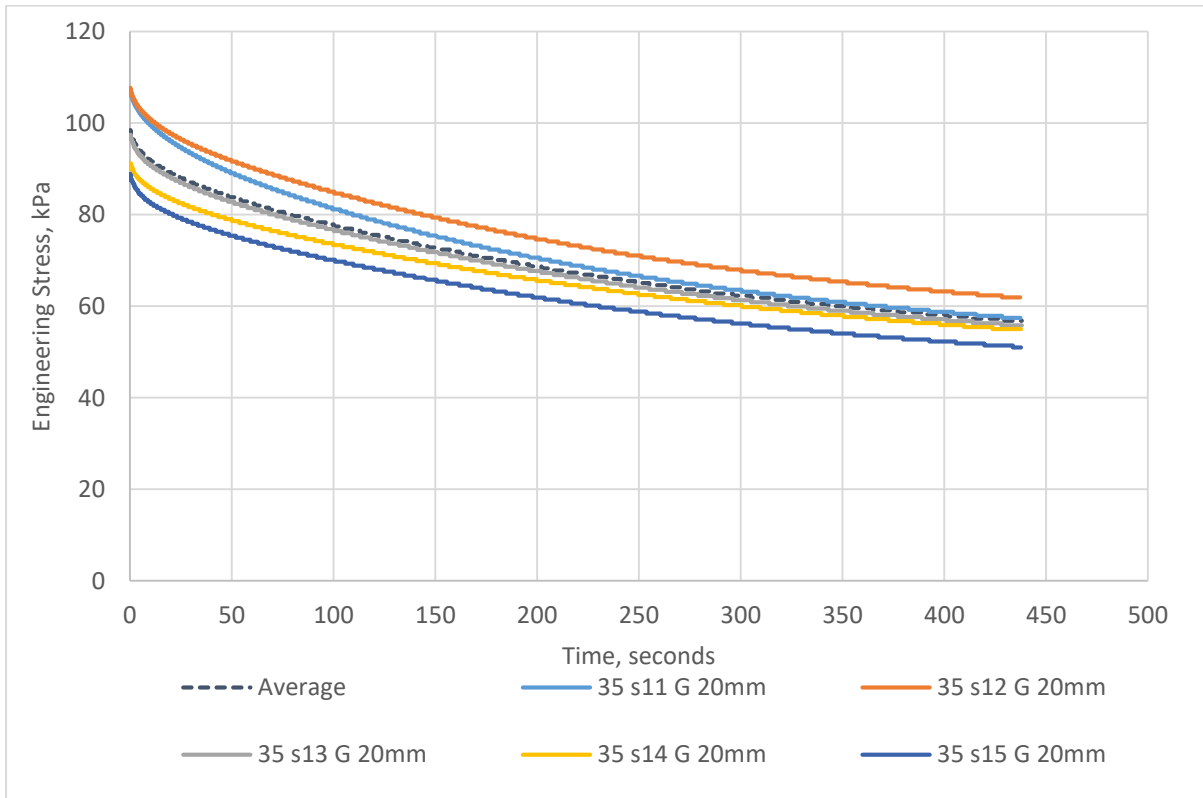


Figure 8-11 Results for creep response of gelatine at 0.25 strain after loading rates of 20mm/min

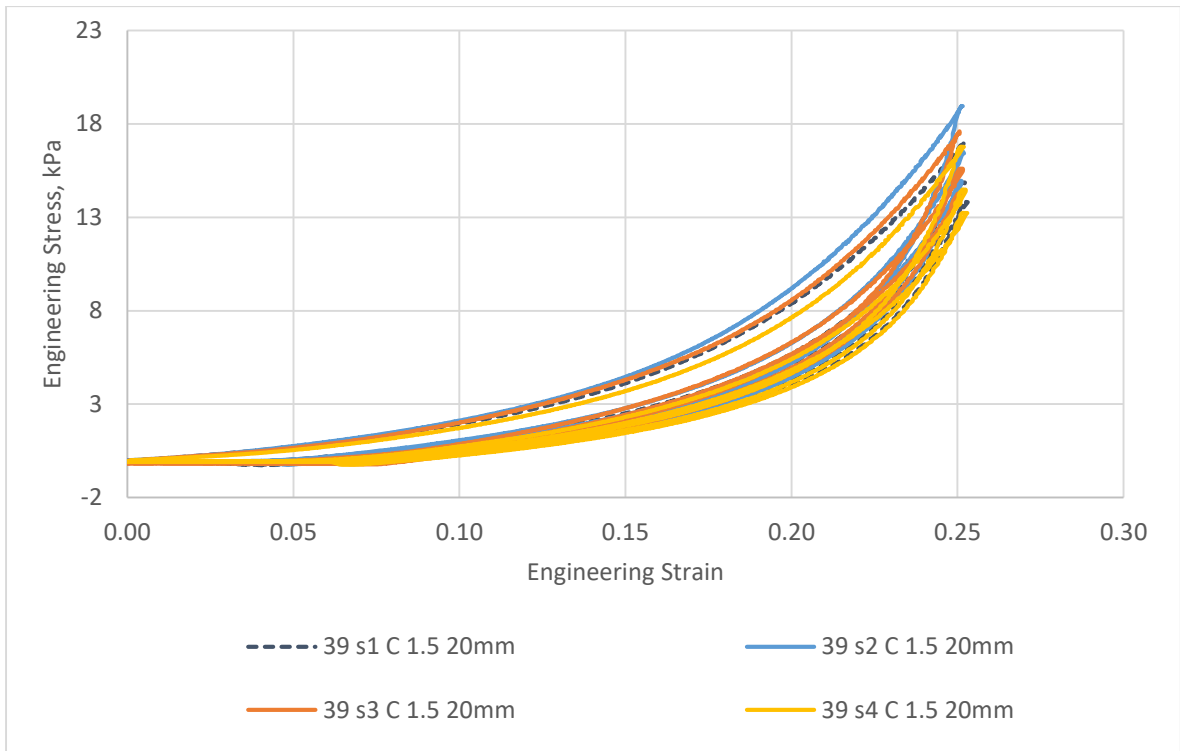


Figure 8-12 Results for cyclic compression response of gelatine at 1mm/min

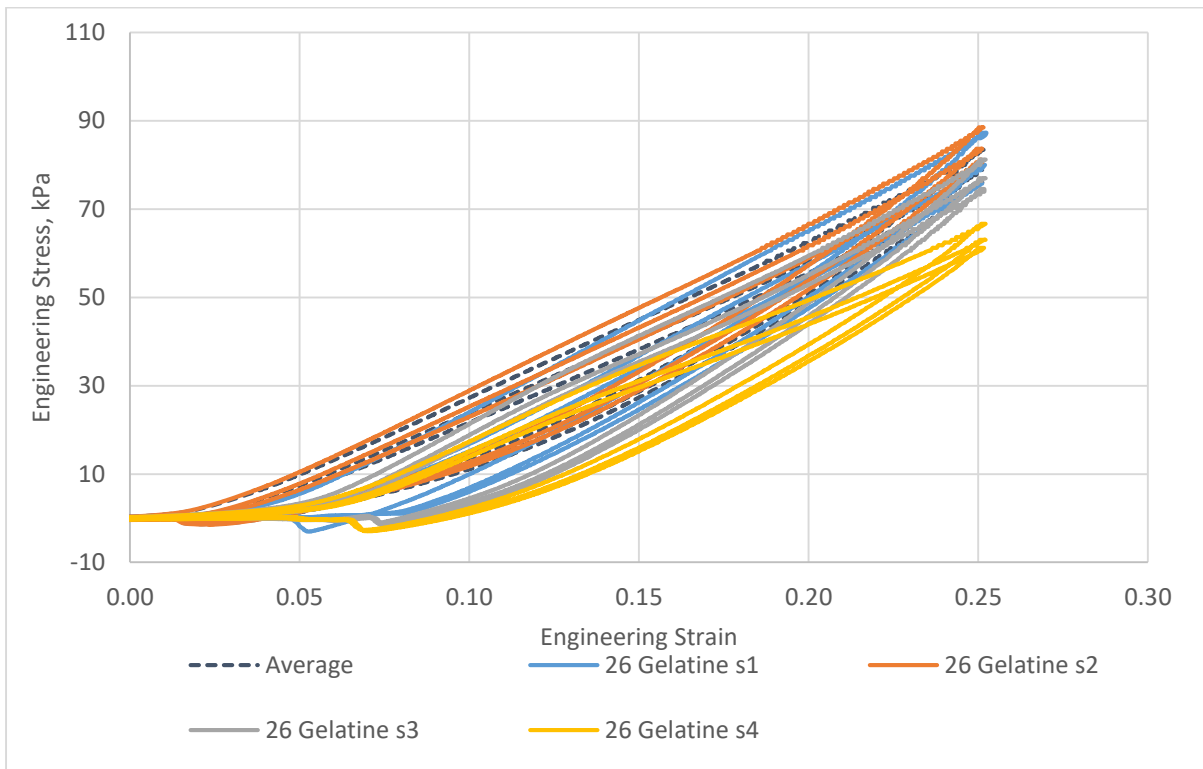


Figure 8-13 Results for cyclic compression response of gelatine at 20mm/min

8.1.3 Compression results: Carrageenan

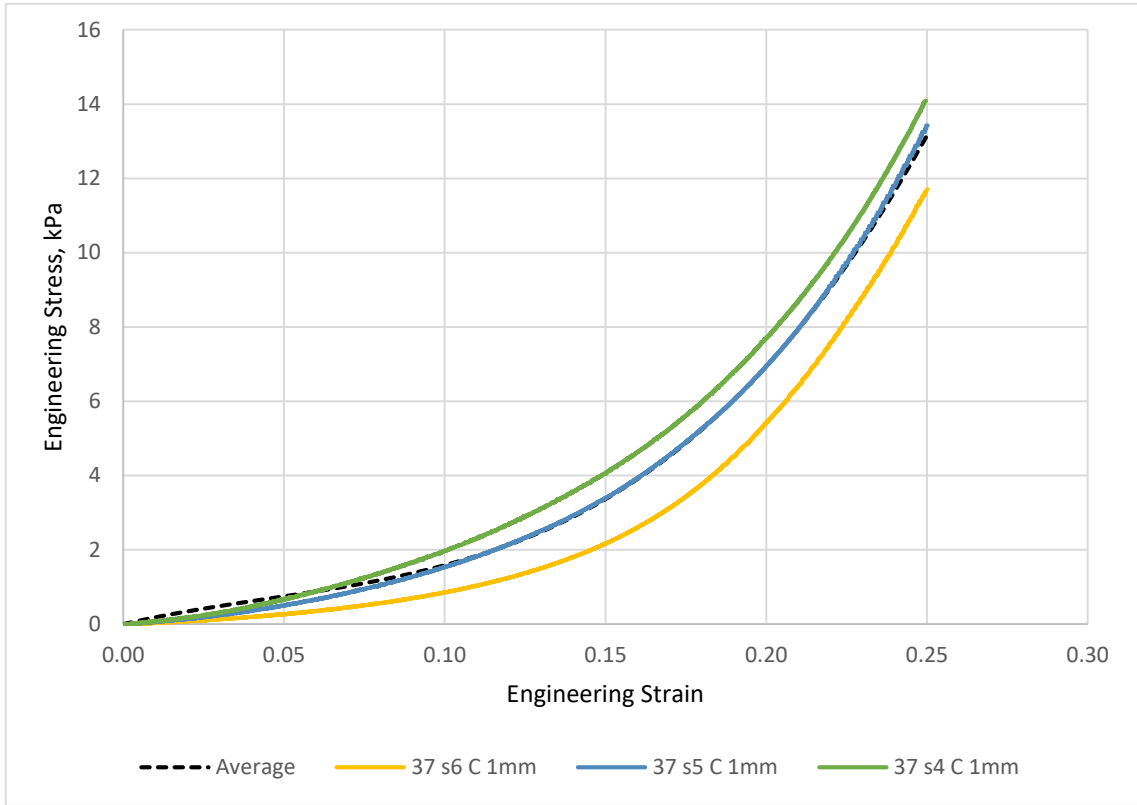


Figure 8-14 Results for compression of carrageenan to 0.25 strain at 1mm/min

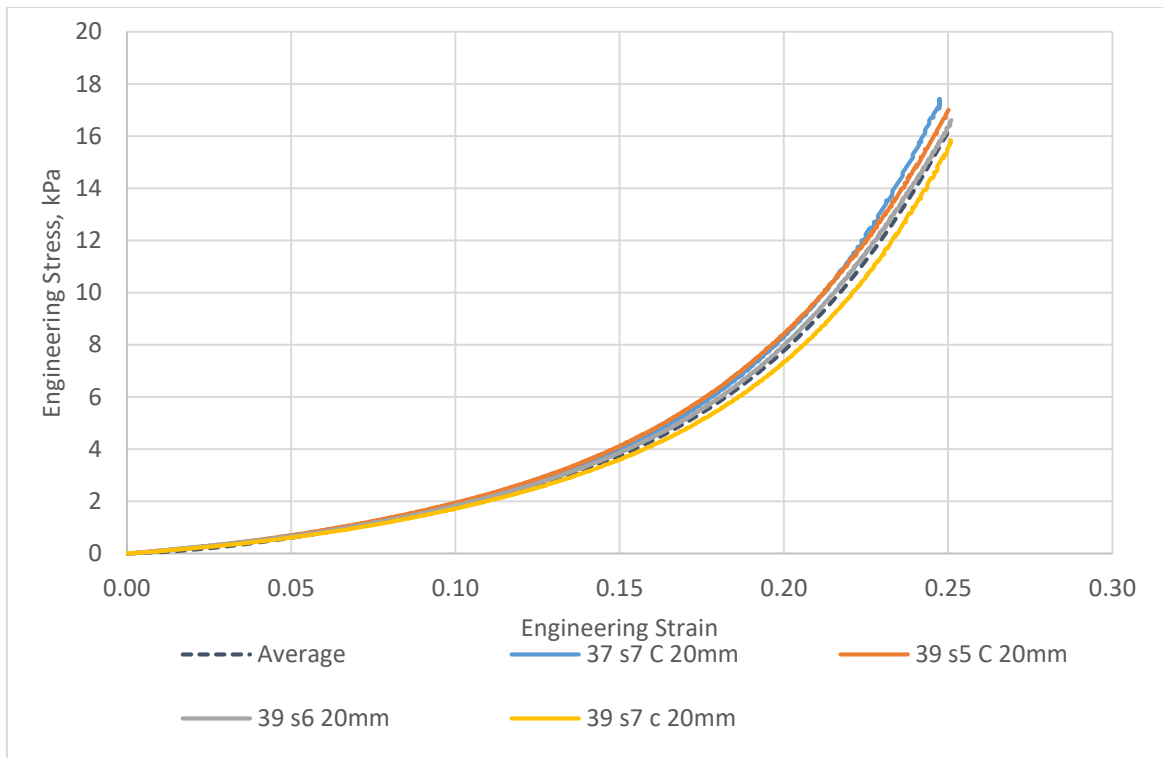


Figure 8-15 Results for compression of carrageenan to 0.25 strain at 20mm/min

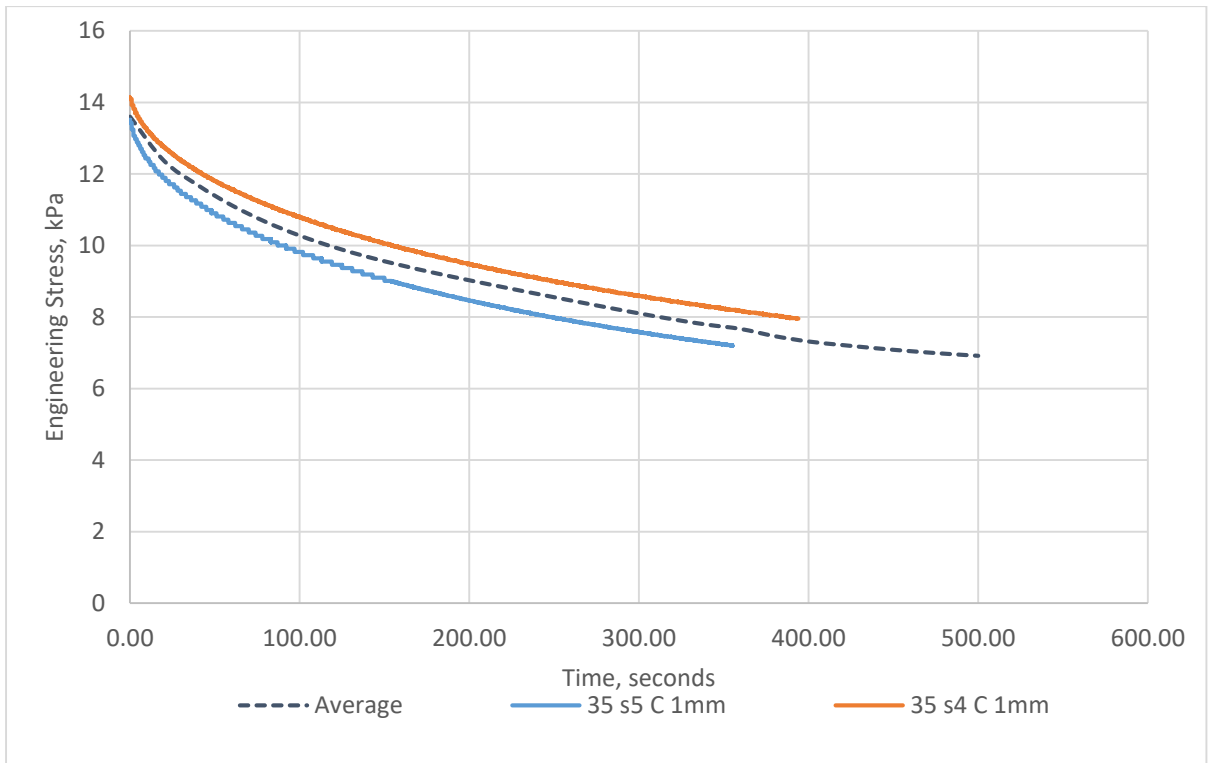


Figure 8-16 Results for creep response of carrageenan at 0.25 strain after loading rates of 1mm/min

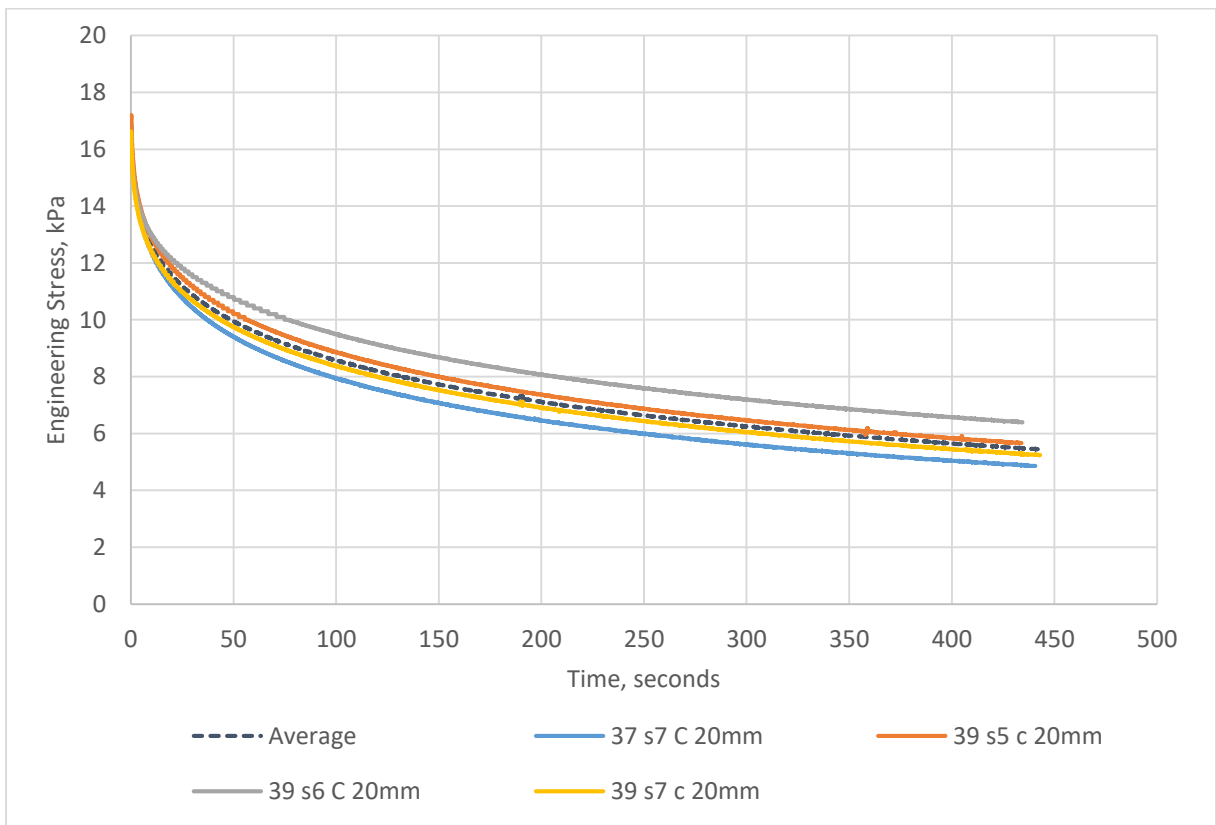


Figure 8-17 Results for creep response of carrageenan at 0.25 strain after loading rates of 20mm/min

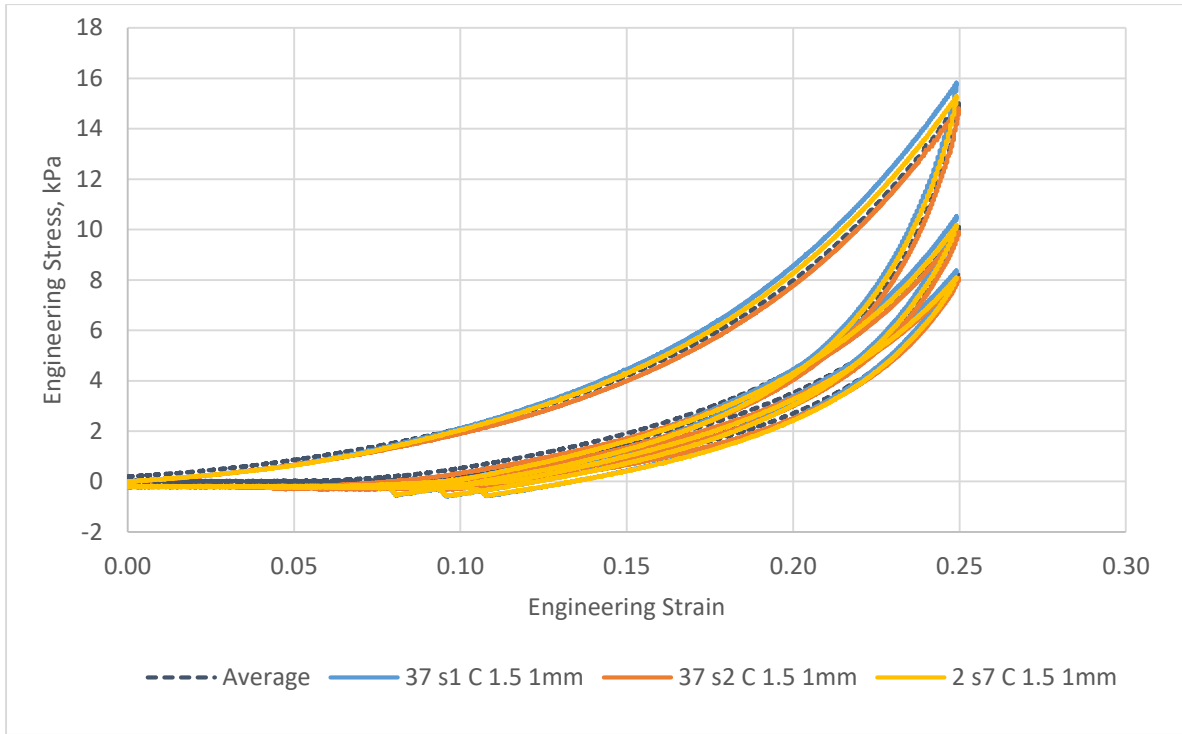


Figure 8-18 Results for cyclic compression response of carrageenan at 1mm/min

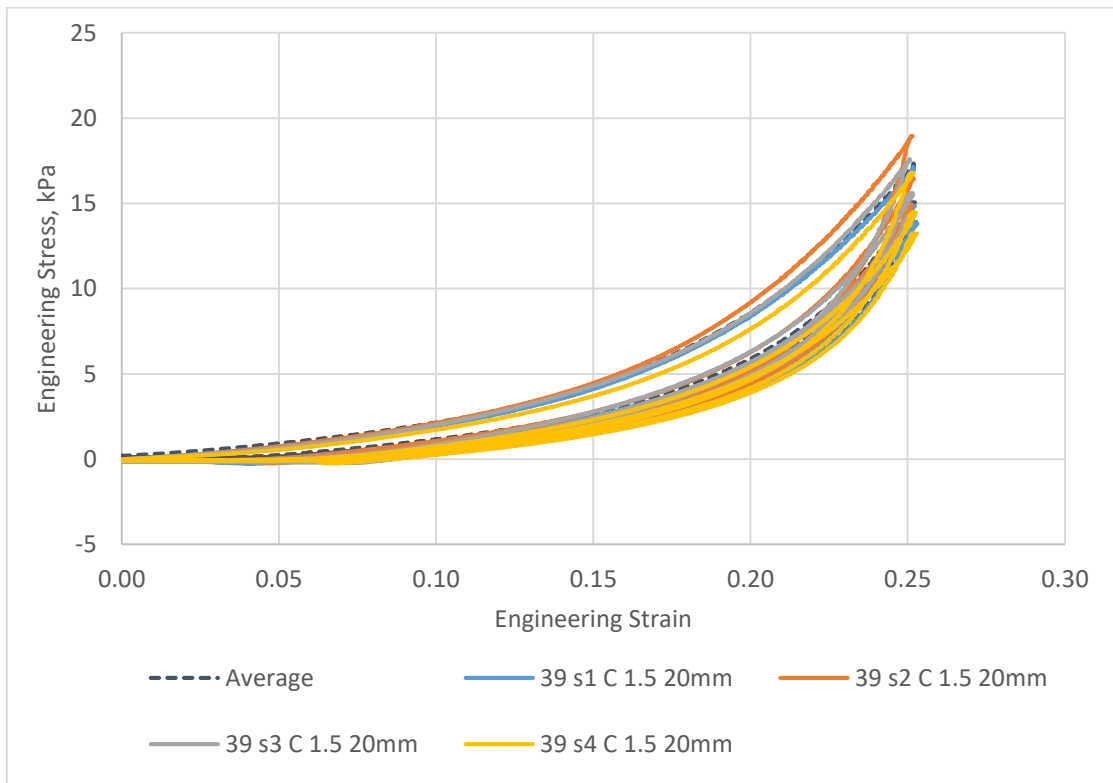


Figure 8-19 Results for cyclic compression response of carrageenan at 20mm/min

8.1.4 Compression results: Konjac

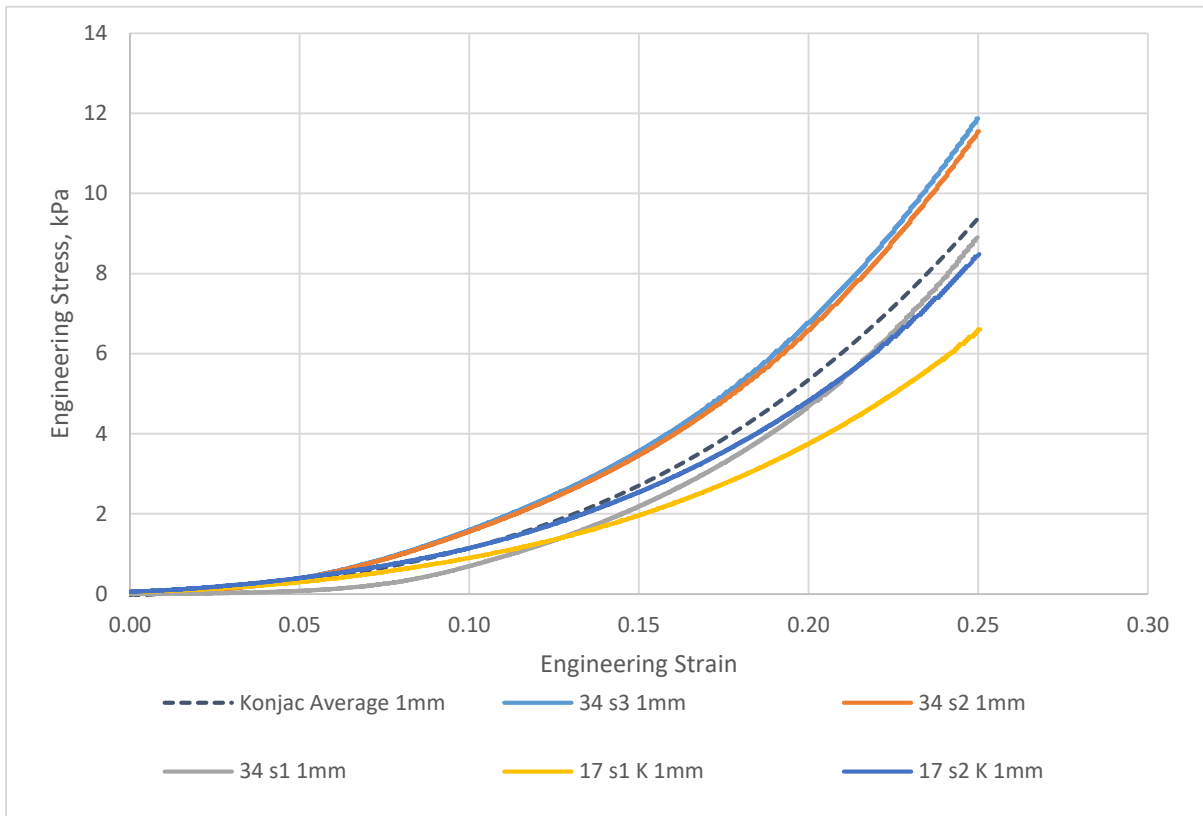


Figure 8-20 Results for compression of konjac to 0.25 strain at 1mm/min

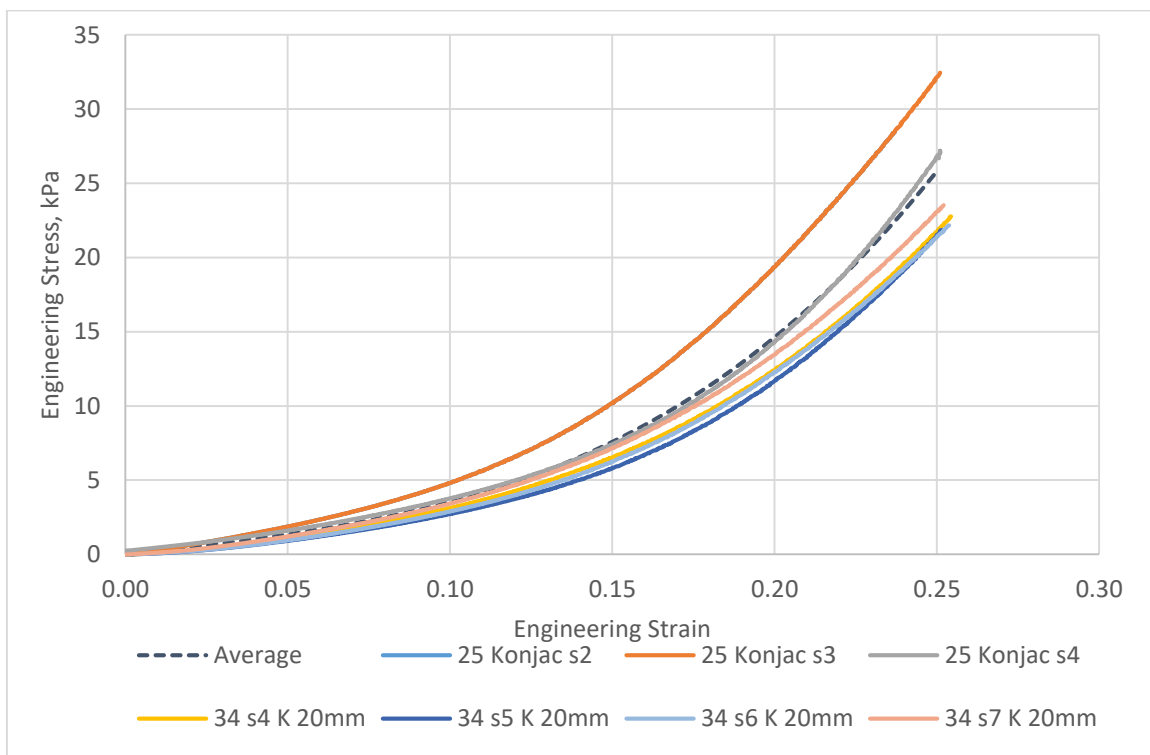


Figure 8-21 Results for compression of konjac to 0.25 strain at 20mm/min

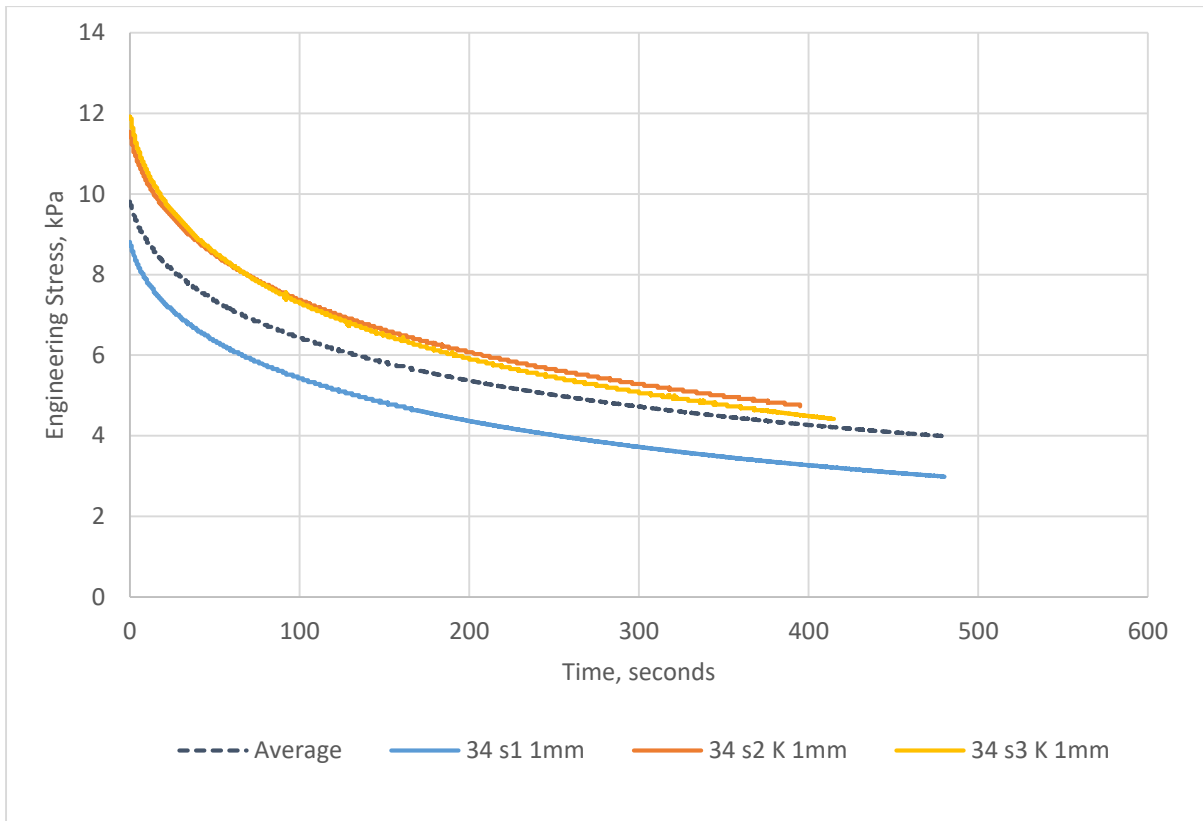


Figure 8-22 Results for creep response of konjac at 0.25 strain after loading rates of 1mm/min

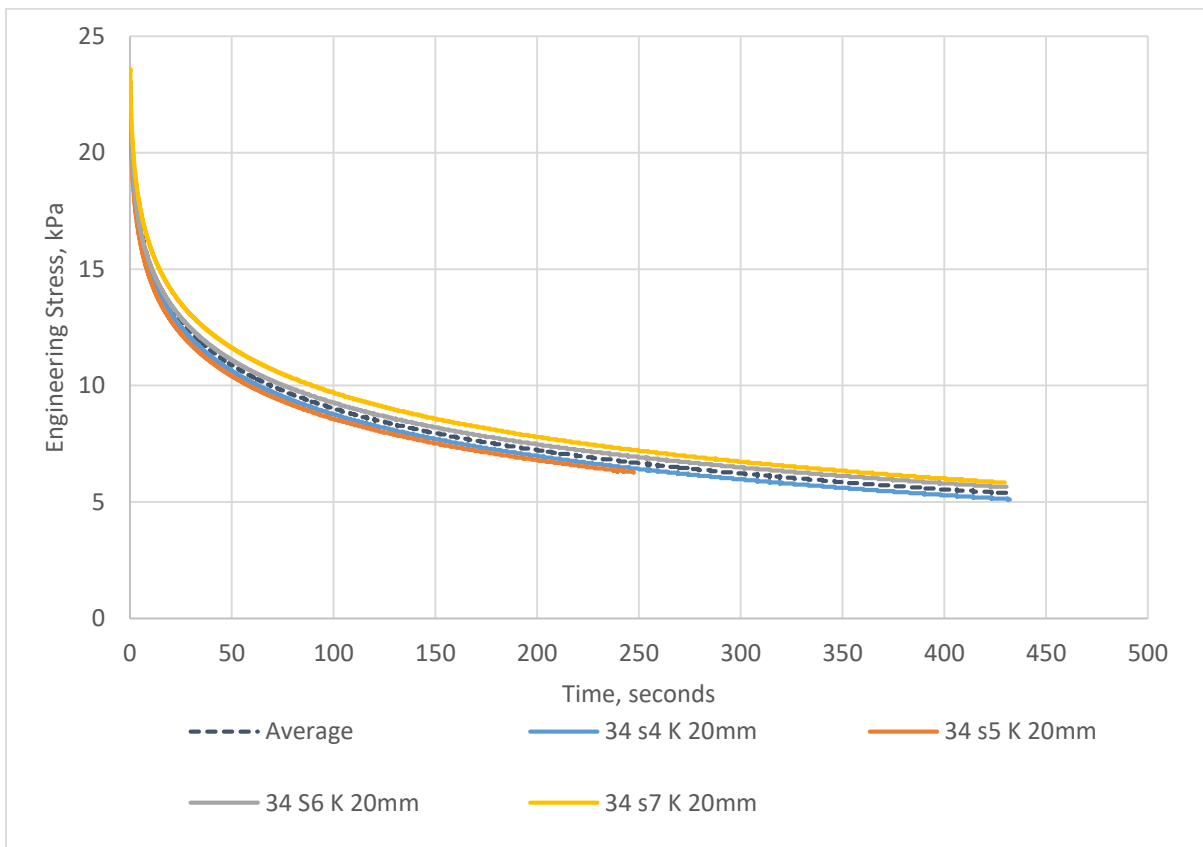


Figure 8-23 Results for creep response of konjac at 0.25 strain after loading rates of 20mm/min

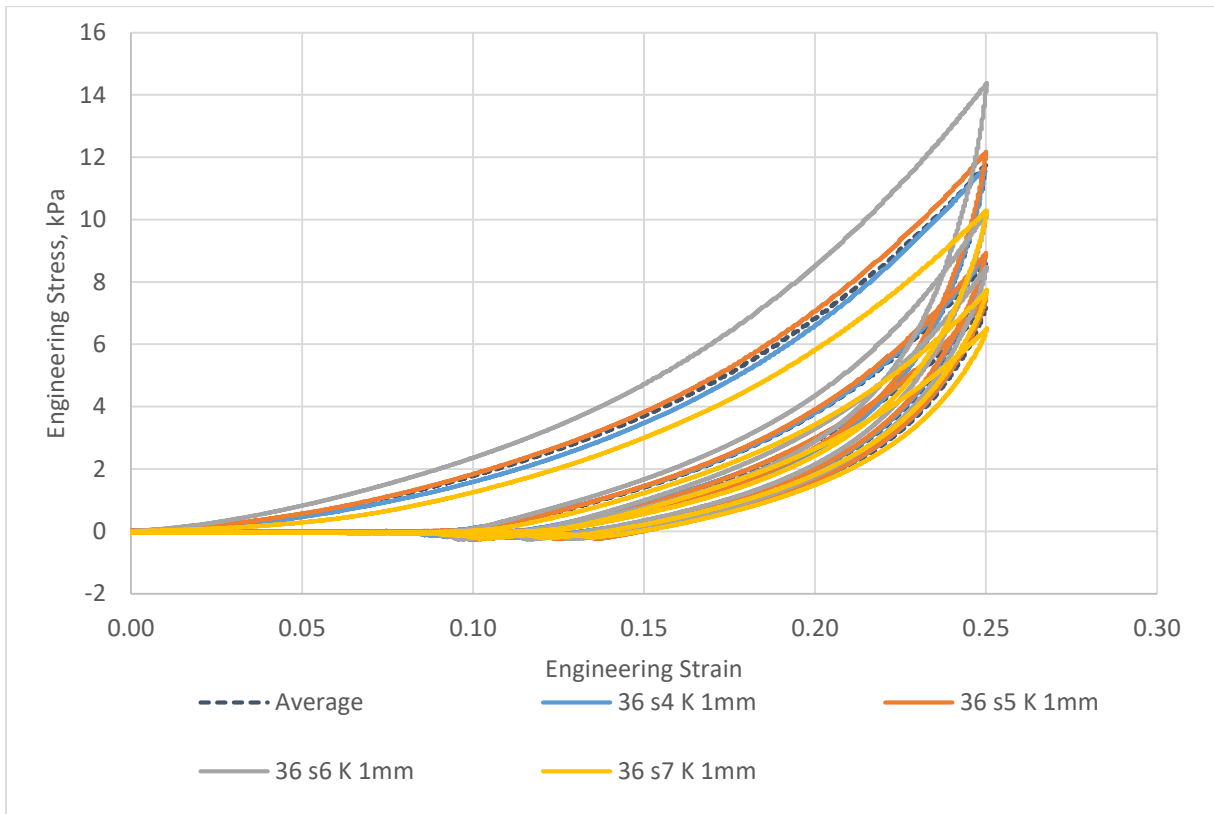


Figure 8-24 Results for cyclic compression response of konjac at 1mm/min

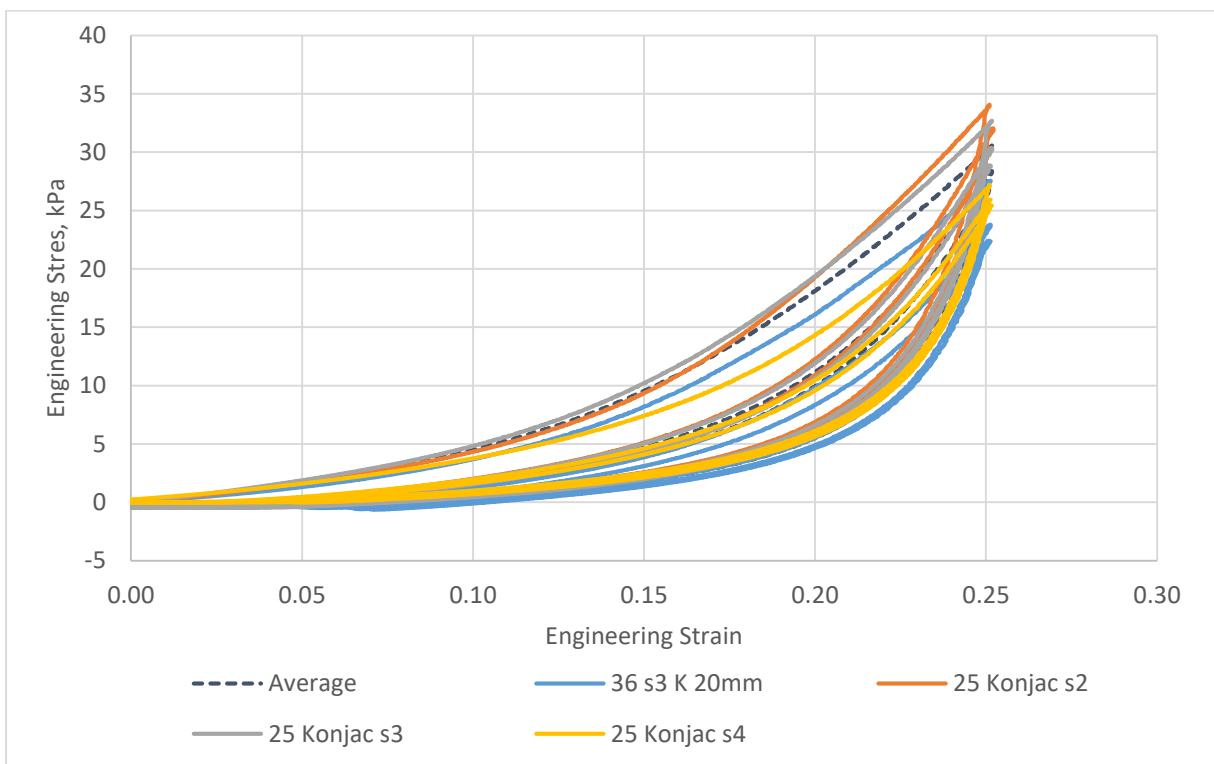


Figure 8-25 Results for cyclic compression response of konjac at 20mm/min

8.1.5 Tensile results: sugar addition

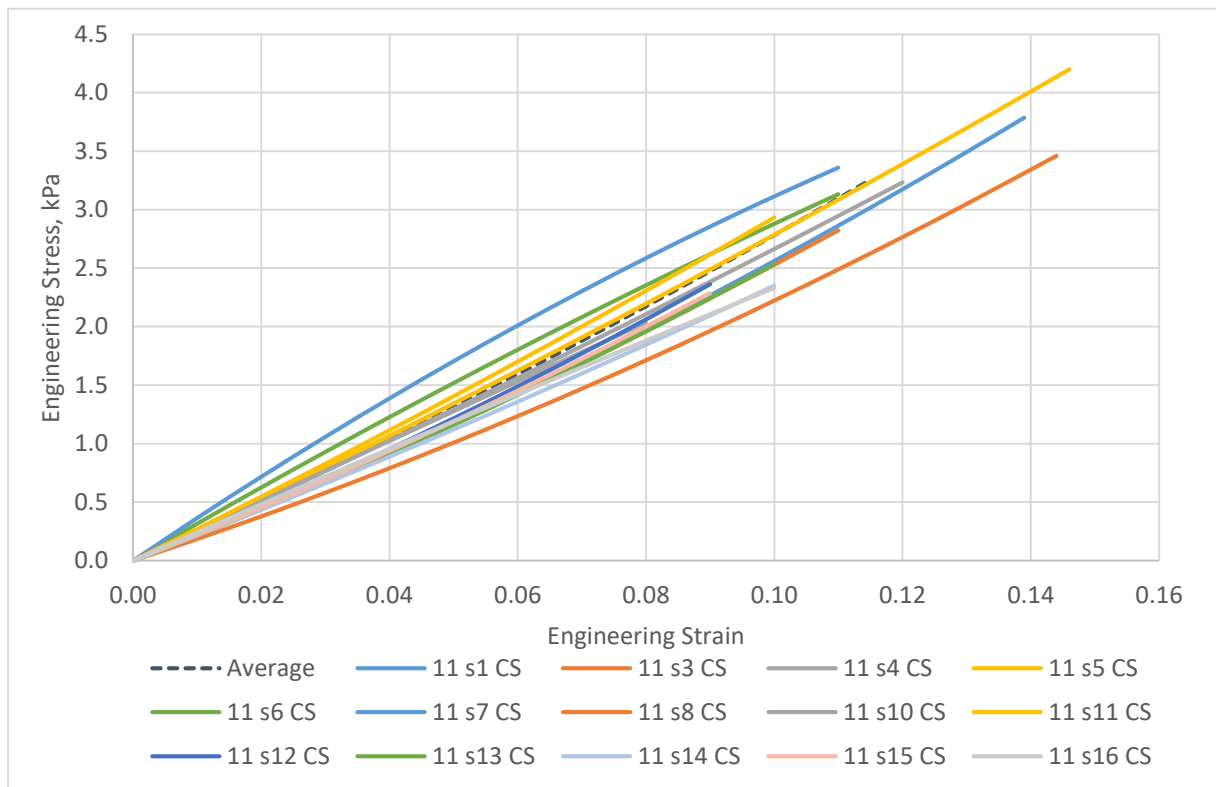


Figure 8-26: Tensile results for carrageenan with sugar

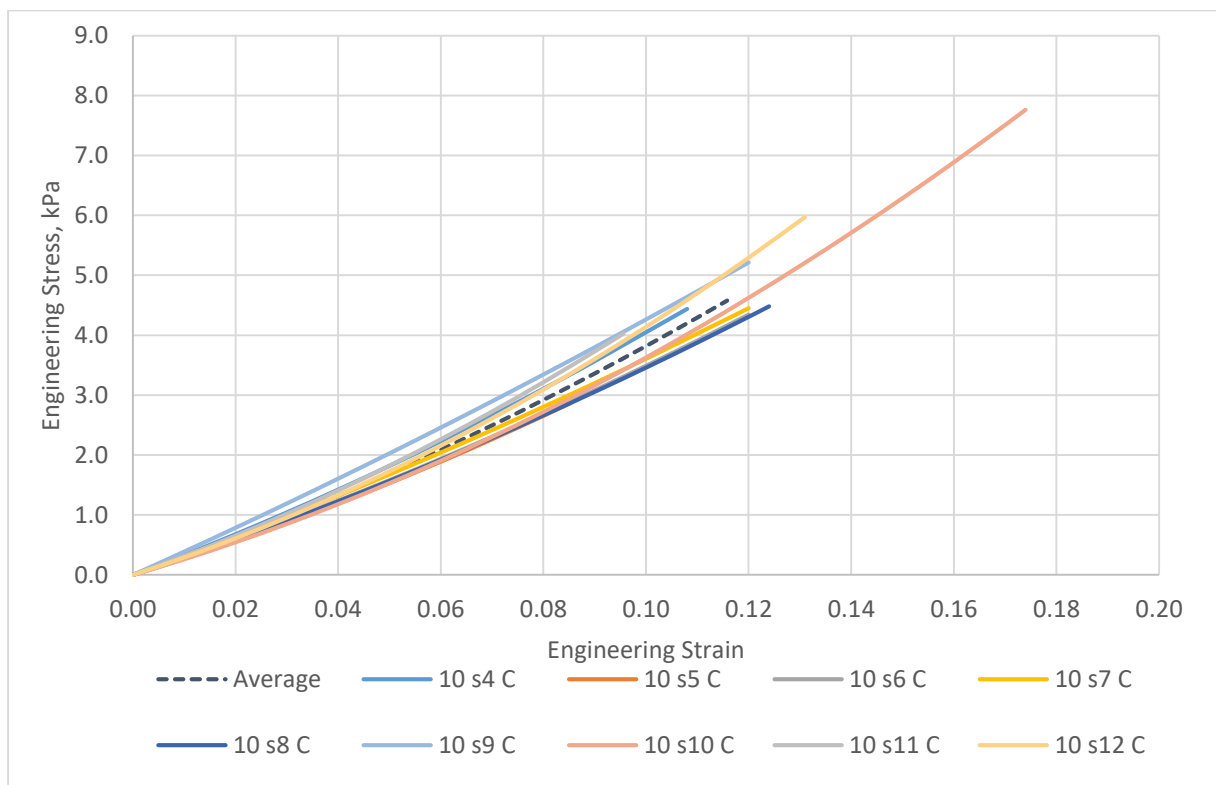


Figure 8-27: Tensile results for carrageenan without sugar

8.1.6 Tensile results: Gelatine

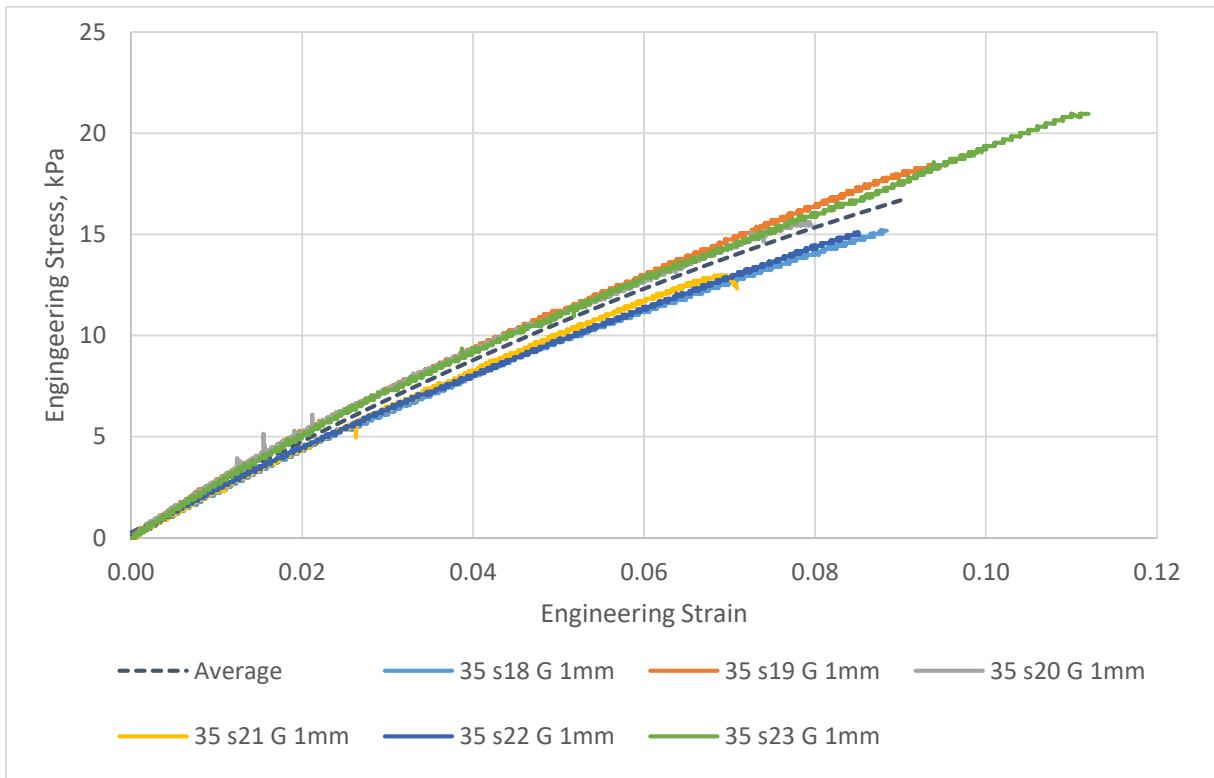


Figure 8-28 Tensile response of gelatine tested at 1mm/min until break

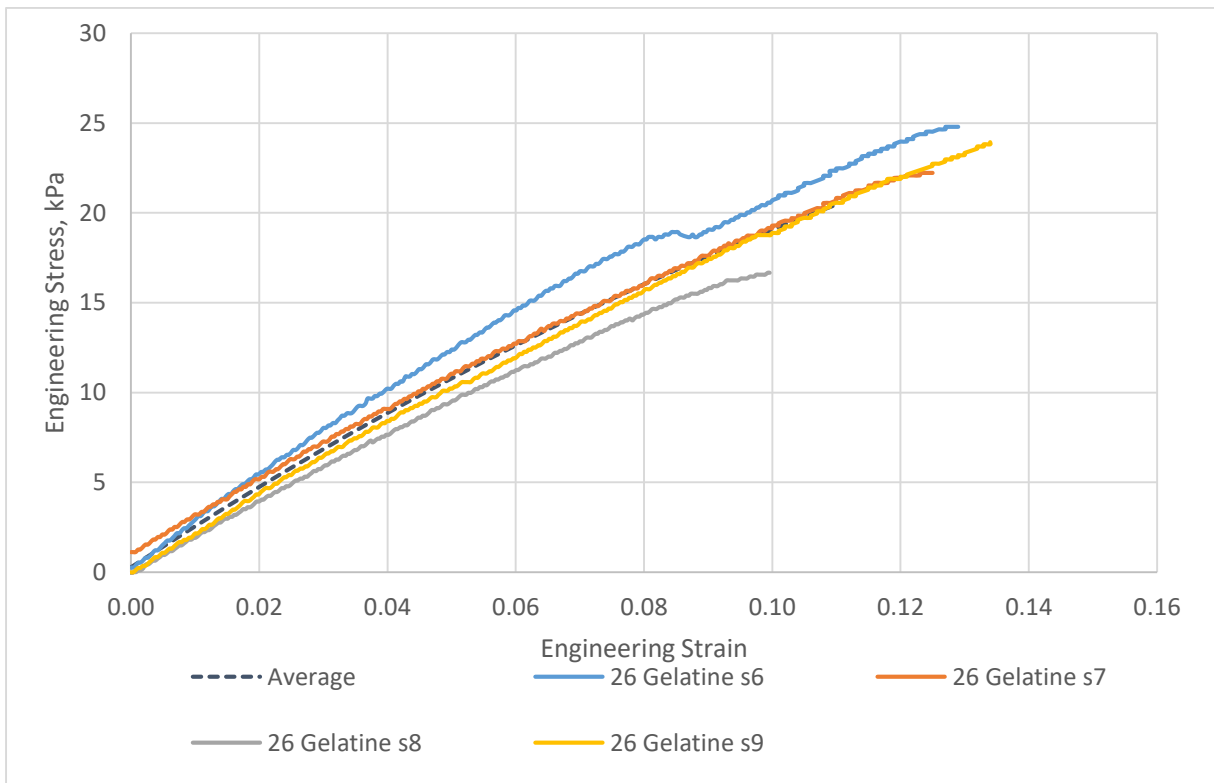


Figure 8-29 Tensile response of gelatine tested at 20mm/min until break

8.1.7 Tensile results: Carrageenan

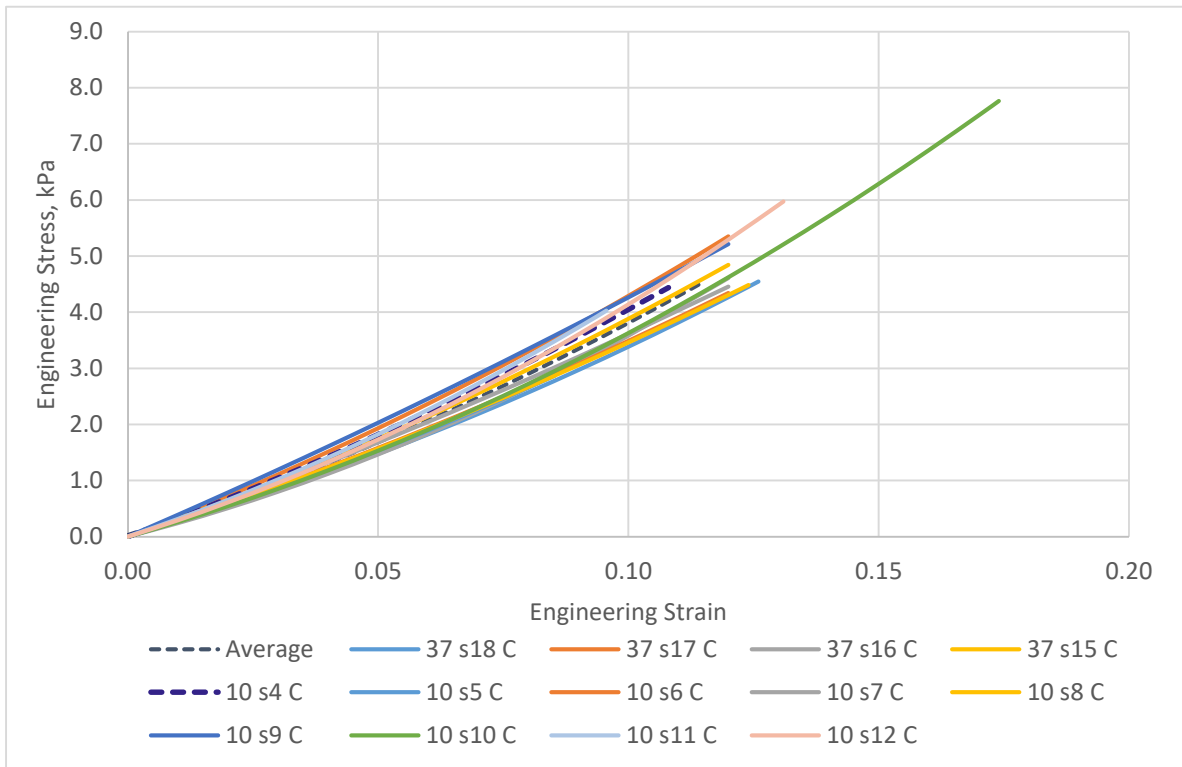


Figure 8-30 Tensile response of carrageenan tested at 1mm/min until break

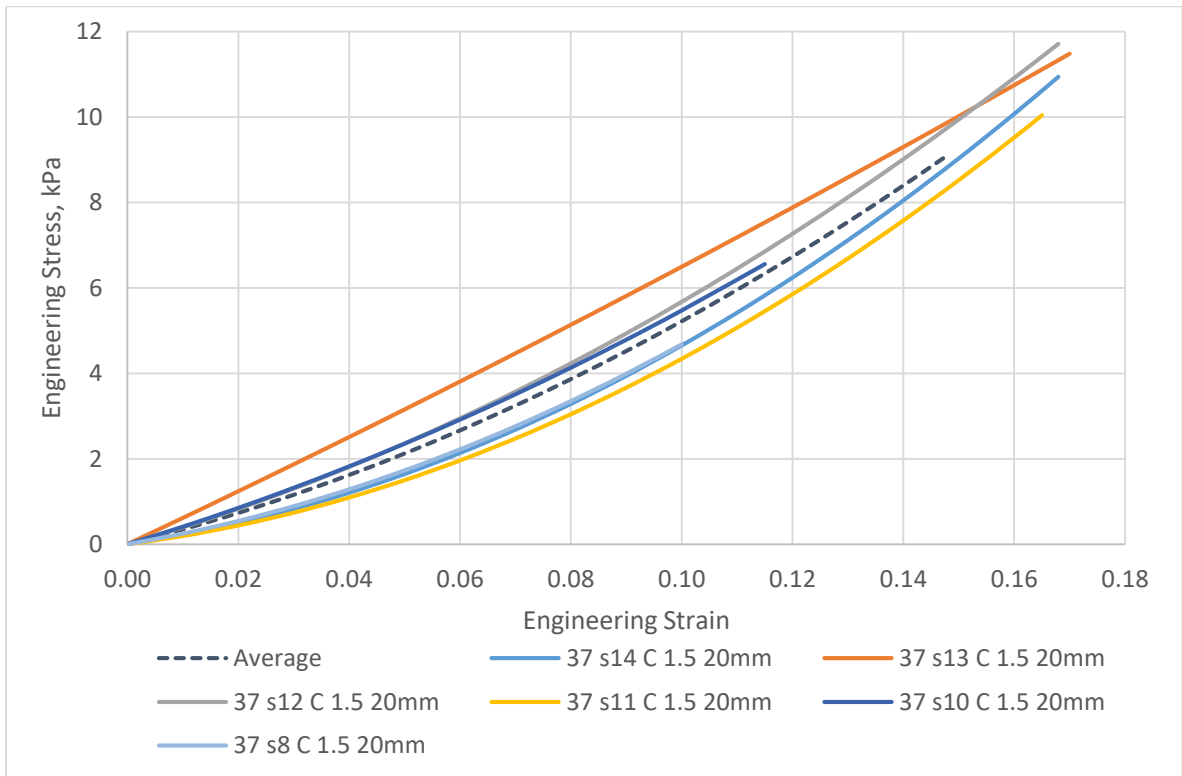


Figure 8-31 Tensile response of carrageenan tested at 20mm/min until break

8.1.8 Tensile results: Konjac

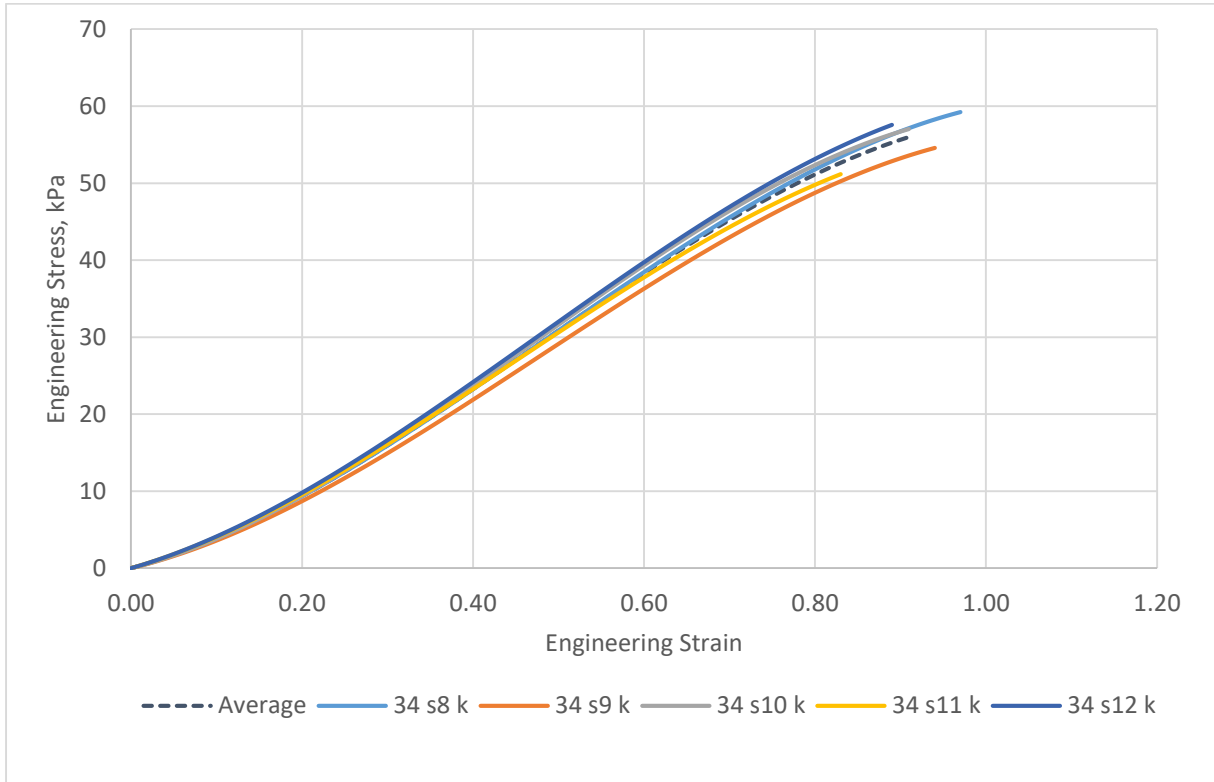


Figure 8-32 Tensile response of konjac tested at 1mm/min until break

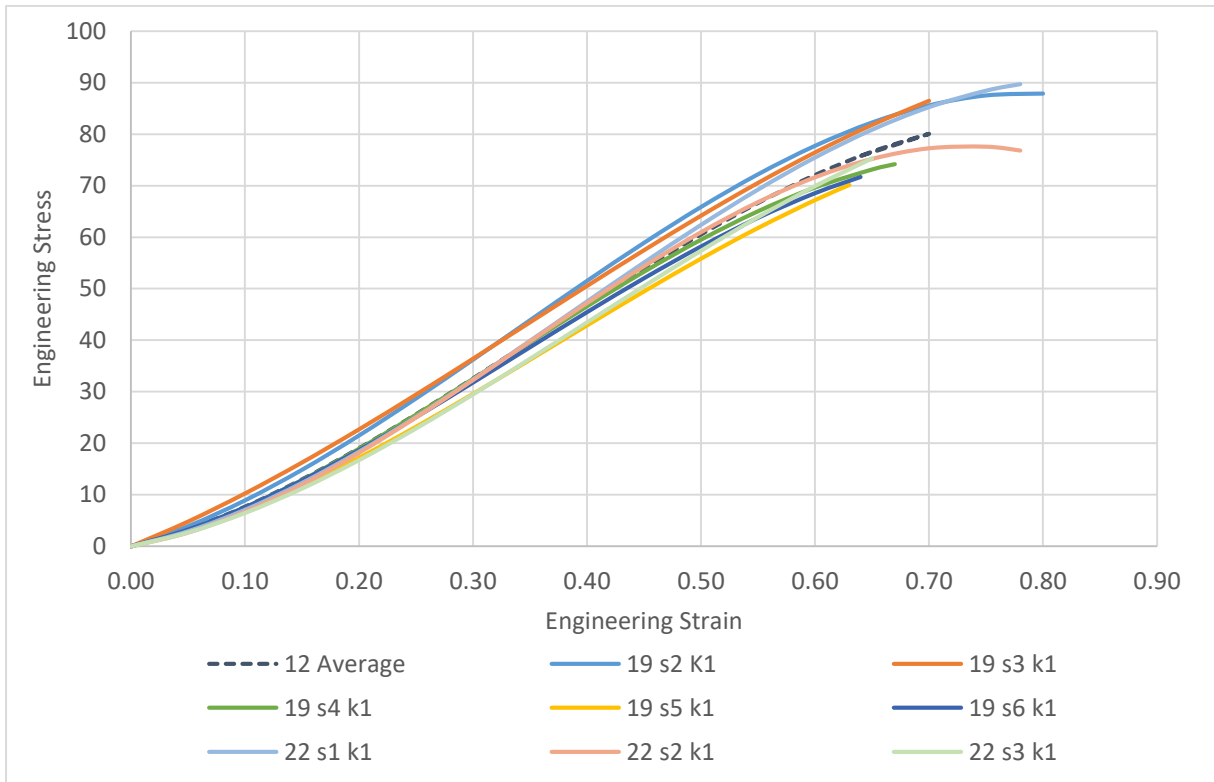


Figure 8-33 Tensile response of konjac tested at 12mm/min until break

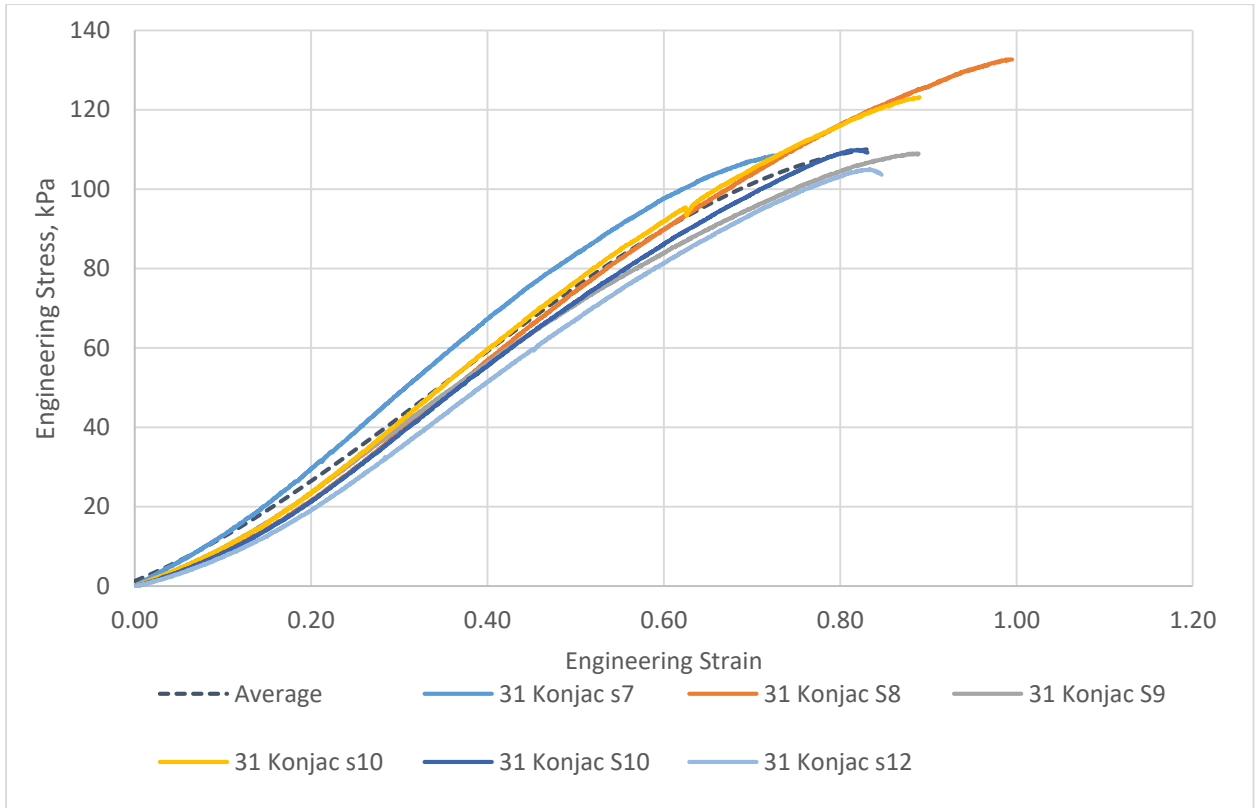


Figure 8-34 Tensile response of konjac tested at 20mm/min until break

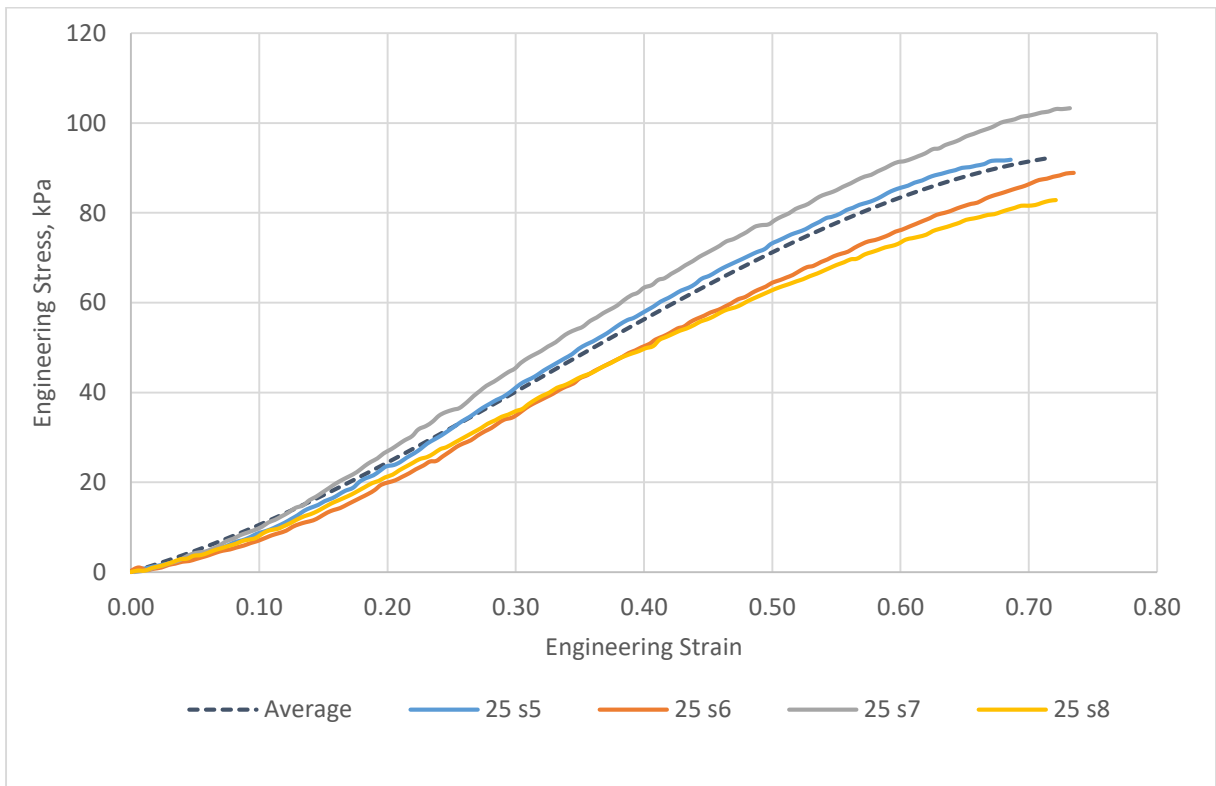


Figure 8-35 Tensile response of konjac tested at 300mm/min until break

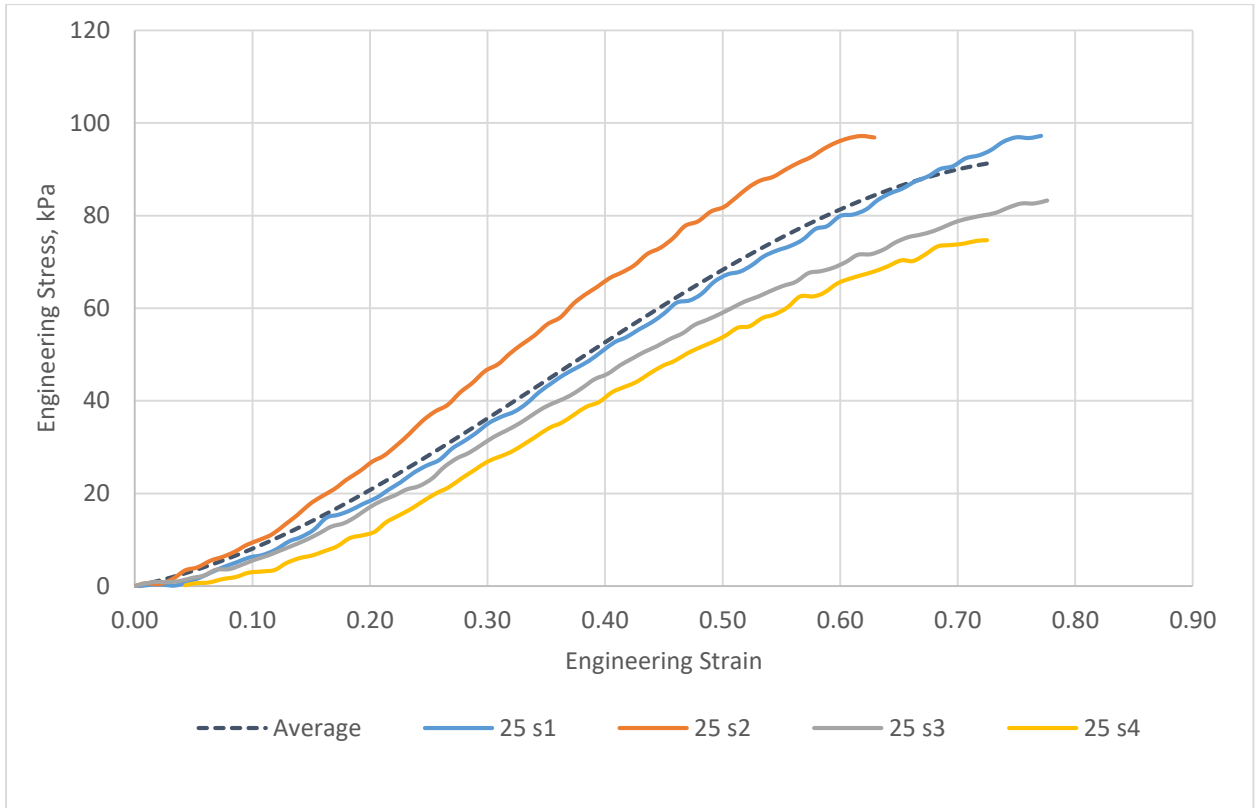


Figure 8-36 Tensile response of konjac tested at 600mm/min until break

8.1.9 Tensile results: with and without puncture hole

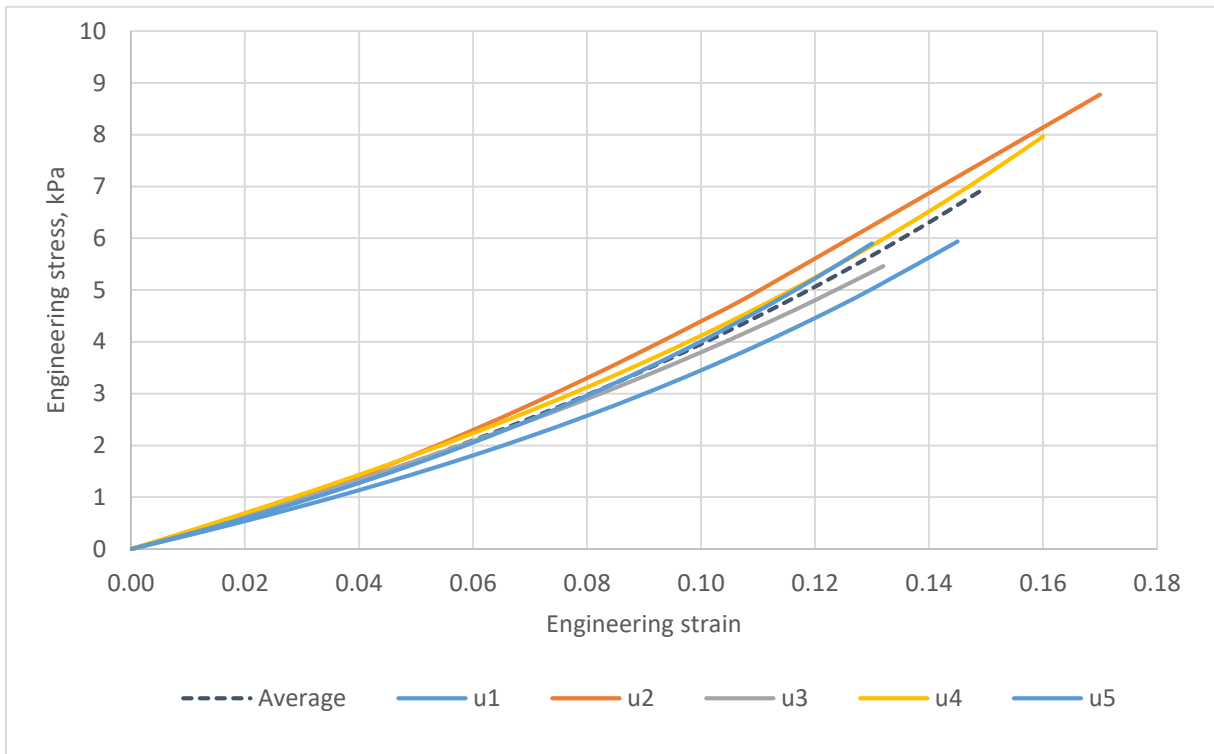


Figure 8-37 Tensile test without puncture

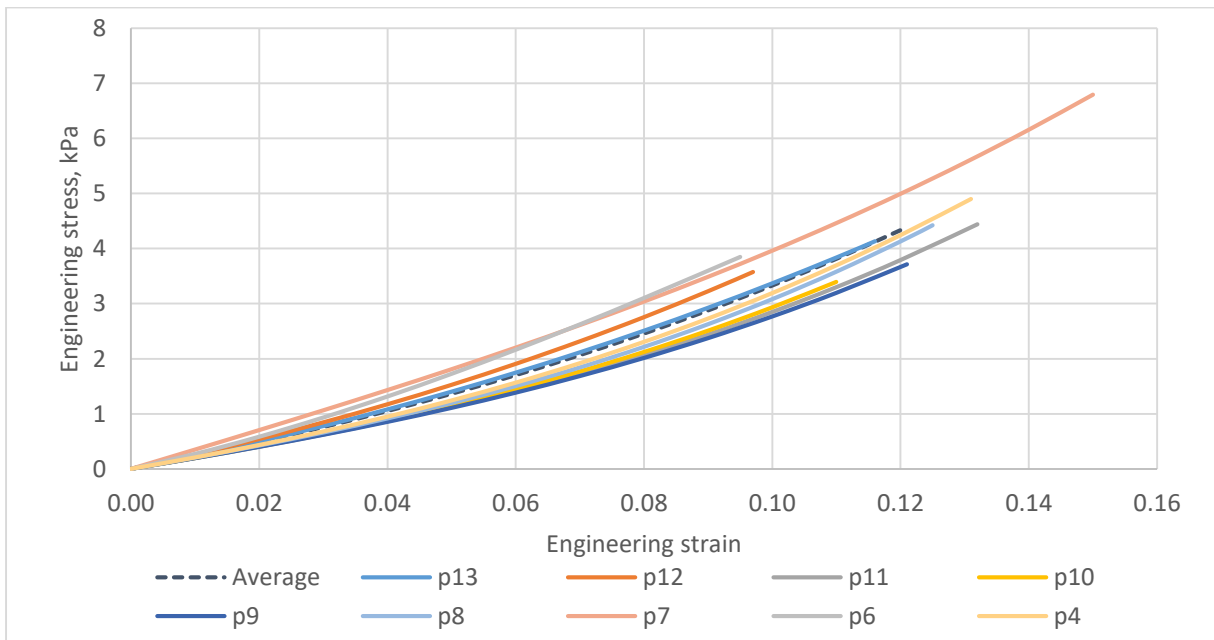


Figure 8-38 Tensile test with puncture

8.2 Numerical results used for determining strain optic coefficient in optical characterisation chapter

Frame		0	10	15	20	25	30	35	40
Sample 8	Retardation, nm	-	9	22	35	47	70	88	80
	x distance, pixels	47	47	48	45	43	44	43	43
	x strain	-	0.00	0.02	-0.04	-0.09	-0.06	-0.09	-0.09
	y distance, pixels	57	61	64	68	67	70	71	73
	y strain	-	0.07	0.12	0.19	0.18	0.23	0.25	0.28
	e1-e2	-	0.07	0.10	0.24	0.26	0.29	0.33	0.37
	Thickness, mm	6.1	6.01	5.92	5.83	5.74	5.65	5.55	5.46
	K software, x10 ⁻⁵	-	Anomaly	3.66	2.55	3.14	4.25	4.79	4.00
Sample 10	Retardation, nm	-	24	42	56	83	90	78	20
	x distance, pixels	54	47	44	42	44	41	40	41
	x strain	-	-0.13	-0.19	-0.22	-0.19	-0.24	-0.26	-0.24
	y distance, pixels	58	60	63	65	67	70	73	78
	y strain	-	0.03	0.09	0.12	0.16	0.21	0.26	0.34
	e1-e2	-	0.16	0.27	0.34	0.34	0.45	0.52	0.59
	Thickness, mm	6.4	6.30	6.24	6.19	6.14	6.09	6.04	5.98
	K software, x10 ⁻⁵	-	2.32	2.48	2.64	3.97	3.30	2.50	0.57
Sample 11	Retardation, nm	-	7	22	34	45	60	82	87
	x distance, pixels	48	47	47	43	45	46	43	42
	x strain	-	-0.02	-0.02	-0.10	-0.06	-0.04	-0.10	-0.13
	y distance, pixels	55	58	59	62	63	65	69	70
	y strain	-	0.05	0.07	0.13	0.15	0.18	0.25	0.27
	e1-e2	-	0.08	0.09	0.23	0.21	0.22	0.36	0.40
	Thickness, mm	5.7	5.58	5.52	5.46	5.40	5.34	5.29	5.23
	K software, x10 ⁻⁵	-	Anomaly	4.26	2.69	4.00	5.02	4.33	4.19

Table 8-1: Numerical results for strain optic coefficient at 20mm/min, part 1/2

Frame		0	10	15	20	25	30	35	40
Sample 12	Retardation, nm	-	23	42	71	90	100	110	110
	x distance, pixels	46	44	44	44	42	43	41	42
	x strain	-	-0.04	-0.04	-0.04	-0.09	-0.07	-0.11	-0.09
	y distance, pixels	53	58	62	64	68	69	71	72
	y strain	-	0.09	0.17	0.21	0.28	0.30	0.34	0.36
	$\varepsilon_1 - \varepsilon_2$	-	0.14	0.21	0.25	0.37	0.37	0.45	0.45
	Thickness, mm	6.99	6.91	6.88	6.84	6.80	6.76	6.72	6.68
	K software, $\times 10^{-5}$	-	2.41	2.86	4.14	3.58	4.03	3.65	3.69
Sample 14	Retardation, nm	-	5	18	29	44	64	90	82
	x distance, pixels	47	45	48	43	42	40	41	40
	x strain	-	-0.04	0.02	-0.09	-0.11	-0.15	-0.13	-0.15
	y distance, pixels	55	59	63	67	67	69	72	74
	y strain	-	0.07	0.15	0.22	0.22	0.25	0.31	0.35
	$\varepsilon_1 - \varepsilon_2$	-	0.12	0.12	0.30	0.32	0.40	0.44	0.49
	Thickness, mm	5.8	5.69	5.63	5.58	5.52	5.46	5.41	5.35
	K software, $\times 10^{-5}$	-	Anomaly	2.57	1.71	2.46	2.90	3.81	3.10
Sample 15	Retardation, nm	-	5	11	25	35	48	68	87
	x distance, pixels	50	48	46	46	48	42	43	41
	x strain	-	-0.04	-0.08	-0.08	-0.04	-0.16	-0.14	-0.18
	y distance, pixels	54	55	59	59	62	64	65	68
	y strain	-	0.02	0.09	0.09	0.15	0.19	0.20	0.26
	$\varepsilon_1 - \varepsilon_2$	-	0.06	0.17	0.17	0.19	0.35	0.34	0.44
	Thickness, mm	5.3	5.18	5.12	5.06	5.00	4.94	4.88	4.82
	K software, $\times 10^{-5}$	-	1.65	1.24	2.86	3.72	2.81	4.05	4.11

Table 8-2: Numerical results for strain optic coefficient at 20mm/min, part 2/2

	Frame	0	10	15	20	25
Sample 5	Retardation, nm	-	20	43	50	84
	x distance, pixels	51	49	48	47	45
	x strain	-	-0.04	-0.06	-0.08	-0.12
	y distance, pixels	57	61	64	68	68
	y strain	-	0.07	0.12	0.19	0.19
	$\varepsilon_1 - \varepsilon_2$	-	0.11	0.18	0.27	0.31
	Thickness, mm	5.1	5.02	4.99	4.95	4.91
	K software, x10 ⁻⁵	-	3.64	4.75	3.72	5.51
Sample 6	Retardation, nm	-	20	35	47	75
	x distance, pixels	51	49	47	45	46
	x strain	-	-0.04	-0.08	-0.12	-0.10
	y distance, pixels	53	56	58	62	67
	y strain	-	0.06	0.09	0.17	0.26
	$\varepsilon_1 - \varepsilon_2$	-	0.10	0.17	0.29	0.36
	Thickness, mm	5.75	5.58	5.53	5.47	5.41
	K software, x10 ⁻⁵	-	3.74	3.67	2.99	3.83
Sample 7	Retardation, nm	-	19	49	61	47
	x distance, pixels	46	46	43	41	39
	x strain	-	0.00	-0.07	-0.11	-0.15
	y distance, pixels	51	56	60	63	63
	y strain	-	0.10	0.18	0.24	0.24
	$\varepsilon_1 - \varepsilon_2$	-	0.10	0.24	0.34	0.39
	Thickness, mm	4.39	4.27	4.21	4.15	4.09
	K software, x10 ⁻⁵	-	4.54	4.81	4.27	2.97
Sample 8	Retardation, nm	-	16	44	42	75
	x distance, pixels	54	48	48	45	42
	x strain	-	-0.11	-0.11	-0.17	-0.22
	y distance, pixels	57	61	64	64	65
	y strain	-	0.07	0.12	0.12	0.14
	$\varepsilon_1 - \varepsilon_2$	-	0.18	0.23	0.29	0.36
	Thickness, mm	5.3	5.22	5.19	5.15	5.11
	K software, x10 ⁻⁵	-	1.69	3.63	2.82	4.05

Table 8-3: Numerical results for strain optic coefficient at 300mm/min

	Frame	0	1	2	3	
Sample 1	Retardation, nm	-	15	34	35	
	x distance, pixels	46	44	43	39	
	x strain	-	-0.04	-0.07	-0.15	
	y distance, pixels	50	55	58	65	
	y strain	-	0.10	0.16	0.30	
	$\varepsilon_1 - \varepsilon_2$	-	0.14	0.23	0.45	
	Thickness, mm	5.35	5.26	5.17	5.08	
	K software, x10 ⁻⁵	-	1.99	2.92	1.52	
Sample 2	Retardation, nm	-	29	42	52	
	x distance, pixels	47	45	41	39	
	x strain	-	-0.04	-0.13	-0.17	
	y distance, pixels	49	53	59	65	
	y strain	-	0.08	0.20	0.33	
	$\varepsilon_1 - \varepsilon_2$	-	0.12	0.33	0.50	
	Thickness, mm	5.11	4.99	4.93	4.87	
	K software, x10 ⁻⁵	-	4.68	2.57	2.15	
Sample 3	Retardation, nm	-	18	48	100	
	x distance, pixels	52	49	47	44	
	x strain	-	-0.06	-0.10	-0.15	
	y distance, pixels	55	55	60	66	
	y strain	-	0.00	0.09	0.20	
	$\varepsilon_1 - \varepsilon_2$	-	0.06	0.19	0.35	
	Thickness, mm	6.5	6.40	6.34	6.29	
	K software, x10 ⁻⁵	-	4.88	4.04	4.49	
	Frame	0	10	15	20	25
Sample 4	Retardation, nm	-	21	58	79	95
	x distance, pixels	52.00	45	42	43	39
	x strain	-	-0.02	-0.09	-0.07	-0.15
	y distance, pixels	55.00	56	64	68	70
	y strain	-	0.08	0.23	0.31	0.35
	$\varepsilon_1 - \varepsilon_2$	-	0.10	0.32	0.37	0.50
	Thickness, mm	6.50	5.38	5.32	5.26	5.20
	K software, x10 ⁻⁵	-	3.96	3.43	4.03	3.66

Table 8-4: Numerical results for strain optic coefficient at 600mm/min

8.3 Full results from needle insertion experiments chapter

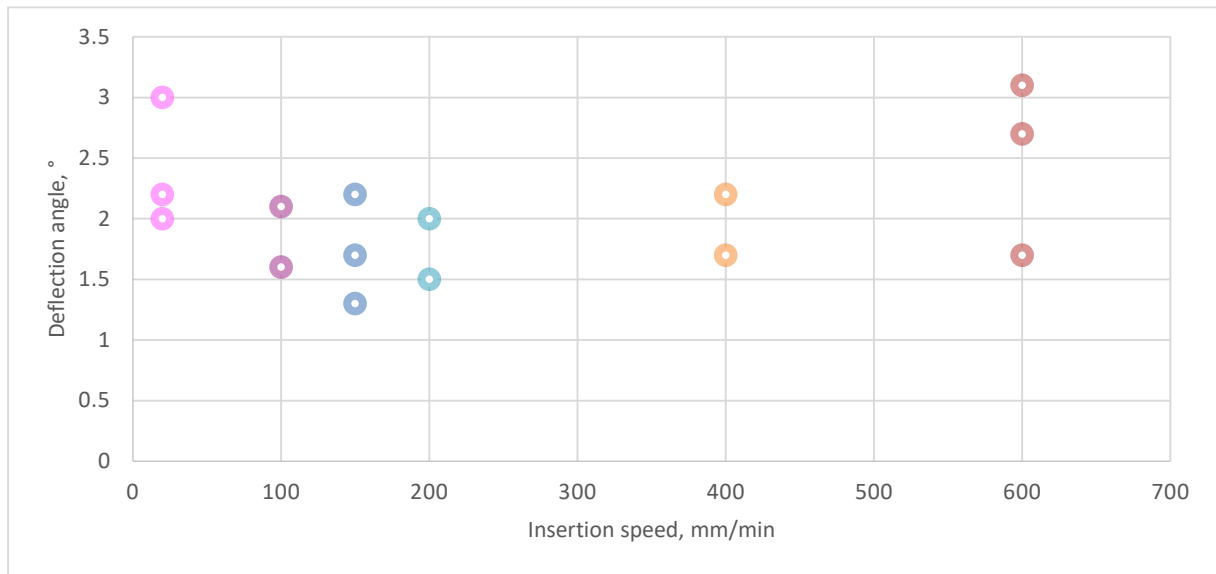


Figure 8-39: Old relationship between needle insertion speed and deflection angle – initial measurement method

8.3.1 Needle response through inhomogeneous laminate surrogates

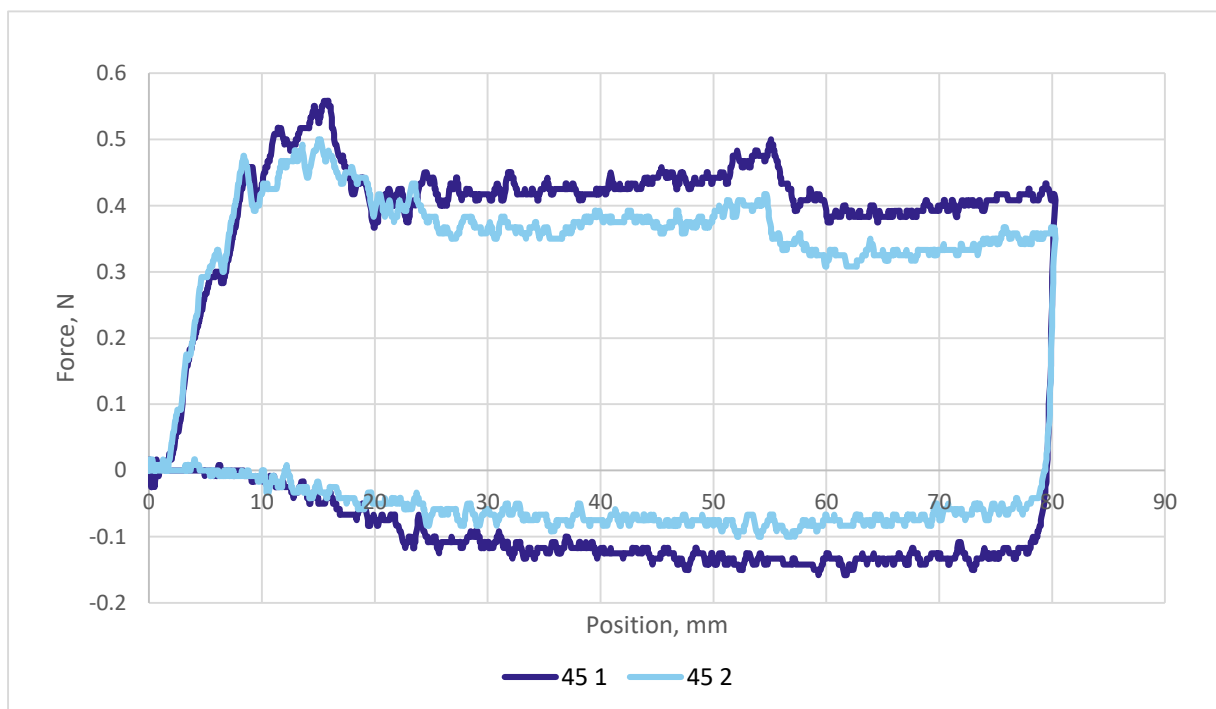


Figure 8-40 Force response for needle insertion at 150 mm/min through inhomogeneous laminate surrogate

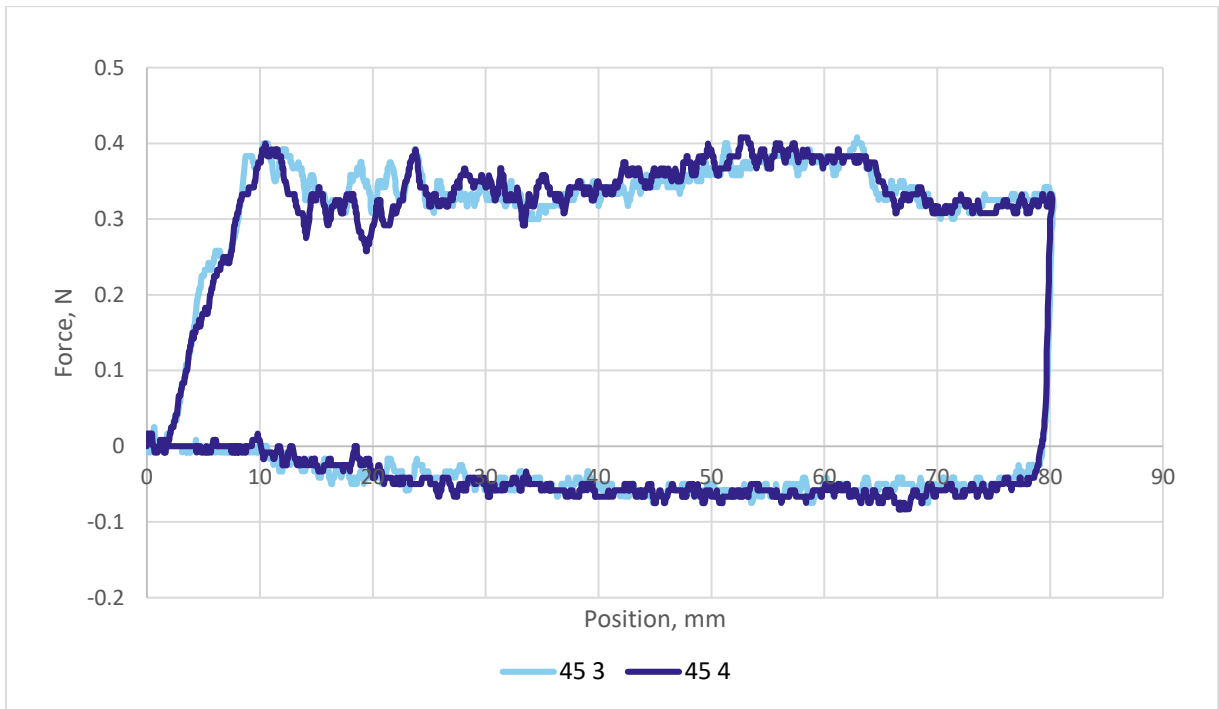


Figure 8-41 Force response for needle insertion at 150 mm/min through inhomogeneous laminate surrogate

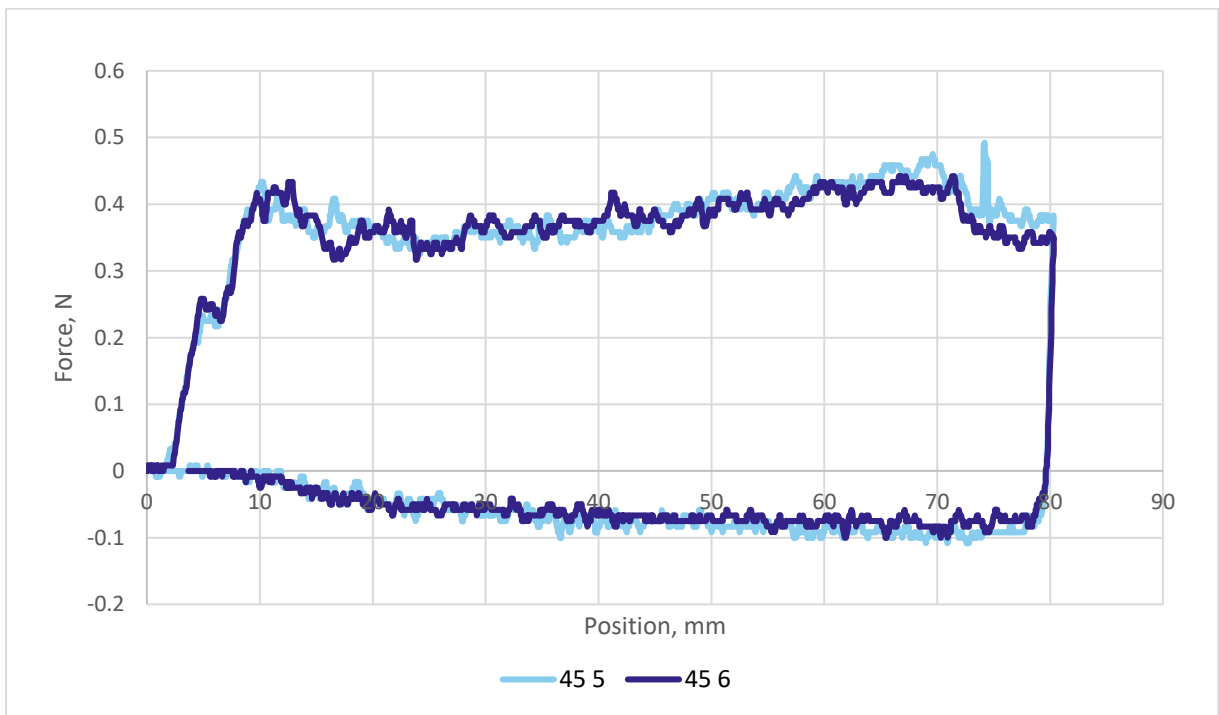


Figure 8-42 Force response for needle insertion at 150 mm/min through inhomogeneous laminate surrogate

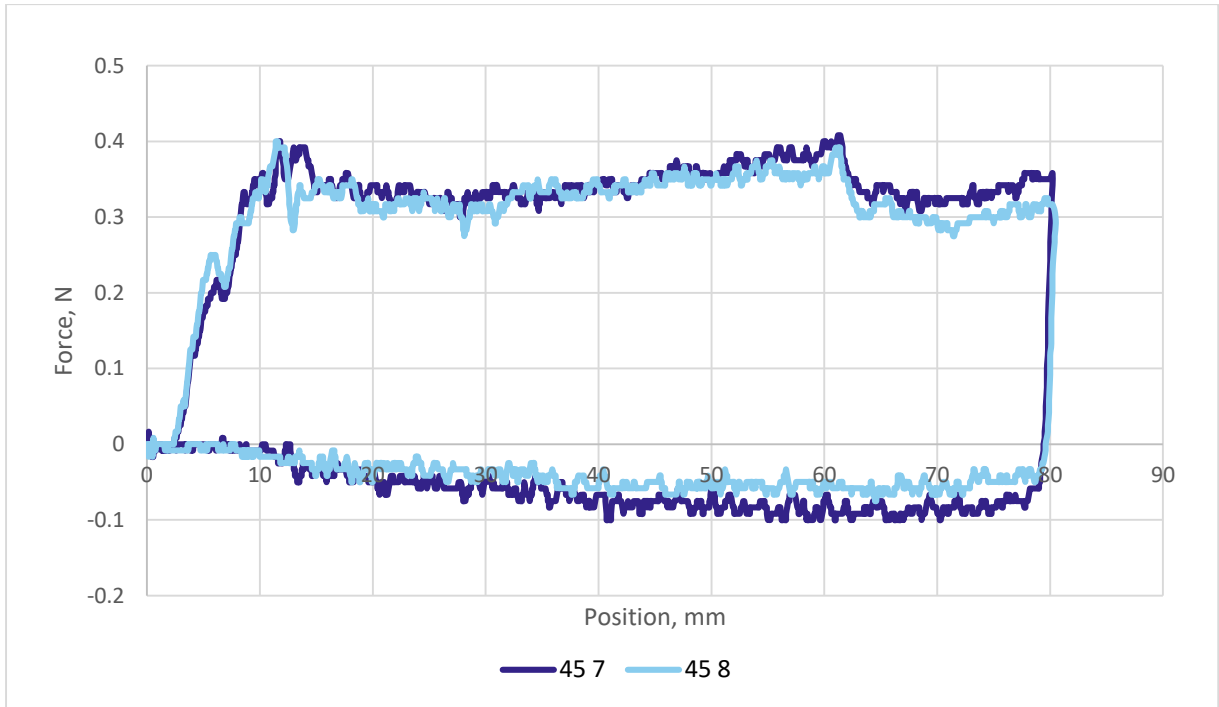


Figure 8-43 Force response for needle insertion at 150 mm/min through inhomogeneous laminate surrogate

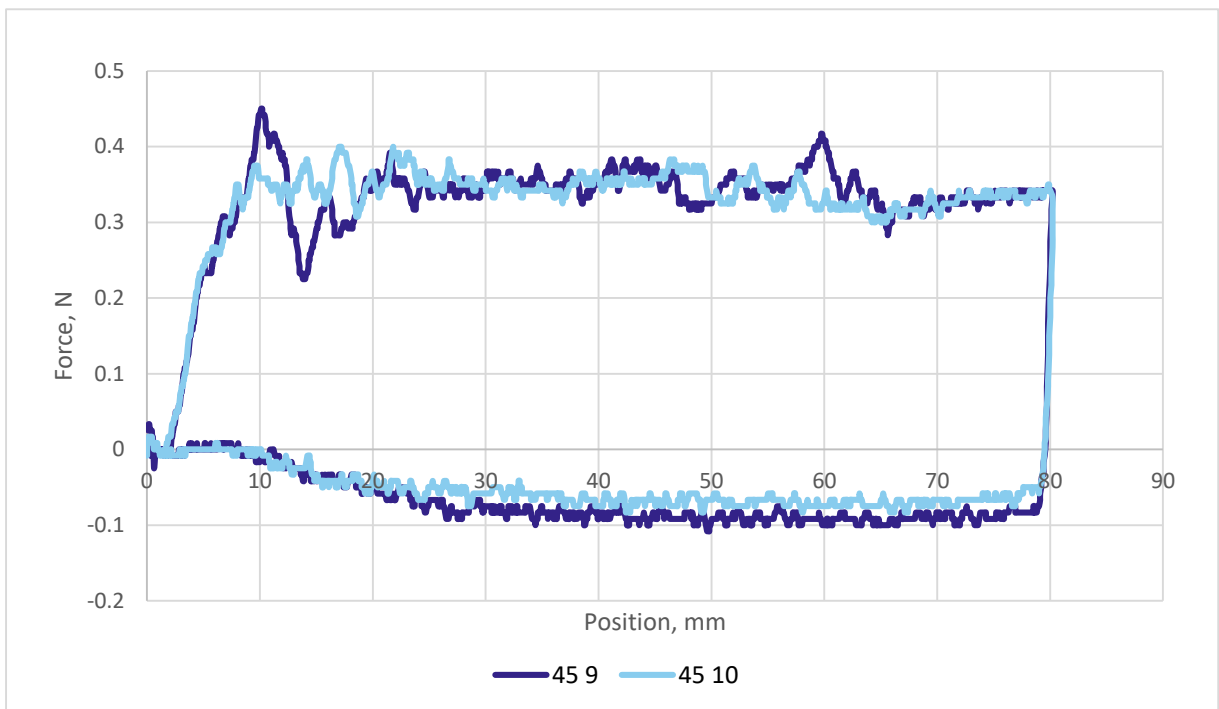


Figure 8-44 Force response for needle insertion at 150 mm/min through inhomogeneous laminate surrogate

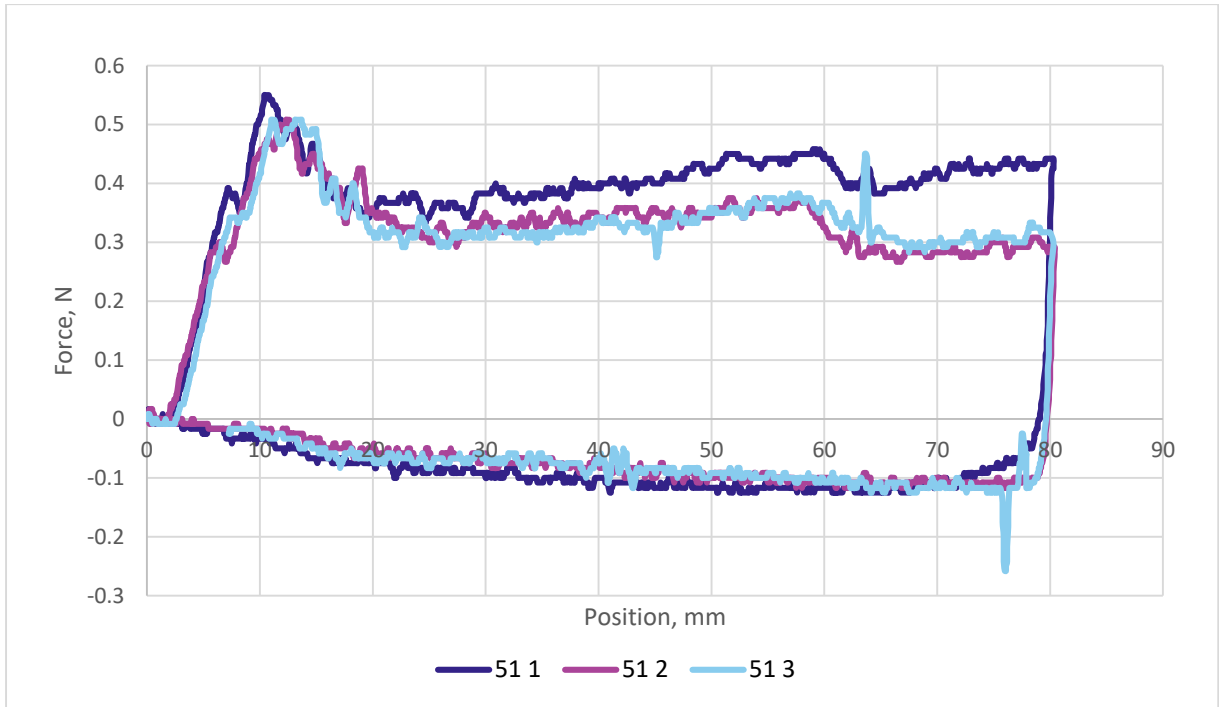


Figure 8-45 Force response for needle insertion at 150 mm/min through inhomogeneous laminate surrogate

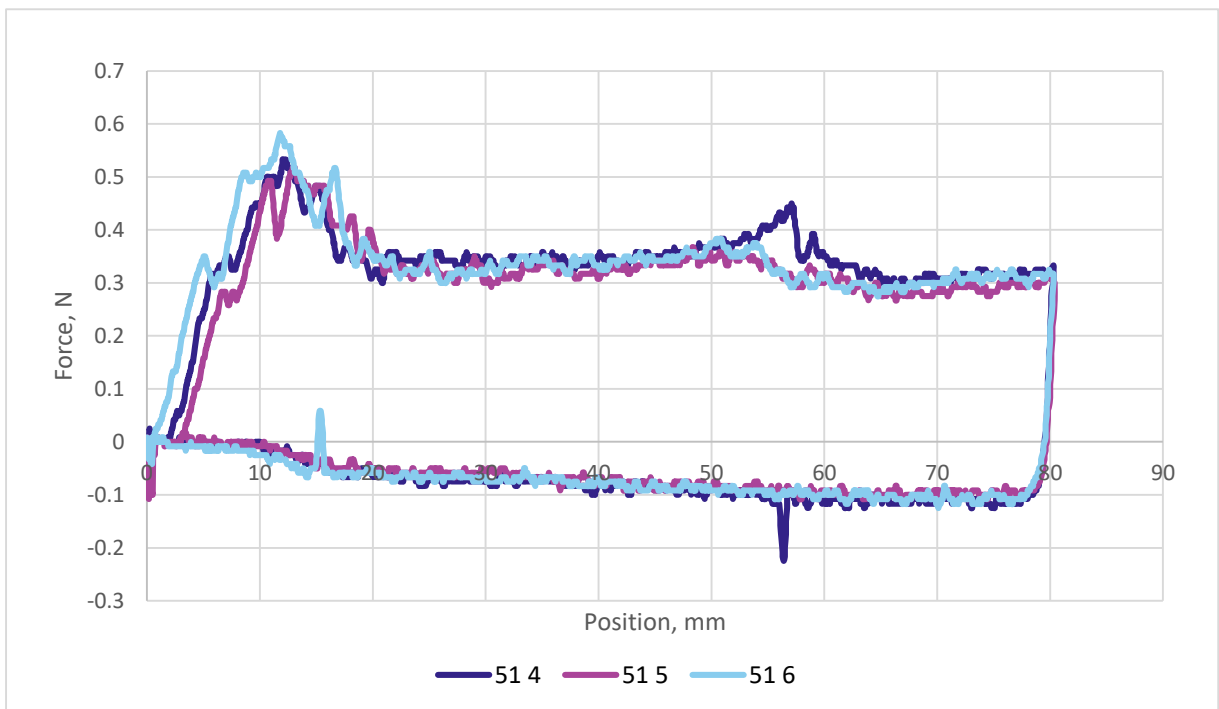


Figure 8-46 Force response for needle insertion at 150 mm/min through inhomogeneous laminate surrogate

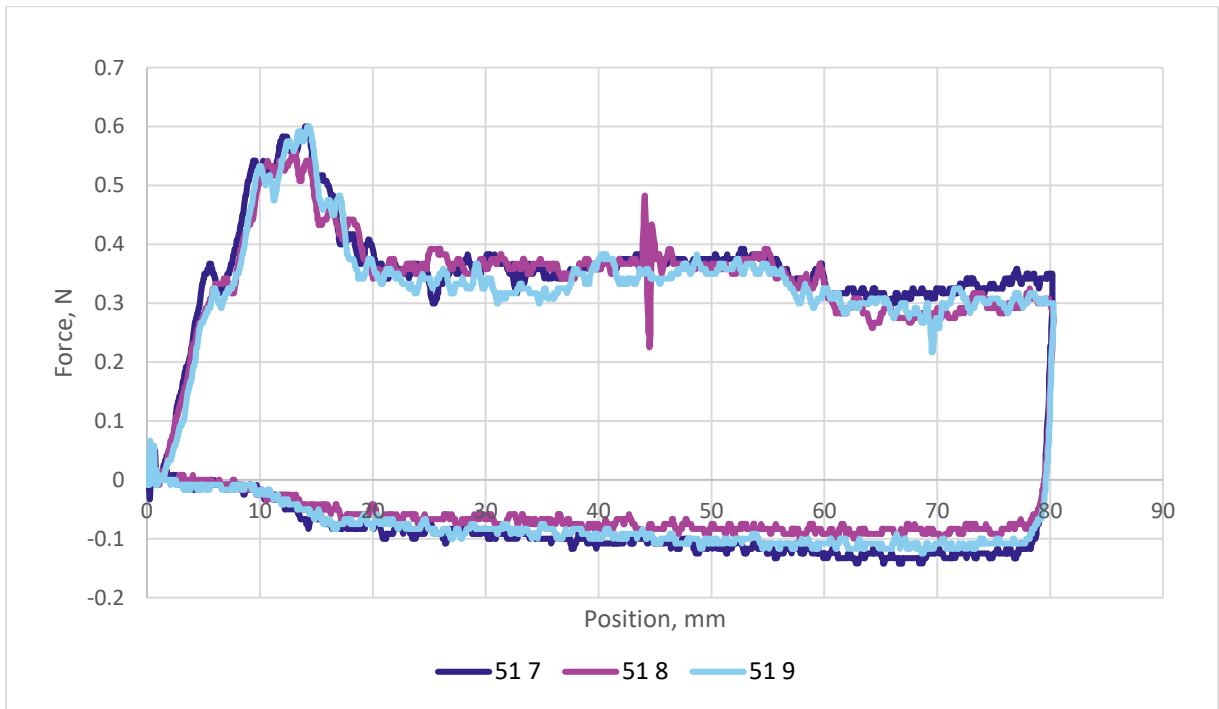


Figure 8-47 Force response for needle insertion at 150 mm/min through inhomogeneous laminate surrogate

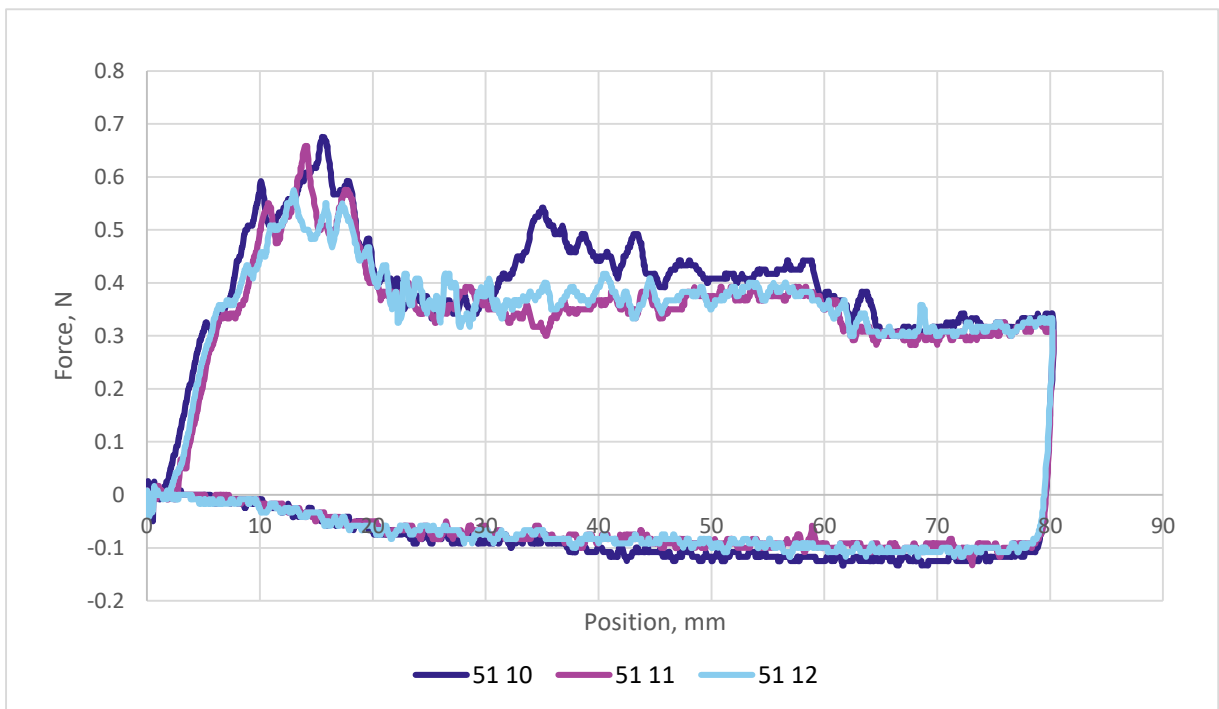


Figure 8-48 Force response for needle insertion at 150 mm/min through inhomogeneous laminate surrogate

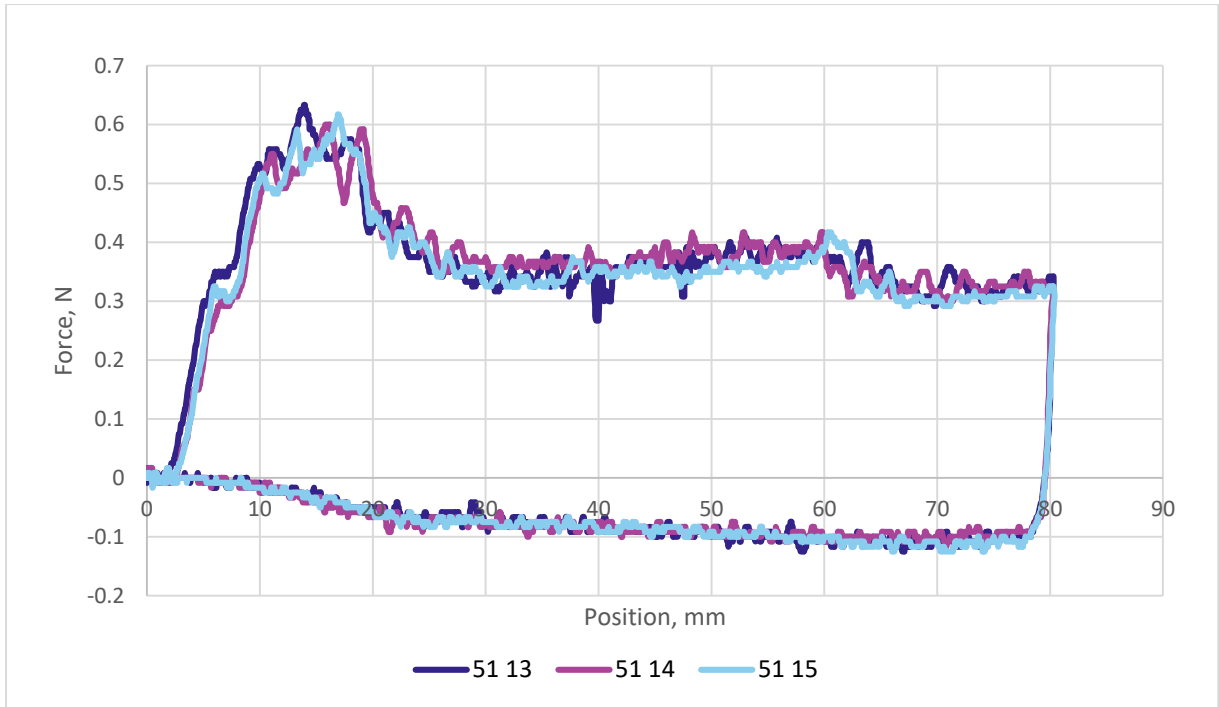


Figure 8-49 Force response for needle insertion at 150 mm/min through inhomogeneous laminate surrogate

8.3.2 Needle response through inhomogeneous particulate surrogates

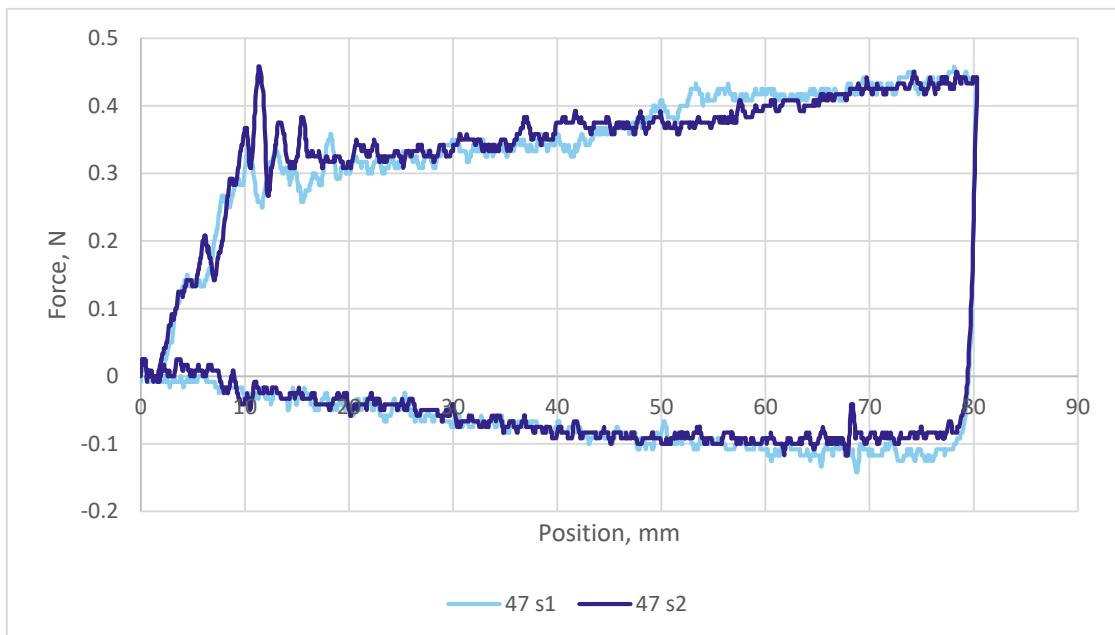


Figure 8-50 Force response for needle insertion at 150 mm/min through inhomogeneous particulate surrogate

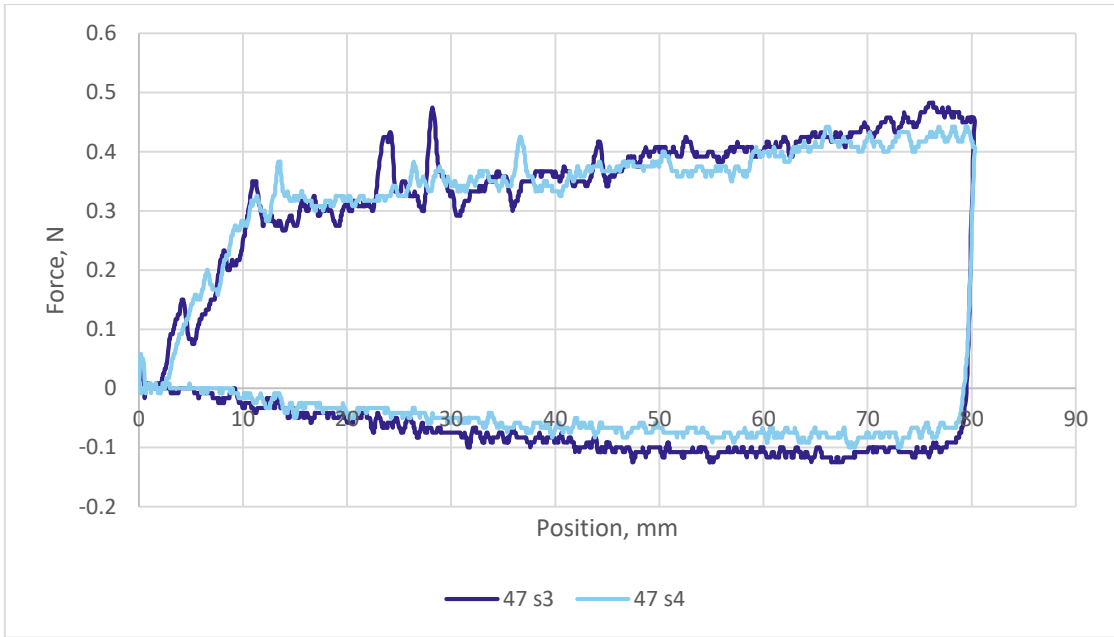


Figure 8-51 Force response for needle insertion at 150 mm/min through inhomogeneous particulate surrogate

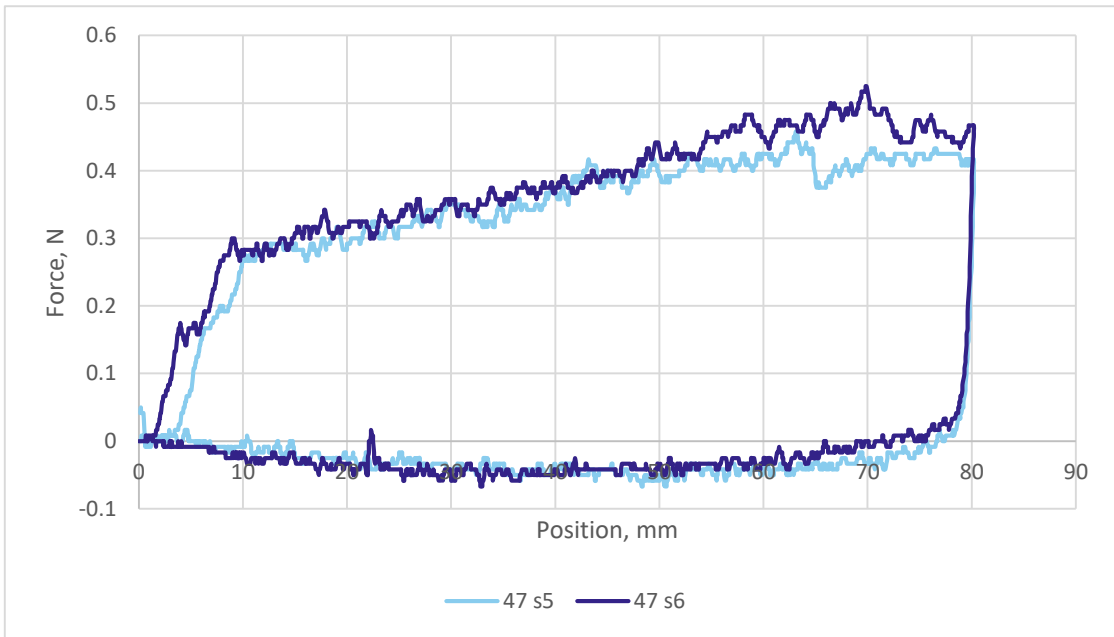


Figure 8-52 Force response for needle insertion at 150 mm/min through inhomogeneous particulate surrogate

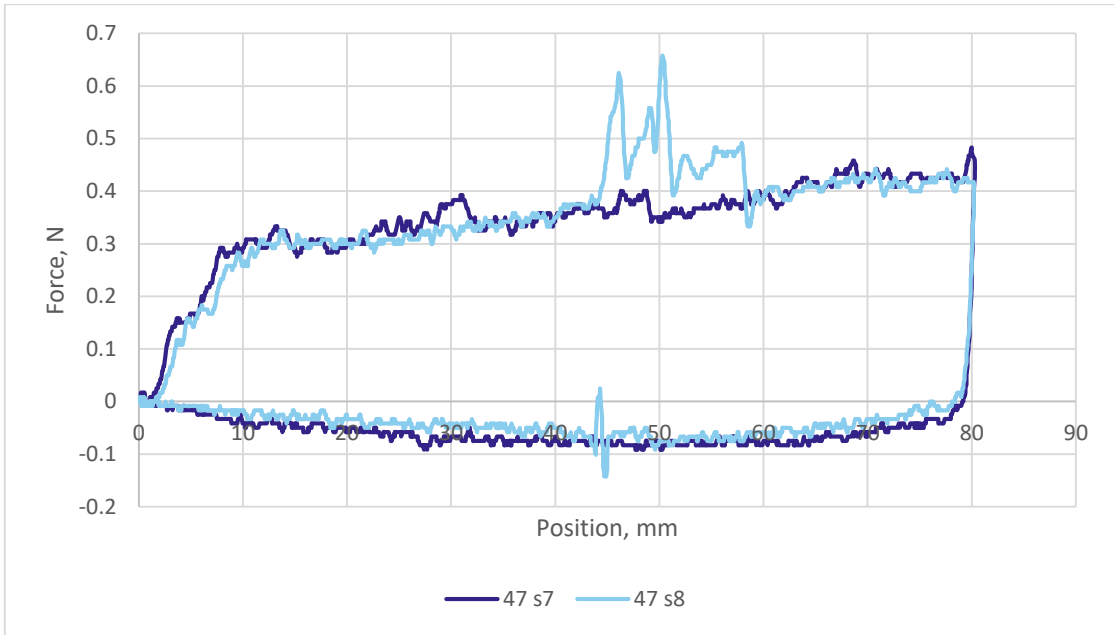


Figure 8-53 Force response for needle insertion at 150 mm/min through inhomogeneous particulate surrogate

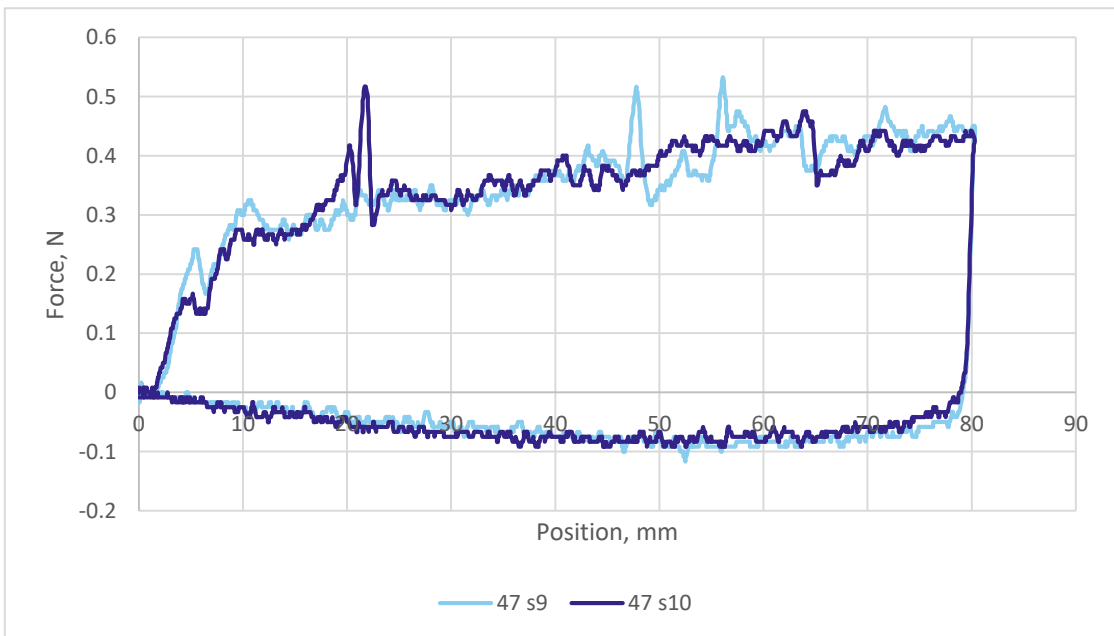


Figure 8-54 Force response for needle insertion at 150 mm/min through inhomogeneous particulate surrogate